

A geochemical study of the Theta Reef of
the Frankfort Mining Complex
in the
Sabie-Pilgrim's Rest Goldfield
South Africa

By
Alexander Richard Metz

Submitted in fulfilment of the degree Master of Science

In the Discipline of Geological Sciences

School of Agricultural, Earth and Environmental Sciences

College of Agriculture, Engineering and Science

University of KwaZulu-Natal,

Durban

South Africa

2015

Abstract

For over a century the Sabie-Pilgrim's Rest Goldfield has been one of the most important gold producers in South Africa. The epigenetic gold deposits are situated at the eastern escarpment of the Eastern Transvaal Drakensberg, approximately 60 km away from the eastern rim of the Bushveld Igneous Complex.

The Theta and Bevets Reef of the Frankfort Mining Complex occur within the Neoarchean dolomite of the Malmani Subgroup and the Paleoproterozoic Pretoria Group, respectively, of the Transvaal Supergroup. While the Theta Reef is situated in the dolomites of the Eccles Formation of the Malmani Subgroup, the Bevets Reef is situated at the contact between a conglomerate, also called the Bevets Conglomerate and the shales of the Rooihoopte Formation of the Pretoria Group, therefore providing two different environments for the ore mineralisation.

The ore-bearing reefs are represented by quartz-carbonate veins. The ore minerals are pyrite, arsenopyrite, chalcopyrite and minor amounts of minerals of the tetrahedrite-tennantite series. The reefs were emplaced along thrust faults developed parallel to bedding which dips at 4-7° west towards the Bushveld Complex. The thrusts are attributed to forces related to the emplacement of the intrusion.

Stable isotope geochemistry revealed that isotopes within a single mineral phase and between two phases are not in isotopic equilibrium. This suggests an episodic mineralisation of the ore-bearing quartz vein.

Oxygen and carbon isotopic compositions of 10.9 – 13.8 (fluid) and -4.1 - -2.8 ‰ (calcite), respectively, indicate that the ore forming fluids are most likely of igneous origin and interacted with the rocks of the Transvaal Supergroup. Sulphur isotopic compositions of -1 – 2.3 ‰ (sulphides) show that fluids and metals seem to have originated from the Bushveld Complex.

Trace element analysis of ore samples from the most northern section of the Theta Reef shows that the gold content within pyrite is generally low. The common trace elements are Cu, As, Ag Sb, Au, Pb and Bi, occurring as minerals or mineral inclusions of the tetrahedrite-tennantite series. Gold occurs as invisible solid solution and/or as Au-As and/or Au-Sb compound in arsenic rich sulphide minerals and occasionally in association with silver as electrum.

The research shows that the intrusion of the Bushveld Complex played a major role in the formation of the gold deposits in the Sabie-Pilgrim's Rest area being responsible for the mineralizing hydrothermal fluids, the ore metals, the heat budget for the hydrothermal cell and the forces that created the thrust faults that acted as pathways for the circulation of the mineralizing fluids. The circa 2.055Ga age of the Bushveld Complex also provides a maximum age for the Au-mineralization.

Preface

The experimental work described in this thesis was carried out in the School of Geological Sciences, University of KwaZulu-Natal, Westville, from March 2011 to November 2014, under the supervision of Prof. McCourt and Prof. Elburg.

These studies represent original work by the author and have not otherwise been submitted in any form for any degree or diploma to any tertiary institution. Where use has been made of the work of others it is duly acknowledged in the text.

As the candidate's supervisor I have approved this thesis for submission and examination.

Signed: _____ Name: _____

Date: _____

As the candidate's co-supervisor I have approved this thesis for submission and examination.

Signed: _____ Name: _____

Date: _____

Signed: _____ Name: _____

Date: _____

Declaration 1 – Plagiarism

I, Alexander Richard Metz declare that:

1. *The research reported in this thesis, except where otherwise indicated, is my original research.*
2. *This thesis has not been submitted for any degree or examination at any other university.*
3. *This thesis does not contain other persons' data, graphs or other information, unless specifically acknowledged as being sourced from other persons.*
4. *This thesis does not contain any other persons writing, unless specifically acknowledged as being sourced from other researchers. Where other written sources have been quoted then:*
 - a. *Their words have been re-written but the general information attributed to them has been referenced*
 - b. *Where their exact words have been used, then their writing has been placed in italics and inside quotation marks, and referenced.*
5. *This thesis does not contain text, graphics or tables copied from the Internet, unless specifically acknowledged, and the source being detailed in the thesis and in the References section.*

Signed: _____ Name: _____

Date: _____

Contents

1. Introduction	1
1.1 General Background	1
1.2 Locality	1
1.3 Geological Setting	3
1.4 Objective and Rationale	5
1.5 Methodology	6
1.5.1 Field Study	
1.5.2 Ore Microscopy and Microscopy	
1.5.3 Geochemistry	
1.6 Historical Review	7
1.7 Literature Review	9
2. Regional Geology	12
2.1 Transvaal Supergroup	12
2.2 Pretoria Group	16
2.3 Dykes and Sills	16
2.4 Bushveld Complex	17
2.5 Age of gold mineralisation within the Transvaal Supergroup	18
3. Bushveld Complex related structures in the Transvaal Supergroup	19
3.1 Bedding	20
3.2 Thrust Faults	21
3.3 Joints	22
3.4 Boudin structures	27
3.5 Discussion	28

4. Ore Mineralisation	31
4.1 The ore-bearing quartz-carbonate vein of Theta- and Bevets- Reef	31
4.2 Ore Mineralogy of the Theta- and Bevets- Reef	33
4.2.1 Methodology	33
4.2.2 Pyrite	34
4.2.3 Arsenopyrite, chalcopyrite and tetrahedrite	40
4.3 Gangue mineralogy of the Theta Reef	42
4.3.1 Methodology	42
4.3.2 Quartz and carbonates within the mineralised quartz carbonate vein	42
4.4 Discussion	44
5. Trace element analysis of sulphide minerals	46
5.1 Methodology	46
5.2 Results	47
5.2.1 Trace elements in sulphide minerals	47
5.2.2 Trace elements associated with Au	53
5.3 Summary	57
6. Pb-Pb Isotopes	58
6.1 Methodology	58
6.2 Results	59
6.3 Discussion	60
7. Stable Isotope Geochemistry	64
7.1 Methodology	70
7.2 Oxygen Isotopes	72
7.2.1 Results	72

7.2.2 Discussion	73
7.3 Carbon isotopes	80
7.3.1 Results	80
7.3.2 Discussion	81
7.4 Sulphur Isotopes	85
7.4.1 Results	85
7.4.2 Discussion	86
7.5 Summary	90
8 Discussion and conclusions	91
8.1 Discussion	91
8.2 Conclusions	94
Acknowledgement	95
9. References	97
10. Appendices	111

1 Introduction

1.1 General Background

The Sabie-Pilgrim's Rest Goldfield is the second oldest gold mining district in South Africa and the oldest in the Transvaal. Gold prospecting started as early as 1872 and mining operations are with minor interruptions ongoing until present.

The Theta Reef, together with the Bevets Reef, form the Frankfort Mining Complex. The Theta Reef is hosted by the Eccles Formation, the uppermost unit of the Malmani Subgroup, while the Bevets Reef is hosted in the lower most unit of the Pretoria Group, the Rooihoopte Formation.

Over the past decades, the area has become an important producer of timber and forest products. Reforestation has affected large areas of land, covering the traces of the mining activities within the goldfield.

1.2 Locality

The study area lies within the Sabie-Pilgrim's Rest Goldfield (SPRG), which is located at the eastern escarpment of the Transvaal Drakensberg in the Ehlanzeni magisterial districts in the province of Mpumalanga, South Africa (Fig. 1.2). The towns of Sabie, Pilgrim's Rest and Graskop lie within the study area, ~70 km north of the city of Mbombela (Nelspruit). The study area is best accessible via the R36, R37, R532, and the R533. Secondary dirt roads and roads used by the mining and forestry companies leading off the main roads provide access to remote areas and to the mines. The Frankfort Mining complex is located along the dirt road from Pilgrim's Rest to Vaalhoek, ~20 km north of Pilgrim's Rest.

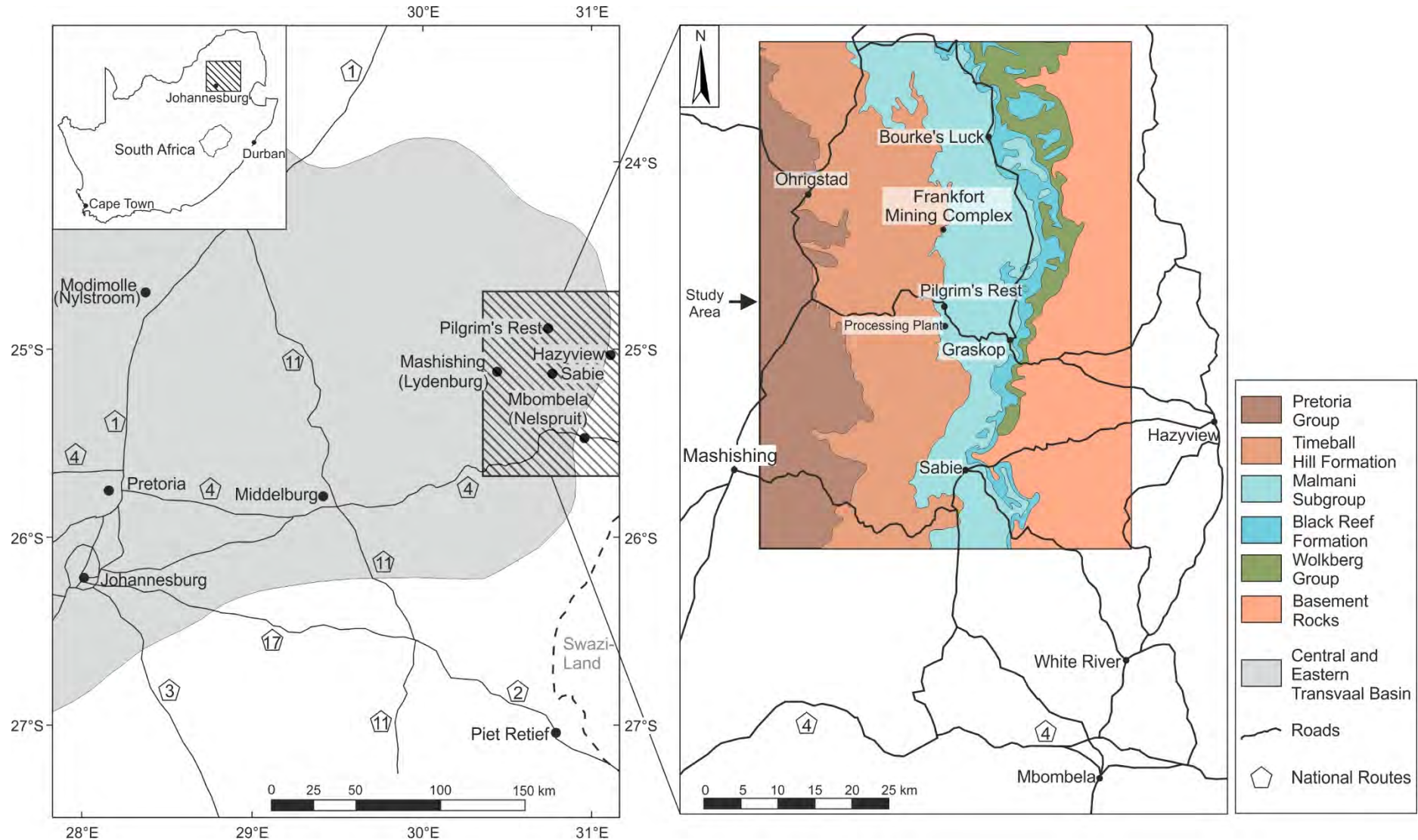


Figure 1.2: Maps showing the geographic location and simplified geology of the study area in relation to the Transvaal Basin (after Harley, 1993; Cawthorn et al., 2006).

1.3 Geological Setting

The Sabie-Pilgrim's Rest Goldfield is the third largest gold producer in South Africa and extends over an area of 600 km² (Boer, 1995). The lithologies present within the goldfield are members of the late Archaean to early Proterozoic Transvaal Supergroup, an approximately 15 km thick series of low-grade metamorphic clastic and chemical sedimentary rocks and volcanics (SACS, 1980), overlying the Archean granitic basement. The sediments were deposited into the Transvaal Basin, one of three structural basins on the Kaapvaal Craton in which rocks of the Transvaal Supergroup are preserved (Eriksson et al., 2006). The Transvaal Supergroup is subdivided into four lithostratigraphic units, namely Wolkberg Group (oldest), Black Reef Formation, Chuniespoort Group and Pretoria Group (youngest), of which the Chuniespoort Group hosts most of the horizontal ore-bearing reefs, of the SPRG (Fig 2.1) (Zietsman, 1967; Boer, 1995).

It is thought that the intrusion of the 2.05 Ga Bushveld Complex (BC) (Fig 1.3) at 2.05 Ga generated the hydrothermal cell that resulted in the ore mineralisation within the Sabie-Pilgrim's Rest Goldfield (Boer, 1995). Although the Bushveld Complex lies in the centre of the Transvaal Basin, some 60 km away from the goldfield (Fig 1.3), it caused low-grade thermal metamorphism within the stratigraphy of the Chuniespoort Group and the lower Pretoria Group (Button, 1986) in the SPRG area, and had an impact on the regional dip of- and jointing within- the country rocks (Visser & Verwoerd, 1960; Harley and Charlesworth, 1994, 1996; Perritt & Roberts, 2007).

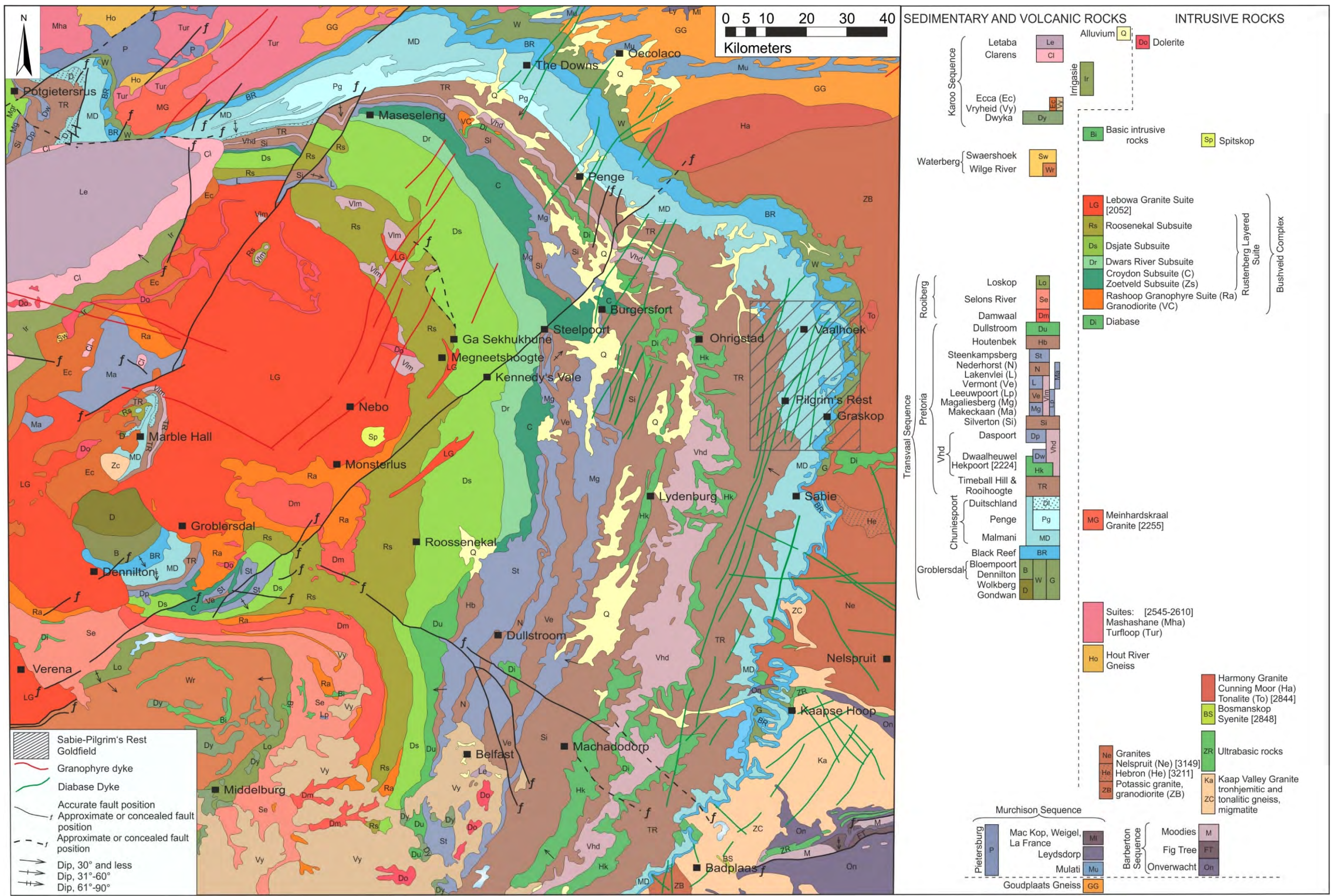


Fig 1.3: Geological map of the eastern limbs of the Bushveld Complex and the eastern Escarpment of the Transvaal Drakensberg (modified after: Geological Map of South Africa, Department of Mineral and Energy affairs. S.J.P Du Plessis et al., 1984)

1.4 Objective and Rationale

The project was based at the University of KwaZulu-Natal in Durban and carried out in cooperation with Stonewall Resources, a Pretoria based mining company who currently hold the mining rights for the Sabie-Pilgrim's Rest Goldfield. Research was concentrated on the Theta Reef of the Frankfort Mining Complex, the only active underground mining operations at the time. The work has been focussed on the most northern section of the reef, where fresh exposures allowed reef mapping and sampling. Representative samples from the Bevets Reef waste dump were collected in order to gain information about the variation between the reefs located within different host rocks.

The aim of the research was to investigate the geochemical characteristics of the ore of the Theta Reef with the latest methods and techniques, in order to reveal a possible source of the fluids and the metals, forming these unique deposits.

The objectives of this study are:

1. To provide a simplified structural analysis of major structures within the Sabie-Pilgrim's Rest Goldfield and to assess the possible impact of Bushveld Complex on the goldfield, and the possible correlation between the vein emplacement of the Theta Reef and these regional structures.
2. A detailed description of the ore-bearing quartz-carbonate veins of the Theta Reef, including reef mapping, petrography and the geochemistry of the sulphide minerals, in order to gain an understanding of the ore forming processes.
3. To collect evidence for a possible link between the gold deposits of the Sabie-Pilgrim's Rest Goldfield and the Bushveld Complex as a source for ore metals and fluids.
4. To compare the Theta Reef with other horizontal and vertical reefs of the SPRG, with special emphasis on the stratigraphically higher Bevets Reef.

1.5 Methodology

1.5.1 Field Study

Geological field mapping of the Chuniespoort Group and the lower Pretoria Group of the Transvaal Supergroup in the Sabie-Pilgrim's Rest Goldfield was carried out under complicated circumstances. Illegal mining activities, mining riots and delays in the admission of the underground mining licenses for the area, restricted the mapping area to road cuts and the area in proximity to the Stonewall gold processing plant (Fig. 1.2.1). Underground mapping was restricted to the Theta Reef of the Frankfort Mining Complex, the only operational mine at the time. A structural interpretation of inaccessible areas was undertaken on Google Earth (www.earth.google.com) satellite images. The structural data collected was processed and plotted using the *Dips* software package (www.rocscience.com).

1.5.2 Ore Microscopy and Microscopy

Ore microscopy has been performed using reflected light microscopy on polished stubs from various reef horizons and localities within the northern section of the Theta Reef and stubs from the Bevets Reef waste dump. Gangue minerals were studied in thin sections using transmitted light microscopy.

1.5.3 Geochemistry

Trace elements analysis of sulphide minerals was carried out on the same polished stubs as used for the ore microscopy. Trace element contents were determined using LA-ICP-MS (laser ablation inductively coupled plasma mass spectrometry) at the University of Kwa-Zulu Natal and element concentrations were calculated in ppm with the data reduction software GLITTER (www.glitter-gemoc.com). To confirm the internal FeO standard setting for the data reduction, electron microprobe analysis has been performed on some sulphides. The concentration of the most abundant isotopes of Pb (on masses: 206, 207 and 208) were, furthermore, used for isotope analysis.

Stable isotopes were analysed, including oxygen, sulphur and carbon isotopes, using a Finnigan Mat 252 gas source mass spectrometer for O- and a Thermo Quest Delta+XL mass spectrometer for C- and S-isotopes Tübingen University in Germany.

1.6 Historical Review

Since 1872 the Sabie-Pilgrim's Rest Goldfield (SPRG) has produced a total of 168 tons of gold and is, therefore, the third largest gold producer in South Africa (Boer et al., 1995)

The first discovery of gold in the area was in 1868 by Karl Mauch. Further discoveries followed in 1871 and 1872 by Edward Button and Tom MacLachlan. They explored the farms around Pilgrim's Rest and started panning for gold. Gold digging in the area became economical in 1873, with the discovery of alluvial gold in the local rivers (Herring, 1928). In 1875 the gold rush hit Pilgrim's Rest and it became a booming city with over 2000 habitants (Fowler, 1968). In the same year the largest nugget to date, with a weight of 283 ounces (8.8kg), was found in the Pilgrim's Creek (MacKenzie, Mine Report, date unknown).

In 1880, after the alluvial gold search became less successful, numerous small companies started underground mining and worked gold-bearing quartz-rich vein horizons in the surrounding mountains. The companies were able to process greater amounts of ore, with the introduction of stamp batteries and set the basis for the Transvaal Mining Estate (TGME) which was founded in 1886 (Fowler, 1968). TGME then restructured the mining economy in the goldfield and replaced all smaller stamp batteries with one sixteen-stamp mill. Allowing the production to be economically more viable, this structure became a great success. Furthermore, low grade ores could be processed profitably, by mixing them with high grade ores (Boer, 1995; MacKenzie).

With the exception of the British annexation of the Transvaal in 1877, the Sekhuni wars between 1876 and 1879 and the Anglo-Boer war from 1880-1881, where mining came almost to a complete stand-still, operations were kept open until 1971 (Fowler, 1968).

Over the years several mining companies were formed, but generally ended up being incorporated into TGME. Rand Mines restarted operations in 1981 by reprocessing old sand slime and rock dumps. A joint venture of Randgold TGME (former Rand Mines) and Simmer & Jack Mines Ltd. started underground mining operations in the area between the farms of Morgenlon and Frankfort. Simmer & Jack became the parent company of TGME in 1999 and was managed by Cheston Minerals (Boer, 1995).

Following the acquisition of TGME Simmer & Jack Mining by the Stonewall Resources in 2011, the Sabie-pilgrim's Rest Goldfield experienced renewed interest.

Since 2011 Stonewall Resources produces gold from the TGME Project tailing operation.

The company produced 11,000 oz/a of gold as a product of tailing and small scale underground operations in 2012 with the target of 40,000 oz/a at the end of 2013. The future plan is to increase production up to 205,000 oz/a in the year 2016 (Stonewall Resources, 2010).

Silver has been mined as a by-product occurring within the mineral electrum. Asbestos, occurring along contact zones of dykes and sills was mined near the village of Graskop, on the farm Normadale (north-west of the farm Frankfort) and at Olifantsgeraamte Asbestos Mine (Zietsman, 1964). Pyrite was mined at Nestor Mine during the Second World War for the production of sulphuric acid (Boer, 1995).

1.7 Literature Review

The first scientific publications on the Sabie-Pilgrim's Rest Goldfield were by Cohen (1883), describing alluvial diggings for gold. About eleven years later O'Donoghue (1884) discovered gold-bearing quartz veins, hosted in the dolomites and set a new research focus for subsequent studies (Penning, 1885; Garnier, 1896; Kuntz, 1896; Bordeaux, 1897; Bousquet, 1897; Krause, 1897).

The first geological overview and economic review of the SPRG was produced by Gray (1905) and got further improved by Hall (1910) and Wyberg (1925). Hall (1910) created the first geological map of the area. Reinecke and Stein (1929) were the first to recognize a close correlation between the ore, the structures and the lithologies in the area and also investigated the relationship between the mineralising fluids and a granitic intrusion. This idea was the basis for one of three models regarding the fluid and metal source. Swiegers (1949) supported this model and published a more detailed description of the orebodies, including the mineralogy and mineral distribution and the ore textures to find more proof. Barnard (1958) extended the model of Reinecke and Stein (1929) and focused on the Bushveld Complex as a possible fluid source and documented the mesothermal character of the deposits in the Sabie-Pilgrim's Rest Goldfield. This model was largely accepted by Visser and Verwoerd (1960), Zietsman (1964,1967), Tyler (1989), Harley and Charlesworth (1992), Harley (1993), Boer (1995) and Meyer et al., (1995) Geological observations within the goldfield between the years 1936 and 1959 were compiled by Joubert, Muller, Söhngé, Verwoerd and van Zyl and published by Visser and Verwoerd (1960) as an interpretation of the Sheet 22, a 1:125,000 map of the Union of South Africa Geological Series, showing the area north of Nelspruit. It was Joubert (Visser and Verwoerd, 1960), who suggested a second model in which the local sills and dykes were considered to be hydrothermal cell, resulting in the mineralisation of the ore deposits of the Sabie-Pilgrim's Rest Goldfield. In this model the mineralising fluid is a mixture of connate waters and metals, leached out of the strata of the Transvaal Sequence. This model was investigated further by Ash and Tyler (1986), Minnit et al., (1973) and Meyer (1988).

As a result of decreasing ore reserves TGME introduced a geological research program which commenced in 1961. A. L. Zietsman assisted Rand Mines Limited in

conducting geological mapping, the reprocessing of mine records and underground plans and geochemical prospecting. Some of these results were incorporated into a M.Sc. thesis (Zietsman, 1964). During this study Zietsman recognised the relationship between the structural geology and deposition of the gold bearing quartz veins. Zietsman continued with a more detailed study of these relationships and their influence on ore genesis and ore control, combined with a detailed description of some individual orebodies (Zietsman 1967). Minnit (1973) studied the gold content in argillaceous sediments from the Wolkberg Group and Black Reef-Formation north of the Sabie-Pilgrim's Rest Goldfield. High gold values, especially within the carbonaceous silt-shale rocks lead to the conclusion that such sedimentary rocks could be the proto-ore of the deposits within the SPRG.

After a rather quiet time in the 1980's concerning research in the Sabie-Pilgrim's Rest goldfield, renewed interests lay within the field of geochemistry. Ash and Tyler (1986) undertook fluid inclusion and stable isotope analysis. The isotopic signature of quartz and pyrite from different mines lead to the conclusion that the ore forming fluids share the same source (Ash and Tyler, 1986). The authors suggested three possible sources for the fluids, volcanic activity during the deposition of the Pretoria Group, the Bushveld Complex or metamorphic devolatilisation of the underlying stratigraphy. Tyler (1986) recognised multiple phases of ore mineralisation and concluded that mineralisation took place at a depth of approximately 5.5 to 7.0 km. In a sedimentological study, Tyler (1989) established a close relation between auriferous veins and shale horizons.

Meyer (1986 and 1988) undertook detailed ore-microscopy on ore from various mines and concluded that ore mineralisation was less complex in Olifantsgeraamte Mine than in the Bevets- or Theta- Reef of the Frankfort Mining Complex. Meyer (1988) also examined different pyrite populations within the quartz vein and shales showing genetic similarities. Meyer confirmed the study by Minnit (1973) indicating that shales within the goldfield have high gold as well as arsenic and copper contents.

Harley and Charlesworth (1992) and Harley (1993) focused their research on the structural evolution of the Elandshoogte Mine, south of Sabie, and came to the conclusion that the bedding-parallel thrusts are a result of the emplacement of the Bushveld Complex. These bedding-parallel thrusts acted as a fluid valve system and finally as the host for the ore-bearing reef. The physico-chemical aspects of the

goldfield were investigated by Boer (1995), who suggested that the Bushveld Complex was the main heat source and the source of a juvenile fluid, transporting the metals, which resulted in the formation of the SPRG. Boer (1995) also concluded that gold precipitated either from a bisulphide- or a chloride- complex as a result of a decrease in sulphur activity caused by sulphide precipitation and changes in the chemistry of the fluid due to fluid immiscibility. Boer (1995) interpreted the stable isotope composition of the ore bearing vein, the lack of evidence for an influence of meteoric water, high Au content with an average of 8.3 g/t and the ore shoot patterns, the sheeted nature of the veins, indicating periodically opening and quartz precipitation events, interrupted by episodes of deformation, typical characteristics of the deposits of the SPRG as mesothermal. However, not all characteristics of the mineralisation are typical for mesothermal deposits, e.g. the possible relation to the large layered mafic intrusion of the Bushveld Complex and its satellites (Boer, 1995). Meyer et al. (1996) investigated the relationship between shale horizons and the ore bearing reefs, indicated by Tyler (1989), further. Meyer (1996) also considered the possibility, that during the diagenesis of the shales, metals can be extracted from the seawater by circulating fluids.

2 Regional Geology

2.1 Transvaal Supergroup

The basal unit of the Transvaal Supergroup within the Sabie-Pilgrim's Rest Goldfield is formed by the poorly preserved Wolkberg Group, which unconformably overlies the 3104 ± 3 Ma (Kamo & Davis, 1994) Nelspruit batholith (Robb et al., 2006). The protobasinal Wolkberg Group consists of immature sandstones, conglomerates and a unit of fine grained sedimentary, argillaceous and carbonate rocks, interbedded with volcanics (Button, 1973b; Eriksson et al 2006). The time equivalent of the Wolkberg group, the Buffelsfontein Group on the north western margin of the Transvaal Basin, suggests an age of ~2.66 Ga for the Wolkberg Group (Armstrong et al., 2001; Eriksson et al., 2006).

The Black Reef Formation separates the Wolkberg Group from the overlying Chuniespoort Group and consists of mature quartz arenites, conglomerates and mudrocks. The deposition of this formation was controlled by continental rifting and thermal subsidence causing deepening and extension of the Transvaal Basin (Meyer & Robb, 1996). The upward fining siliciclastic sedimentary series progresses from matrix supported conglomerates through trough and planar cross-bedded sandstones to arenites and carbonaceous mudstones (Henry et al., 1990) and disconformably overlies the Wolkberg Group (Boer, 1995; Good 1999). In some areas detrital gold has been recovered from conglomerates of the Black Reef Formation (Coetzee, 1976).

The ~2588-2480 Ma Chuniespoort Group (Eriksson et al., 2006), as exposed within the area, consists of four formations, namely, Oaktree, Monte Christo, Lyttelton, Eccles, also referred to as the Malmani Subgroup. The fifth member, the Frisco Formation is missing within the stratigraphy of the goldfield (Harley, 1993). Based on the zircon ages for the Oaktree Formation (2588 ± 6 Ma) Martin et al. (1998) suggested a hiatus between the Oaktree- and the underlying Black Reef Formation (assuming an age of 2642 ± 3 Ma for the Black Reef Formation).

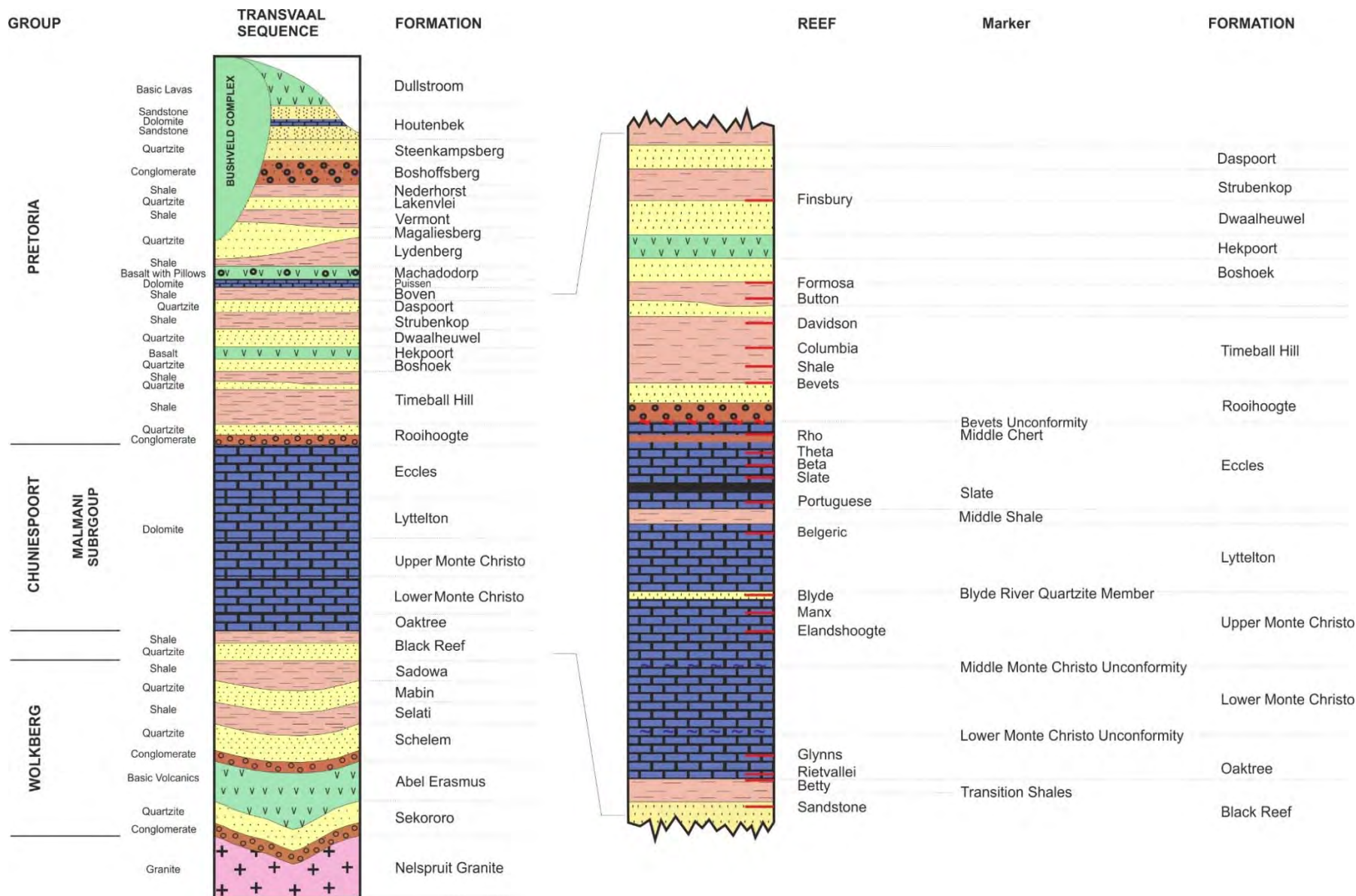


Figure 2.1: Stratigraphy of the Pilgrim's Rest area, with special reference to the mineralised reefs in the Malmani Subgroup and the lower part of the Pretoria Group (unpubl. mine report from Stonewall Resources Ltd).

The classification of the formations largely dependent on the chert content and the nature of the stromatolites (Fig 2.2) (Button, 1973b; Eriksson et al., 2006), which occur throughout the dolomite succession. The Malmani Subgroup is from an economic perspective the most important unit in the Chuniespoort Group (Zietsman, 1967; Boer, 1995).

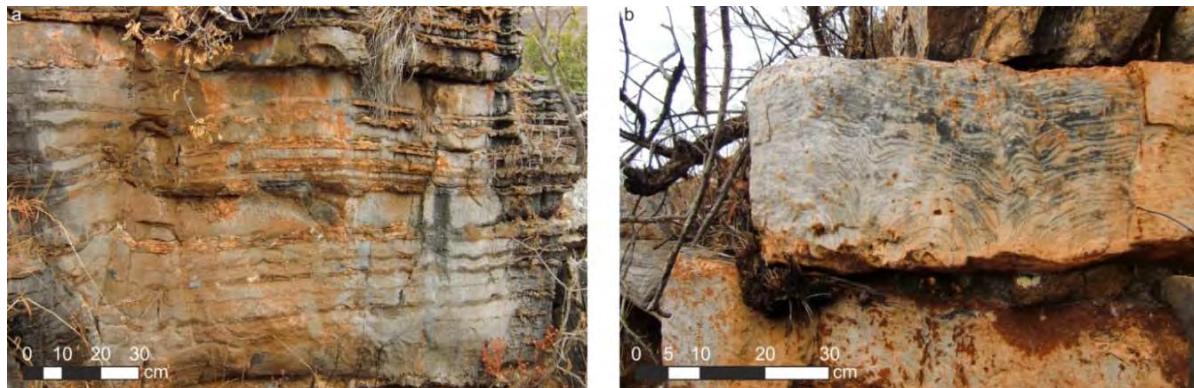


Figure 2.2: Dolomite interbedded with chert layers (a) and stromatolite reef (b) of the Malmani Subgroup in the Sabie-Pilgrim's Rest Goldfield.

The Theta Reef*, which is the main focus of this thesis, is located in the upper Eccles Formation (Fig. 2.1). The formation consists of cherty dolomites and a series of locally auriferous erosion breccias (Eriksson et al., 2006) and displays stromatolite domes and columns ranging from centimetre size to mega-stromatolites (up to 2m). The deposition of the sediments of the Eccles Formation took place in a shallow-water subtidal environment (Tyler & Tyler, 1996). The Theta Reef and the Bevets Reef are both exploited in the Frankfort Mining Complex (Fig. 2.3).

The Bevets Reef* is situated between the Bevets Conglomerate, and black carbonaceous shale of the Rooihoopte Formation (Fig. 2.1). The Rooihoopte Formation, the basal formation of the Pretoria Group, unconformably overlies the Malmani Subgroup, and consists of an upward-fining conglomerate (Bevets Conglomerate) with a thickness of 0.5 to 1.5 m, overlain by a quartzite unit (Harley, 1993).

* A detailed description of the Theta and Bevets Reef is provided in chapter 4.

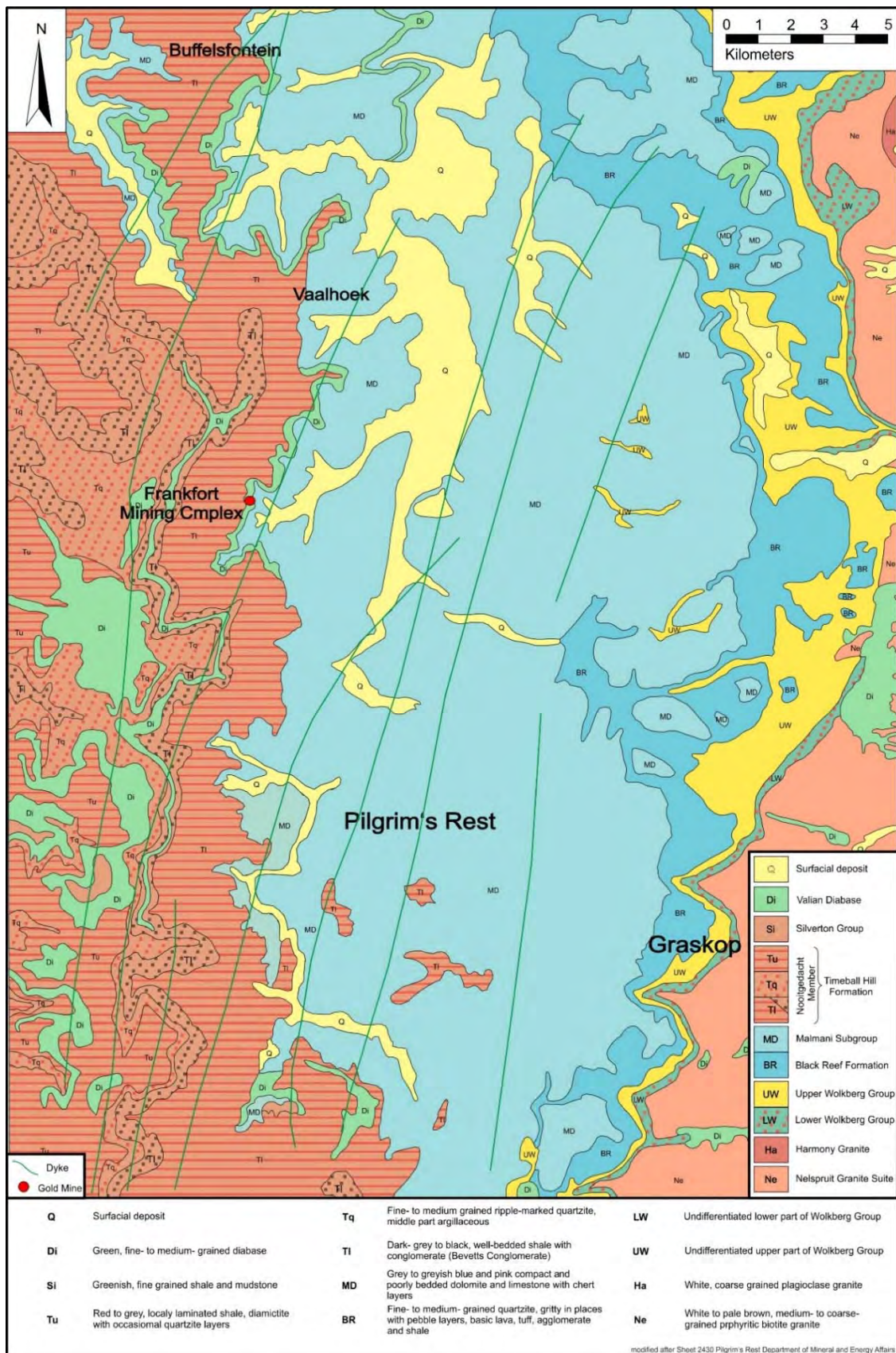


Figure 2.3: Detailed geological map of the SPRG around Graskop and Pilgrim's Rest showing the location of the Frankfort Mining Complex. (Modified after map 2430 Pilgrim's Rest, Department of Mineral and Energy Affairs, J. H. Steyn, 1986).

2.2 Pretoria Group

The Pretoria Group is a series of alternating mudrocks alternating with quartzitic sandstones, significant amounts of basaltic-andesitic lava and subordinate conglomerate, diamictite and carbonate (Eriksson et al., 2006). Only the lower formations of the Pretoria Group are of economic interest with respect to gold mineralisation (Harley 1993).

2.3 Dykes and sills

The Transvaal Supergroup was intruded by numerous dykes and sills, which together have an estimated thickness of 2500m (Sharpe, 1984; Harley and Charlesworth; 1991). Dykes and sills in the region are usually altered pyroxenitic or diabasic and follow a north-northeasterly trend (Zietsman, 1967). Boer (1995) observed that dykes and sills typically intrude along planes of weakness or along the contact between two units. Willemse (1969) and Sharpe (1981) distinguished between pre- and syn-Bushveld dykes and sills: the former are intersected by the ore-bearing quartz veins, while the latter are crosscutting the ore bearing quartz veins. Harmer and von Gruenewaldt (1991) differentiated between diabase and pyroxenitic dykes and sills and connected the former to pre- and the latter to syn-Bushveld magmatism. Klausen et al. (2010) provided an age of 1.90 Ga for the north-east trending dykes in the Kaapvaal craton.

Many of the deposits in the SPRG are spatially related to dykes and sills within the area (Zietsman, 1967). Sill related deposits are distinguished by a higher content of copper minerals than dyke-related deposits (Harley and Charlesworth, 1990).

2.4 Bushveld Complex

Following the deposition of the Transvaal Supergroup the emplacement of the Bushveld Complex took place (Cawthorn et al., 2006) at 2055 ± 0.2 to 2054.89 ± 0.37 Ma (Zeh et al., 2014). A subdivision of the rocks of the Bushveld Complex into four groups, representing different emplacement events, is currently accepted, namely the felsic-volcanic Rooiberg Group, the mafic-ultramafic rocks of the Rustenburg Layered Suite, the Rashoop Granophyre Suite and the Lebowa Granite Suite (Cawthorn et al., 2006)

In Sabie-Pilgrim's Rest area, the Bushveld Complex intruded into the Chuniespoort and Pretoria Group (Harley, 1993). However, thermal metamorphism only affected the Malmani Subgroup where the rocks of the Bushveld Complex are in direct contact with carbonates (Schidlowski et al., 1975; Buchanan et al., 1981; Button, 1986; Boer, 1995). It is thought that the BC is the main heat source, generating the hydrothermal cell, resulting in the formation of the gold deposits of the Sabie-Pilgrim's Rest Goldfield (Boer et al., 1995), although no unequivocal evidence for this hypothesis has been presented yet.

In addition to the thermal effect on the rocks in the SPRG, the intrusion of the Bushveld Complex had a major impact on the structural geology within the study area. The intrusion of the magmas caused doming of the sedimentary sequence and after cooling, the density of the thick pile of mafic rocks forming the Rustenburg Layered Suite caused subsidence of the host rocks resulting in the regional dip present in the SPRG (Boer 1995). (Boer, 1995).

2.5 Age of gold mineralisation within the Transvaal Supergroup

The nature of the mineralisation in the Sabie-Pilgrim's Rest Goldfield has frustrated attempts to date the age of ore formation by direct means (Boer et al., 1995) and the age of mineralisation within the goldfield can only be narrowed down by interpreting the relation between mineralised veins and their surrounding rocks.

The maximum age of the Transvaal Supergroup in the Transvaal Basin has not been directly determined but is indicated by unpublished SHRIMP ages of 2657 and 2659 Ma on felsic lavas of the Buffelsfontein Group which lies directly below the Transvaal Supergroup on the northwest margin of the basin (Eriksson et al. 2006). These ages are compatible with a published age of 2642 ± 3 Ma (Walraven and Martini, 1995) for the Vryburg formation which defines the base of the Transvaal Supergroup in the Gruiqualand West Basin.

As a maximum age constraint for the Transvaal Supergroup the age of 2.66 Ga (Eriksson et al., 2006) for the Wolkberg Group is generally accepted. A tuff layer within the sediments of the upper Oaktree Formation of the Malmani Subgroup was dated ~2.585 Ga and indicates that the earliest deposition of the Transvaal sediments must be similar in age (Martin et al., 1998; Eriksson et al., 2006).

The uppermost ore body within the stratigraphy of the SPRG is the Finsbury Reef. The reef is located between the Strubenkop and the Dwaalheuwel Formations of the Pretoria Group (Boer et al., 1993). Burger and Coertze (1973) used the Rb-Sr-method to date the underlying Hekpoort Formation at 2224^{+21}_{-13} Ma, indicating that the mineralisation must be younger. Boer (1995) established an age of 2027 ± 39 Ma for a diabase sill, using the $^{87}\text{Sr}/^{86}\text{Sr}$ method. This sill was cross-cut by the auriferous quartz vein of the Olifantsgeraamte Mine, giving the maximum age of mineralisation.

These ages permit the mineralisation to be related to the emplacement of the Bushveld Complex. High precision U-Pb dating of zircons from the Rustenberg Layered Suite indicates a crystallisation between 2055.81 ± 0.20 and 2054.89 ± 0.37 Ma (Zeh et al. 2014).

3 Bushveld Complex-related structures in the Transvaal Supergroup

The suggestion that the emplacement of the Bushveld Complex had an impact on structures such as thrust faults within the Sabie-Pilgrim's Rest Goldfield has been discussed by several previous workers (Zietsman, 1967; Harley & Charlesworth, 1992, Tyler & Tyler, 1996; Eriksson et al., 2001). Those structures are important for the emplacement model of the ore deposits of the SPRG and are the key point of this chapter.

The limited access to some parts of the study area made it difficult to acquire compass readings throughout the goldfield. Therefore, readings had to be taken in quartzite, shale and dolomite horizons in road cuts and in the area around the TGME plant (Fig 3.1)

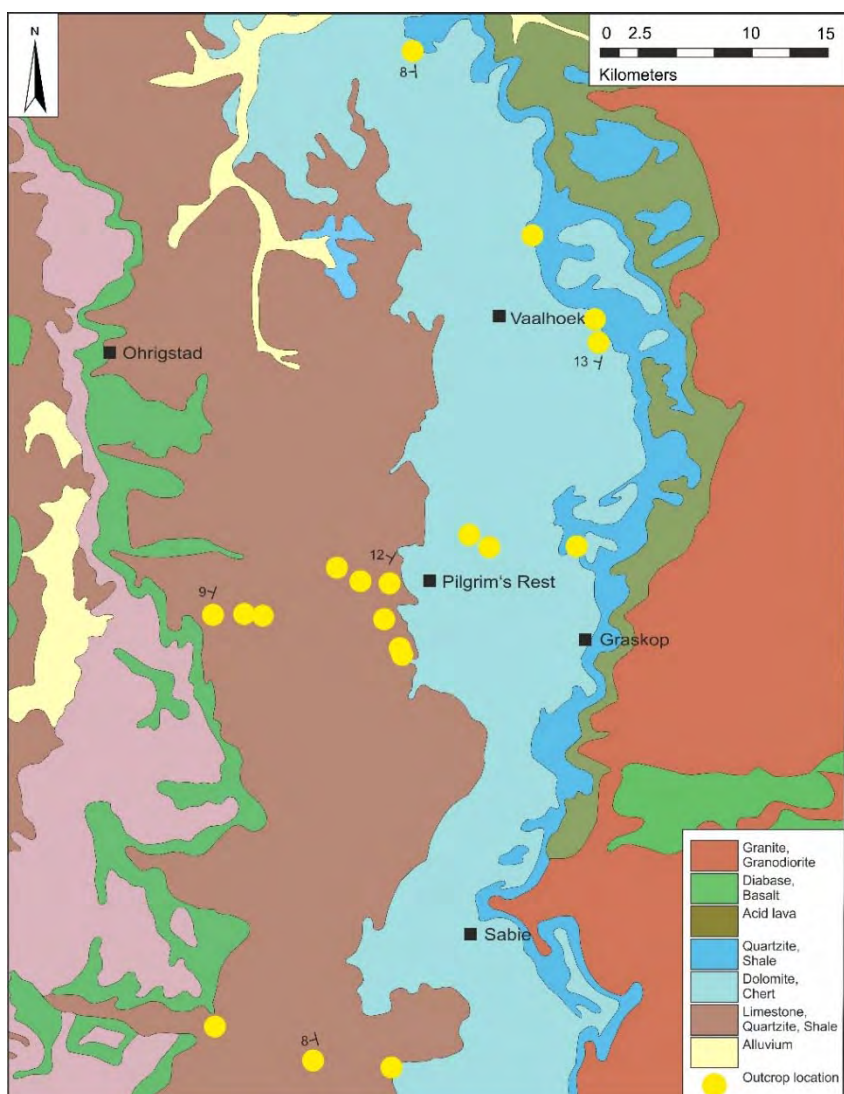


Figure 3.1: Simplified geological map of the area around Pilgrim's Rest showing locations where orientation data were taken (yellow circles); bedding is indicated.

3.1 Bedding

Bedding planes in the goldfield generally dip between $4 - 13^\circ$ to the west, with rare readings of up to 20° (Fig 3.2). The dip within the eastern part of the Transvaal Basin increases gradually from sub-horizontal in the east towards the adjacent Bushveld Complex (Zietsman, 1967), and indicates that the intrusion of the magmas responsible for the Complex had an impact on the attitude of the host rocks. The strike of the bedding changes from WSW ($\sim 205^\circ$) in the north to WNW ($\sim 295^\circ$) in the centre to W ($\sim 270^\circ$) in the south.

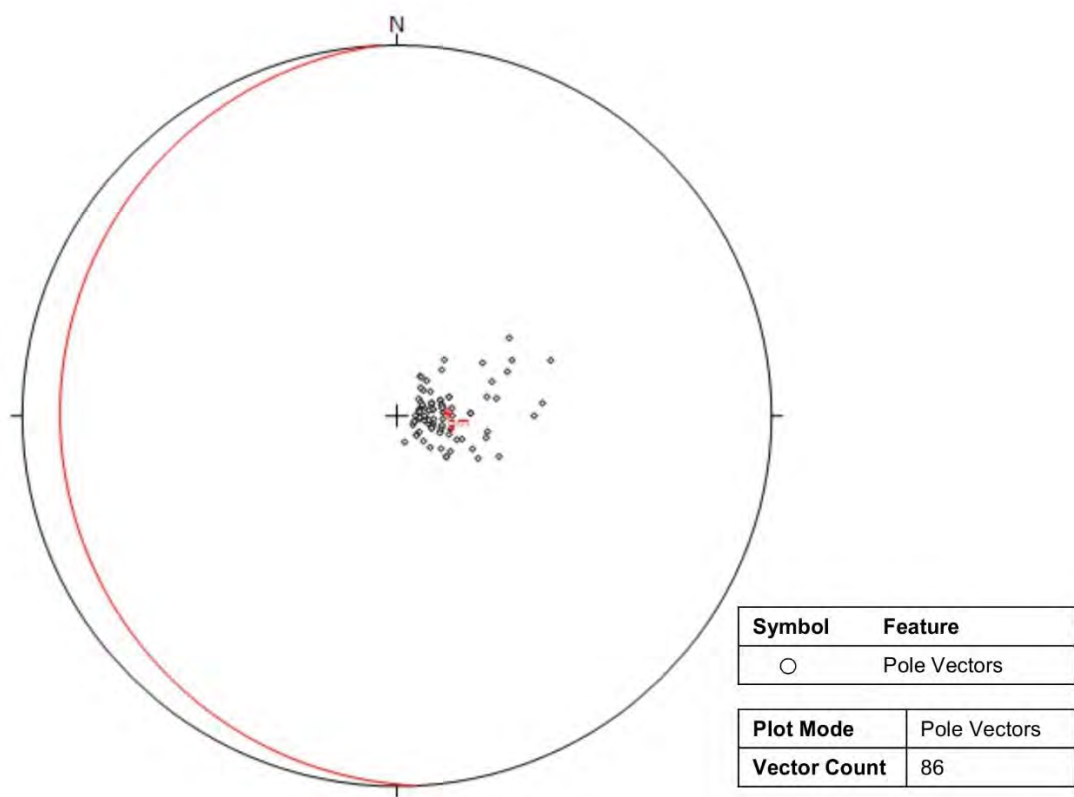


Figure 3.2: Lower hemisphere equal area projection of poles to bedding in the Sabie-Pilgrim's Rest Goldfield.

3.2 Thrust faults

Evidence for east to south-east directed bedding-parallel thrusting in the rocks of the Transvaal Supergroup has been documented by a number of researchers and is well summarised by Harley and Charlesworth (1991). The flat reef deposits in the Sabie-Pilgrims rest Goldfield are bedding-parallel and Harley and Charlesworth (1991) describe pressure shadows around pyrite and asymmetric folds in shale as evidence for thrust-sense bedding parallel simple shear during Au mineralisation at the Elandshoogte Mine. Fold vergence is to the east and is related to Stage 1 the ductile phase of the deformation history (Harley and Charlesworth, 1991). Within the study area, the graphitic mudrock and the black carbonaceous shale occurring at the contact between the host rock and the Theta and Bevets Reef, could represent the same incompetent layer linked to thrust-related simple shear by Harley and Charlesworth (1991). However the mineralised veins associated with the Theta Reef do not show evidence of significant strain as indicated by the occurrence of mineralised but recognisable stromatolitic structures in fragments of host rock within the reef (Fig. 3.3). The lack of direct evidence for bedding parallel thrusting in the exposures and samples studied needs to be substantiated by a detailed study throughout the mine once better access to the underground workings are available.

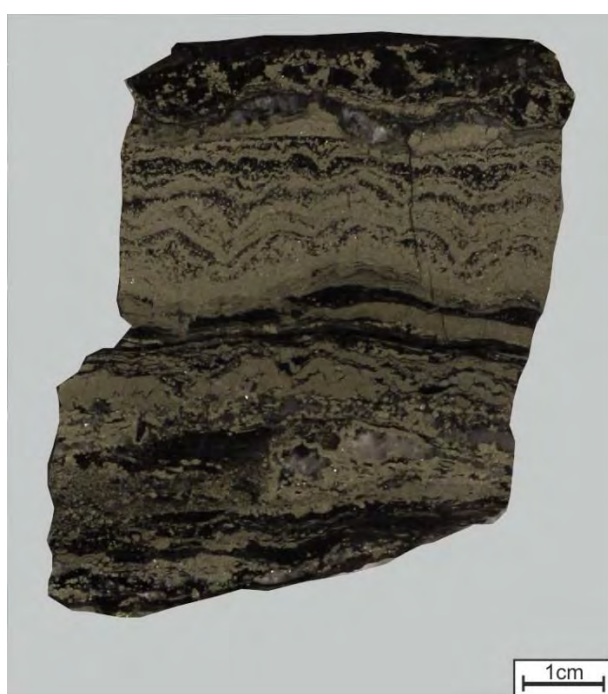


Figure 3.3: Mineralised stromatolite structure occurring within the quartz-carbonate vein of Theta Reef indicating that the reef did not undergo major deformation subsequent to mineralisation.

3.3 Joints

Jointing is common and highly distinctive within the Sabie-Pilgrim's Rest Goldfield (Fig. 3.4). The prominent directions of jointing throughout the study area are ENE and SE (Fig. 3.5 a, b and c), forming a conjugate joint set, and N-NNE. These trends have also been observed at Theta Reef of the Frankfort Mining Complex (Fig. 3.5 d). A distinct change in strike of about 020° from north to south is observed.

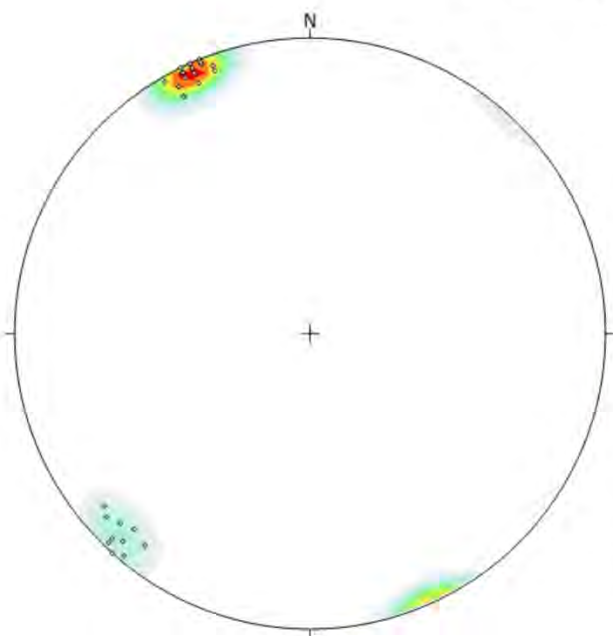


Figure 3.4: Trace of ENE trending joint surfaces in quartzite layer from the Sabie-Pilgrim's Rest Goldfield. (On the R36 at the Trichardt Potgieter Gedenkplaat; 24°43'29.0" S, 30°50'53.8")

The acute angle between the conjugate fracture sets varies between the northern and the southern part of the study area. The acute angle in the southern part of the study area is the lowest (~44°) followed by the centre (~59°) and the highest angle is measured in the north (~68°) indicating that the maximum stress was the highest in the south. The bisector of the acute angle of all measured conjugate joint sets is parallel to the maximum principal stress (σ_1) and orientated 88-268 degrees, the mean attitude of this plane is 268/90 (strike/angle of dip).

a)

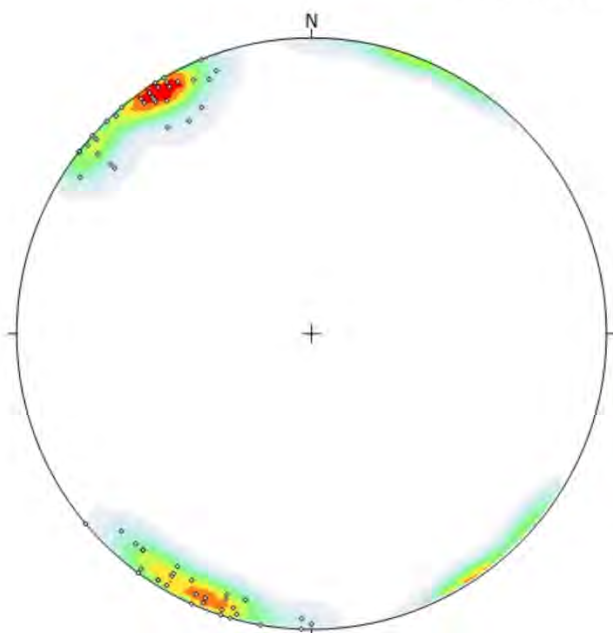
North Section



Symbol	Feature
○	Pole Vectors
Colour	Density Concentrations
	0.0 - 6.3
	6.3 - 12.6
	12.6 - 18.9
	18.9 - 25.2
	25.2 - 31.5
	31.5 - 37.8
	37.8 - 44.1
	44.1 - 50.4
	50.4 - 56.7
	56.7 - 63.0
Maximum Density	62.15%
Contour Data	Pole Vectors
Contour Distribution	Fisher
Counting Circle Size	1.0 %
Plot Mode	Pole Vectors
Vector Count	31

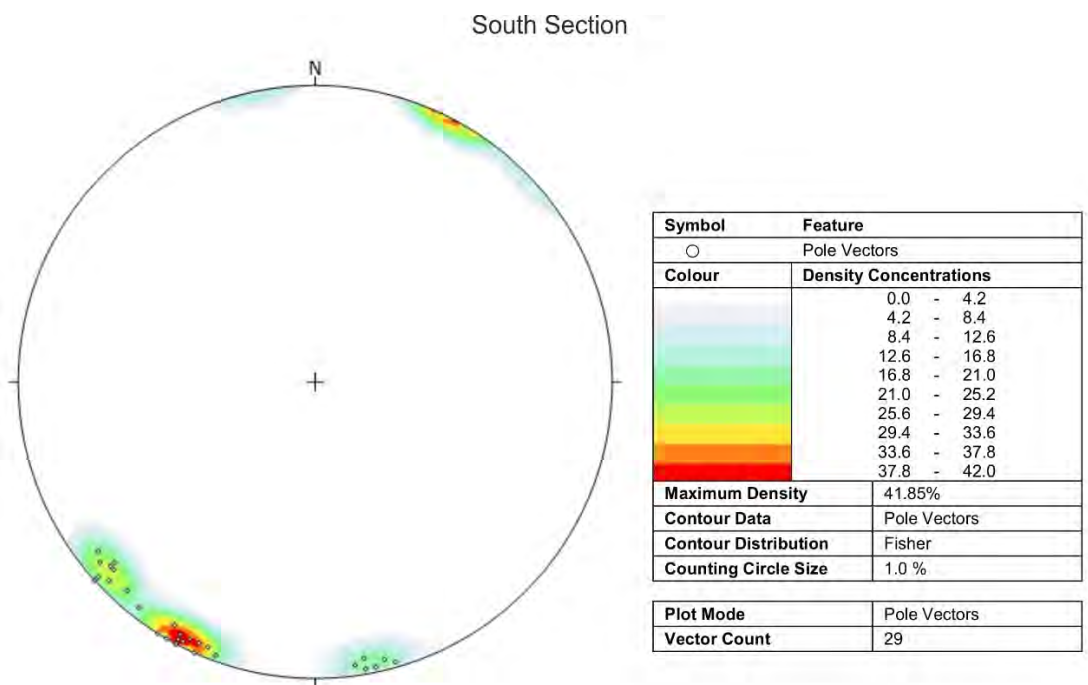
b)

Central Section



Symbol	Feature
○	Pole Vectors
Colour	Density Concentrations
	0.0 - 2.2
	2.2 - 4.4
	4.4 - 6.6
	6.6 - 8.8
	8.8 - 11.0
	11.0 - 13.2
	13.2 - 15.4
	15.4 - 17.6
	17.6 - 19.8
	19.8 - 22.0
Maximum Density	21.80%
Contour Data	Pole Vectors
Contour Distribution	Fisher
Counting Circle Size	1.0 %
Plot Mode	Pole Vectors
Vector Count	63

c)



d)

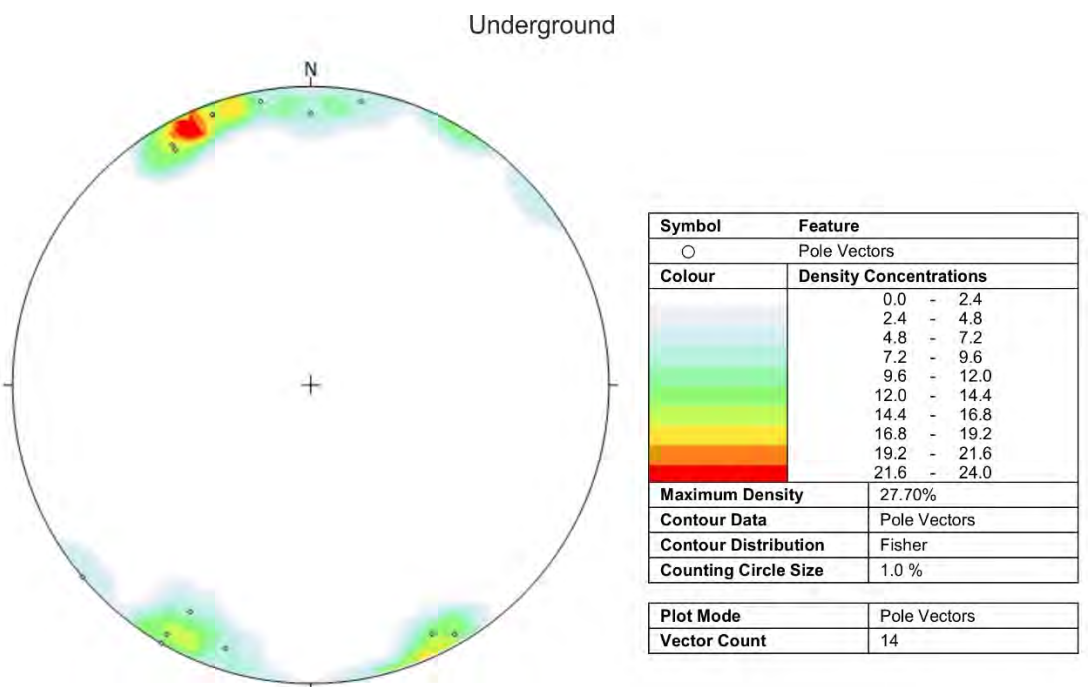
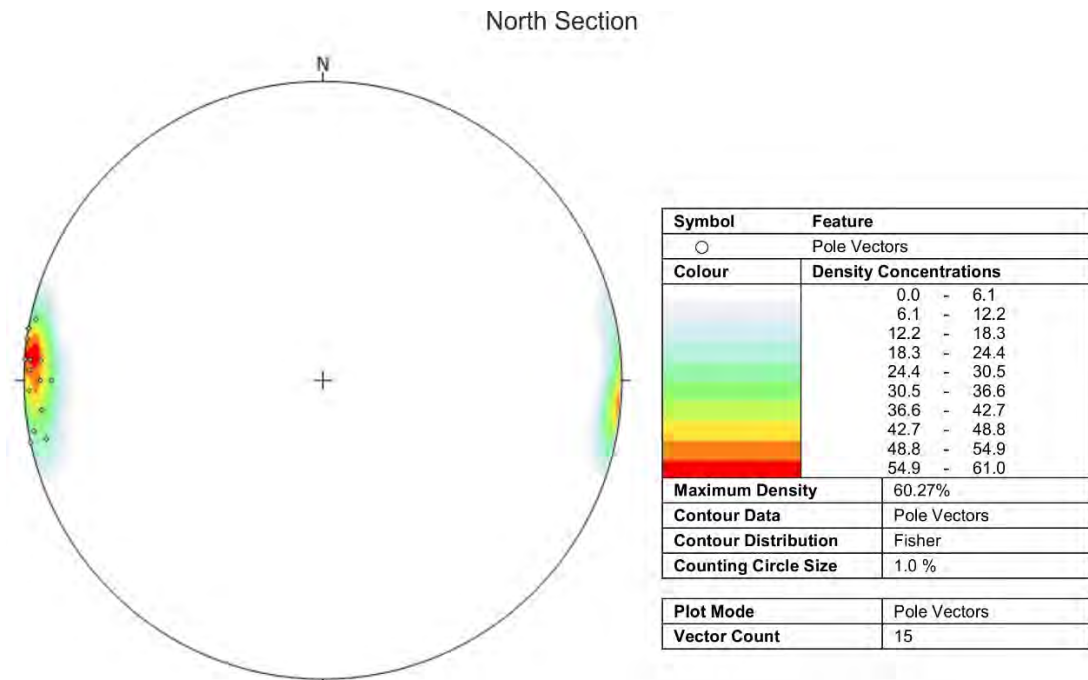


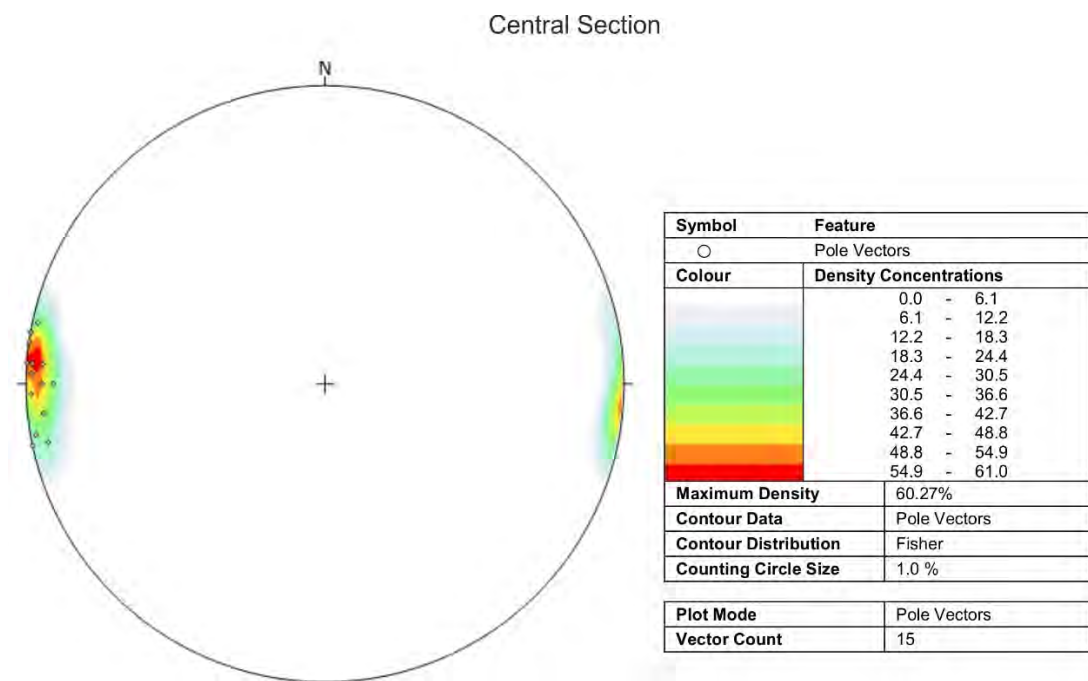
Figure 3.5: Lower hemisphere equal area projections of prominent conjugate joints sets within the Sabie-Pilgrims Rest Goldfield (a, b and c) and underground at Theta Mine of the Frankfort Mining Complex (d).

A third, N-NNE trending direction is apparent within the goldfield, trending between 350 and 040°. Aerial photographs show that some dykes within the SPRG follow the same trend. The direction of this trend changes from north to south, similar to the change in direction already observed in the conjugate joints. While the trend is N/S in the northern and central section of the study area (Fig. 3.6 a and b), it is NE/SW in the south and underground (Fig 3.6 c and d) at Theta Reef.

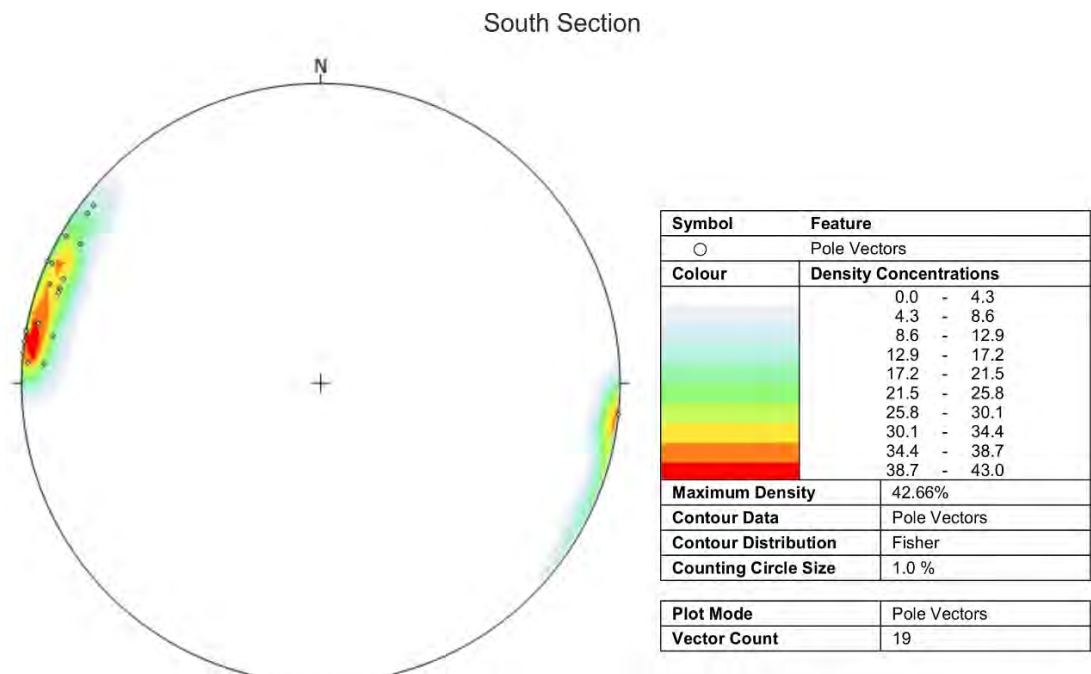
a)



b)



c)



d)

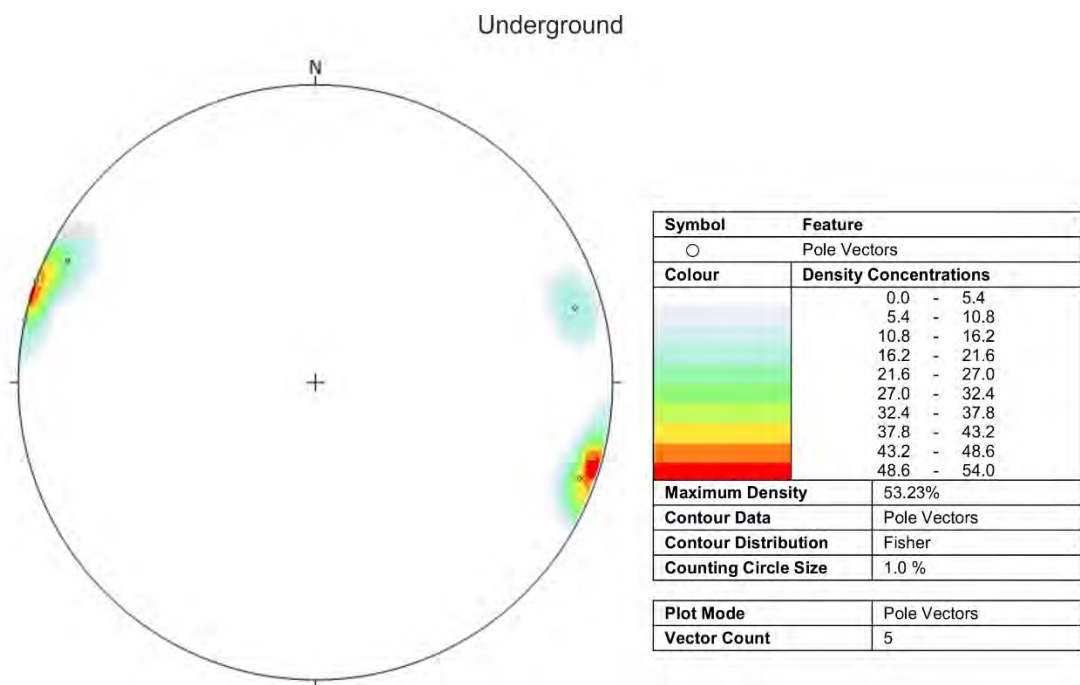


Figure 3.6: Lower hemisphere equal area projections of the prominent N-NNE-trending joints within the Sabie-Pilgrims Rest Goldfield (a, b and c) and underground at Theta Mine of the Frankfort Mining Complex (d).

3.4 Boudin structures

Boudins were observed within chert layers in the dolomites (Fig 3.7). The boudins indicate E-W extensional stress. Thin chert layers show low amplitude folding (A) and a reverse fault within a 10 – 15 cm thick chert layer (B) indicate compression of the layers.



Figure 3.7: Bedding parallel, boudinaged chert layer within dolomite; photo taken looking south, indicating E-W extensions. (Location: dirt road leading to the TGME Project Plant outside Pilgrim's Rest. S 24°54'34.2", E 30°34'57.2")

3.5 Discussion

The emplacement of the Bushveld Complex is most likely responsible for compression of the lithologies of the Transvaal Supergroup, resulting in bedding-parallel thrust-faults within the lithologies. These faults would therefore be the first Bushveld-related deformational features. (Tyler & Tyler, 1996). Merle and Vendeville (1992) used the term “push from the rear” to describe the compression-like thrusting caused by the lateral expansion of the complex. The extensional stress seems to be represented by boudinaged chert layers within the Malmani Subgroup. The intrusion of the magmatic body might have caused tensional and/or extensional conditions resulting in gravity gliding, pushing the layers away from the dome. This is indicated by boudinaged chert layers within the Chuniespoort Group. Uken (1998) described boudins sub-parallel to local dip direction in the Dwaalheuwel Quartzite Formation, suggesting that they were developed during tensile failure under brittle-ductile conditions.

The ore deposits are closely related to the thrust faults, and can therefore be described as thrust zone-hosted gold deposits (Harley & Charlesworth, 1996). The graphitic mudrock and the carbonaceous shale occurring above and below the Theta and Bevets Reef respectively are layers of low resistance which could have acted as zones of detachment for the propagation of thrust faults. The resulting thrust fault system probably provided suitable conduits for the ore-forming fluids that gave rise to the deposits of the SPRG (Tyler & Tyler, 1996).

σ_1 of conjugate joints is 088°-268° and indicates that the maximum principal stress direction is east-west, supporting the suggestion that the emplacement of the E-W oriented Bushveld Complex was responsible for the development of the conjugate joint system. Zietsman (1967) suggested that the change of the general direction of the joints might be related to the difference in deformational behaviour between dolomite and quartzite, the data obtained for this study, however, suggest rather a change of the orientation of the general stress.

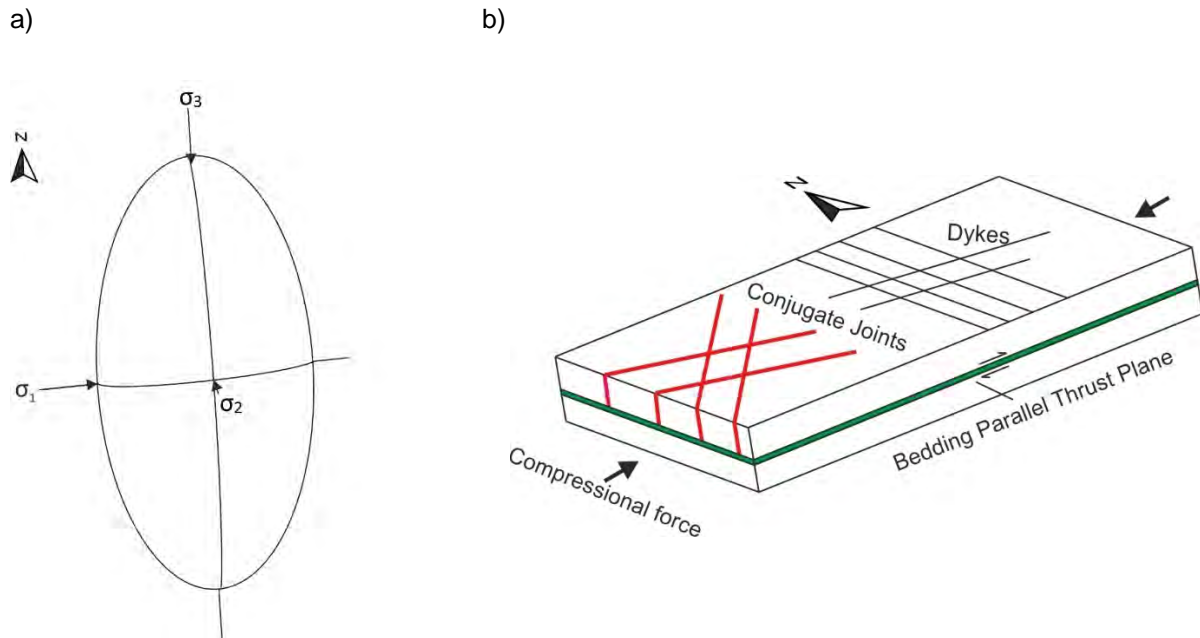


Figure 3.8: a) Stress ellipsoid showing the principal direction of stress σ_1 , σ_2 and σ_3 as occurring in the SPRG. b) Schematic model of compression-induced faulting in the Sabie-Pilgrim's Rest area.

The N to NNE striking joints are sub-parallel to the trend of dyke swarms visible on aerial photographs (Fig 3.9). These dykes intrude the Palaeoproterozoic cover rocks and are interpreted to be part of the northeast trending Olifants River dyke swarm. The dykes are believed to be Karroo in age, intruding into pre-existing fractures. (Watkeys, 2002)

The increase in the dip of the bedding towards the margin of the Bushveld Complex is most likely caused by subsequent sagging of the high density rocks of the igneous complex (Eriksson et al., 2001), resulting in downward bending of the rocks of the Transvaal Supergroup.

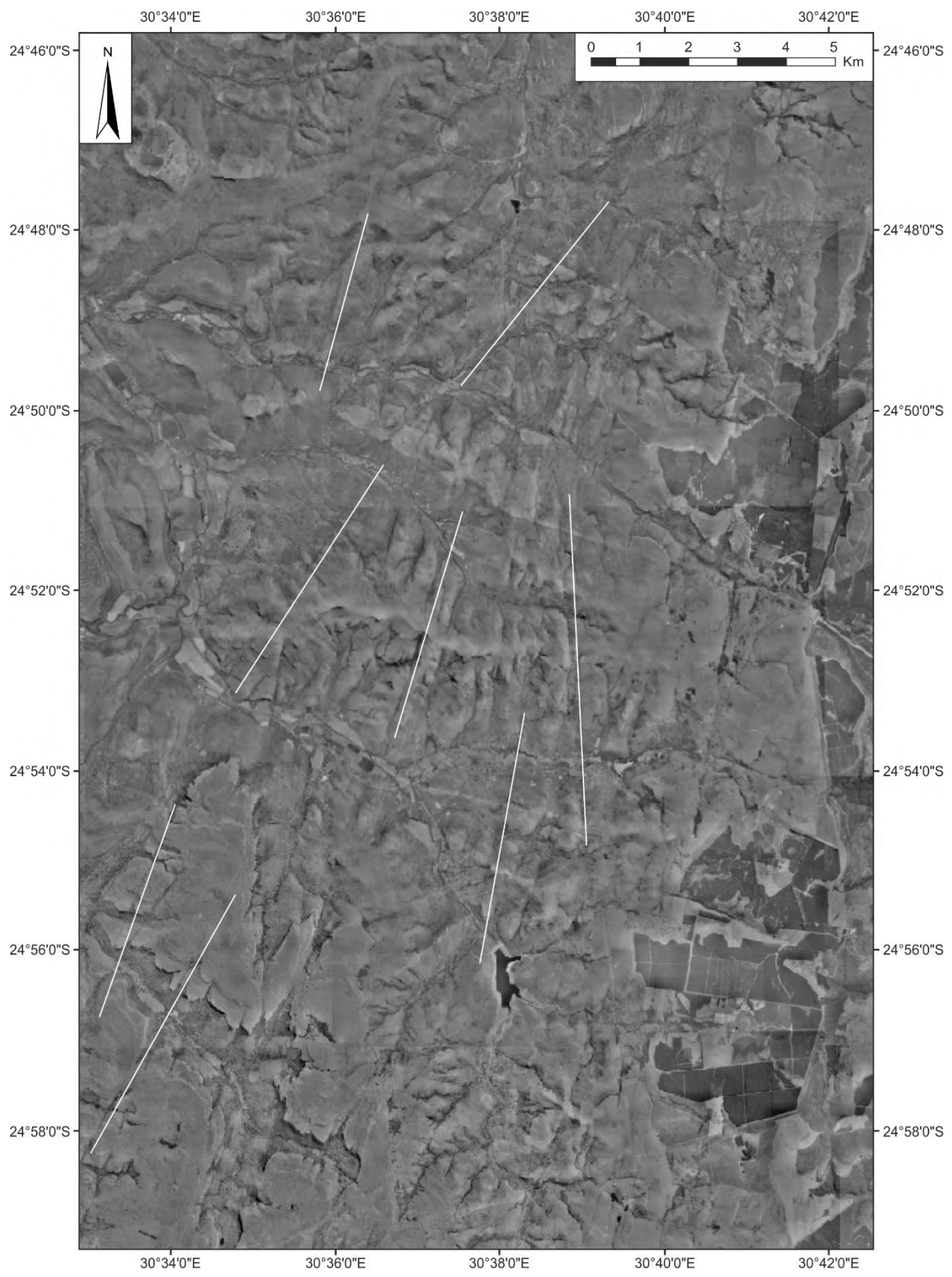


Figure 3.9: Aerial photo of the western part of the study area showing N-NNE trending lineaments.

4 Ore Mineralisation

4.1 The ore-bearing quartz veins of Theta- and Bevets- Reef

Theta Reef is located within the dolomites of the Eccles formation of the Malmani Subgroup and the Bevets Reef occurs at the contact between a quartzite (Bevets Quartzite) and a black carbonaceous shale of the Timeball Hill Formation. The reefs have an average thickness of ~40 and ~60 cm for the Theta and Bevets Reef respectively. An immediate difference in appearance between Theta and Bevets Reef became apparent during underground work. The northern section of the Theta Reef generally occurs as one mineralised vein (Fig. 4.2 a) and b) or in some areas as two veins, divided by a ~10 cm thick chert band (Fig. 4.2 c and d). The reef contains inclusions of dolomite host rock or vugs of quartz and/or carbonate. The Bevets Reef developed multiple quartz-carbonate seams, divided by thin, mm-cm thick, black carbonaceous shale or graphitic layers. These layers give rise to, the for the Sabie-Pilgrim's Rest deposits typical, sheeted nature of some reefs (Fig. 4.1) and probably acted as zones of detachment for thrust fault propagation (Chapter 3.2).

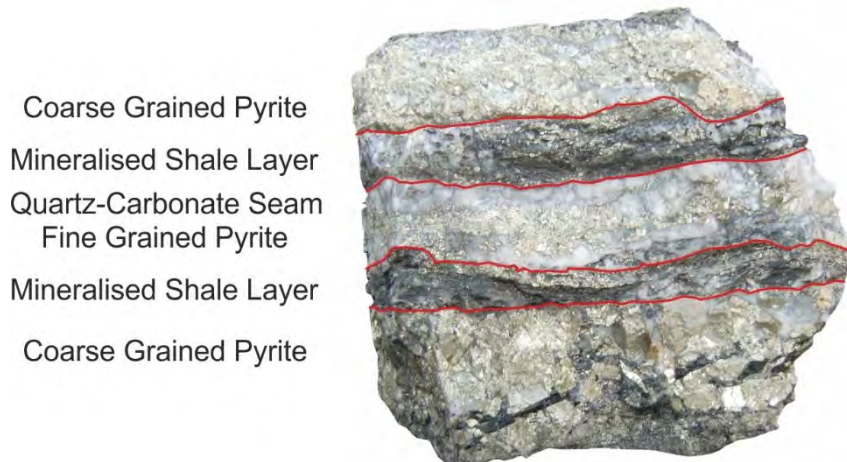


Figure 4.1: A 40cm wide sample of a typical Bevets Reef section showing the typical sheeted nature of some reefs of the Sabie-Pilgrim's Rest Goldfield.

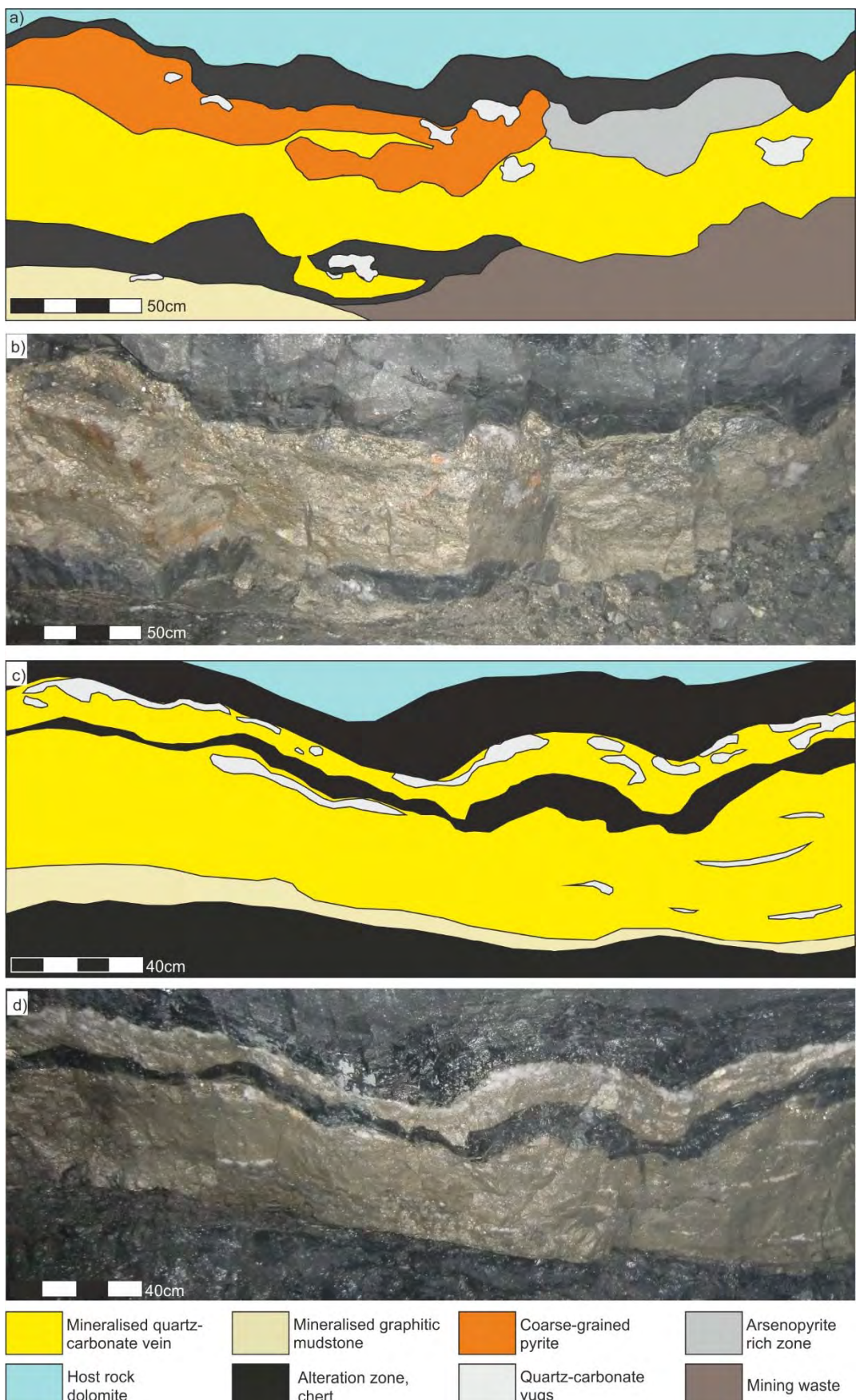


Figure 4.2: Schematic W-E sidewall sections (a and c) and photographs (b and d) of the ore body as present in the northern section of the reef. a) and b) show the Theta Reef occurring as one vein c) and d) as two veins.

4.2 Ore mineralogy of the Theta and Bevets Reef

Four ore minerals are commonly present within the northern section of Theta Reef, namely pyrite, with arsenopyrite, chalcopyrite and tetrahedrite as accessory phases.

The aim of this chapter is to give a detailed mineralogical description of the northern section of the ore-bearing quartz vein at Theta Reef and to establish a possible temporal evolution of the ore minerals.

4.2.1 Methodology

Fifteen polished stubs from reef and host rock samples of the northern most section of the Theta workings (Fig. 4.3) and six polished stubs from Bevets waste sample have been prepared at the University of KwaZulu-Natal in order to produce a representative mineralogical description of Theta and Bevets Reef of the Frankfort Mining Complex.



Figure 4.3: Simplified plan of the northern most section of the underground workings of the Theta Reef at the Frankfort Mining Complex. Samples FTh 100 to 500 stand for STh 1 and 2, NTh 3, 4 and 5 respectively. (Coloured areas are representing stoped areas, the cross hashed area indicates collapsed stopes).

The ore minerals have been characterised and measured using reflected light microscopy at the microscopy laboratory of the School of Geological Sciences of the University of Kwa-Zulu Natal.

4.2.2 Pyrite

Pyrite is the most abundant ore mineral within Theta and Bevets Reef. Table 4.4 shows that Theta Reef pyrite occurs in association with quartz, chert, carbonate, arsenopyrite, chalcopyrite and tetrahedrite. The grains appear in all habits (eu- (EH), Sub- (SH) and an-hedral (AH)) and are 5 µm – 3 mm in size. In the Bevets Reef the mineral is generally associated with quartz, carbonate, arsenopyrite and chalcopyrite, as 5 µm – 2 cm (with some exceptions up to 4 cm), sub- to euhedral grains.

In this study pyrites have been divided into three groups, namely type 1, 2 and 3. This classification is dependent on their appearance (grain size and habit) within the vein or their occurrence within host rocks and/or their amount of inclusions (in this thesis referred to as porosity). (Type 1; 2; 3 are not representing a temporal evolution).

In Figure 4.5, an idealised reef has been reconstructed, using the characteristics of different pyrite types and their preferred appearance within the Theta (Fig. 4.5 a and b) and Bevets Reef (Fig. 4.5 c).

Reef	Host	description of ore bearing Vein	Appearance	Size	Habit	Porosity	Associated gangue	Associated ore minerals	Type
FTh	Dolomite	Graphitic mudrock within the quartz-carbonate vein	Fine grained, disseminated or in veinlets	100 - 200 µm	EH-SH	P - HP			1
FTh	Dolomite	Graphitic mudrock	Fine – medium grained, disseminated and cluster	0.1 - 2 mm	EH-SH	HP	Qtz		1
FTh	Dolomite	Chert	Fine-medium, disseminated and cluster	5 µm-2 mm	EH-SH	NP-SP	Chert, quartz, minor carbonate		1
FTh	Dolomite	Calcite replacement within stromatolites	Fine grained, cluster	5 - 200 µm	EH-SH	P	Qtz		1
FTh	Dolomite	Quartz-carbonate vein	Fine - medium grained, cluster	0.5 - 2 mm	SH	HP	Qtz, carbonate		2
FTh	Dolomite	Quartz-carbonate vein	Medium - coarse, grained, cluster	1 - 3 mm	EH-AH	P-HP	Qtz, carbonate		2
FTh	Dolomite	Quartz veinlets within stromatolites	Fine grained	10 - 400 µm	EH-SH	P - HP	Qtz, carbonate	Ccp overgrowth	2
FTh	Dolomite	Quartz-carbonate vugs	Fine-medium, grained cluster	0.5 - 2 mm	EH-AH	SP-P	Qtz		2
FTh	Dolomite	Chert rich zone within the quartz-carbonate vein	Fine - coarse grained, cluster	0.2 - 5 mm	EH-AH	NP -SP	Qtz, carbonate, chert	Apy, Ccp overgrowth, Ccp and Ttr fracture fill	3
FTh	Dolomite	Quartz-carbonate vein	Fine grained, clusters	5 - 400 µm	SH-AH	NP-HP	Qtz, carbonate		3
BeW	Conglomerate, black shale	Black shale	Coarse grained, cluster	0.2 – 1 cm	EH-SH	HP	Qtz	Ccp fracture fill	1
Bew	Conglomerate, black shale	Black shale layer within the Quartz-carbonate vein	Fine grained, disseminated	5 - 100 µm	EH-SH	HP	Quartz, minor carbonate		1
BeW	Conglomerate, black shale	Quartz-carbonate vein	Coarse grained, cluster	0.2 - 1 cm up 4 cm	SH	P-HP	Qtz, minor carbonate	Apy, Ccp	2

Table 4.4: Occurrence of pyrite within the Theta and Bevets Reef. (AH: anhedral; SH: subhedral; EH: euhedral; HP: highly inclusion rich P: inclusion rich; SP: inclusion poor; NP: no inclusions). All BeW samples have been recovered from mine dumps.

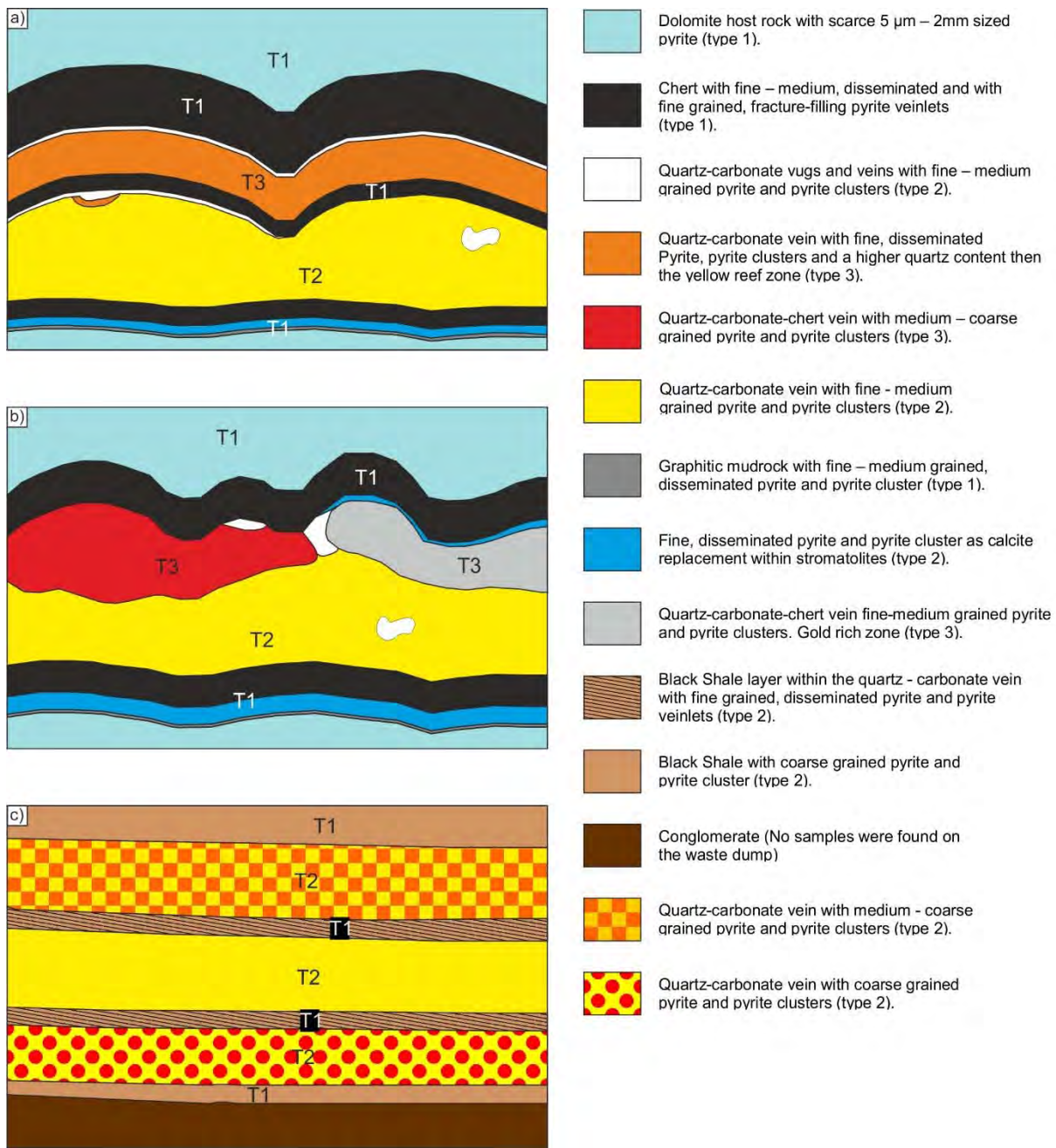
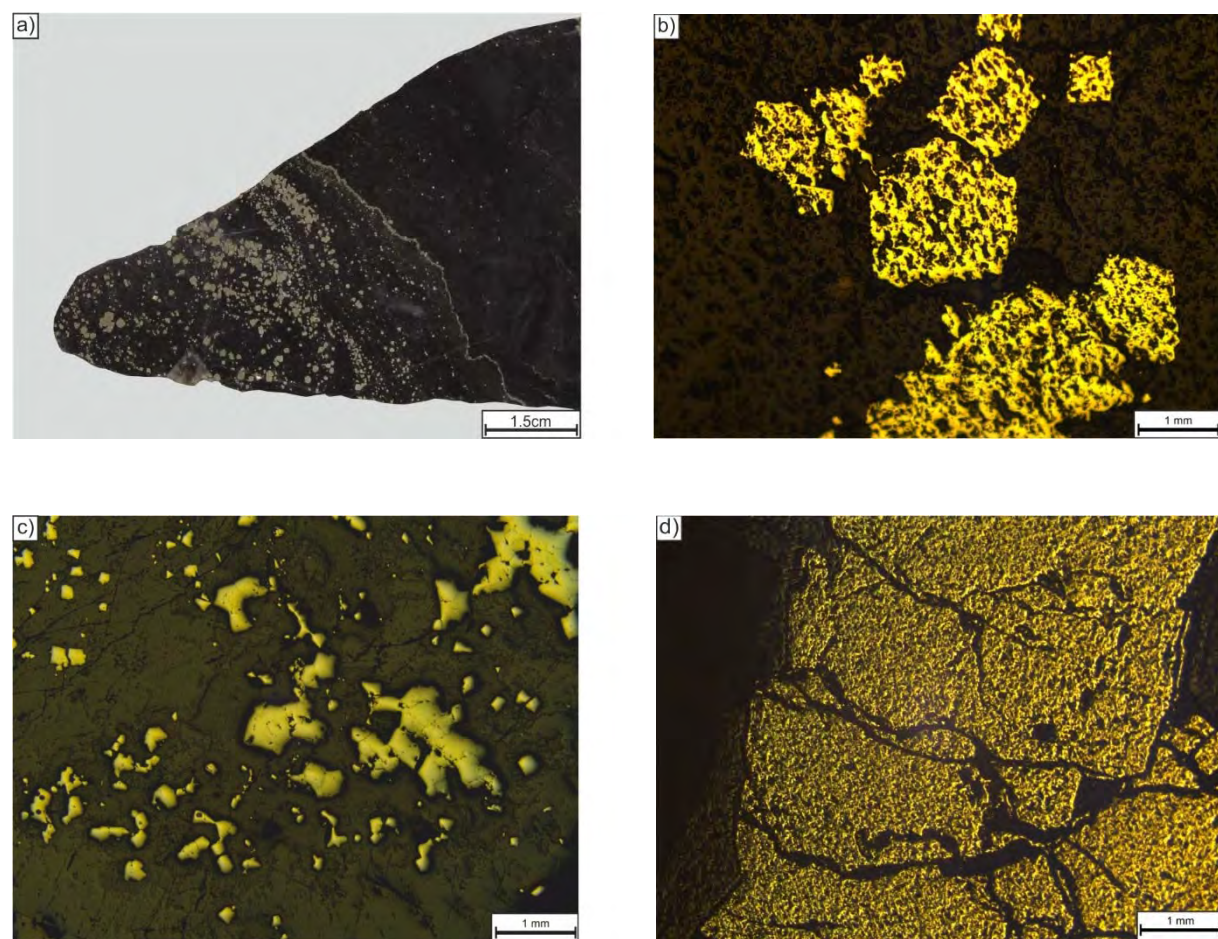


Figure 4.5: Schematic reef sections of the ore-bearing reefs at Frankfort Mining Complex. a) The ore bearing Theta Reef occurring as an upper and a lower reef, divided by a chert layer. The chert layers indicate that the reef replaced stromatolitic structures. b) That Reef occurring as one vein. These sections have a higher content of arsenopyrite and chalcopyrite, commonly occurring in the upper parts of the reef. The overlying chert layer is representing stromatolitic features. c) The ore-body at Bevets Reef, showing the typical sheeted nature of the quartz-carbonate in the Sabie-Pilgrim's Rest Goldfield typical. (T: Type)

Type 1 pyrite

All the pyrites occurring within the dolomite host rock, the chert layer and the graphitic mudrock at Theta Reef and within the black carbonaceous shale at Bevets Reef are classified as type 1 in this study and occurs as disseminated pyrite or in veinlets (Fig. 4.6 a), commonly associated with quartz. The crystal habit is sub- to euhedral and minerals have no inclusions or are highly inclusion rich.

In the dolomite host rock, chert layer and graphitic mudrock, below and above the ore body at Theta Reef grain sizes this type range 0.1 – 2 mm (Fig. 4.6 b and c), whilst within the black carbonaceous shale below and above the Bevets Reef sizes range from 0.2 – 1 cm in size (Fig. 4.6 d). Type 1 pyrite occurring in mudrock layers and fragments and black shale layers within the quartz-carbonate vein of Theta and Bevets Reef, respectively, are generally smaller (5 – 200 μm) and occur more often within veinlets than as disseminated pyrite.



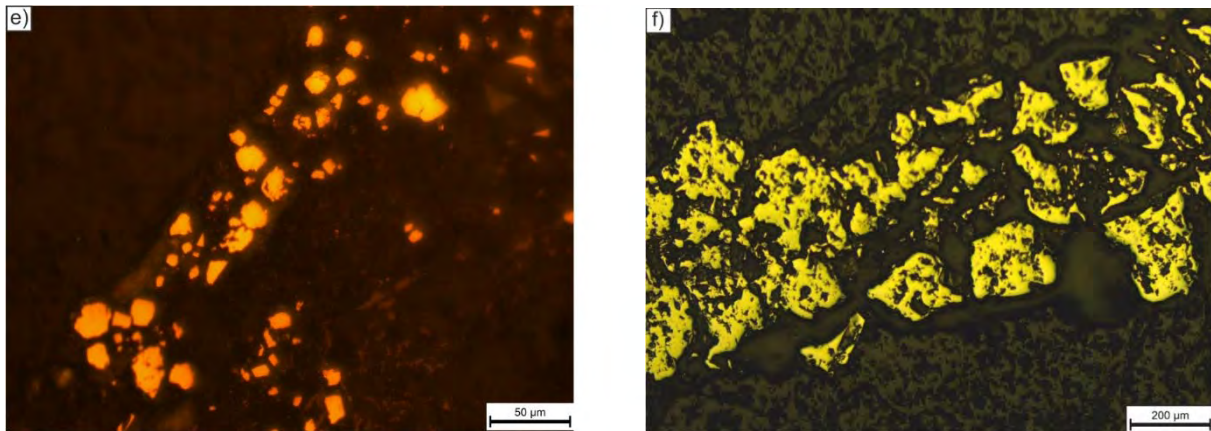


Figure 4.6: a) Hand specimen showing disseminated pyrite and pyrite veinlets within chert from Theta Reef. b) Sub- to euhedral, highly inclusion rich, disseminated pyrite within graphitic mudrock underlying Theta Reef. c) An- to euhedral, no inclusions, disseminated pyrite within dolomite overlying Theta Reef. d) Sub- to euhedral, highly inclusion rich, pyrite within black shale underlying Bevets Reef. e) Sub- to euhedral pyrite grains occurring in veinlets in graphitic mudrocks within Theta Reef. f) Sub- to euhedral, highly inclusion rich pyrite from veinlets in black shale fragment within Bevets reef.

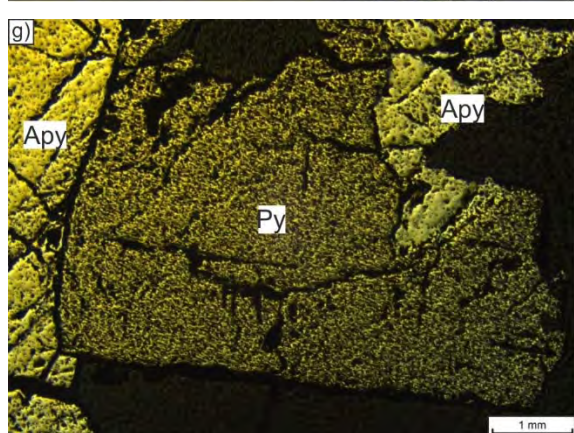
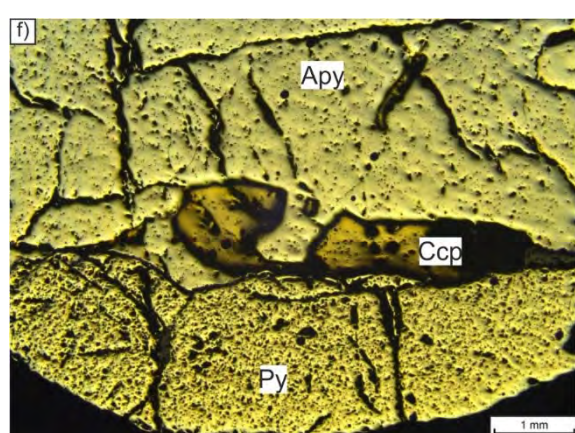
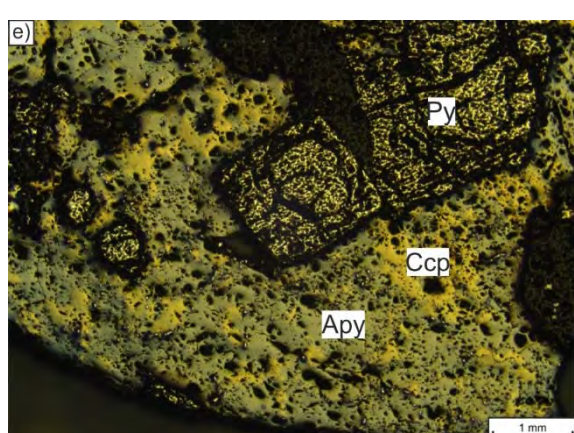
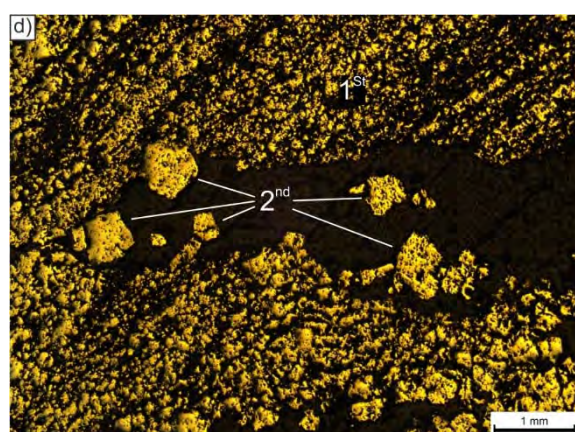
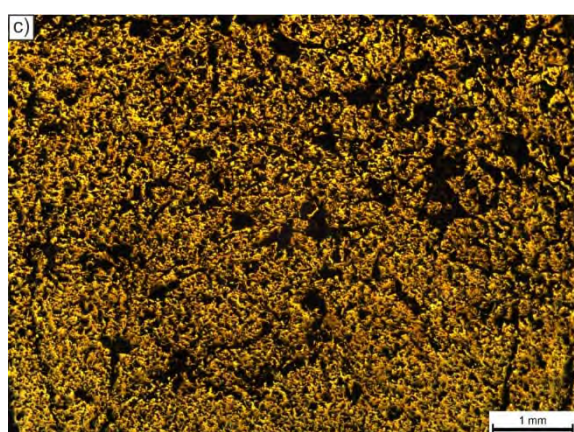
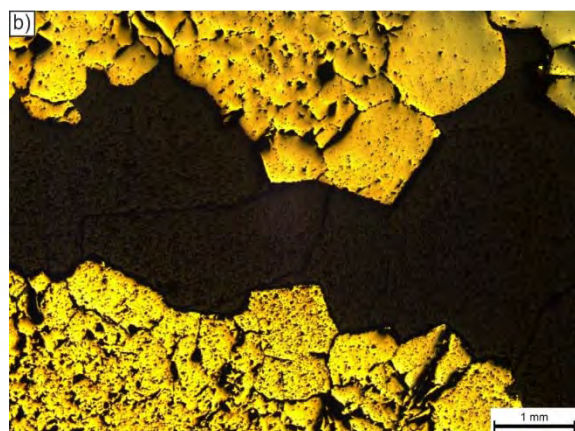
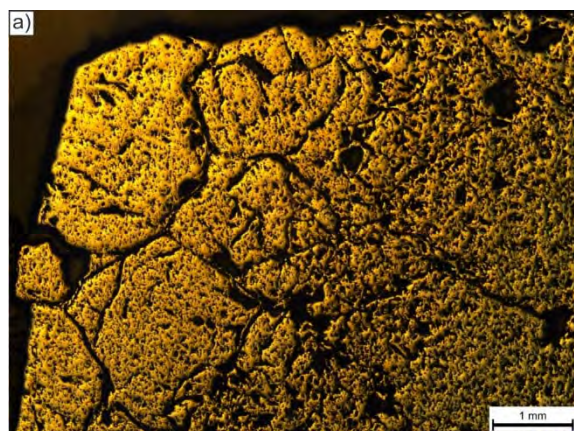
Type 2 pyrite

Type 2 pyrite is the most abundant pyrite within Theta and Bevets Reef and occurs in association with quartz and carbonate and occasionally chert and is in some zones intergrown by arsenopyrite and chalcopyrite. In Theta Reef this pyrite occurs as subhedral, inclusion poor to highly inclusion rich, from 0.5 – 2 mm sized grains (Fig. 4.7 a and b) and highly inclusion rich, 1 – 2 cm sized aggregates Fig. 4.7 a and c). Figure 4.7 d shows that Type 2 pyrite formed later than pyrite replacing the calcite within the stromatolitic structure and before the precipitation of arsenopyrite and chalcopyrite (Fig. 4.7 e).

In Bevets Reef only subhedral pyrite grains are observed. The grains are inclusion rich or highly inclusion rich and generally range, with some exceptions of up to 4cm, from 0.2 to 1 cm (Fig. 4.7 f and g). The replacement of pyrite by arsenopyrite in Figure 4.7 g indicates that pyrite precipitated first.

Figure 4.7 (opposite site):

- a) *Highly inclusion rich or inclusion rich sub-hedral type 2 pyrite and a pyrite aggregate within Theta Reef.*
- b) *Subhedral inclusion poor to inclusion rich type 2 pyrite growing into open space within Theta Reef.*
- c) *Type 2 to pyrite aggregate within Theta Reef.*
- d) *Type 2 pyrite within a fracture in a stromatolitic structure at Theta Reef, indicating that type 2 pyrite is younger than pyrite occurring as calcite replacement within the stromatolitic structures.*
- e) *Type 2 pyrite within arsenopyrite and chalcopyrite intergrowth. Indicating that this type pyrite precipitated earlier.*
- f) *Subhedral inclusion rich to highly inclusion rich pyrite (g) within Bevets Reef. g) Indicates that pyrite precipitated before arsenopyrite.*



Type 3 pyrite

This scarce type includes all inclusion poor pyrites and pyrites with no inclusions, occurring as sub-euhedral grains or pyrite aggregates within chert rich zones within the quartz-carbonate vein of Theta Reef (Fig 4.8). Eu- to subhedral grains range from 5 – 500 µm and usually occur within arsenopyrite and chalcopyrite intergrowth. Aggregates of massive, anhedral, 50 µm – 2mm pyrites reach sizes of up to 2 cm and are the only pyrite, hosting fracture filling chalcopyrite and tetrahedrite. This type of pyrite has not been observed at Bevets Reef.

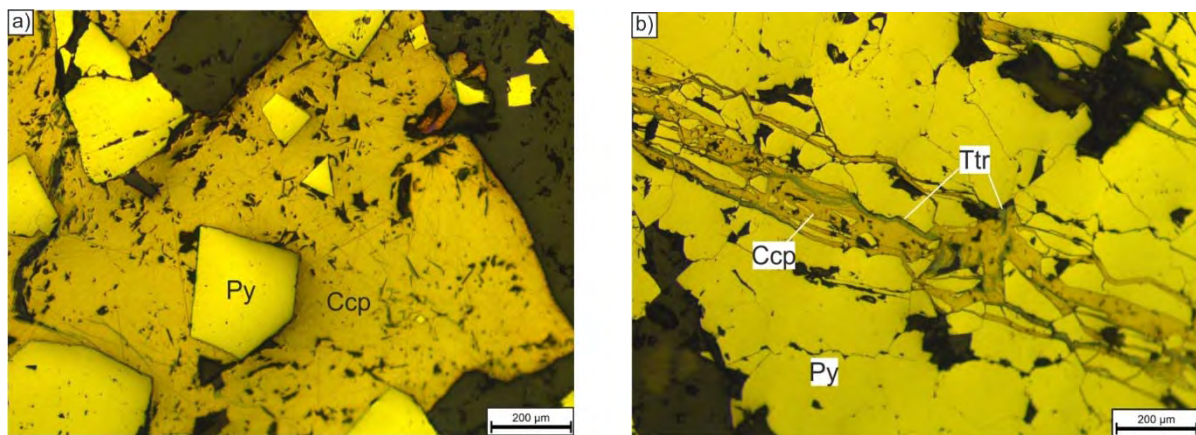


Figure 4.8: a) Sub- to euhedral, inclusion poor pyrite or pyrites with no inclusions intergrown with chalcopyrite in chert rich zones of the quartz carbonate vein at Theta Reef. b) Aggregate of massive, anhedral pyrite with fracture filling chalcopyrite and tetrahedrite.

4.2.3 Arsenopyrite, chalcopyrite and tetrahedrite

Arsenopyrite and chalcopyrite are the second and third most abundant ore minerals, respectively, within the Theta and Bevets Reef. In the Theta Reef these minerals generally occur as intergrowths (Fig. 4.9 a) including anhedral to subhedral inclusion rich pyrite grains (Fig. 4.9 b), indicating that they are secondary. In comparison to the pyrite, arsenopyrite and chalcopyrite have less inclusions. Chalcopyrite also occurs as fracture-filling material associated with tetrahedrite (Fig. 4.9 c).

Arsenopyrite within the Bevets Reef is generally subhedral and grain sizes range from ~5 mm to ~1 cm. Chalcopyrite occurs more often as fracture-filling material (Fig. 4.9 c) and only occasionally as a subhedral mineral. Arsenopyrite can be subdivided into two types, one inclusion rich type and one inclusion poor type (Fig. 4.9 d). The minerals seem to have replaced earlier pyrite grains.

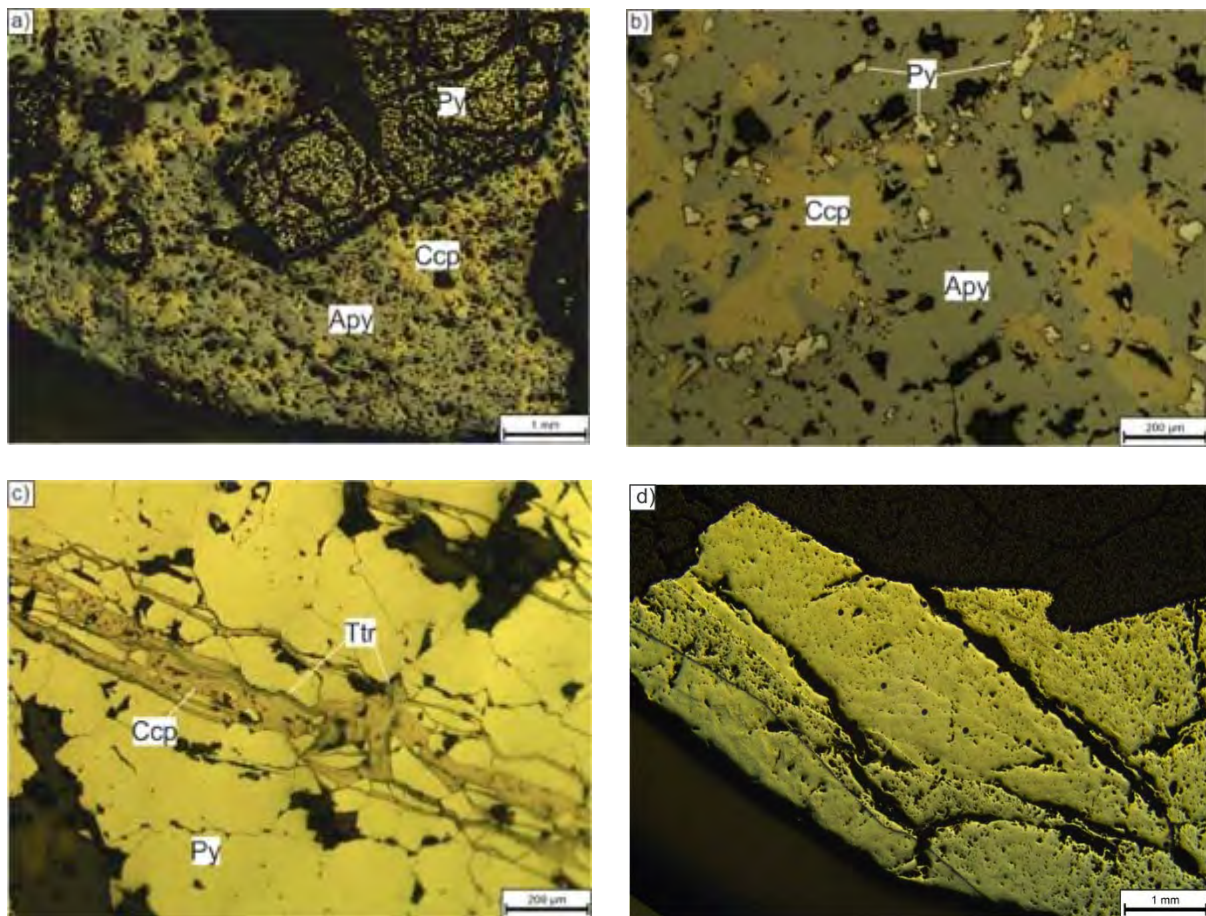


Figure 4.9: a) Arsenopyrite and chalcopyrite intergrowth between highly inclusion rich subhedral to euhedral pyrite within Theta Reef. b) Arsenopyrite and chalcopyrite intergrowth including 5-50 μm sized pyrite grains, with no inclusions, within the Theta Reef. C) Fracture-filling chalcopyrite and tetrahedrite pyrite within the Theta Reef. d) Subhedral arsenopyrite and fracture-filling chalcopyrite within inclusion poor arsenopyrite and inclusion rich pyrite within the Bevets Reef. d) Inclusion-poor pyrite within the Bevets Reef.

4.3 Gangue mineralogy of the Theta Reef

Two major gangue minerals have been observed within the ore-bearing vein of the Theta Reef, namely quartz and carbonate (calcite and dolomite). The differentiation between calcite and dolomite is problematic as these minerals are indistinguishable within the thin sections and have, therefore, been referred to as carbonate minerals.

4.3.1 Methodology

Thin sections of the quartz-carbonate vein were studied in order to describe the gangue mineralogy of the northern section of the Theta Reef of the Frankfort Mining Complex. The study was performed at the microscopy laboratory at the University of Kwa-Zulu Natal, using transmitted light microscopy.

4.3.2 Quartz and carbonates within the mineralised quartz carbonate vein

Carbonates quartz and chert occur as a groundmass, including medium to coarse - grained pyrite (Fig. 4.10 a). Carbonate crystals generally have an anhedral to euhedral habit and grain sizes range from millimetre to centimetre size. Two generations of carbonates have been observed: primary euhedral grains are included in secondary subhedral carbonates (Fig. 4.10 b).

Quartz occurs as fine grained-subhedral grains within quartz-carbonate groundmass, as 0.5 mm sized rounded grains within subhedral to euhedral carbonates and as fine grained fracture-filling material within carbonates and the quartz-carbonate-chert groundmass (Fig. 4.10 d and e). Anhedral quartz occurs in association with pyrite and seems to have overgrown primary carbonates (Fig. 4.10c).

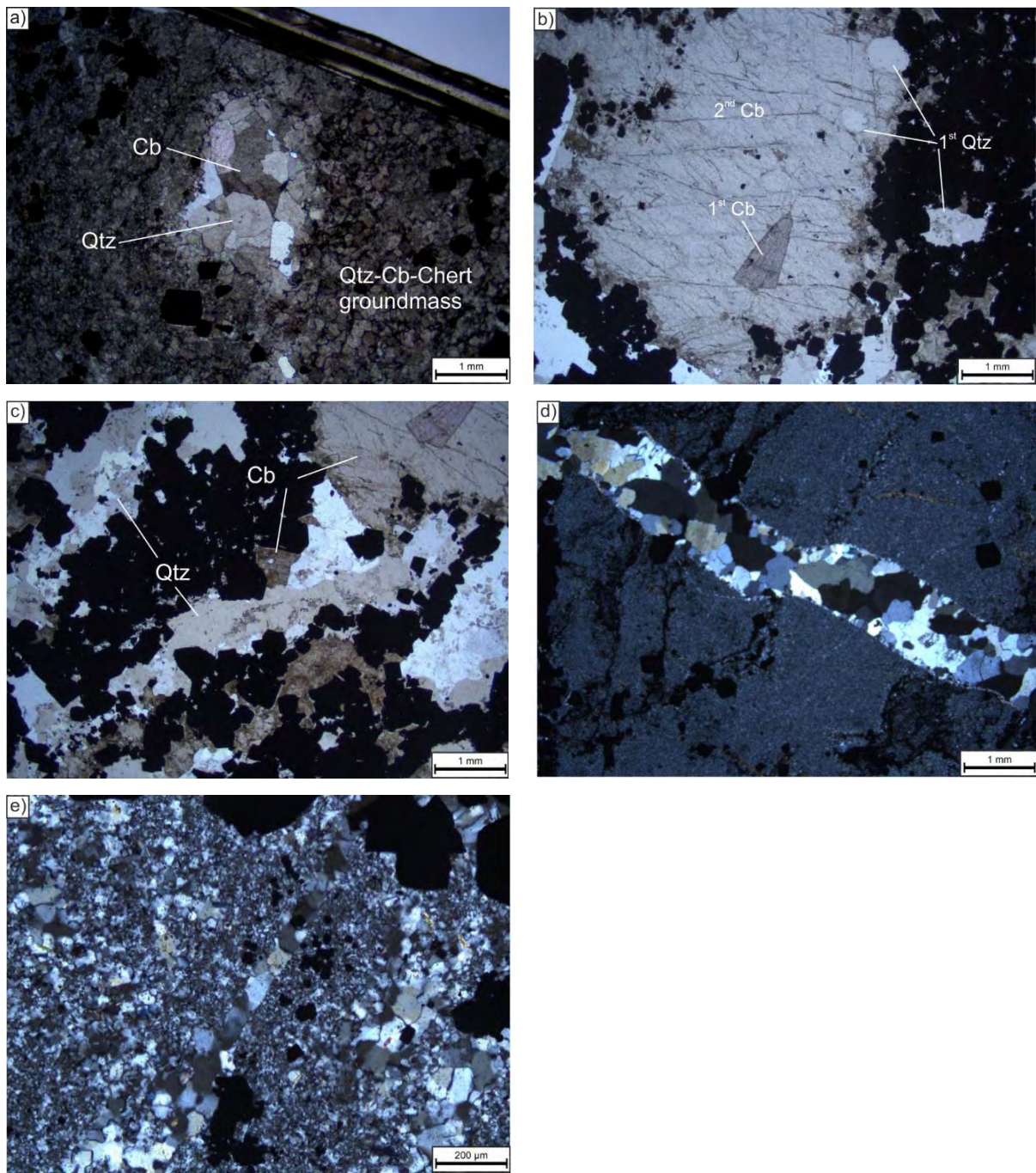


Figure 4.10: a) A cluster of subhedral carbonates and quartz within a quartz-carbonate groundmass. b) Secondary subhedral calcite including euhedral primary carbonates and rounded quartz. c) Anhedral quartz in association with subhedral to euhedral pyrite, overgrowing primary gangue minerals. d) Fracture-filling, fine-grained, subhedral to euhedral quartz within carbonates. e) Seam of fine grained quartz-carbonate minerals in a quartz-carbonate ground mass.

4.4 Discussion

The Theta reef is emplaced at the contact between mudstone and dolomite this contact could have provided an area of low resistance for the ore forming fluids to intrude. However, the minerals are not deformed and do not show any evidence for stress or strain, this is supported by the occurrence of stromatolitic structures within the reef. Furthermore, the dolomite probably provided a reducing environment supporting the precipitation of the metals and provoking the ore mineralisation. This specific environment is believed to be one explanation for the location of these deposits.

At least two generations of ore minerals have been observed within the Theta and Bevets reef ores. One generation pyrite (Type 1) occurs within the dolomite host rocks, host rock fragments, chert, mineralised stromatolitic structures and graphitic mudrock of the Theta Reef, and within layers of a black carbonaceous shale within the Bevets Reef. A second generation is observed within the quartz-carbonate veins.

Two types (Type 2 and 3) of pyrite have been observed within the Theta vein. Type 2 is subhedral to euhedral and shows different degrees of porosity. Type 3 pyrite occurs as euhedral inclusion poor grains with no inclusion and anhedral, inclusion poor or with no inclusion, clusters. The spatial relation of this type pyrite, and arsenopyrite and chalcopyrite suggests, that they formed at the same time.

Type 2 pyrite is observed in fractures within mineralised stromatolites, indicating that this type pyrite precipitated at a later stage than Type 1 pyrites. Arsenopyrite and chalcopyrite seem to have precipitated predominantly during a secondary mineralisation stage, overgrowing earlier generations of Type 2 pyrites, indicating a third mineralisation episode. The precipitation of chalcopyrite and minerals of the tetrahedrite-tennantite series within fractures coeval to the mineralisation of arsenopyrite and chalcopyrite.

The mineralisation within the Bevets Reef appears to be different to that of the Theta reef. In a first stage highly inclusion rich and inclusion rich subhedral pyrite precipitated, followed by second stage arsenopyrite and chalcopyrite. The third stage is represented by fracture-filling chalcopyrite. Inclusions of tetrahedrite have not been observed. The similarity of the mineralogy of the Bevets and Theta Reef suggest that the emplacement of the reefs was time equal.

The different stages of ore mineralisation have been accompanied by the precipitation of the gangue mineral quartz and carbonate. It seems that Type 1 pyrite is generally associated with quartz, Type 2 pyrite with quartz and carbonates and Type 3 with quartz, carbonate and chert, while carbonates only precipitated in association with quartz and Type 2 and 3 pyrite. Quartz veinlets within the quartz-carbonate and quartz-carbonate-chert groundmass indicate, that at a later stage only quartz precipitated from the hydrothermal fluids and no carbonates.

Primary rounded quartz could be of detrital origine and during the mineralisation be overgrown by subhedral and anheadral gangue minerals. However, no further evidence for detrital minerals has been observed within the Theta Reef.

5 Trace element analysis of sulphide minerals

Trace element concentrations in sulphide ores have been analysed by laser ablation inductively coupled mass spectrometry (LA-ICP-MS) in order to obtain information about the geochemical composition of the ore-forming fluid as well as base and precious metal distribution (Norman et al., 2003). LA-ICP-MS output traces of single spot analyses can provide information about the occurrence of gold within the ore, e.g. as invisible nano-sized inclusions giving an apparent homogeneous distribution or as larger isolated micron-sized inclusions within the sulphides (Maslennikov et al., 2009; Zhang et al., 2014). Gold is generally transported as a soluble chloride- or bisulphide-complex and often precipitated as Au-As and Au-Sb compounds (Zhu et al., 2011). Commonly associated trace elements within Au bearing sulphides are As, Sb, Tl and Hg within Carlin type Au deposits (Cline et al., 2005); Au, Ag, As, Sb, Pb, Cu, Bi, Hg, Mo, Sn, Te and Zn within high-sulphidation epithermal gold deposits., Au, Ag, As, Sb, Se, Hg, Mo, Tl and W within low-sulphidation epithermal gold deposits (Simmons et al., 2005). Gold in intrusion-related gold deposits is generally associated with As, Ag, Bi, Cu, Mo, Pb, Sb, Te, W and Zn (Groves et al., 2003) and orogenic gold deposits with As, Hg, Sb and Te (Groves et al., 2003; Goldfarb et al., 2005).

5.1 Methodology

Trace elements were analysed using a NWR UV-213 Laser (spot size 40 µm) connected to a Perkin-Elmer Nexion quadrupole MS at the School of Geological Sciences, University of KwaZulu Natal. The devices are connected using argon as a carrier gas. Calibration was done after the widely accepted method using the MASS-1 pressed synthetic polymetal sulphide standard (including all trace elements analysed in this study) from the USGS (Wilson et al., 2002) and Fe as the internal standard for data reduction. The MASS-1 standard is the most suitable standard for sulfide minerals, due to the lack of sulfide reference materials.

Data reduction was done with the GLITTER software (Van Achterbergh et al., 2001), using Fe as an internal standard, assuming idealised stoichiometry for the different sulphides analysed (pyrite: 47 wt.% Fe; arsenopyrite 36.5 %; chalcopyrite 30.4 %; tetrahedrite/tennantite 7.5 %). In this study a set of 25 trace elements was analysed: S, V, Cr, Mn, Fe, Co, Ni, Co, Ni, Cu, Zn, Ga, As, Se, Mo, Ag, Cd, In, Sn, Sn, Te, W, Ir, Au, Hg, Pb (on masses 206, 207 and 208) and Bi.

A more detailed into the data reduction software GLITTER is given in the appendix (p. 151).

5.2 Results

A total of 307 (173 on Theta Reef and 134 on Bevets Reef samples) spot analyses have been conducted on sulphides, including pyrite (Py), arsenopyrite (Apy), chalcopyrite (Ccp) and minerals of the tetrahedrite-tennantite series (Ttr), from ten polished stubs to determine the trace element content.

5.2.1 Trace elements in sulphide minerals

The differentiation between the sulphide minerals (e.g. pyrite, arsenopyrite, chalcopyrite and the minerals of the tetrahedrite-tennantite series) is important to set the internal standard in order to receive accurate ppm concentrations for the different trace elements. Figure 5.1 shows the distribution of major trace elements Cu, As, Sb and Bi occurring in sulphides of the Theta and Bevets Reef. The trace element concentrations are generally more variable in the Bevets Reef sulphides in comparison to the Theta Reef, where they occur in clusters. This makes the sulphide classification easier in the Bevets Reef.

The Bevets Reef sulphides are arsenopyrite, having the lowest sulphur content (~125,000 ppm), chalcopyrite with sulphur contents around 250,000 ppm and pyrite, with a sulphur content of around 400,000ppm.

The sulphur distribution in the Theta Reef sulphides seems to be more complex. Four sulphide minerals have been observed in chapter 3, namely pyrite, arsenopyrite, chalcopyrite and minerals of the tetrahedrite tennantite series. The sulphur content within minerals of the tetrahedrite-tennantite series ranges from ~100,000 to ~250,000 ppm. Arsenopyrite has an S content of ~100,000 - ~350,000 ppm and chalcopyrite of 150,000 to 450,000 ppm coinciding with the values of arsenopyrite and chalcopyrite from the Bevets Reef. All values higher than 400,000 ppm are classified as pyrite for the purpose of this study.

The copper distribution (Fig. 5.1 a) appears to be similar in both reefs. The different Cu contents can be attributed to different minerals. Values <1,000ppm have been measured within pyrite and arsenopyrite. A content of 1,000 – 250,000ppm has been analysed in minerals of the tetrahedrite-tennantite series and copper contents above 250,000 ppm are considered to be related to chalcopyrite.

Figure 5.1 b shows that the majority of the samples analysed have an As content between ~1,000 and ~10,000 ppm. Sb, Bi occur, with some exception, only in low concentrations (< ~100 ppm) within the Bevets Reef samples.

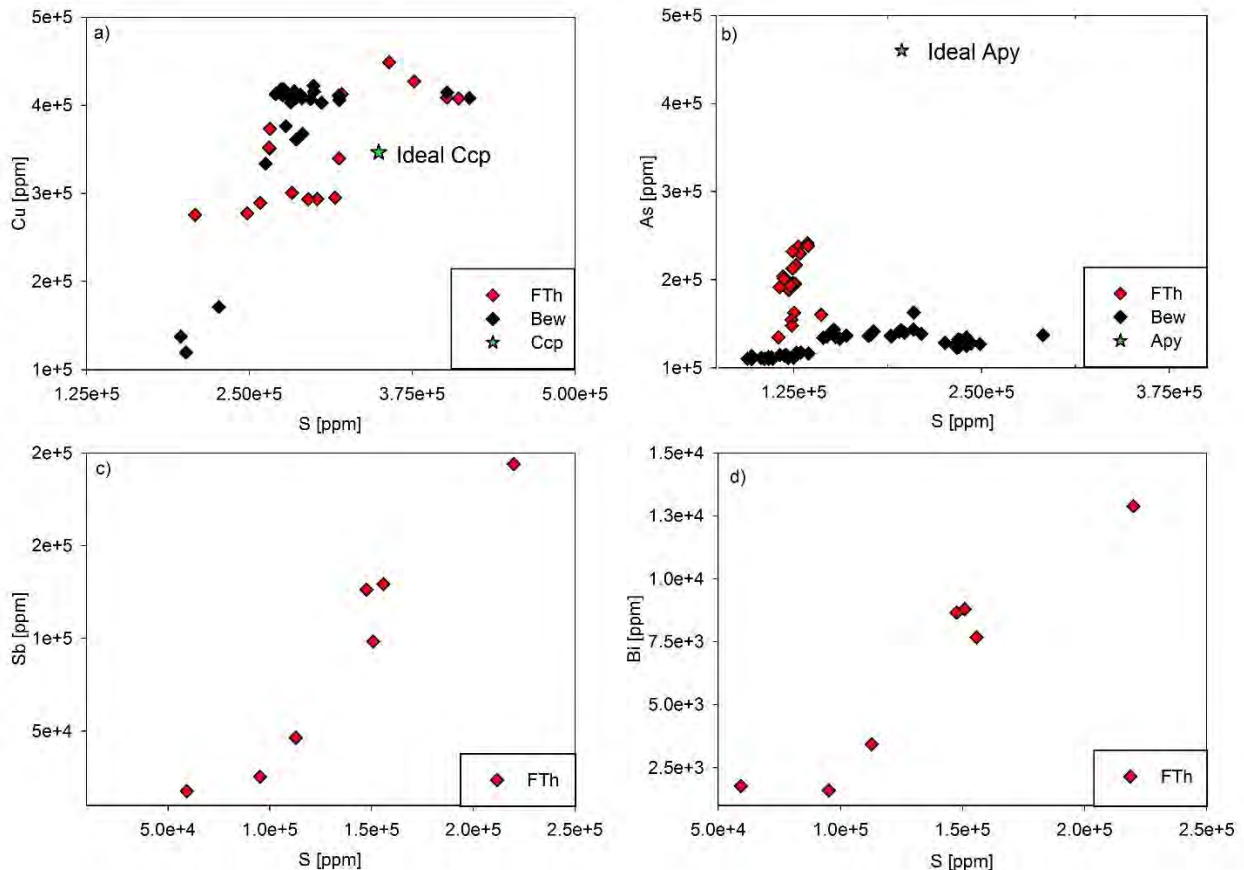


Figure 5.1: Distribution of the major element occurring within Chalcopyrite (a), arsenopyrite (b) and tetrahedrite (c and d) of Theta (FTh) and Bevets Reef (BeW). The green stars indicate the ideal stoichiometric composition of the minerals chalcopyrite (Fig 5.1 a) and arsenopyrite (Fig.5.1b).

In the Theta Reef, higher concentrations of Sb and Bi occur within minerals herein referred to as the minerals of the tetrahedrite-tennantite series. It is however obvious that the distribution patterns of Sb and Bi are very similar, indicating that these elements probably occur in association.

Trace element concentrations within pyrites (not shown in the graphs) are the most variable and can reach concentrations of up to 100,000 ppm. Those peaks probably represent inclusion of other sulphides, such as minerals of the tetrahedrite-tennantite series within the pyrite. Such spikes are not as prominent in arsenopyrite and chalcopyrite where the concentration of these trace elements usually does not exceed 10,000 ppm.

The dominant metallogenic elements within the sulphides are Cu, Ag, Au, Pb and Bi and generally form minerals of the tetrahedrite-tennantite series, $(\text{Cu},\text{Ag})_{10}(\text{Fe},\text{Zn},\text{Hg},\text{Cu},\dots)_2(\text{Sb},\text{As})_4\text{S}_{13}$ (Vaughan & Rosso, 2006). Higher concentrations of Au (up to 63 and 83 ppm for Theta and Bevets Reef respectively) primarily occur within arsenopyrite and higher concentrations of silver (up to ~1500 ppm) within tetrahedrite. The trace element distribution in tetrahedrite is quite even. Larger clusters of fracture filling tetrahedrite only occur within the Theta Reef (Chapter 3) and can contain the highest amounts of Ag (up to ~1500 ppm).

The higher concentrations of Cu and As appearing within one spot (Fig 5.2 f) are most likely caused by the fact that during the ablation the laser ablated through chalcopyrite into arsenopyrite.

Figure 5.1 indicates that the sulphur content within pyrite, arsenopyrite and chalcopyrite is in an order of tens of thousands of ppm lower than the idealised composition. This shift could have been caused by the fact that a lot of the minerals include inclusions of other sulphide minerals, causing difficulties in setting the internal standard. Another reason could be that sulphur MASS-1 standard oxidised to sulphate.

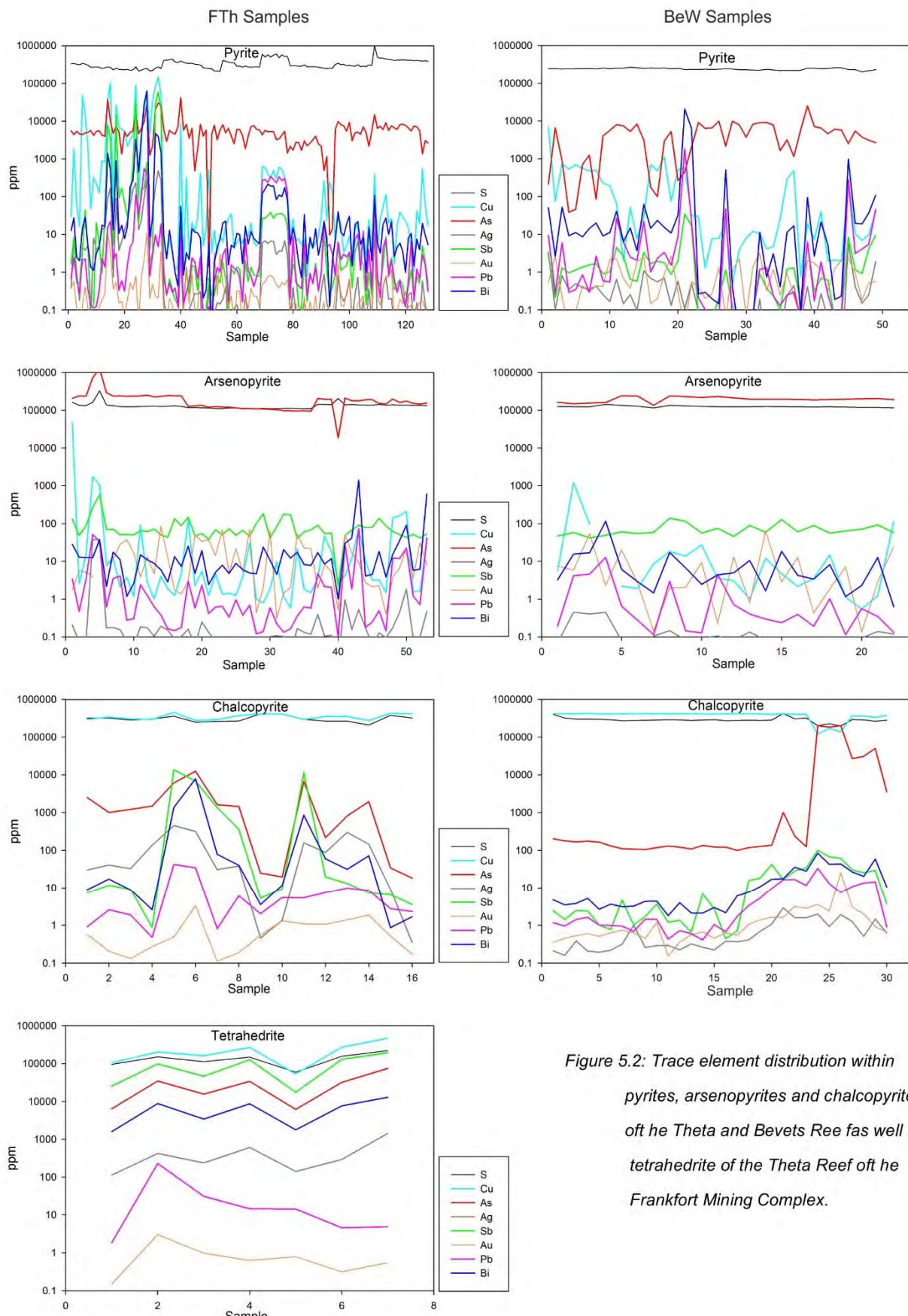


Figure 5.2: Trace element distribution within pyrites, arsenopyrites and chalcopyrites of the Theta and Bevets Reefs as well as tetrahedrite of the Theta Reef of the Frankfort Mining Complex.

Figure 5.3 shows the trace element distribution of sulphides in the Theta Reef in relation to their classification in chapter 4. It is obvious that the trace element concentrations are, except for fracture-filling minerals of the tetrahedrite-tennantite series, generally below 10,000ppm.

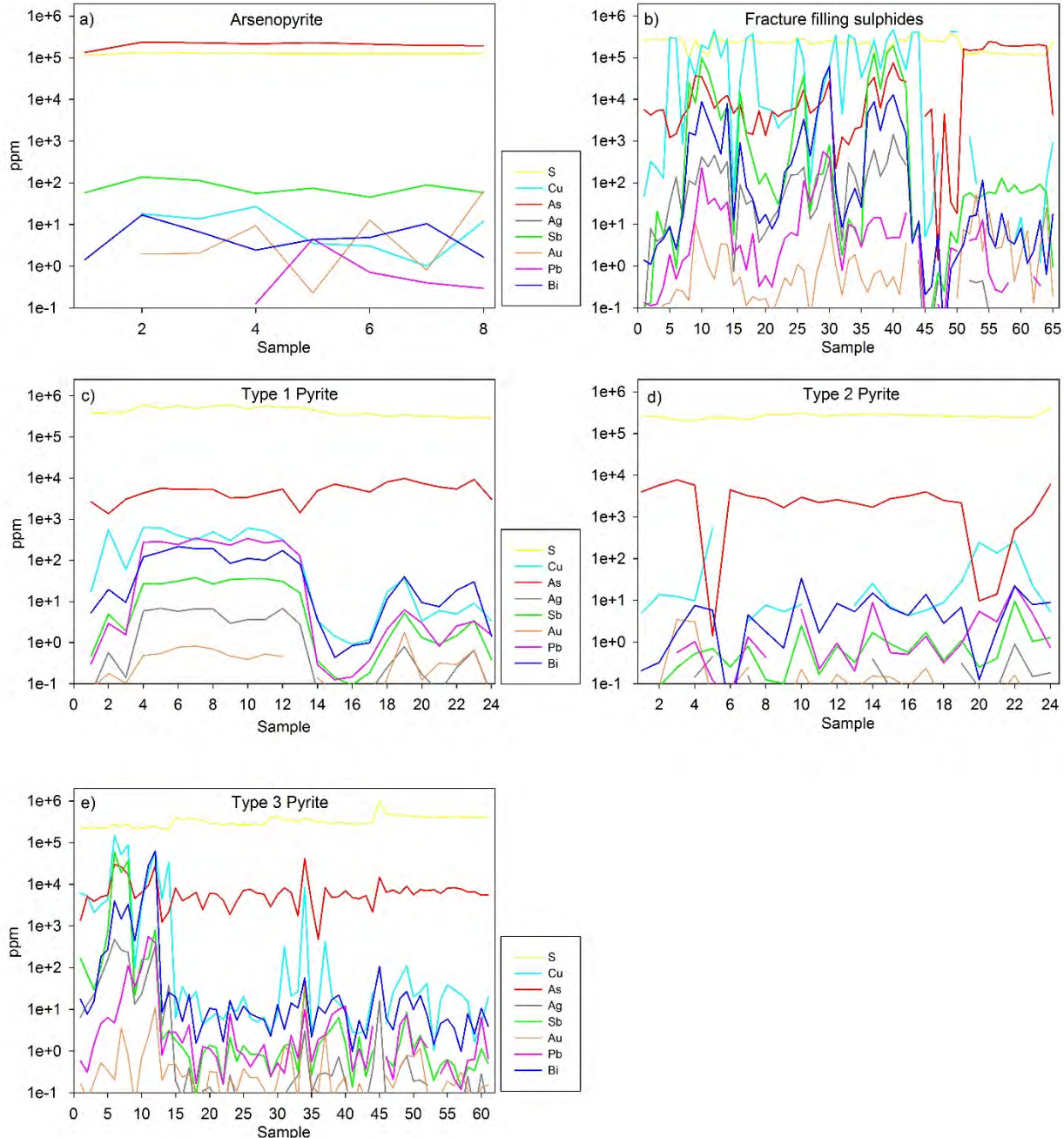


Figure 5.3: Trace element distribution in sulphide minerals of the Theta Reef, showing the most important trace elements in arsenopyrite, fracture filling sulphides and pyrites. The pyrites are classified according to chapter 4 in Type 1, 2 and 3.

The trace element distribution within Type 1 pyrite (Chapter 4), is remarkably homogeneous in contrast to Type 2, 3 and fracture-filling pyrite of the Theta Reef. Figure 5.3 a), b and e) suggest that Au predominantly occurs within Type 3 pyrite, arsenopyrite and minerals of the tetrahedrite-tennantite series. Small amounts of Au (~1 ppm) occur as electrum inclusions within Type 1 pyrite (Fig 5.3 c). Also within fracture filling sulphides (Fig 5.3 b) and Type 3 pyrites (Fig 5.3 e) seems to be a relation between higher silver content and gold. Type 2 pyrites (Fig 5.3 d) are generally Au-poor and the trace element composition of this type appears to be relatively constant in comparison to Type 3 pyrite.

Trace elements are less abundant within the Bevets Reef sulphides analysed and except for Cu, As and occasionally Bi do not exceed 1,000 ppm.

Gold is more abundant within the Bevets Reef than within Theta Reef sulphides analysed. The higher concentrations of Au occur within arsenopyrite (Fig 5.4 c), indicating that major amounts of gold precipitated at a later stage of mineralisation (Chapter 4), together with As.

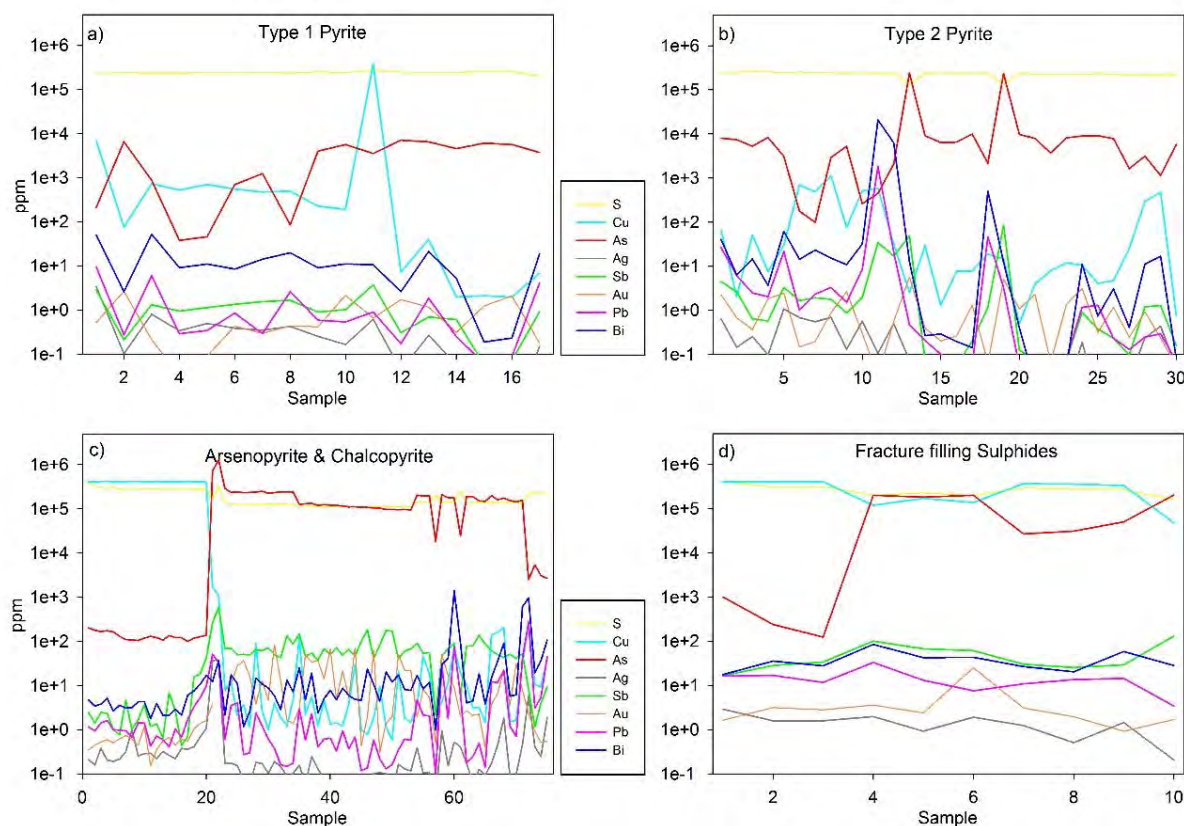


Figure 5.4: Trace element distribution in sulphide minerals of the Bevets Reef, showing the most important trace elements. The pyrites are classified according to chapter 4 in Type 1 and 2.

5.2.2 Trace elements associated with Au

The gold content of the samples analysed for this study is generally low, with maximum values of 63 and 83 ppm for the Theta and Bevets Reef respectively, with gold being more abundant within the Bevets Reef samples analysed. Furthermore, the Au content between different spot analyses within a single mineral varies by an order of magnitude (Tbl. 5.5).

Time-resolved LA-ICPMS analyses show that the Au distribution within a single spot is relatively constant (Fig 5.6), suggesting that gold occurs as solid solution or nanoparticles within the pyrite lattice (Zhang et al., 2014), rather than micron-sized nuggets. Table 5.5 shows that gold predominantly occurs in arsenic-rich pyrites, often referred to as “arsenian pyrite”. This type of pyrite contains ppm to weight percent amounts of arsenic (Reich et al., 2005).

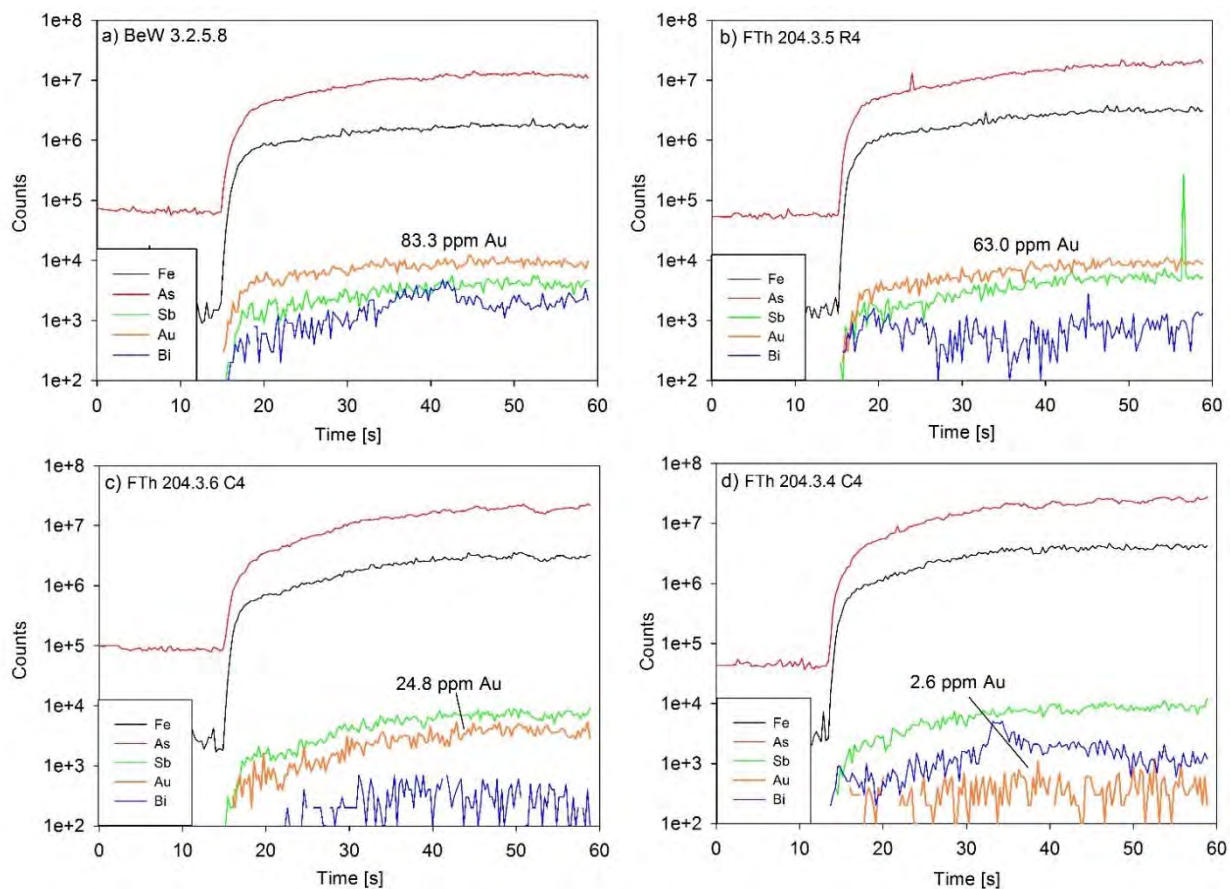


Figure 5.6: Time-resolved depth profiles for arsenian pyrite showing the occurrence of gold in comparison to other trace elements which are commonly related to the Au in the SPRG. The parallel trends for Au and As suggest that gold occurs as solid solutions or as nanoparticles, rather than micron sized nuggets.

Table 5.5: LA-ICP-MS analyses of selected gold- and silver-bearing sulphides. All values are in ppm. FTh= Theta, BeW= Bevets Reef

Au Sample	Sulphide Type	Sulphide	Cr	Mn	Co	Ni	Cu	Zn	As	Se	Ag
FTh 204.3.4 C4	FF	Apy	4.4	5.8	<0.1	<0.3	1.9	9.8	237623	28.7	0.1
FTh 204.3.5 R4	SH	Apy	5.1	5.5	<0.1	<0.3	11.9	<0.9	195259	17.9	<0.1
FTh 204.3.6 C4	FF	Apy	4.5	5.5	<0.1	0.4	112	52.9	191396	18.8	<0.1
FTh 409.3.4 R1	SH	Py	6.7	34.9	0.8	1.6	8377	13.8	41461	16.7	3.1
BeW 3.2.5.8	SP	Apy	7.7	7.9	0.1	0.8	1.0	0.8	225691	24.5	0.1
BeW 3.4.2.2	SP	Apy	5.4	5.2	0.7	1.1	73.7	28.4	176414	32.9	0.5
Ag Samples											
FTh 405.2.8.2	FF	Py	7.9	12.3	0.3	3.4	18741	9.7	9421	2.8	92.0
FTh 405.2.5.3 R1	FF	Ttr	2.6	4.7	0.1	1.0	202245	15387	34668	10.8	421
FTh 405.2.7.4	FF	Py	9.3	14.4	0.1	1.7	51482	2330	26332	3.7	266
FTh 405.2.7.1 C1	FF	Py	9.3	13.1	0.4	3.3	3265	46.4	5034	1.4	61.0
FTh 405.2.5.11 C1	FF	Ccp	7.9	10.1	0.6	1.8	289365	178	1613	10.4	30.8
Au Sample	Sulphide Type	Sulphide	Sn	Sb	Te	W	Au	Hg	Pb	Bi	
FTh 204.3.4 C4	FF	Apy	<0.5	54.4	0.5	<0.0	2.6	1.2	0.3	2.9	
FTh 204.3.5 R4	SH	Apy	<0.7	58.6	<1.0	<0.0	63.0	1.4	0.3	1.7	
FTh 204.3.6 C4	FF	Apy	<0.5	56.9	<0.9	0.0	24.8	1.7	<0.1	0.6	
FTh 409.3.4 R1	SH	Py	1.9	38.1	10.8	0	47.3	1.0	9.7	56.4	
BeW 3.2.5.8	SP	Apy	0.7	71.3	0.2	0.1	83.3	0.7	0.6	8.8	
BeW 3.4.2.2	SP	Apy	0.5	89.8	0.9	0.1	9.24	0.6	74.2	1399	
Ag Samples											
FTh 405.2.8.2	FF	Py	5.7	165	1.7	0.0	2.2	1.0	558	28308	
FTh 405.2.5.3 R1	FF	Ttr	3.9	98367	3.7	0.1	3.0	52.8	230	8792	
FTh 405.2.7.4	FF	Py	5.9	19144	3.8	0.1	3.7	81.7	18.8	1483	
FTh 405.2.7.1 C1	FF	Py	0.6	105	0.1	0.0	0.5	1.6	4.6	183	
FTh 405.2.5.11 C1	FF	Ccp	11	1357	0.8	0.0	0.1	9.8	0.8	78.4	

Abbreviations: FF= fracture-filling; SH= subhedral; SP= inclusion poor

In general there is a positive relation between Au and Pb, if Pb is above detection limit (Fig 5.7 c, d), while in sample Bew 3.4.2.2 (arsenopyrite) a negative correlation between Au and Pb, Bi, Cu, Sb has been observed (Fig. 5.7 b).

Au sometimes correlates with Ag, which suggests the presence of nanoparticles or micron-sized nuggets of electrum (Fig. 5.7 a). This association, however, is rare.

Silver generally occurs in minerals of the tetrahedrite-tennantite series, $(\text{Cu},\text{Ag})_{10}(\text{Fe},\text{Zn},\text{Hg},\text{Cu},\dots)_2(\text{Sb},\text{As})_4\text{S}_{13}$ and has only been detected in sample FTh 405.2 (Tbl. 5.5). Tetrahedrite-tennantite inclusions within other sulphide samples only contain some ppm (<5 ppm) silver.

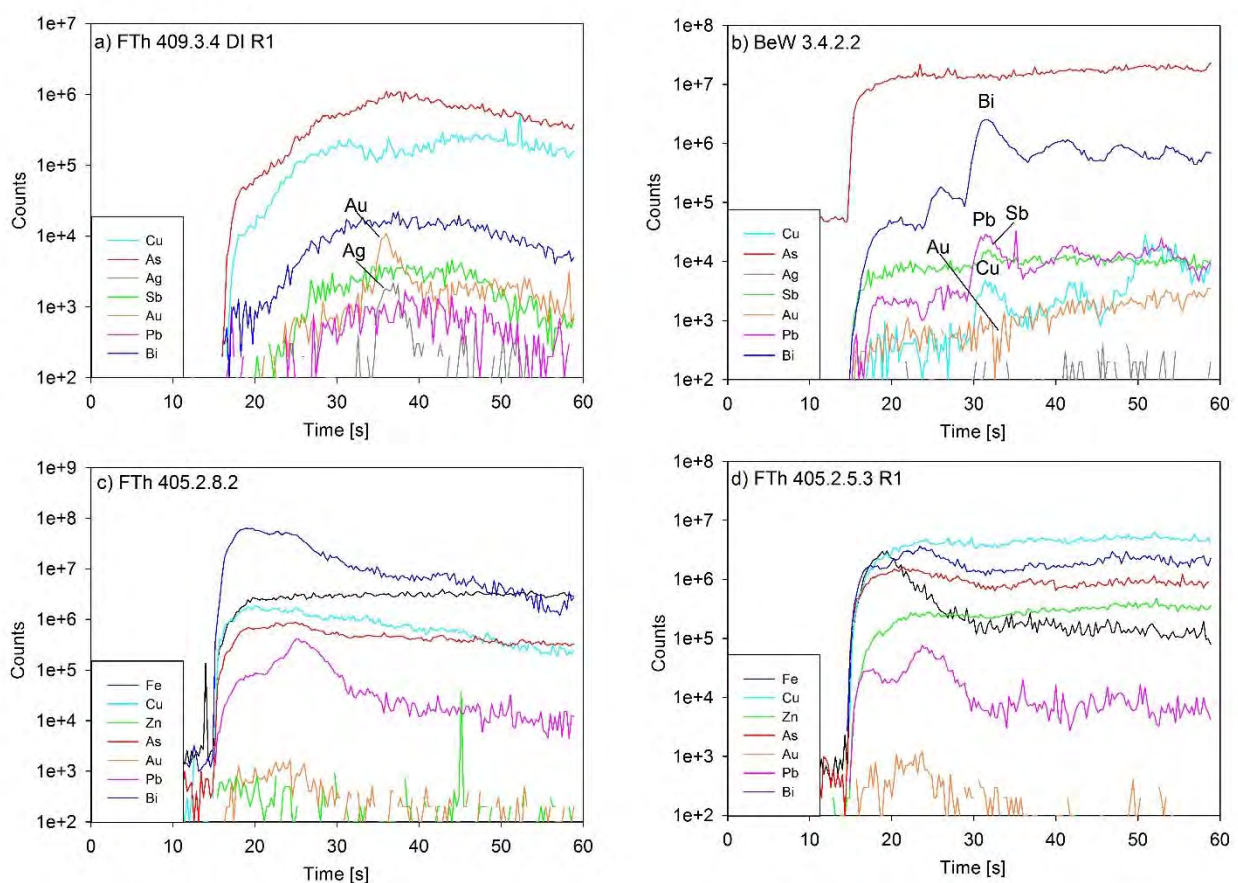


Figure 5.7: Time-resolved depth profiles showing the behaviour of gold in relationship with Ag as electrum (a), negative correlation with Bi, Pb, Sb and Cu (b) and positive correlation with Pb and Bi (c and d) in minerals of the tetrahedrite-tennantite series.

The mineral structure of the tetrahedrite-tennantite series allows extensive substitutions (Vaughan & Rosso, 2006), e.g. As and Sb can be partially replaced by Bi (Breskovska & Tarkian, 1994; Klünder et al., 2003; Vaughan & Rosso, 2006), which has been observed in close relation with silver (Fig. 5.8 b).

Higher concentrations of Pb, with maximum values 558 and 1829 ppm for Theta and Bevets Reef respectively, have been measured in some samples as substitutions in minerals of the tetrahedrite tennantite series, as possible inclusions of galena or as an incorporation into a solid solution. Trace elements, such as Cr, Mn, Co, Ni, Se, Cd Te and Hg are present in low concentrations (Tbl. 5.5) and probably substitute for S, Fe, Cu, As, Sb and Bi within minerals of the tetrahedrite-tennantite series (Vaughan & Rosso, 2006), while Ga, Ir and W are close to or below their detection limits.

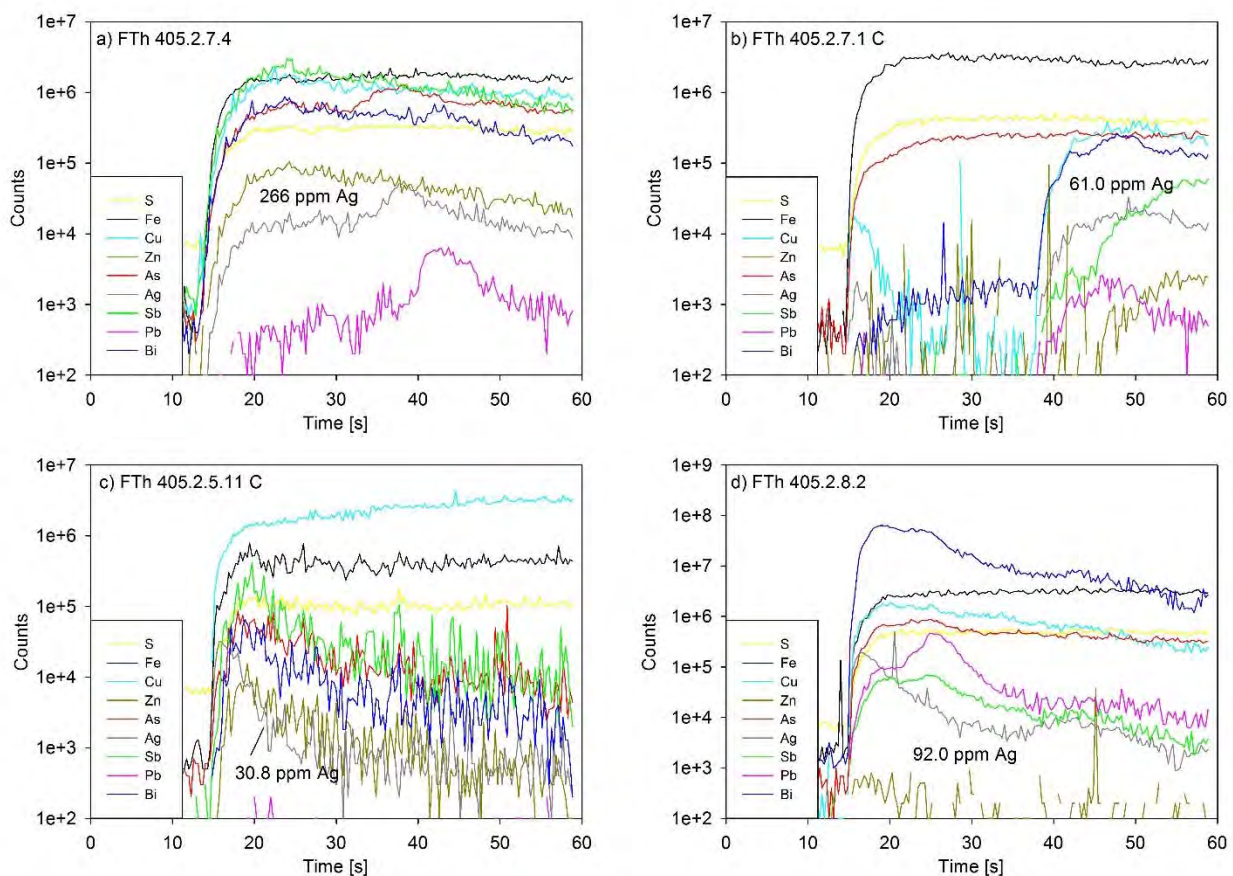


Figure 5.8: Time-resolved depth profiles showing silver and associated trace element in minerals/mineral inclusions of the tetrahedrite-tennantite series. While in plot a) and b) silver is distributed more evenly throughout the mineral (a) or mineral inclusion (b), in plots c) and d) Ag spikes at the beginning of the ablation indicating possible inclusions of argento-tennantite.

5.3 Summary

Trace elements appear to be more abundant within the Theta Reef sulphides than within Bevets Reef sulphides. The common trace elements are Cu, As, Ag Sb, Au, Pb and Bi and generally occur as minerals or mineral inclusions of the tetrahedrite-tennantite series. Minerals of the tetrahedrite-tennantite series typically occur within hydrothermal veins formed at low to medium temperature (Bideaux & Nichols, 2003).

Gold within the Theta and Bevets Reef occurs as invisible solid solution and/or as Au-As and/or Au-Sb compound in arsenic rich sulphide minerals. Gold rarely occurs in association with silver as electrum inclusions within pyrite. Silver usually occurs within Type 3 pyrites and minerals of the tetrahedrite-tennantite series, which precipitated as fracture-filling material at a late stage of mineralisation.

The Au concentration within the various pyrite types of the ore-bearing reef varies generally with the As content as already mentioned above (Fig. 5.8). Higher contents of gold occur predominantly in arsenic rich (>100,000ppm arsenic) and arsenopyrite within Theta and Bevets Reef., indicating that gold only precipitated from secondary fluid events. The only higher gold content within an arsenic poor pyrite was observed within pyrite as an inclusion of electrum in pyrite from the Theta Reef (Fig. 5.8 a). The low gold contents in Type 1 and 2 pyrites lead to the hypothesis, that gold might have been leached from these type pyrites.

Fig 5.8 b shows that the As content within a specific pyrite type is relatively constant. Higher concentrations of silver are only observed within sample FTh 405.2 and occur only within fracture filling material (Chapter 4).

Trace element spot analysis from mineral cores and rims did not show evidence for significant trace element zoning

6 Pb-Pb Isotopes

Lead is a widely distributed element within the earth and occurs as radiogenic and common lead. Radiogenic Pb is the daughter of U and Th and occurs in minerals with high U and Th contents and accumulates over time (Faure & Mensing, 2005). Common lead is generally a trace element within U- and Th-poor minerals, e.g. sulphides, and its isotopic composition does not change after the minerals have been formed. However, the isotopic composition of “common” lead has evolved over time as a result of the continuous decay of U and Th, of which the daughter products were mixed with primeval Pb and formed minerals under the exclusion of the radioactive parent. The isotopic composition of these minerals records the isotopic composition of the initial reservoir where it evolved, at the time of withdrawal (Faure & Mensing, 2005).

The time of withdrawal of common lead from a reservoir can be used for age determination. Based on the analysis of galena crystals of different ages, Stacey and Kramers (1975) suggested an evolution curve for common Pb, with ratios at 3.7 Ga of $\left(\frac{^{206}\text{Pb}}{^{204}\text{Pb}}\right) = 11.152$, $\left(\frac{^{207}\text{Pb}}{^{204}\text{Pb}}\right) = 12.998$ and, $\left(\frac{^{208}\text{Pb}}{^{204}\text{Pb}}\right) = 31.230$

and present-day ratios of

$$\left(\frac{^{206}\text{Pb}}{^{204}\text{Pb}}\right) = 18.700, \left(\frac{^{207}\text{Pb}}{^{204}\text{Pb}}\right) = 15.628 \text{ and, } \left(\frac{^{208}\text{Pb}}{^{204}\text{Pb}}\right) = 38.630.$$

All points that plot on this growth curve (Fig. 6.3.1) can be interpreted as reflecting a point in time where common lead was removed from a reservoir (Faure & Mensing, 2005).

6.1 Methodology

Pb isotopes (on masses 206, 207 and 208) were measured as part of the laser LA-ICP-MS trace element analysis (Described in detail in Chapter 5). $^{207}\text{Pb}/^{206}\text{Pb}$ and $^{208}\text{Pb}/^{206}\text{Pb}$ ratios were calculated with the trace element content in counts per seconds (cps) and have been normalized against the real- (GeoRem, 2014) and the measured mean-Pb ratios of the USGS MASS-1 standard.

6.2 Results

The data are divided into two clusters scattering around the average $\left(\frac{^{207}\text{Pb}}{^{206}\text{Pb}}\right) / \left(\frac{^{208}\text{Pb}}{^{206}\text{Pb}}\right)$ values of 0.8723 / 2.0112 and 0.9805 / 2.2486 (Tbl. 6.1). The analytical error for $\left(\frac{^{207}\text{Pb}}{^{206}\text{Pb}}\right)$ is ± 0.0360 and ± 0.0382 for $\left(\frac{^{208}\text{Pb}}{^{206}\text{Pb}}\right) \pm 0.0885$ and ± 0.0701 for the low and high ratio respectively.

Sample	Mineral	Crystal Habit	Pb 207/206	Pb 208/206
FTh 405.2.4.4	Py	Type 3	0.9	2.1
FTh 405.2.4.1	Ttr	FF	0.9	2.1
FTh 405.2.4.2	Ttr	FF	0.9	2.0
FTh 405.2.5.3 R1	Ttr	FF	0.9	2.0
FTh 405.2.5.5	Ttr	FF	0.9	2.0
FTh 405.2.5.7	Py	Type 3	0.9	2.2
FTh 405.2.5.8	Ccp	FF	0.9	1.9
FTh 405.2.7.1 R1	Py	Type 3	0.9	2.1
FTh 405.2.7.4	Py	Type 3	0.9	2.0
FTh 405.2.7.6	Py	Type 3	0.9	2.0
FTh 405.2.8.1 C1	Py	Type 3	0.9	2.0
FTh 405.2.8.1 R1	Py	Type 3	0.9	2.0
FTh 405.2.8.2	Py	Type 3	0.9	2.0
FTh 405.2.8.3	Py	Type 3	0.8	2.0
FTh 406.1.2 C1	Py	Type 3	0.9	2.0
FTh 406.1.2 R1	Py	Type 3	0.9	2.0
FTh 406.4.4 C1	Apy	IG	0.9	2.0
FTh 406.4.4 C2	Apy	IG	1.0	2.2
FTh 406.4.5 R2	Apy	IG	1.1	2.3
FTh 406.4.5 C3	Apy	IG	0.9	1.8
FTh 409.1.2 C1	Py	Type 1	1.0	2.2
FTh 409.1.2 C2	Py	Type 1	1.0	2.2
FTh 409.1.2 C4	Py	Type 1	1.0	2.3
FTh 409.1.2 C5	Py	Type 1	1.0	2.2
FTh 409.1.3.1	Py	Type 1	1.0	2.3
FTh 409.1.3.2	Py	Type 1	1.0	2.3
FTh 409.1.3.3	Py	Type 1	1.0	2.3
FTh 409.1.3.4	Py	Type 1	1.0	2.3
FTh 409.1.3.5	Py	Type 1	1.0	2.4
FTh 409.1.4 C2	Py	Type 1	1.0	2.3
FTh 409.1.4 C6	Py	Type 1	0.8	1.9
FTh 409.1.7.1	Py	Type 1	1.1	2.3
FTh 409.5.2.3	Py	Type 2	0.9	1.9
FTh 409.5.2.4	Py	Type 2	0.9	2.1
FTh 409.5.3.2 R.2	Py	Type 2	0.9	2.0

BEW3.1.1.8	Py	Type 2	0.8	2.0
BEW3.1.1.1	Py	Type 2	0.9	2.0
BEW3.1.1.2	Py	Type 2	0.7	1.8
BEW3.2.4.4	Ccp		0.9	2.0
BEW3.2.3.10	Py	Type 2	1.0	2.2
BEW3.2.3.5	Py	Type 2	1.0	2.2
BEW3.2.3.2	Py	Type 2	0.9	2.0
BEW3.2.3.1	Py	Type 2	1.0	2.2
BEW3.2.2.3	Py	Type 2	0.9	2.1
BEW3.2.2.1	Py	Type 2	0.9	2.0

Table 6.1: Lead isotope ratios of various sulphide minerals from Theta (FTh) and Bevets Reef (BeW).

(Abbreviations: Py = pyrite, Apy = arsenopyrite, Ccp = chalcopyrite, AH = anhedral, SH = subhedral, EH = euhedral, FF = fracture filling, IG = intergrowth HP = highly inclusion rich, P = inclusion rich and SP = inclusion poor).

In the Theta Reef, the lower ratio was generally measured in secondary sulphides occurring as fracture-filling material and in some euhedral inclusion rich pyrite, while the higher ratio was commonly measured in euhedral and euhedral, inclusion rich pyrite. In the Bevets Reef, all values were measured in euhedral, inclusion rich pyrite and cover the whole range of values (Tbl. 6.1).

6.3 Discussion

The wide spread range of $\left(\frac{^{207}\text{Pb}}{^{206}\text{Pb}}\right) / \left(\frac{^{208}\text{Pb}}{^{206}\text{Pb}}\right)$ makes it difficult to obtain a meaningful age on the ore mineralisation of the Theta and Bevets Reef (Fig. 6.2). Only values of the cluster with the higher $\left(\frac{^{207}\text{Pb}}{^{206}\text{Pb}}\right) / \left(\frac{^{208}\text{Pb}}{^{206}\text{Pb}}\right)$ ratios plot on the Stacey and Kramer curve.

The ages obtained from these ratios range from ~1.5 to ~2.1 Ga, overlapping with the age of 2.05 Ga of the Bushveld Complex (Johnson et al., 2005). The fact that only very few ages are older than the BC supports the idea that the age of the complex can probably be taken as the maximum age constraint for the mineralization of the Theta and Bevets Reef.

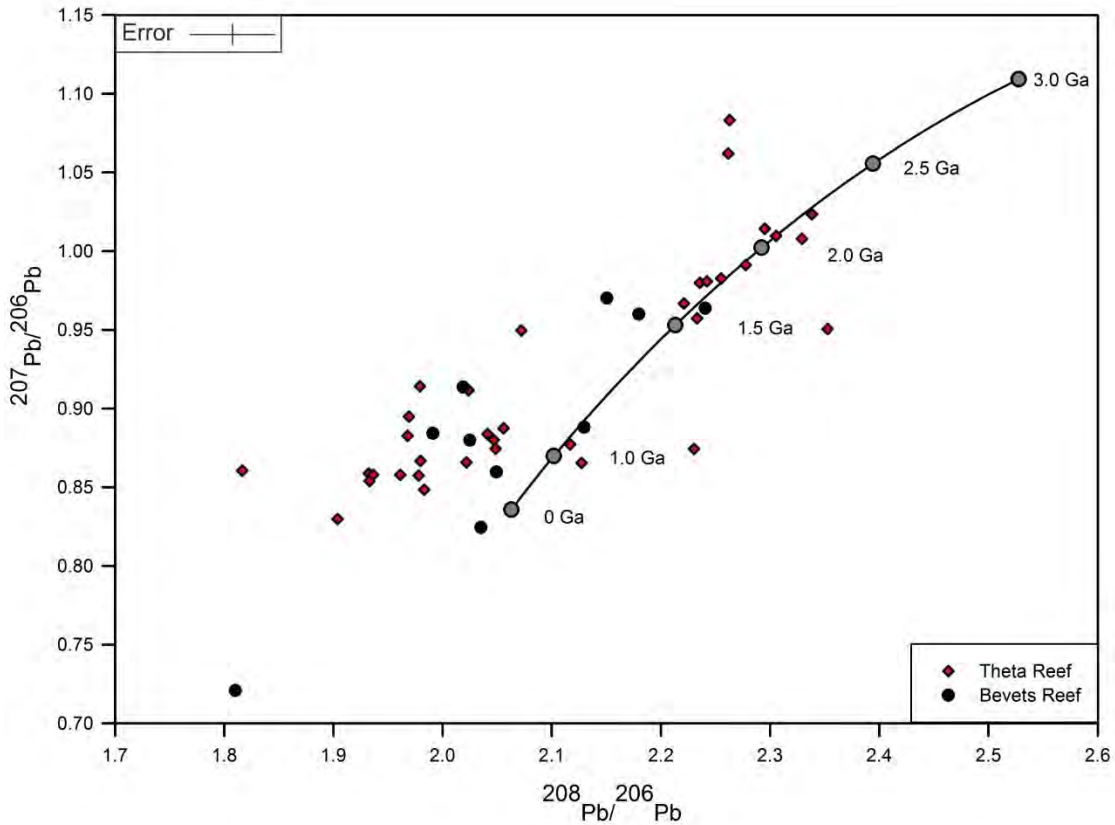


Figure 6.2: $^{207}\text{Pb}/^{206}\text{Pb}$ vs. $^{208}\text{Pb}/^{206}\text{Pb}$ diagram showing the lead isotopic composition of sulphide minerals from Theta and Bevets Reef of the Frankfort Mining Complex and the Stacey and Kramers common Pb curve (Stacey & Kramers, 1975). The error bar given (top left corner) is the typical error for all plots.

In general fracture filling minerals have a low $\left(\frac{^{207}\text{Pb}}{^{206}\text{Pb}}\right) / \left(\frac{^{208}\text{Pb}}{^{206}\text{Pb}}\right)$ ratio, while higher ratios were predominantly measured in, in this thesis referred to as Type 1 pyrites (Chapter 4). This indicates that the two major cluster might be related to different fluid events.

The lead isotopic compositions from the Theta and Bevets Reef have been compared with lead isotopic data from the Bushveld Complex, the Black Reef Formation and the Murchison Belt (Fig. 6.3).

The figure shows that the data from the Bushveld Complex overlaps with the cluster of the higher ratios of this study, indicating that the Bushveld Complex could have been a possible source of lead. Mathez and Kent (2007) described these ratios as non-representative for the initial lead isotopic composition of the parental magmas.

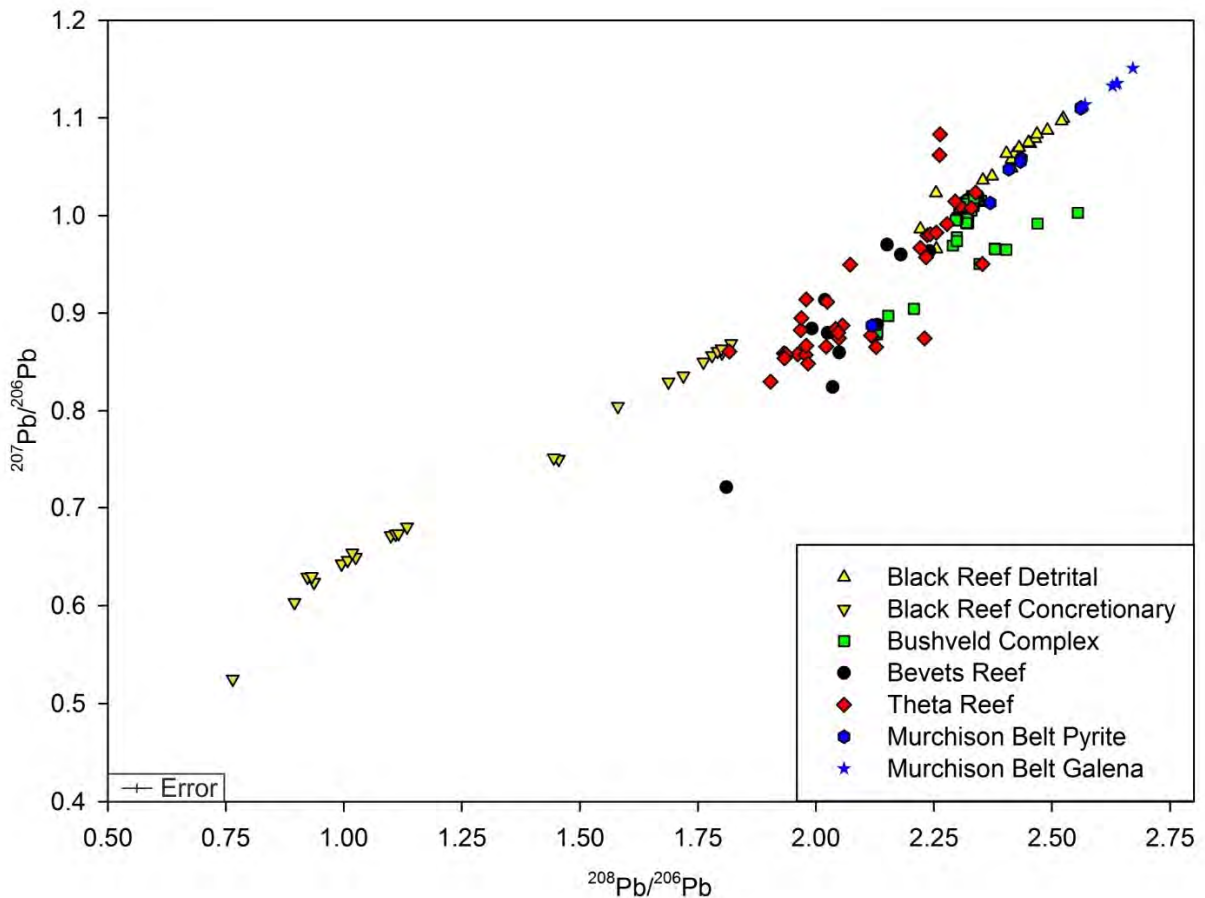


Figure 6.3: Binary $^{207}\text{Pb}/^{206}\text{Pb}$ vs. $^{208}\text{Pb}/^{206}\text{Pb}$ diagram showing the lead isotopic composition of sulphide minerals from Theta and Bevets Reef in comparison to data from the Bushveld Complex (Mathez & Waight, 2003; Mathez & Kent, 2007), the Black Reef Formation (Barton & Hallbauer, 1996) and the Murchison Belt (Saager et al., 1976). The error bar given (bottom left corner) is the typical error for all plots.

Mathez and Kent (2007) suggest that the variation in Pb-isotopic ratios and therefore in apparent age are related to redistribution of younger, radiogenic lead by fluids external to the Bushveld Complex.

The lead isotopic compositions of galena and pyrite within the Murchison Belt (Saager et al., 1976) are much higher than those of the SPRG. This data does not suggest any relation between the gold deposits of the Murchison Belt and those of the Sabie-Pilgrim's Rest Goldfield.

The lower lead isotope ratios analysed do not represent any known Pb isotopic

composition within the study area (Fig. 6.3), but are, however, close to those of the concretionary pyrites of the Black Reef Formation. The higher lead isotopic composition occurs predominantly within Type 1 pyrite. Type 2 pyrite shows both compositions, low and high while the lower Pb isotopic composition occurs predominantly in Type 3 and fracture filling pyrites. Stable isotope geochemistry (Chapter 7) suggests that the isotopic signatures have been altered by the host rocks of the ore-bearing reefs, this proposes that the lower Pb-isotopic signature represents that of the Malmani dolomites. Assuming a relation between different fluid events and the isotopic compositions of the sulphides suggests that the primary sulphides represent the isotopic composition of the rocks of the Bushveld Complex and secondary sulphides the composition of the dolomite host rocks. This subsequently indicates that in the primary mineralisation episode higher volumes of fluids interacted with smaller volumes of host rocks while in the second mineralisation event smaller volumes of fluids interacted with larger volumes of rocks, preserving the lead isotopic composition of the host rock. This leads to the conclusion that at least two major mineralisation events have led to the formation of the Theta and Bevets Reef.

Isotopic ratios which are not closely related to the ratios of the BC or the dolomites could have been altered by rocks with a similar Pb-isotopic composition to the Black Reef.

7. Stable Isotope Geochemistry

Stable isotope ratios are used to determine the temperature of vein formation but more commonly to determine the identity of the hydrothermal fluids (Bons et al., 2012) as well as the origin of metals precipitated from these fluids. The possible fluid sources are: ocean, meteoric, connate, magmatic and metamorphic (White, 1974). Unfortunately the isotopic compositions of these reservoirs are not always unique, as some isotope fields show a strong overlap (Hoefs, 2009; Bons et al., 2012).

To successfully determine these sources, the isotopic enrichment or depletion of hydrothermal fluids due to possible host rock interaction has to be taken into account (Clayton et al., 1968). If fluids percolate through rocks surrounding a heat source (e.g. the Bushveld Complex) the isotopic signature of the hydrothermal fluid will change as a result of equilibration with the host rock. At low fluid-rock ratios the host rock isotopic signature, and at high fluid:rock ratios the initial isotopic composition of the fluid will dominate. During fluid:rock interaction metals may be leached out of the rocks and later be re-deposited in fractures or cavities as a result of decreasing temperatures, a drop in pressure or due to a chemical reaction, such as pH changes within the fluid (Faure & Mensing 2005; Robb, 2005).

Isotope data are commonly reported in δ -notation and represent the ratio of the sample relative to a standard.

$$\delta = \left(\frac{R_{sample}}{R_{standard}} - 1 \right) \times 10^3 \quad (\text{Formula 7.1})$$

R representing the ratio of the isotopic abundance of the heavy isotope over the light isotope (Faure & Mensing, 2005), therefore, applied to oxygen isotopes, it is:

$$R = \frac{^{18}\text{O}}{^{16}\text{O}} \quad (\text{Formula 7.2})$$

The standard materials by definition have $\delta = 0\text{‰}$. Therefore a sample with a δ value +5 would be enriched by 5 ‰ in the heavier isotope (e.g. ^{13}C , ^{18}O or ^{34}S) relative to the standard material (Taylor, 1974).

The isotopic ratios between two solid phases in isotopic equilibrium is a function of temperature and the identity of the phases. This difference can be expressed as the fractionation factor, α (Hoefs, 2009) and is defined by:

$$\alpha_{A-B} = \frac{R_A}{R_B} \quad (\text{Formula 7.3})$$

The fractionation factor α is related to Δ , the fractionation between two phases.

$$\Delta_{A-B} = \delta_A - \delta_B \quad (\text{Formula 7.4})$$

$$\Delta_{A-B} \approx 10^3 \ln \alpha \quad (\text{Formula 7.5})$$

To calculate the equilibrium temperature T between two phases the equation suggested by Bigeleisen and Mayer (1947), Bottinga and Javoy (1973) and Sharp and Kirschner (1994) is most adequate.

$$10^3 \ln \alpha = a + \frac{b \times 10^6}{T^2} \quad (\text{Formula 7.6})$$

Because a is a experimentally determined constant which is generally 0 for mineral-mineral determined fractionation (Sharpe & Kirschner, 1994) the formula can be written as

$$T = \sqrt{\frac{b \times 10^6}{10^3 \ln \alpha}} \quad (\text{Formula 7.7})$$

b is the fractionation coefficient and T is the temperature in Kelvin (Sharpe & Kirschner, 1994; Faure & Mensing, 2005; Hoefs, 2009)

The $\delta^{18}\text{O}$ compositions of coexisting quartz and calcite, for instance, precipitated from hydrothermal fluids, can be used to calculate isotopic the temperature of vein formation (Kirschner et al., 1995; Bons et al., 2012). The equilibrium temperature of coexisting minerals is uniquely defined by the experimentally determined mineral/mineral fractionation and its temperature dependency (Chacko et al., 2001). The best isotope thermometers are provided by mineral pairs that have a divergent affinity for isotopes (Bons et al., 2012). Provided the mineralisation temperature is known, the oxygen isotopic composition of the ore forming-fluid in equilibrium with the analysed quartz and calcite can be calculated.

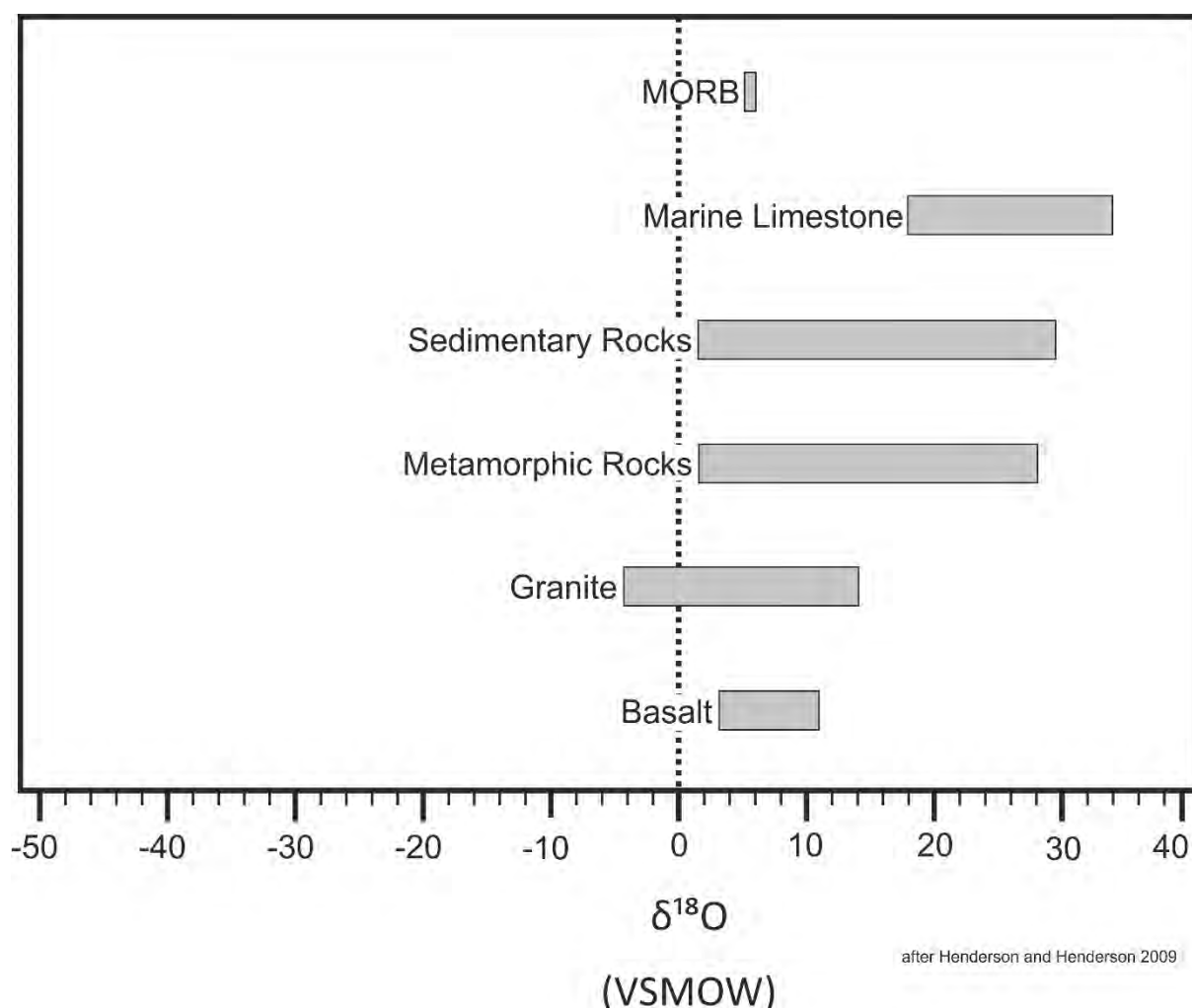


Figure 7.1: $\delta^{18}\text{O}$ values of selected natural materials. All values are in ‰ (per mil) relative to Vienna Standard Mean Ocean Water (VSMOW).

If the determined fluid isotopic signature has not been obscured by fluid-rock interaction, this signature can be related to a fluid source (Fig. 7.1) (Hoefs, 2009). Most ore-forming fluids have been interpreted to be a combination of meteoric and magmatic/metamorphic fluids (Bons et al., 2012 and references there within).

The analysis of sulphur- and carbon- isotopes of hydrothermal minerals in precipitated equilibrium with each other can provide information about the origin and the physical chemical conditions, such as pH and $f\text{O}_2$, of the hydrothermal fluid (Rye & Ohmoto, 1974). Sulphur isotope thermometry has been conducted especially on sulphide deposits, but has not been proved to be a useful tool (Valley, 2001). One reason is that the isotopic fractionation between specific mineral pairs, e.g. pyrite-chalcopyrite, pyrite-arsenopyrite and pyrite-tetrahedrite, is very small.

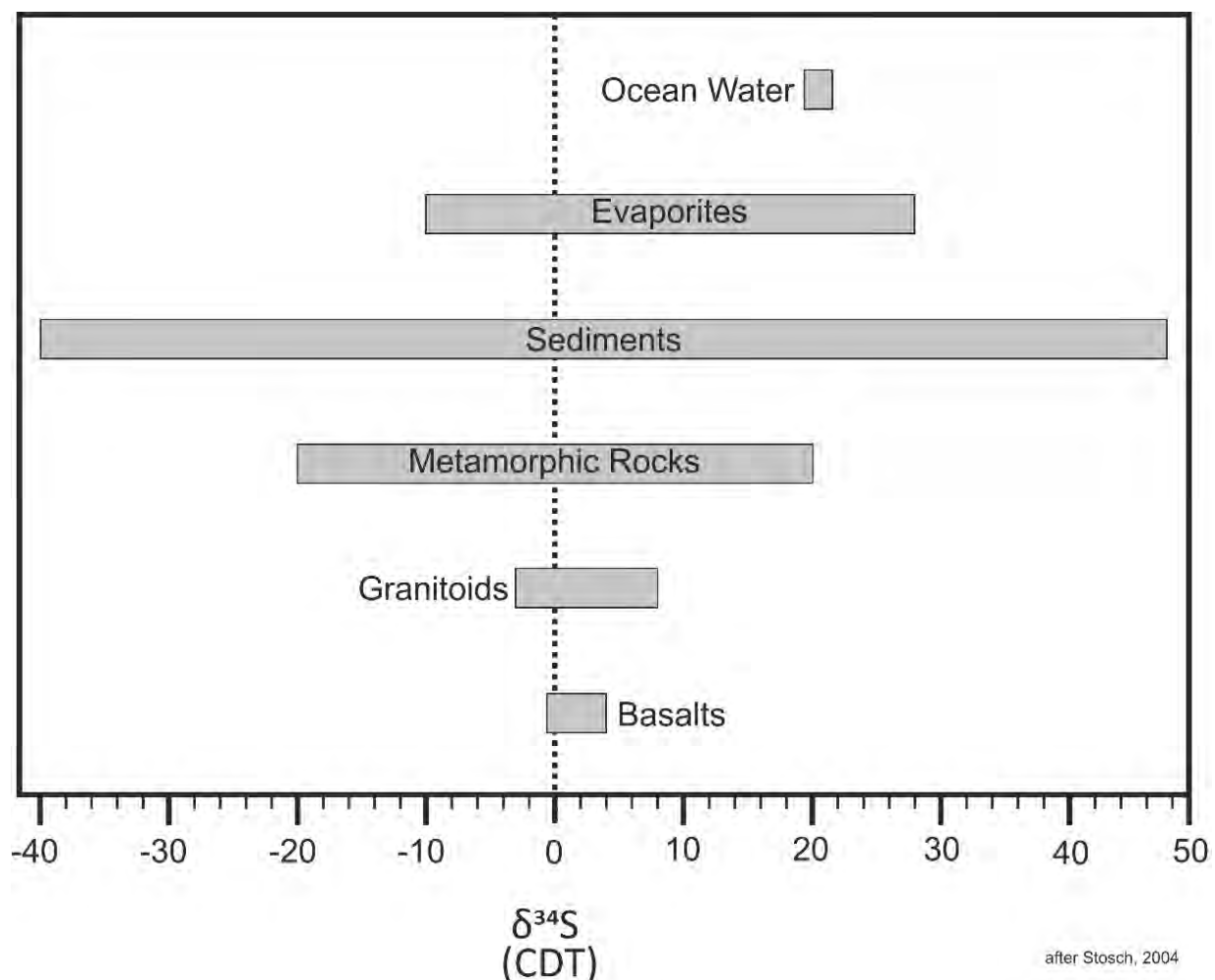


Figure 7.2: $\delta^{34}\text{S}$ isotopic compositions of selected natural materials. All values are in ‰ (per mil) relative to CDT (Cañon Diablo Troilite).

Another reason is that the sulphur isotopic data of sulphides do not necessarily represent the sulphur isotopic composition of the ore-forming fluid from which they precipitated, due to a strong control by pH and oxygen fugacity (Faure & Mensing, 2005).

$\delta^{34}\text{S}$ values of sulphides from igneous sources (Fig. 7.2) are assumed to be similar to the $\delta^{34}\text{S}$ of sulphides from meteorites and therefore have an S-isotopic composition of 0 ‰ relative to CDT (Cañon Diablo Troilite), but the isotopic signature of biogenic sulphur is typically more negative and the $\delta^{34}\text{S}$ ratios tend to be more variable (Faure & Mensing, 2005).

Carbon isotopes of vein carbonates are usually compared to the C-isotopic signature of the host rocks, in order to establish a potential source (Dietrich et al., 1983; Bons et al., 2012).

Carbon generally occurs, as organic matter and natural gas, in sedimentary rocks, marine limestone and shales as well as in igneous and metamorphic rocks e.g. as graphite (Rye & Ohmoto, 1974, Faure & Mensing, 2005). It also occurs as CO₂ in the atmosphere and as bicarbonate ions within the hydrosphere (Faure & Mensing 2005).

These sources can be differentiated by their $\delta^{13}\text{C}$ signature (Fig. 7.3). Furthermore, organic carbon is usually highly negative in comparison to inorganic carbon. Carbon isotopic compositions of marine carbonates are around 0 ‰, the VPDB standard itself being marine calcite and aragonite (Faure & Mensing, 2005).

Carbon isotope thermometry between organic and inorganic carbon is highly unreliable. Organic carbon is highly resistant to equilibration and, therefore, does not represent the mineralisation temperature (Faure & Mensing, 2005).

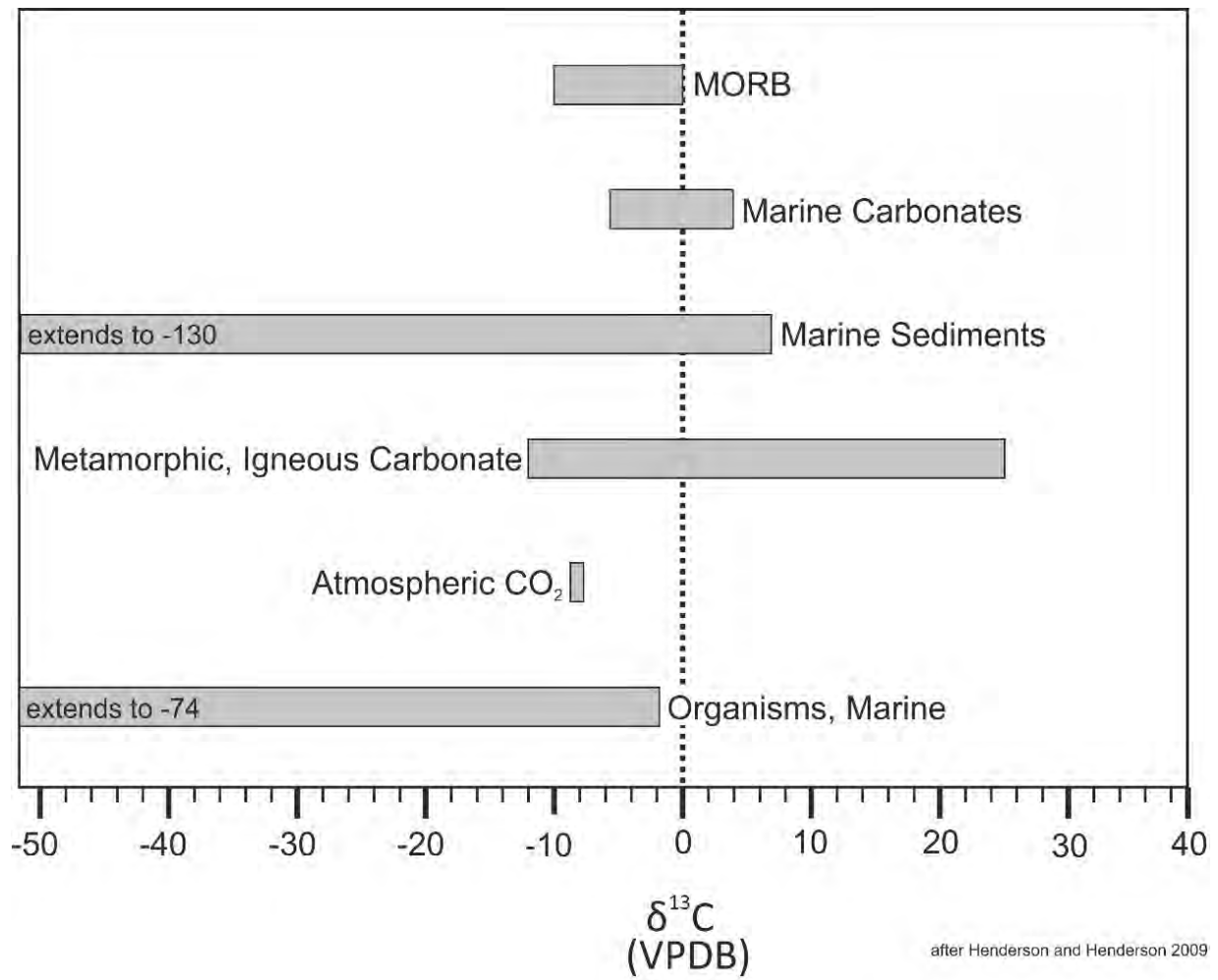


Figure 7.3: $\delta^{13}\text{C}$ values of natural materials. All values are in ‰ (per mil) relative to Vienna Pee Dee Belemnite standard.

7.1 Methodology

Sample material was collected at Theta Reef and the Bevets waste dump of the Frankfort Mining Complex.

All samples were crushed to mm size and separated by hand picking. The isotopic analysis for various minerals has been performed on bulk samples and represents the isotopic composition of the ore and gangue minerals.

Carbon- and oxygen- isotopic compositions of calcite were determined using a Thermo Finnigan Gasbench II/ CTC Combi-Pal autosampler device connected online with a Finnigan Mat 252 gas source mass spectrometer. He is used as a carrier gas, with both devices connected using the continuous flow technique. About 0.1 mg of dried sample powder is set to 72°C, purged with pure He gas and then dissolved in 4-6 drops of 100% phosphoric acid. After ~90 min the released CO₂ is transferred to the mass spectrometer using a GC gas column to separate other components. Isotopic ratios were calibrated against the standards Laser marble and NBS-19. All values are reported in δ-notation in per mil (‰) relative to VPDB (Vienna Pee Dee Belemnite) for δ¹³C and in VPDB and VSMOW (Vienna Standard Mean Ocean Water) for δ¹⁸O results. The external reproducibility of the sample analysis is better than ±0.3 per mil for δ¹³C and δ¹⁸O and ±0.1 per mil for standards. The results for the standard calibration were δ¹³C = -5.00 ‰ and δ¹⁸O = -22.96 ‰ relative to VPDB for NBS-18 and δ¹³C = 1.95 ‰ and δ¹⁸O = -2.20 ‰ relative to VPDB for NBS-19 (external reproducibility is better than 0.1 ‰). The external reproducibility for the carbonate-content is better than ±10 %. The phosphoric acid fractionation factor for calcite was applied to improve the accuracy of the analysis.

Carbon isotope compositions of graphite were measured using a Carlo-Erba Elemental Analyser/Combustion II Interface connected, using the continuous flow technique with a He stream as the carrier gas, to a Thermo Quest Delta+XL mass spectrometer. 20mg of bulk sample is treated with a 5% solution of HCl to remove all inorganic carbon. Afterwards the samples are washed in ultra clean water and dried at 60 °C. Depending on the carbon concentration, 0.05 to 1.3 mg of sample wrapped in tinfoil and loaded into the auto-sampler. Combustion in an oxygen stream at 1050°C is followed by a reduction furnace at 650 °C, releasing CO₂, which will then be

analysed in the mass spectrometer. Carbon isotope values were calibrated against the USGS 24 standard and reported in δ -notation in per mil (\textperthousand) relative to VPDB (Vienna Pee Dee Belemnite). The reproducibility is $\pm 0.1 \text{\textperthousand}$ for $\delta^{13}\text{C}$ measurements and $\pm 10\%$ for the carbon content. The result of the $\delta^{13}\text{C}$ standard calibration was -16 \textperthousand relative to VPDB.

Oxygen isotopes compositions of quartz were measured employing the CO₂-laser fluorination method and a Finnigan Mat 252 dual-inlet isotope ratio mass spectrometer. A Pt-sample holder with 2 to 4 mg material is pumped out to a $\sim 10^{-6}$ mbar vacuum. The CO₂-laser is heating the samples in 50 mbar pure F₂ in a preflourinated sample chamber. The extracted O₂ will be separated from excess F₂ and collected on a molecular sieve and analysed by a mass spectrometer, calibrated against the NBS-28 quartz standard. Results are reported in δ -notation in per mil relative to VSMOW. The overall reproducibility of samples and standard of $\delta^{18}\text{O}$ is $\pm 0.2 \text{\textperthousand}$.

Sulphur isotope compositions of pyrite, arsenopyrite and tetrahedrite were measured using a NC 2500 elemental analyser connected to a Thermo Quest Delta+XL mass spectrometer. S isotopic ratios are calibrated against the NBS 123, NBS 127, IAEA-S-1 and IAEA-S-3 standard. All results are in δ -notation in per mil and relative to CDT. The reproducibility of $\delta^{34}\text{S}$ for this analysis was $\pm 0.3 \text{\textperthousand}$ and the reproducibility for the sulphur content was $\pm 5\%$. The $\delta^{34}\text{S}$ values for the standard measurements were 17.10 \textperthousand for NBS 123, 20.31 \textperthousand for NBS 127, -0.30 \textperthousand for IAEA-S-1 and -32.10 \textperthousand for IAEA-S-3 (all results are relative to CDT).

(Spötl & Vennemann, 2003; Giesemann et al., 1994; Kasemann et al., 2001; Rumble & Hoering 1994; Sharp 1990; Valley et al., 1995)

7.2 Oxygen Isotopes

7.2.1 Results

Four calcite and nine quartz samples from the northern stoping area of the Theta Reef were analysed for their $\delta^{18}\text{O}$ composition (Table 7.4). The ^{18}O isotopic ratios of calcite range from 16.2 to 18.3 ‰ and for quartz from 16.3 to 18.8 ‰.

Sample No.	$\delta^{18}\text{O}$ (Calcite)	$\delta^{18}\text{O}$ (Quartz)	$\delta^{18}\text{O}$ (Fluid)	Remark
FTh203a	16.5		12.0	reproducibility 0.2‰
FTh 203b	16.6		12.1	reproducibility 0.2‰
FTh 301a		18.0	11.8	
FTh 301b		17.1	10.9	
FTh 400		17.9	11.7	
FTh 401	16.2		11.7	reproducibility 0.3‰
FTh 402		16.3	10.1	
FTh 406	18.3	17.5	13.8 / 11.3	
FTh 502		18.5	12.3	
FTh 503a		18.4	12.2	
FTh 503b		17.9	11.7	
FTh 505		18.8	12.6	

Table 7.4: $\delta^{18}\text{O}$ compositions of calcite and quartz samples from the Theta Reef at Frankfort Mine.

All values are in ‰ (per mil) relative to VSMOW. The reproducibility is better than 0.1 ‰ if not marked otherwise. $\delta^{18}\text{O}_{\text{Fluid}}$ values have been calculated with the formulae suggested by Clayton et al. (1972) and O'Neil et al. (1969) for an average temperature of 320 °C. The calcite samples FTh 203 a, b and FTh 401 have a low carbonate content (<17%). This is most likely caused by a contamination of the sample with quartz.

7.2.2 Discussion

There is no obvious trend in the O-isotopic compositions of the samples and their occurrence within the reef, or their textural position within the individual samples. Figure 7.5 shows that a number of oxygen isotopic values plot around ~16.4 ‰ and 18.2 ‰ for calcite and quartz respectively. Assuming that these quartz and calcite values represent the quartz-calcite mineral pair in isotopic equilibrium, the isotopic equilibrium temperature would be between ~125 and ~175 °C using the formula by Chiba et al. (1989).

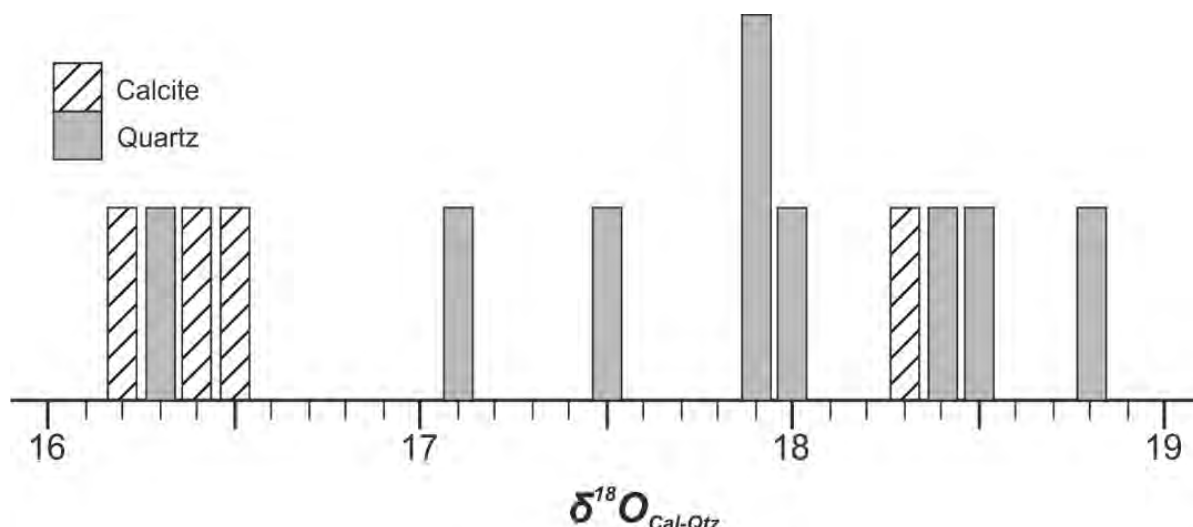


Figure 7.5: Histogram of $\delta^{18}\text{O}$ values for quartz and calcite within Theta Reef.

Those temperatures are not consistent with the mineralisation temperature of ~320 °C determined by fluid inclusion analysis by Boer et al. (1993), and would suggest that quartz and calcite are not in oxygen isotopic equilibrium, as will be explored further in the section below. However, the temperature estimation of ~320°C (Boer et al., 1993) allows to calculate oxygen isotopic composition of the fluid that formed the quartz and calcite within the vein, using the formulae by Clayton et al. (1972) for Qtz-H₂O and by O'Neil et al. (1969) for Cal-H₂O (Fig. 7.7). Assuming that the mineralisation temperature of ~320°C is correct, the majority of the $\delta^{18}\text{O}$ values calculated for the fluid composition fall within the range of 11.7 to 12.3 ‰ (Fig. 7.6).

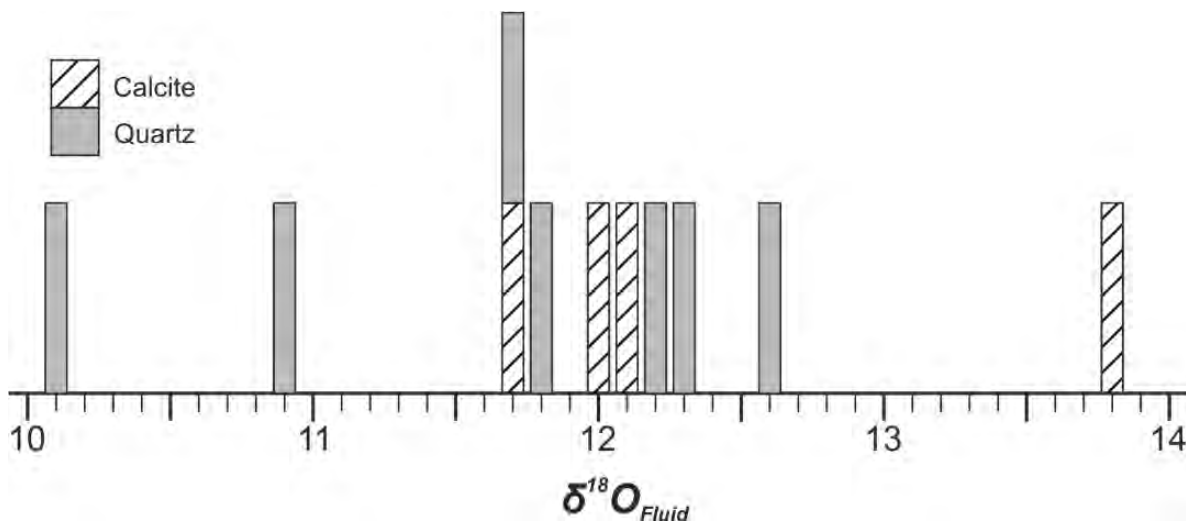


Figure 7.6: $\delta^{18}\text{O}$ compositions of the ore-forming fluid calculated from quartz and calcite values employing the formula suggested by O'Neil et al. (1969) for the calcite- H_2O and by Clayton et al. (1972) for the quartz- H_2O equilibrium.

Given this range, the ore-forming fluid of the Theta Reef had presumably an initial $\delta^{18}\text{O}$ composition of $\sim 12 \pm 0.3 \text{ ‰}$.

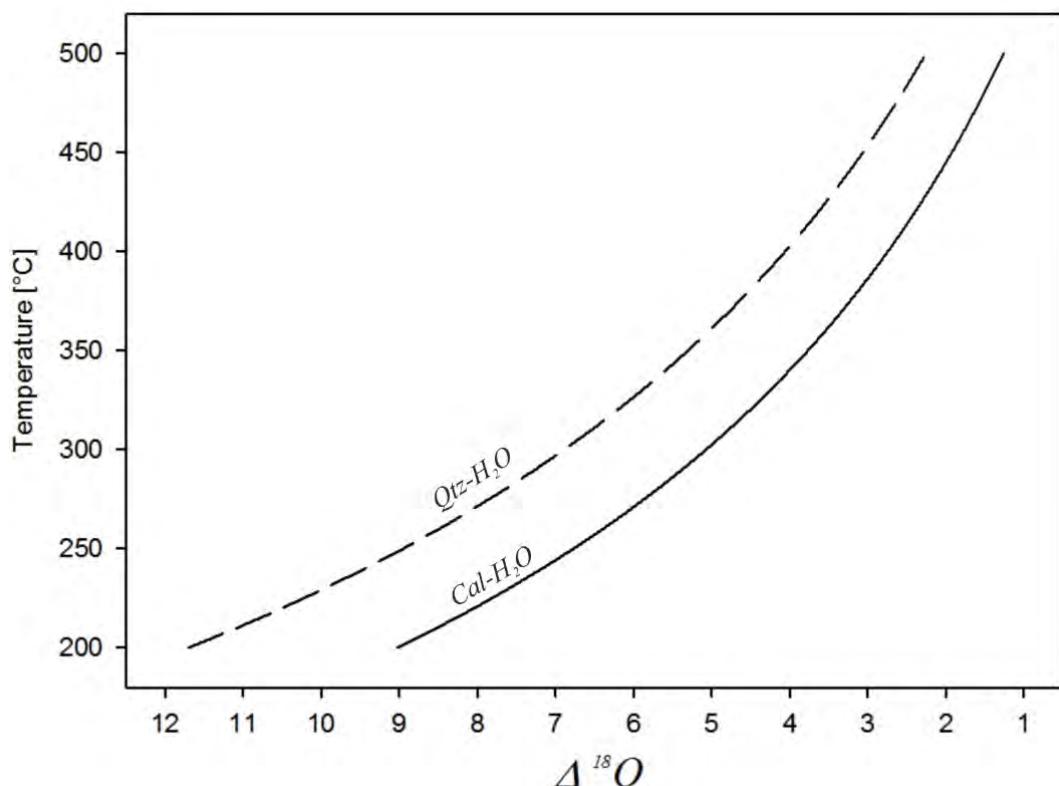


Figure 7.7: Equilibrium temperatures in the $\text{O}_{\text{Qtz}-\text{H}_2\text{O}}$ (black dashed curve) and $\text{O}_{\text{Cal}-\text{H}_2\text{O}}$ - (black curve) oxygen isotope system. The temperatures have been calculated for the temperature range from 200-500 $^{\circ}\text{C}$, after Clayton et al. (1972) for $\text{Qtz}-\text{H}_2\text{O}$ and after O'Neil et al. (1969) for $\text{Cal}-\text{H}_2\text{O}$.

In order to determine a temperature relation between quartz and calcite minerals, all calcite samples have been matched with all quartz samples to calculate equilibrium temperatures for each possible quartz-calcite mineral pair.

For the calculation the formula $\Delta_{Qtz-Cal} = \frac{0.38 \times 10^6}{T^2}$ was used (Hoefs, 2009).

The temperatures for these calculations are widely spread (Fig. 7.8) and support the idea that quartz and calcite were not in equilibrium.

The mineralisation temperature within a specific reef however, is believed to be constant during the time of ore formation. Therefore, temperature-related fractionation may be less significant than differences in the $\delta^{18}\text{O}$ composition of the ore-forming fluids.

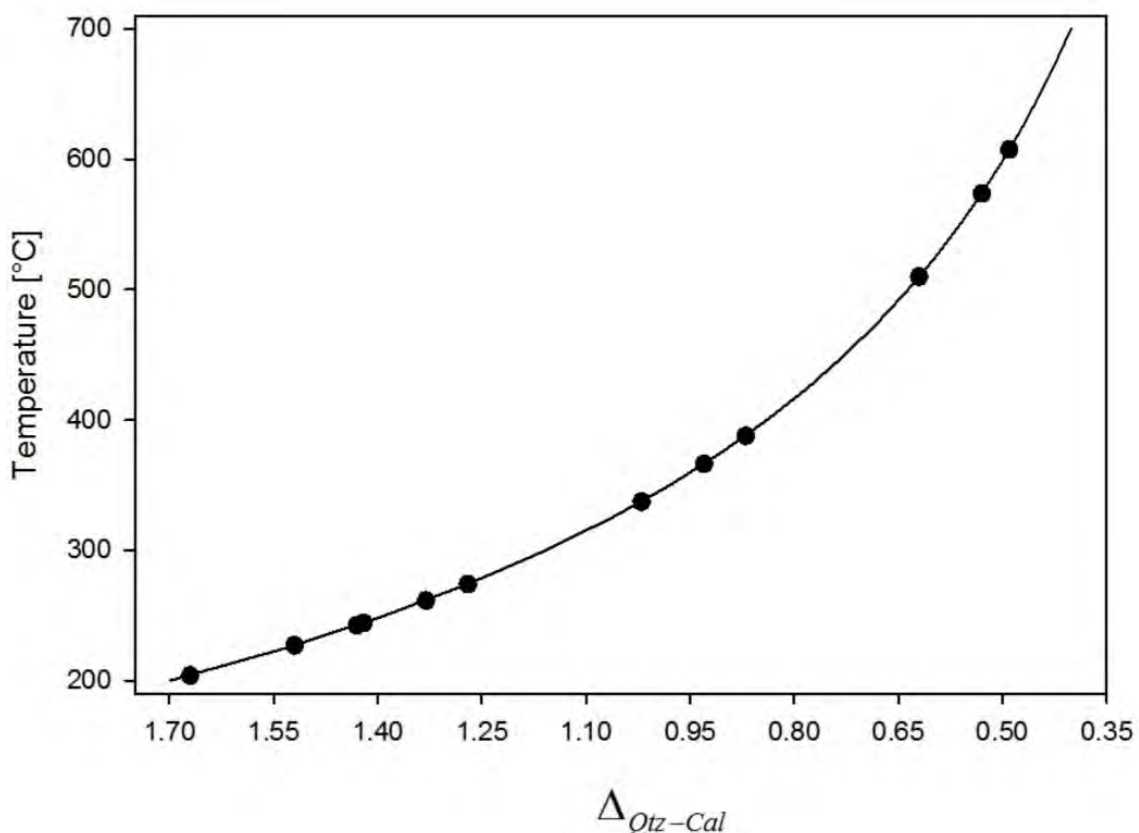


Figure 7.8: Equilibrium temperatures in the $\Delta^{18}\text{O}_{\text{Qtz-Calc}}$ oxygen isotope system for the temperature range from 200 to 700 °C (after Chiba et al., 1989). The black circles represent the temperature for Qtz-Cal mineral pairs from Theta Reef.

The different oxygen isotopic compositions within the analysed samples could be related to different fluid generations. Meyer et al. (1988) described different pyrite generations related to different fluid flows. In this study at least two generations of calcite have been observed (Chapter 4). One generation has an oxygen isotopic composition around 16.5 ‰ and the other one of around 18.3 ‰.

Various studies on oxygen isotopic compositions from quartz minerals within the hydrothermal veins and the surrounding host rocks throughout the Sabie-Pilgrim's Rest Goldfield have been conducted by previous workers.

Boer (1995) published $\delta^{18}\text{O}$ compositions around 14.3 ‰ for quartz from a hydrothermal vein at Nestor Mine, hosted within the shales of the Black Reef Formation. The Black Reef shales have an oxygen isotopic composition ranging from 7.5 - 10.6 ‰ (Shieh & Zhang, 1988).

Schidlowski et al. (1975) published $\delta^{18}\text{O}$ ratios from dolomite of the Malmani Subgroup in the vicinity of the SPRG ranging between 21.5 and 22.9 ‰. Quartz from the (dolomite-hosted) Theta Reef has an oxygen isotopic composition ranging from 16.3 to 18.8 ‰ (Fig. 7.9). Isotopic fractionation between dolomite and quartz is minor to negligible (Bau et al., 1999), indicating that the hydrothermal minerals of the Theta Reef are not in isotopic equilibrium with the dolomite host rock, taking the data presented by Schidlowski et al. (1975) and the mineralisation temperature provided by Boer et al. (1993) into consideration. Also the quartz of the ore bearing quartz vein at Nestor Mine is not in isotopic equilibrium with the host rock shale of the Black Reef Formation regarding the O-isotopic data presented by Shieh & Zhang (1988), Boer et al. (1993) and the mineralisation temperature presented by Boer (1995) (Fig. 7.9)

The comparison of the average $\delta^{18}\text{O}$ composition of quartz from Theta Reef with $\delta^{18}\text{O}$ average composition from quartz from the Nestor Mine shows that, if the ore-forming hydrothermal fluid would have the same initial source for both reefs, then the oxygen isotopic composition of the mineralising fluid is a combination of the signature of the initial fluid, the isotopic composition of the host rocks and temperature-related fractionation (Fig. 7.9)

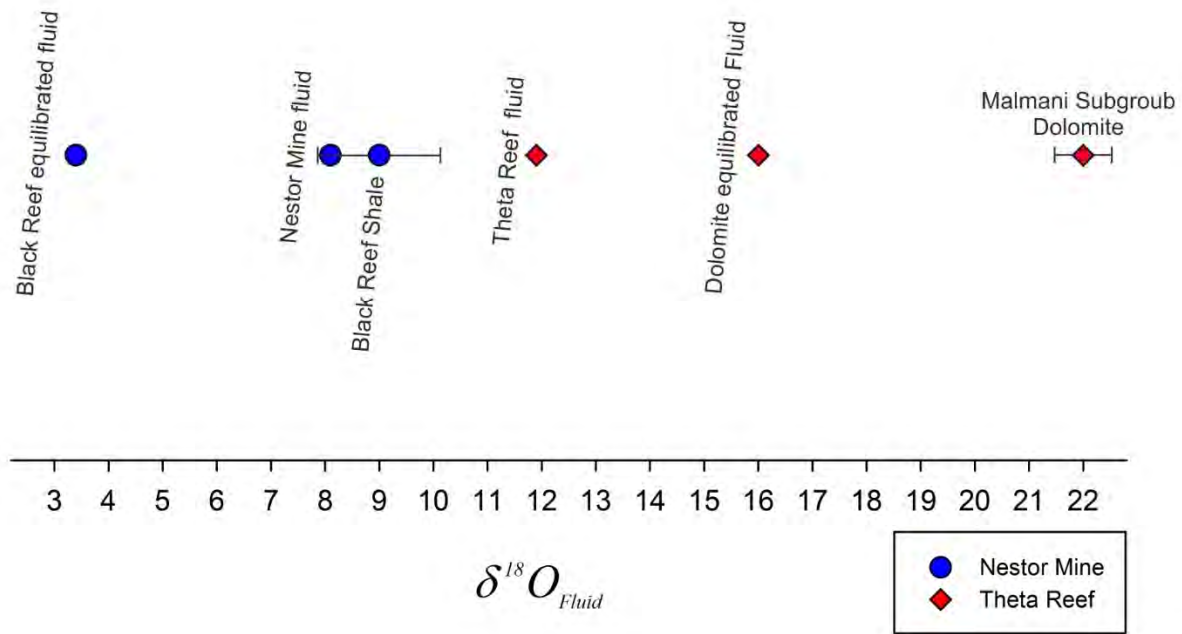


Figure 7.9: Isotopic compositions of the ore forming fluids of Theta Reef and Nestor Mine and their relation to the fluids in isotopic equilibrium with the host rock, indicating that the deposits are not in oxygen isotopic equilibrium with the host rock. (The Error bars are indicating the isotopic variation of the Black Reef shales and the Malmani Subgroup dolomite).

Figure 7.9 shows that the isotopic fractionation between the Theta Reef fluid and the Nestor Mine fluid of ~5 ‰ does not correspond to a calculated temperature-related fractionation between quartz minerals from the two reefs of approximately -0.6 ‰, assuming a geothermal gradient of 25 °C/km and a mineralisation temperature for the Theta Reef of ~320 °C. This confirms that temperature-related fractionation alone is not the reason for the different oxygen isotopic compositions of the two ore-bearing reefs (Fig. 7.9).

Fig 7.9 shows the oxygen isotopic compositions of the ore forming-fluids in relation to the fluids in oxygen isotopic equilibrium with the host rock at temperatures between 320 and 340 °C. The values used are the average values from the data presented in Table 7.2.1 and presented by Shieh and Zhang, (1988), Schidlowski et al. (1975) and Boer (1995). The difference in the isotopic composition of fluids in equilibrium with the

host rock and the ore-forming fluids indicate that a large volume of fluid interacted with a smaller volume of rock, otherwise the isotopic signature of the ore-forming fluid would be adjust to that of the host rock fluid.

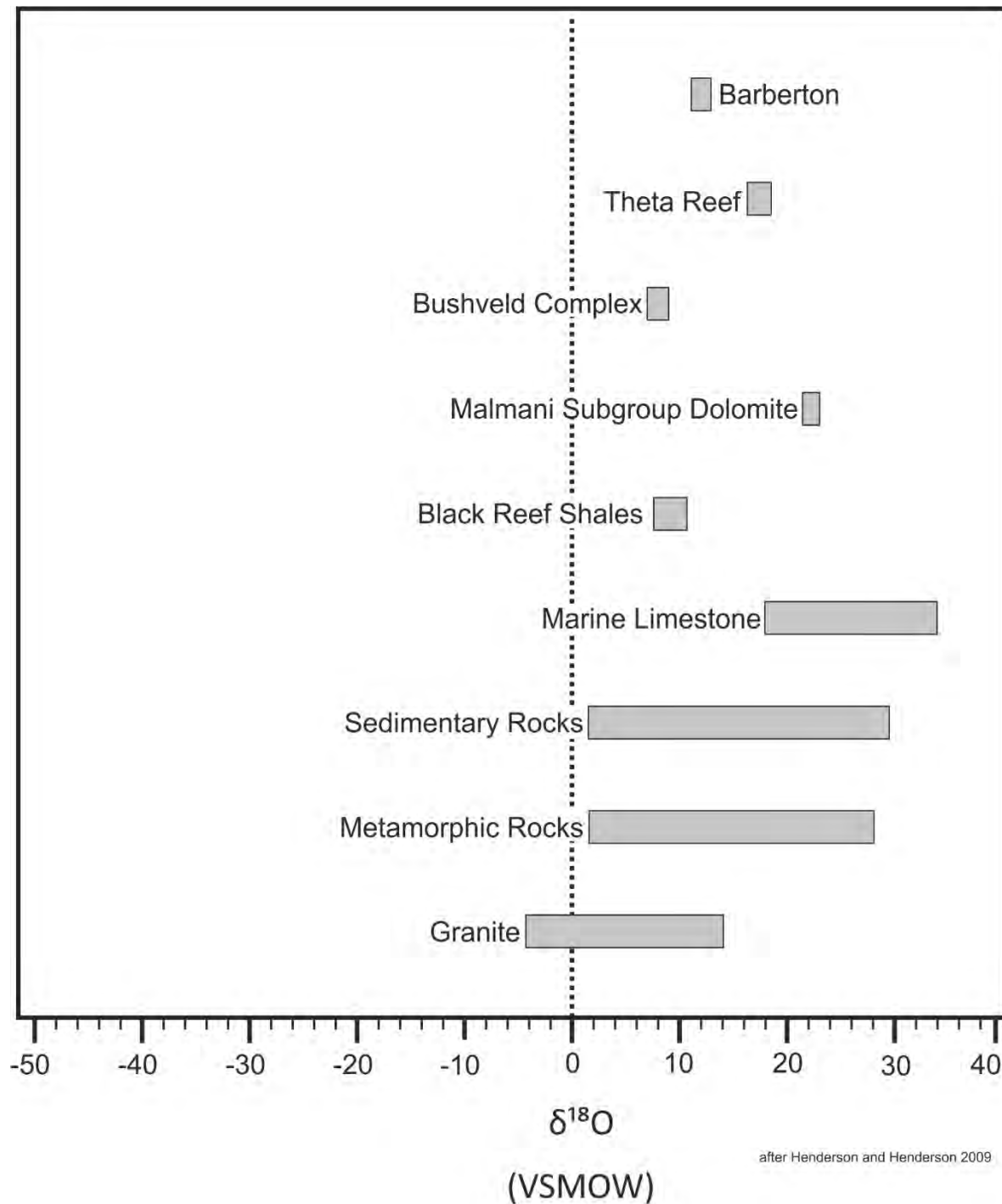


Figure 7.10: $\delta^{18}\text{O}$ values of Theta Reef of the SPRG plotted against oxygen isotopic compositions of selected rock types. All values are in ‰ (per mil) relative to Vienna Standard Mean Ocean Water (VSMOW).

The fact that the lines for the isotopic signatures of the ore-forming fluids plot between the lines of the fluids in equilibrium with the host rock (Fig. 7.9) could mean that the initial fluid has an isotopic composition which plots between the two lines for the ore forming fluid, with an approximate $\delta^{18}\text{O}$ ratio of $\sim 10\text{ ‰}$. This ratio coincides with the isotopic characteristic for an igneous fluid (Fig 7.10).

The oxygen isotopes of carbonates and quartz from the Barberton shear zone hosted gold deposits range from $\delta^{18}\text{O}_{\text{carbonate}}$ 11 to 13 ‰ and $\delta^{18}\text{O}_{\text{qtz}}$ 12 to 13 ‰ (Ronde et al., 2008). Considering a mineralisation temperature between 290 and 310 °C (Ronde et al., 2008) the ore forming fluids would have an isotopic composition ranging between 6 and 8 ‰, pointing towards a possible source of fluids.

Harris and Chaumba (2001) mentioned a fluid with an oxygen isotopic composition of $\sim 7 - 9\text{ ‰}$, related to the emplacement of the Bushveld Complex, forming quartz-granophyre veins. The authors believe that this fluid originates from the source region of Bushveld magmas interacting with the dolomite host rock. This fluid could have been further altered by interaction with the carbonate host rock (Frauenstein et al., 2009).

Considering a similar fluid source for the SPRG fluids as for the fluids forming the quartz-granophyre veins in the Bushveld Complex, this process could create a fluid with an oxygen isotopic composition of $\sim 10\text{ ‰}$ forming the ore bearing-quartz veins in the Sabie-Pilgrim's Rest Goldfield.

7.3 Carbon isotopes

7.3.1 Results

Four calcite and three graphitic mudrock samples from the Theta Reef have been analysed for their $\delta^{13}\text{C}$ content. The calcite was sampled within the ore-bearing quartz vein, while the graphitic mudrock underlies the ore body. The mudrock was sampled at various locations in stoped sections in the most northern area of the mine.

The measured values vary between -4.1 ‰ and -2.8 ‰ within calcite and range from -31.6 ‰ to -30.2 ‰ in the graphitic mudrocks (Tbl. 7.11).

Sample No.	$\delta^{13}\text{C}$ (‰ V-PDB)	C- / CO_3 - Content (% C / % CaCO_3)	Remarks
FTh 202 Gra	- 30.2	18.8	
FTh 301 Gra	- 31.6	2.4	
FTh 501 Gra	- 30.8	30.1	
FTh 203 a	- 4.0	14.7	reproducibility 0.2‰
FTh 203 b	- 4.0	16.0	reproducibility 0.2‰
FTh 401	- 4.1	12.1	reproducibility 0.3‰
FTh 406	- 2.8	97.2	

Table 7.11: $\delta^{13}\text{C}$ compositions of graphitic mudrock (sample names with Gra) and calcite samples from the Theta Reef at Frankfort Mine. All values are in ‰ (per mil) relative to V-PDB. The reproducibility is better than 0.1 ‰ unless stated otherwise. The calcite samples FTh 203 a, b and FTh 401 have a low carbonate content (<17%). This could be caused by contamination of the calcite sample with quartz.

7.3.2 Discussion

The difference of >26 ‰ between the $\delta^{13}\text{C}$ ratios of calcite and graphite within the Theta Reef indicates that the carbon of the two minerals originates from two different carbon reservoirs. Chacko et al. (1991, 2001) suggests a fractionation factor of ~9 ‰ for the calcite-graphite mineral pair in C-isotopic equilibrium at 320 °C (Fig. 7.12). The low carbon isotopic values ranging from -31.6 to -30.2 ‰ of the graphite suggests an organic origin, while the higher values obtained from calcite, falling within the range of -4.2 and -2.8 ‰ suggest an igneous or metamorphic origin (Fig. 7.13).

Strauss and Beukes (1996) presented $\delta^{13}\text{C}$ ratios for limestones, dolomites and organic material within the dolomite of the Transvaal Supergroup. Ratios for minimally altered organic matter range from -43 to -31 ‰, Hayes et al. (1983) presented a value of -30.7 ‰ for organic carbon of the Malmani Subgroup and Hoering (1962) a $\delta^{13}\text{C}$ composition of -28.9 ‰ for organic carbon within the Transvaal Supergroup. The carbon isotopic composition from the graphite of the Theta Reef falls within this range. The inorganic carbon with $\delta^{13}\text{C}$ ratios between -4.2 and -2.8 ‰ probably precipitated from CO_2 with a C-isotopic composition between ~ -6 and ~ -8 ‰ (Fig. 7.12), assuming a temperature of 320 °C (Boer, 1995)

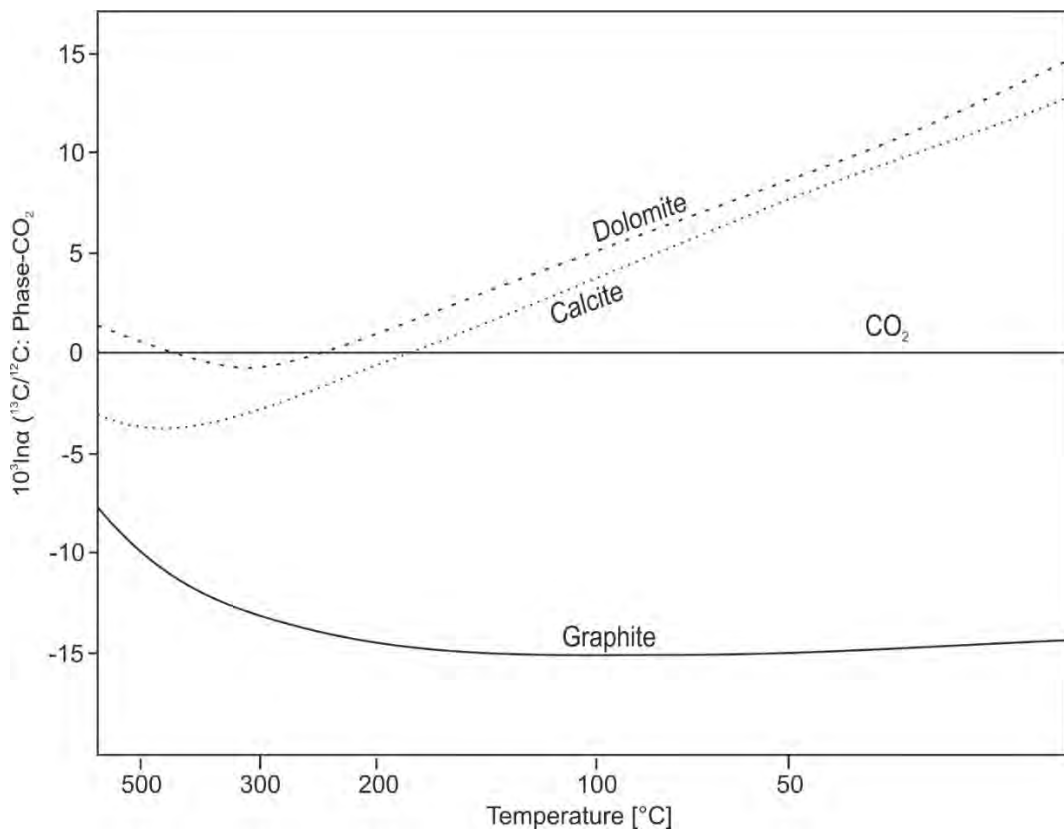


Figure 7.12: Carbon isotopic fractionation between gaseous CO_2 and the minerals graphite, calcite, dolomite (after Chacko et al., 2001).

Veizer et al. (1992) presented a carbon isotopic composition of $-0.9 \pm 0.7\text{ ‰}$ for carbonates of the Malmani Subgroup, indicating a typical marine signature (Fig. 7.13). Calcite in isotopic equilibrium with the dolomitic host rock would have a carbon isotopic composition of $\sim -1.8 \pm 0.7\text{ ‰}$ (Sheppard & Schwarcz, 1970). The $\delta^{13}\text{C}$ composition of the calcite within the reef is 0.3 to 1.6 ‰ lower than calcite in equilibrium with the dolomite host rock, indicating that the vein calcite is not in carbon isotopic equilibrium with the host rock.

$\delta^{13}\text{C}$ measured in carbonates from the Barberton Au-quartz veins range from -4.5 to -2.0 ‰ (Ronde et al., 2008) overlapping with the values from the SPRG deposits. This indicates, that the ore forming fluids and the surrounding lithologies at the Barberton gold deposits could have been similar.

Pronost et al. (2008) presents carbon isotope data ranging from -6.4 to -3.7 ‰ in the Platreef of the Bushveld Complex. The carbon composition within these samples is a combination of carbon from the initial fluid source and carbon from the surrounding

host rock. This suggests that the initial CO_2 value is probably ~ -9.6 to -6.9 ‰ at a mineralisation temperature $\sim 700 \text{ }^\circ\text{C}$ for the Platreef (Sharman-Harris, 2006). This $\delta^{13}\text{C}$ compositions points towards the Bushveld as a source for the initial carbon-bearing fluid, which then partially equilibrated with the host rock.

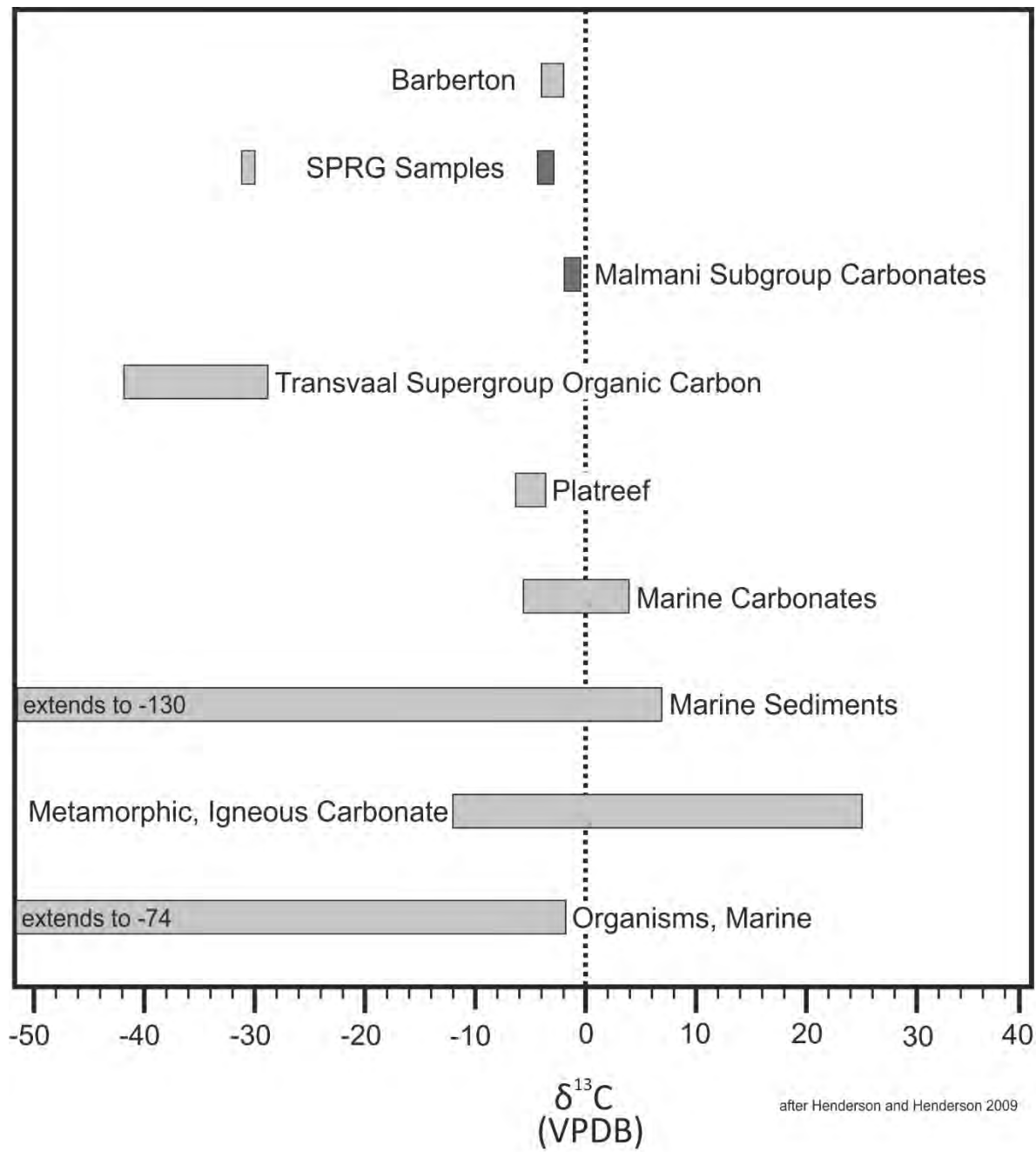


Figure 7.13: $\delta^{13}\text{C}$ values of graphite (light grey) and calcite (dark grey) from the SPRG compared to the whole rock carbon isotopic compositions of the Platreef of the Bushveld Complex (Pronost et al., 2008), organic carbon from the Transvaal Supergroup (Strauss & Beukes, 1996) and carbonates from the Malmani Subgroup (Veizer et al., 1992) and of selected other rock types. All values are in ‰ (per mil) relative to Vienna Pee Dee Belemnite standard.

The $\delta^{13}\text{C}$ values for calcite suggest a similar fluid-rock interaction as for the oxygen isotopes, it is possible that the initial carbon source is spatially closely related to the initial fluid source, experiencing CO₂ enrichment due to devolatilisation of the carbonate host rocks of the Malmani Subgroup.

The carbon isotopic data from the graphitic mudrock is comparable to the $\delta^{13}\text{C}$ values from minimally altered organic matter within the sediments of the Transvaal Supergroup presented by Strauss and Beukes (1996). This would indicate that the carbon within the graphite is primary, produced by autotrophic carbon assimilation, involving close to maximal isotopic fractionation between the inorganic and organic compound (Strauss & Beukes 1996). Thus, the isotopic fractionation between the inorganic carbon and the organic carbon was ~30 ‰, considering a $\delta^{13}\text{C}$ ratio of 0.9 ± 0.7 ‰ for the Malmani Dolomite (Veizer et al., 1992).

7.4 Sulphur Isotopes

7.4.1 Results

Twenty-three samples from Theta Reef and three samples from the Bevets Reef waste dump have been analysed for their $\delta^{34}\text{S}$ signature, being seventeen pyrite samples, five tetrahedrite samples and one arsenopyrite sample.

Sample No.	Sulphur content	$\delta^{34}\text{S}$ (Pyrite)	$\delta^{34}\text{S}$ (Tetrahedrite)	$\delta^{34}\text{S}$ (Arsenopyrite)
FTh 201	51.4 / 26.3	2.2	1.2	
FTh 202	52.4	2.1		
FTh 301	49.0	1.9		
FTh 401	52.0 / 26.5	2.1	1.3	
FTh 402	50.2 / 34.9	2	1.6	
FTh 403	48.6	2.2		
FTh 404	48.7	1.8		
FTh 405	48.8	2.1		
FTh 406	51.6	2.2		
FTh 407	29.9		1.4	
FTh 501	51.6	2.0		
FTh 502	53.2	2.2		
FTh 503	52.8	2.2		
FTh 504	50.7	2.3		
FTh 505	51.3	2.1		
FTh 506	51.7 / 26.3	2.1	1.4	
BWa 1	51.5	-1.0		
BWa 2	52.1	-0.2		
BWa 3	21.9			0.0

Table 7.14: $\delta^{34}\text{S}$ compositions of pyrite, tetrahedrite and arsenopyrite samples from the Theta Reef (sample number FTh) and Bevets waste dump (sample numbers BWa) of the Frankfort Mining Complex. All values are in ‰ (per mil) relative to CDT. The reproducibility is better than 0.3 ‰ for the $\delta^{34}\text{S}$ measurements and $\pm 5\%$ for the sulphur content.

The sulphur isotopic composition of Theta Reef sulphides ranges from 1.8 to 2.3 ‰ within the pyrites and from 1.2 to 1.6 ‰ in tetrahedrite. The $\delta^{34}\text{S}$ ratios of the three Bevets Reef waste samples (two pyrites, one arsenopyrite) are slightly negative and range from -1.0 to 0.0 ‰.

7.4.2 Discussion

Isotopic fractionation between pyrite and other sulphide minerals at temperatures <700°C (Ballhaus & Stumpfl, 1986) is negligible (Fig. 7.17), as the fractionation is within the analytical error. There is however a distinct difference between the $\delta^{34}\text{S}$ composition of pyrite and tetrahedrite. All the S-isotopic ratios of tetrahedrite are lower than those of pyrite, indicating that the tetrahedrite could have precipitated at a different mineralisation stage than the pyrite. This hypothesis is supported by the fact that tetrahedrite generally occurs as fracture filling material (Chapter 4).

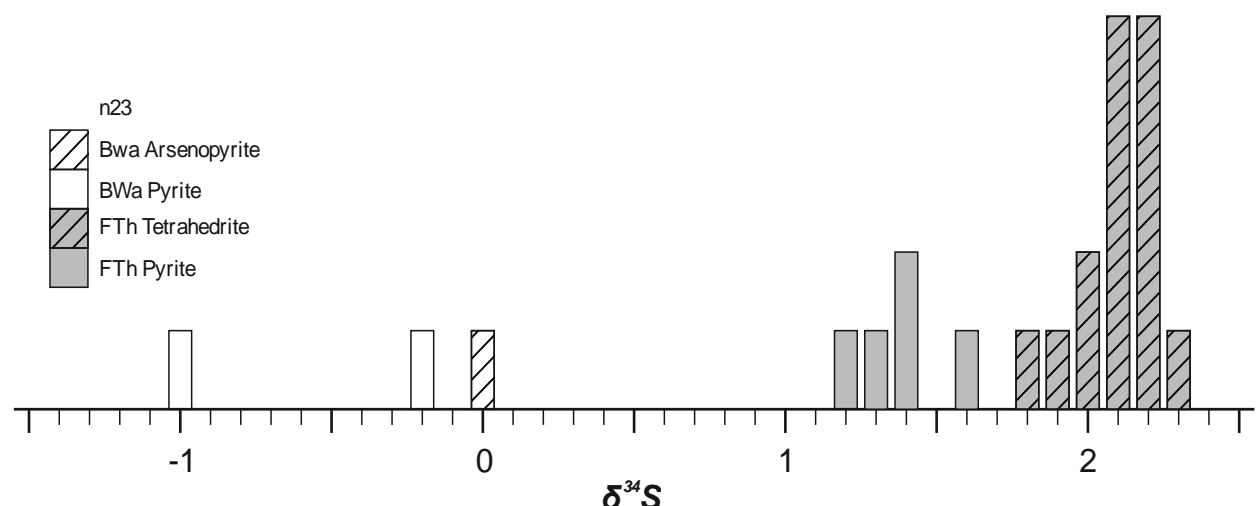


Figure 7.15: Distribution of $\delta^{34}\text{S}$ values of the different sulphide minerals and the different reefs

The $\delta^{34}\text{S}$ values of a specific mineral within single reef are remarkably homogeneous and show a maximum deviation of $\pm 0.5\text{ ‰}$ from their average- which is in marked contrast to the variable signature of oxygen and carbon isotopes. A narrow range of sulphur isotopic ratios close to zero is typical for an igneous source (Fig. 7.15) (Faure & Mensing 2005), whereas only those with a $\delta^{34}\text{S}$ deviating more than 7 ‰ from $\delta^{34}\text{S} = 0$, are more likely of biogenic or sedimentary origin (Jensen, 1967).

Boer (1993) proposed that the ore forming fluid was a bisulphide complex, also suggesting a magmatic-hydrothermal, rather than biogenic origin of the sulphur.

Penniston-Dorland et al. (2012) published sulphur isotopic data from whole rock samples and sulphide separates from the UG2 Chromitite, Merensky Reef and the Main Zone with $\delta^{34}\text{S}$ ratios of $2.7 \pm 0.3\text{‰}$, $1.7 \pm 0.6\text{‰}$ and $1.4 \pm 0.1\text{‰}$, respectively and an average $\delta^{33}\text{S}$ ratio for all reefs of 0.12‰ . The $\Delta^{33}\text{S}$ ratio indicated that these are not typical mantle signatures but a combination of surface derived sulphur, e.g. the Transvaal Supergroup or from metamorphosed mid- to lower- crust (Penniston-Dorland et al., 2012).

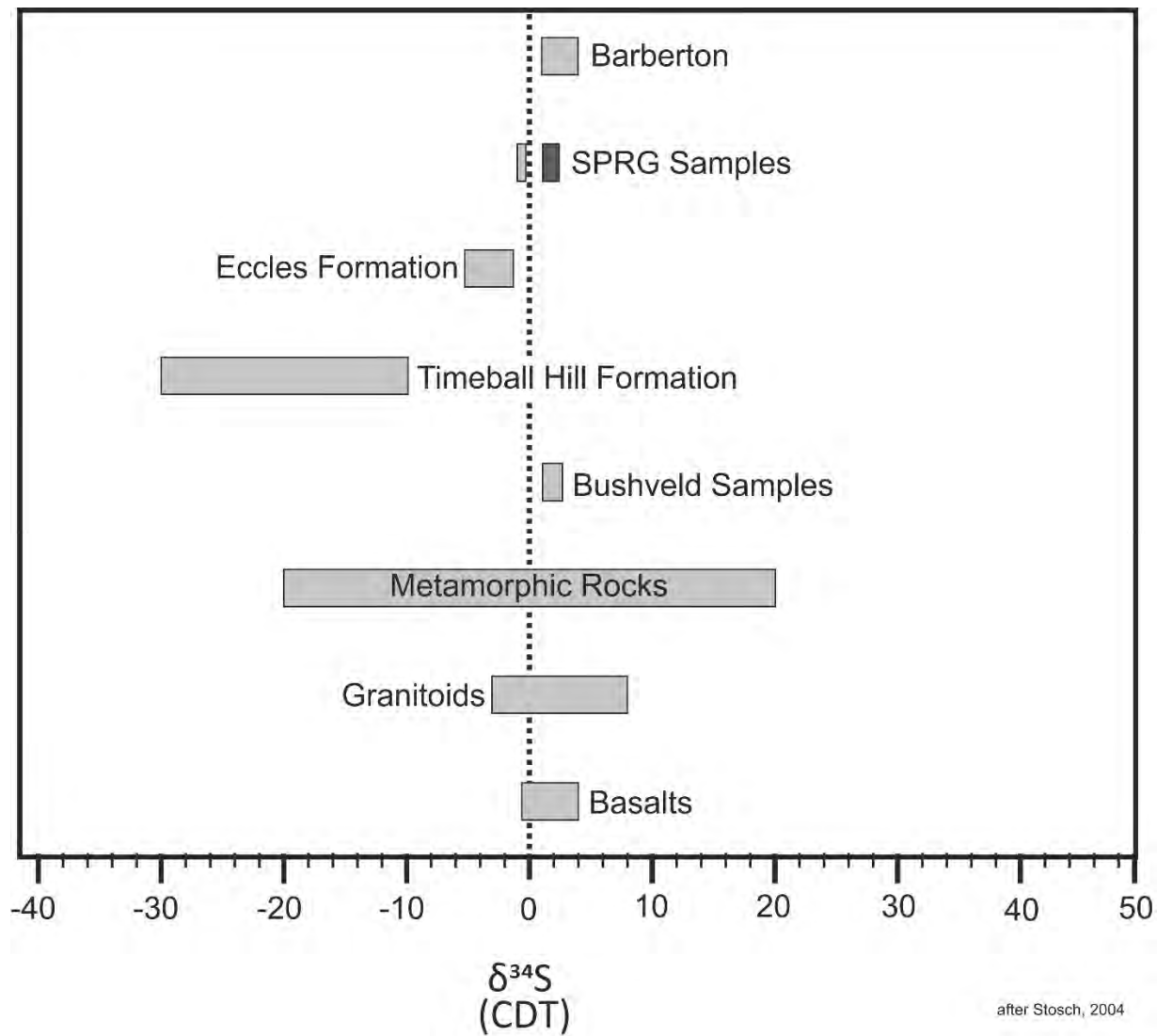


Figure 7.16: $\delta^{34}\text{S}$ isotopic compositions of selected natural materials. The light grey SPRG bar represents the pyrite and arsenopyrite data from the Bevets waste dump and the dark grey bar the pyrite and tetrahedrite data from the Theta Reef. The data presented for the Bushveld Complex is reported in Penniston-Dorland et al. (2012), the Timeball Hill and the Eccles Formation data in Cameron (1982). The minimum value for the Eccles Formation is estimated. All values are in ‰ (per mil) relative to CDT (Cañon Diablo Troilite).

Sulphur isotopic data from whole rock analysis from the Bushveld Reefs shows that the $\delta^{34}\text{S}$ ratios from Theta Reef overlap those from the Merensky reef. This indicates that the initial sulphur source for the sulphides of the Sabie-Pilgrim's Rest Goldfield is similar to the source for the reefs within the Bushveld Complex.

It is however possible that the sulphur isotopic signature, similar to the oxygen and carbon isotopes, has been altered by the sediments of the Transvaal Supergroup (Penniston-Dorland, 2012).

Assuming that the ore forming fluids of the Bevets Reef have the same source as those of the Theta Reef, the slightly negative values for the Bevets samples can be explained by fluid interaction with the host rock. The S isotopic composition of the Bevets Reef-hosting Rooihoopte and the overlying Timeball Hill Formation lie within the range of -10 and -30 ‰. The Eccles Formation, hosting the Theta Reef, on the other hand shows only slightly negative $\delta^{34}\text{S}$ values (> -5 ‰) (Cameron, 1982).

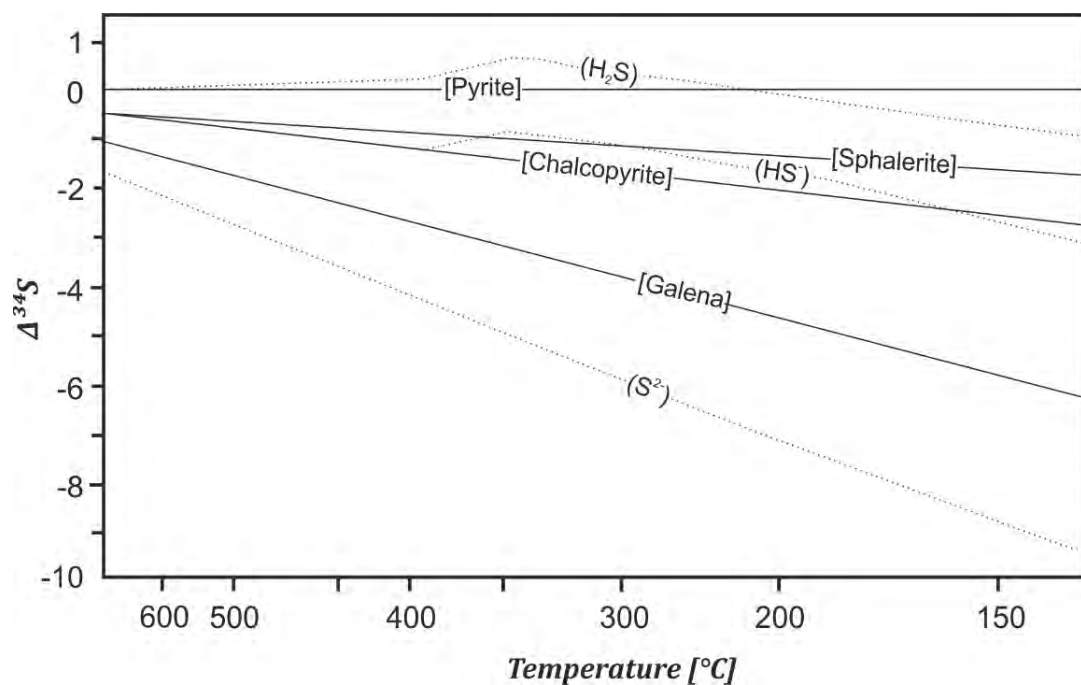


Figure 7.17: $\delta^{34}\text{S}$ fractionation between hydrothermal minerals [] and sulphur species () plotted relative to pyrite as a function of temperature. Solid lines represent minerals and dashed lines solutions. All values are in ‰ CDT (after Rye and Ohmoto, 1974)

This would explain why the isotopic compositions of the Theta Reef sulphides more closely resemble those of the Bushveld Complex than those of Bevets Reef. Furthermore, the limited changes of the sulphur isotopic composition indicate, as the oxygen and carbon isotopes do, that fluid-rock interaction was limited.

Sulphur isotopic compositions from the Barberton sulphides range from 1 to 4 ‰ (Ronde et al., 2008) and are, therefore, higher as those of the Theta and Bevets Reef. If the Barberton gold deposits would be considered as the source of metals, the ore forming fluids would have been altered by the surrounding host rock.

7.5 Summary

The stable isotope analysis shows that the isotopes within a single mineral phase and between two phases are not in isotopic equilibrium, suggesting episodic mineralisation of the ore-bearing quartz vein. The limited alteration of the ore-forming fluids by the host rock proposes that fluid-rock interaction was limited, this would exclude the Barberton gold deposits as a source of fluids and metals.

The oxygen isotopes indicate that the ore-forming fluids derived from the Bushveld complex and are a mixture of magmatic, crustally contaminated and meteoric water, of which the isotopic composition was then still affected by the interaction with the host rocks of the ore bodies.

Carbon isotopic ratios originated from two different carbon reservoirs. The organic compound corresponds to those measured for organic matter within the dolomite of the Transvaal Supergroup, while the higher ratios of -4.1 ‰ and -2.8 ‰ indicate an igneous source for this carbon.

The sulphur isotopic ratios show that the ore-forming fluids most likely derived from the Bushveld Complex. The S isotopic composition of BC-related sulphur is a unique combination of larger amount of mantle-derived sulphur with minor amounts of surface-derived sulphur, e.g. the Transvaal Supergroup or from metamorphosed mid-to lower- crust. This isotopic signature seems to be present within the sulphides of Theta and Bevets Reef.

8 Discussion and conclusions

8.1 Discussions

The northern section of the Theta Reef of the Frankfort Mining Complex seems to represent different deposit characteristics than most of the other gold deposits described by various authors, within the Sabie-Pilgrim's Rest Goldfield. Even though, Theta Reef seems to be a thrust zone hosted gold deposit. The thrust plane is represented by a thin graphitic mudrock layer below the ore bearing reef. No evidence for any further structural deformation is observed. This is supported by mineralised stromatolitic structures associated with the reef. Those structures have not been described in detail to date and might have been miss interpreted as structural deformation, such as sigmoidal drags, tight isoclinal folds or C-S fabrics, within reefs hosted in the Malmani Subgroup dolomites.

Three types of pyrite and, arsenopyrite and chalcopyrite intergrowth as well as fracture-filling chalcopyrite and minerals of the tetrahedrite-tennantite series indicate at least three mineralisation episodes for the formation of the Theta Reef and two episodes for the Bevets Reef. In the first episode, Type 1 pyrite associates with quartz precipitated within the layer of graphitic mudrock, the dolomite host rock and as calcite replacement within stromatolites. Type 2 pyrite occurs in fractures in the stromatolitic structures and as fine to medium grained pyrite within a medium grained quartz-carbonate groundmass and Type 3 pyrite within a quartz-carbonate chert groundmass. While there is no evidence for a different mineralisation event for Type 2 and 3 pyrite, it is obvious that arsenopyrite, chalcopyrite and minerals of the tetrahedrite-tennantite series precipitated in a third mineralisation episode.

Pb isotopes support at least two mineralisation stages. The data shows, that Type one mineralisation precipitated from a fluid with a lead isotopic composition close to that from sulphides from the Bushveld Complex, Type two represents a mixture of Pb isotopic composition of Bushveld Complex sulphides and most likely the Pb isotopic composition of the Malmani dolomites and Type 3 is thought to predominantly represent the isotopic composition of the dolomite host rock. In this hypothesis it is assumed that the Pb-Pb ratios of the dolomite are slightly higher than the ratio of the

Black reef Formation. The almost gradual change from higher to lower Pb-Pb ratios would suggest a gradual increase in higher fluid-rock interaction towards the later stages of ore-mineralisation.

The similarity of the Pb isotopic ratios from the Theta and Bevets Reef samples and those from the Bushveld Complex suggest that the mineralisation within the goldfield is synchronous to the emplacement of the Bushveld Complex, and that the ore-forming fluids derived from the same. Penniston-Dorland et al. (2012) describes the ore-fluids of the UG-2 Chromitite and the Merensky Reef as juvenile. Furthermore, the lead isotopic compositions of the Black Reef formation, representing the Witwatersrand gold deposits and of the Murchison Belt do not indicate any relation to the SPRG deposits.

This idea of a magmatic fluid is supported by aqueous fluid inclusions analysed within quartz from the Bushveld Complex (Schiffries, 1990). Also the stable isotopic compositions of quartz, calcite and sulphides indicate a magmatic fluid source. The stable isotopes follow the same trend as the lead isotopes, the initial composition of the ore-forming fluids seems to be represented by Type 1 pyrites of the Theta and Bevets Reef. The Oxygen isotopic compositions of quartz and carbonates and the carbon isotopic composition of carbonates would exclude the Barberton greenstone Belts as a possible source of the ore forming fluids. $\delta^{34}\text{S}$ compositions and the carbon isotopic composition of the Barberton gold deposits however indicate, that the ore forming fluids of these deposits could have been similar to those of the SPRG deposits. Age constraints of the mineralisation however would rather support a relationship between the Bushveld Complex and the Sabie-Pilgrim's Rest deposits than with the Barberton Greenstone Belts which is almost 1Ga older.

The variation in the isotopic composition of the ore and gangue minerals indicates that possible Bushveld Complex-derived ore-forming fluids of Theta and Bevets Reef gradually equilibrate with the host rocks of the reefs.

The carbonaceous hosts provide a reducing environment and would promote the precipitation of gold, if transported within a bisulfide complex. The high variations within the stable isotope ratios did not allow any stable isotope geo-thermometry. But

assuming that the Pretoria group overlaid the Sabie Pilgrim's Rest Goldfield at the time of mineralisation the geothermal gradient would imply a temperature of ~320°C.

Sulphur isotopes suggest that the Bushveld Complex is also the source of metals, such as: Cu, As, Ag, Sb, Au, Hg, Pb and Bi (Sharman-Harris et al., 2005; Cawthorn, 2006; Zintwana et al., 2012). Which are the common trace elements within the ore minerals of the Theta Reef. Those elements are enriched in minerals of the tetrahedrite-tennantite series, a mineral which has not been observed within the Bevets Reef samples analysed.

The Gold content within the samples of the northern section of the Theta Reef is generally low. Gold occurs as invisible gold, predominantly in arsenic-rich and arsenian pyrite as an Au-As or Au-Sb compound. Gold is also observed associated with Ag forming electrum.

8.2 Conclusion

The mineralisation style within the most northern section of the Theta Reef seems to be different to those described by other authors and, further, indicates that there is not only a vertical variation between the different deposits, but also a lateral variation within a single deposit.

The Reef does not show the for the Sabie-Pilgrim's Rest typical sheeted nature of the veins. Also structural deformation of the ore-body is rather limited as indicated by the stromatolitic textures within the reef.

The geochemical analysis suggests that the magmatic ore-forming fluids and metals derived from the Bushveld Complex and have been altered by the lithologies of the Transvaal Supergroup. The Barberton Greenstone Belts as a possible fluid source would have to be investigated further and in more detail. The age of the mineralisation of the Barberton deposits would support another fluid source as it is 1 Ga older. The

Bushveld Complex is the only obvious heat source available of sufficient size to generate the hydrothermal cell that is assumed to have been necessary for the formation of the Sabie-Pilgrim's Rest Goldfield. The regional geology of the SPRG and the surrounding Transvaal Supergroup support a relation of the mineralisation within the goldfield and the Bushveld Complex.

The carbonaceous rocks of the Transvaal Supergroup provide a suitable environment for the ore-precipitation. The ore minerals revealed at least three mineralisation episodes, with gold occurring within the second and the third stage. Gold occurs as invisible gold in arsenic rich pyrites or with silver as electrum.

Acknowledgement

This thesis is the result of a passion which began in 2007 when I went on my first geological field trip with the Ruprecht-Karls-University Heidelberg. At this stage it was beyond imagination to come this far and write this part of a Master's Thesis after having spent almost four years in South Africa.

The production of this thesis has been a wild roller-coaster trip which involved many people. In particular I must thank my co-supervisor Professor Marlina Elburg, who took over disorganised project, for her ideas (for making this study a successful project), guidance, support, academic and general input throughout this study.

Professor McCourt must be thanked for the supervision of this project and his input, especially regarding the Geology of South Africa.

Dr. Ron Uken has provided me with the opportunity to join the University of KwaZulu-Natal for this Master

Mario Ruygrok and the management of the Stonewall TGME Project generously allowed me access to valuable information on the gold mines of the Sabie-Pilgrim's Rest Goldfield.

Prof. Michael Watkeys, Dr. Jürgen Reinhard, DR. Maria Ferentinou and Dr. Andrew Green must be thanked for always having had an open door (in academic, managerial or personal matters).

The Geology post grad team Errol Wiles (your help has been appreciated in many ways) Carlos Loreio, Lauren Hoyer, Lauren Pretorius, Shannon Dixon, Leslee Salzmann, Nku Dladla, Jannie Weitz (many thanks for your editorial help), Riaan Botha and Warwick Hastie impacted on this work in various ways, let it be professional advice, interesting conversations in diverse fields or simply highly appreciated distraction in stressful times.

I also want to thank my family and non-varsity friends, particularly Sabrina Pfister and Trevor Stevens but also all the people who made my time in South Africa an unforgettable experience and my German friends who will always make me feel home whenever I Come to Heidelberg, my sister, Dörte Merk and my brothers, Hendrik and Robert Metz, who will hopefully understand at some stage why this

thesis has been such a mission and fight to complete.

Special thanks go to Frances, Medwyn, Andrew and Sam du Bois who will always make me feel welcome and at home and have supported me in many ways.

Finally to Claire du Bois, you became a very important part of my life over the past four years, thank you for always standing by me in stressful times, accepting me being away for the many hours I needed to work, days I have been away, keeping me sane and always celebrating the great moments in life with me. Without this backup, life would have been very difficult.

Lastly I want to thank my parents, Dagmar and Wolfgang Metz, without whom this Master would not have been possible.

References

- Armstrong, R.A., Compston, W., Retief, E.A. Williams, I.S., Welke, H.J.**, 1991, Single Zircon ion microprobe studies bearing on age and evolution of the Witwatersrand triad. *Precamb Res.* 53, p. 243-66.
- Ash, J.P., Tyler, N.**, 1986, A preliminary investigation of fluid inclusions in the Pilgrim's Rest Goldfield. *Econ. Geol. Res. Unit, University of Witwatersrand, Johannesburg*, Information Circular 180, 21 pp.
- Ault, W.U., Kulp, P.L.**, 1960, Sulphur isotopes and ore deposits. *Econ. Geol.*, Vol 55, p.73-100
- Ballhaus, C.G., Stumpf, E.F.**, 1986. Sulphide and platinum mineralization in the Merensky Reef: Evidence from hydrous silicates and fluid inclusions. *Cont. Miner. Petrol.*, 94, p. 193–204.
- Barnard, K.**, 1958, The Geology of the Bourke's Luck Mine, Eastern Transvaal. M.Sc. Thesis (*Unpubl.*, University of the Witwatersrand).
- Barton, E.S., Hallbauer, D.K.**, 1996, Trace-element and U-Pb isotope compositions of pyrite types in the Proterozoic Black Reef, Transvaal Sequence, South Africa: Implications on genesis and age. *Chem. Geol.*, 133, p 173-199.
- Belousova, E.A. et al.**, 2001. Two age populations of zircons from the Timber Creek kimberlites, Northern Territory, Australia, as determined by laser-ablation ICPMS analysis. *Australian Journal of Earth Sciences*, in press
- Beukes, N.J.**, 1973, Precambrian iron-formations of South Africa. *Econ. Geol.* 68, p. 960-1004
- _____, 1978, Die Karbonaatgesteentes en ysterformasies van die Ghaap-Groep van die Transvaal-Supergroep, in Noord-Kaapland. Ph.D. thesis (*unpubl.*) *Rand Afrikaans University*,South Africa
- _____, 1983, Paleoenvironmental setting of iron-formations in the depositional basin of the Transvaal Supergroup, South Africa, In: *Iron Formations: Facts and Problems*. (eds. Trendall, A.F. & Morris, R.C.), *Elsevier, Amsterdam*, p 131-209
- _____, 1987, Facies relations, depositional environments and diagenesis in a major Early Proterozoic stromatolitic carbonate platform to basinal sequence, Campbellrand Subgroup, Transvaal Supergroup, Southern Africa. *Sediment. Geol.*, 54, p.1-46.

- _____, Klein, C., Kaufmann, A.J., Hayes, J.M., 1990. Carbonate petrography, kerogen distribution, and carbon and oxygen isotope variations in Early Proterozoic transition from limestone to iron formation deposition, Transvaal Supergroup, South Africa. *Econ. Geol.*, 85, p. 663–690.
- Bideaux, A., Nichols, B.**, 2003 Handbook of Mineralogy, Elements, Sulfides and Sulfosalts. *Mineralogical Society of America*. Vol 1, 588 pp.
- Bigeleisen, J., Mayer, M.G.**, 1947. Calculation of equilibrium constants for isotopic exchange reactions. *The Journal of Chemical Physics*, 15, 261–267.
- Boer, R.H., Meyer, F.M., Robb, L.J., Graney, J.R., Vennemann, T.W.**, 1993, The nature of gold mineralization in the Sabie-Pilgrim's Rest Goldfield, eastern Transvaal, South Africa. *Economic Geology Research Unit, Univ. Witwatersrand, Johannesburg, Information Circular* 262, 33 pp.
- _____, Meyer, F.M., Robb, L.J., Graney, J.R., Vennemann, T.W. & Kessler, S.E., 1995, Mesothermal-Type Mineralization in the Sabie-Pilgrim's Rest Gold Field, South Africa. *Econ. Geol.*, 90, p. 860-76.
- _____, 1995, Physico-chemical conditions of mineralisation in the Sabie-Pilgrim's Rest Goldfield, Eastern Transvaal. PhD thesis (*unpubl.*) *University of the Witwatersrand Johannesburg, South Africa*.
- _____, 1996, Report on the Ore Mineralogy of Auriferous Samples from the Theta Reef, Frankfort Mine. *Randgold & Exploration Company Ltd.*
- Bons, P.D., Elburg, M.A., Gomez-Rivas, E.**, 2012, A review of the formation of tectonic veins and their microstructures. *Journal of Structural Geology*, 43, p. 33-62.
- Bottinga, Y.**, 1969, Calculated fractionation factors for carbon and hydrogen isotope exchange in the system calcite - carbon dioxide – graphite – methane – hydrogen – water vapour. *Geochemica et Cosmochimica Acta*, 33, p. 49 – 64.
- _____, Javoy, M., 1973. Comments on oxygen isotope geothermometry. *Earth Planetary Science Letters*, 20, p. 251–265.
- Breskovska V., Tarkian, M.**, 1994. Compositional variation in Bi-bearing Fahlores. *N.Jb. Mineral. Mh.*, H., 5, p. 230-240.
- Buchanan, L.J.**, 1981, Precious metal deposits associated with volcanic environments in the southwest: *Arizona Geological Society Digest*, 14, p. 237–262.

- _____, Reimold, W.U., 1998, Studies of the Rooiberg Group, Bushveld Complex, South Africa: No evidence for an impact origin. *Earth & Planet. Sci. Lett.*, 155, p. 149-65.
- Burger, A.J., Coertze, F.J.**, 1973, Radiometric age measurements on rocks from Southern Africa to the end of 1971. *Bull. Geol. Surv., S. Afr.*, 58, 46 pp.
- Button, A.**, 1973b, The depositional history of the Wolkberg proto-basin, Transvaal Supergroup. *Journal of Sedimentary Petrology*, 43, p. 160-167.
- _____, 1973, A regional study of the stratigraphy and development of the Transvaal Basin in the eastern and northeastern Transvaal. Ph.D. thesis (*unpubl.*) *University of the Witwatersrand. South Africa*.
- _____, 1986, The Transvaal sub-basin of the Transvaal Sequence. In *Mineral deposits of South Africa*. Vols I & II. (eds.: Anhaeusser, C.R., & Maske, S.) *Geol. Soc. S. Afr.* p. 811-17.
- Cameron E.N.** 1982, The upper critical zone of the eastern Bushveld Complex—precursor of the Merensky Reef. *Econ. Geol.* 77, p. 1307–1327.
- Cawthorn, R.G., Eales, H.V., Walraven, F., Uken, R., Watkeys, M.K.**, 2006, The Bushveld Complex. In *The Geology of South Africa*. (eds. Johnson, M.r., Anhaeusser, C.R., Thomas, R.J.,). *Geol. Soc. S. Afr and the Council of Geoscience*. p. 261-89.
- _____, 2006, The centenary of the discovery of platinum in the Bushveld Complex (10th November, 1906). *International Platinum Conference 'Platinum Surges Ahead', The Southern African Institute of Mining and Metallurgy*, 2006.
- Chacko, T., Mayeda, T.K., Clayton, R.N., Goldsmith, J.R.**, 1991. Oxygen and carbon isotope fractionations between CO₂ and calcite. *Geochimica Cosmochimica Acta*, 55, p. 2867–2882.
- Cole, D.R., Horita, J.**, 2001. Equilibrium oxygen, hydrogen and carbon isotope fractionation factors applicable to geologic systems. In *Stable Isotope Geochemistry* (eds. Valley, J.W., Cole, D.R.). *Reviews in Mineralogy and Geochemistry*, 43, p. 1–81.
- Chiba H., Chacko T., Clayton R.N., Goldsmith J.R.**, 1989, Oxygen isotope fractionations involving diopside, fosterite, magnetite, and calcite: applications to geothermometry. *Geochimica et Cosmochimica Acta*, 53, p. 2985–2995
- Clayton, R.N., Muffler, L.J.P, White, D.E.**, 1968, Oxygen isotope study of calcite and silicates of the River Ranch No.1 well, Salton Sea geothermal field, California. *American Journal of Science*, 266, p. 968-979.

- _____, O'Neil, J.R., Mayeda, T.K., 1972 Oxygen isotope exchange between quartz and water. *Journal of Geophysical Research* 77, p. 3057–3067.
- Clendenin, C.W.**, 1989, Tectonic influence on the Evolution of the Early Proterozoic Transvaal Sea, Southern Africa. Ph.D. thesis (*unpubl.*) *University of the Witwatersrand*, South Africa, 367pp.
- Cline, J.S., Hofstra, A.H., Muntean, J. L., Tosdal, R.M., Hickey, K.A.**, 2005, Carlin-Type Gold Deposits in Nevada: Critical Geologic Characteristics and Viable Models. In Economic Geology 100th Anniversary Volume (eds. Hedenquist, J. W., Thompson, J. F. H., Goldfarb, R. J. & Richards, J. P.) *Society of Economic Geologists*, p.451-484.
- Clubley-Armstrong**, 1977, The geology of the Selonsrivier area, north Middelburg, Transvaal, with special reference to the structure of the regions southeast of the Dennilton Dome. M.Sc. thesis (*unpubl.*) *University of Pretoria*, South Africa. 107pp.
- Coetzee, C. B.**, 1976, Mineral resources of the Republic of South Africa, 5th edition (ed.) Handbook 7 *Geol. Surv. of S. Afr.*, 86 pp.
- Cox, S.F., Wail, V.J., Etheridge, M.A. and Potter, T.F.**, 1991. Deformational and metamorphic processes in the formation of mesothermal vein-hosted gold deposits--examples from the Lachlan Fold Belt in central Victoria. *Ore Geol. Rev.*, 6, p. 391-423.
- Van Deventer, J.L., Eriksson, P.G., Synman, C.P.**, 1986, The Thabazimbi iron-ore deposits northwest Transvaal. in *Mineral Deposits of S. Africa. Vols I & II.* (eds.: Anhaeusser, C.R., & Maske, S.) *Geol. Soc. S. Afr.* p. 923-29.
- Dietrich, D., McKenzie, J.A., Song, H.**, 1983. Origin of calcite in syntectonic veins as determined from carbonisotope ratios. *Geology* 11, p. 547-551.
- Engelbrecht, J.P.**, 1986, Die Bosveldkompleks en sy vloergesteentes in die omgewing van Nietverdiend, Wes- Transvaal. Ph.D. thesis (*unpubl.*) *University of Pretoria*, South Africa.
- Eriksson, Schreiber, U.M., van der Neut, M., Labuschagne, H., van der Schyff, W., Potgieter, G.**, 1993a, Alternative marine and fluvial models for the non fossiliferous quartzitic sandstones of the Early Proterozoic Daspoot Formation, Transvaal Sequence of southern Africa. *J. Afr. Earth Sci.*, 16, p. 355-66.
- _____, Schweitzer, J.K., Bosch, P.J.A., Schreiber, U.m., van Deventer, J.L., Hatton, C.J., 1993b, The Transvaal Sequence: an overview. *J. Afr. Earth Sci.*, 16, p. 52-51.

- _____, **Schreiber, U.M., van der Neut, M.**, 1991, A review of the sedimentology of the Early Proterozoic Pretoria Group, Transvaal Sequence, South Africa: implications for tectonic setting. *J. Afr. E. Sci.*, 13, p. 107-19.
- _____, **Clendenin, C.W.**, 1990, A review of the Transvaal Sequence, South Africa. *J. Afr. E. Sci.* 10 p. 101-16.
- _____, 1988, The sedimentology of the Rooihuigte Formation, Transvaal Sequence. *S. Afr. J. Geol.*, 91, p. 477-89.
- _____, **Meyer, R. Botha, W.J.**, 1986, A hypothesis on the nature of the Pretoria Group basin. *S. Afr. J. Geol.*, 81, p. 490-97.
- _____, **McCarthy, T.S., Truswell, J.F.**, 1975, Limestone formation and dolomitization in a lower Proterozoic succession from South Africa. *J. Sedim. Petrol.*, 45, p. 604-14.
- _____, **Altermann, W., Catuneanu, O., van der Merwe, R., Bumby, A.J.**, 2001. Major influences on the evolution of the 2.67–2.1 Ga Transvaal basin, Kaapvaal craton. *Sediment. Geol.* 141–142, p. 205–231.
- _____, **Alerman, W., Hartzer, F.J.**, 2006, The Transvaal Supergroup and its Precursors. In The Geology of South Africa (eds. Johnson, M.r., Anhaeusser, C.R., Thomas, R.J.). *Geol. Soc. S. Afr. and the Council of Geoscience*. p. 237-260.
- Faure, G., Mensing, T. M., 2005**, Isotopes Principles and Applications. Third Edition, *John Wiley & Sons, Inc., Hoboken, New Jersey*.
- Fowler, A.R.C.**, 1968, Mining in the Transvaal Gold Mining Estate, Limited 1872-1967. *Jour. S. Afr. Inst. Of Mining and Metallurgy*. p. 291-335.
- Frauenstein, F., Veizer, J., Beukes, N., Van Niekerk, H.S., Coetzee, L.L.**, 2009, Transvaal Supergroup carbonates: Implications for Paleoproterozoic $\delta^{18}\text{O}$ and $\delta^{13}\text{C}$ records. *Precambrian Research*, 175, p. 149-160.
- GeoRem (<http://georem.mpch-mainz.gwdg.de/>)**, 2014, Geological and Environmental Reference Materials. *MPI für Chemie, Mainz, Germany. Application Version 17*.
- Giesemann, A., Jäger, H., Norman, A., Brand, W.**, 1994, On-line sulphur isotope determination using an Element Analyzer coupled to Mass Spectrometer. *Analytical Chemistry*, 66, p. 2816-2819.

- Goldfarb, R.J., Baker, T., Dubé, B., Groves, D.I., Hart, C.J.R., Gosselin, P.**, 2005, Distribution, Character, and Genesis of Gold Deposits in Metamorphic Terranes. In *Economic Geology* 100th Anniversary Volume (eds Hedenquist, J.W., Thompson, J.F.H., Goldfarb, R.J. & Richards, J.P.) *Society of Economic Geologists*, p.407-450.
- Good, N.**, 1999, Structural and Thermal Control on basinal fluid flow and mineralisation beneath the Bushveld Complex and along the adjacent Thabazimbi-Murchison Lineament; Kaapvaal Craton, South Africa. Ph.D. Thesis (Unpubl.), *University of Cape Town, South Africa*.
- Gray, J.**, 1905, Note on the geology of the Lydenburg Goldfields. *Trans. Geol. Soc. S. Afr.*, 8.
- Hall, A. L.**, 1910, The geology of the Pilgrim's Rest gold mining district. *Mem. S. Afr. Geol. Surv.* 5, 159 pp.
- Harley, M. Charlesworth, E.G.**, 1990 The mineralisation at Elandshoogte Gold Mine, eastern Transvaal, South Africa. *Economic Geology Research Unit, Univ. Witwatersrand, Johannesburg, Information Circular* 226, 16 pp.
- _____, **Charlesworth, E.G.**, 1992, Thrust-controlled gold mineralisation at the Elandshoogte Mine, Sabie-Pilgrim's Rest goldfield, South Africa. *Mineral. Deposita* 27, p. 122-128.
- _____, 1993, The Geology of the Sabie-Pilgrim's Rest Goldfield, with special reference to Elandshoogte Mine. PhD thesis (*unpubl.*) *University of the Witwatersrand Johannesburg, South Africa*.
- _____, **Charlesworth, E.G.**, 1994, Structural development and controls to epigenetic, mesothermal gold mineralization in the Sabie-Pilgrim's Rest goldfield, Eastern Transvaal, South Africa. *Explor. Min. Geol.*, 3, p. 231-246.
- _____, **Charlesworth, E.G.**, 1996, The role of fluid pressure in the formation of bedding-parallel, thrust-hosted gold deposits, Sabie-Pilgrim's Rest goldfield, eastern Transvaal. *Precambrian Research*, 79, p. 125-140.
- Harris, C., Chaumba, J.B.**, 2001. Crustal contamination and fluid-rock interaction during the formation of the Platreef, northern limb of the Bushveld Complex, South Africa. *Jour. Petrol.* 42, p. 1321–1347.
- Harmer, R.E., Von Gruenewaldt, g.**, 1991, A review of the magmatism associated with the Transvaal Basin – implications for its tectonic setting. *S. Afr. J. of Geol.* 94, p. 104-22.
- Hartzer, F.J.**, 1987, Die geologie van die Krokodilrivier-fragment, Transvaal. Msc thesis (*unpubl.*), *Rand Afrikaans University, South Africa*.

_____, 1995 Transvaal Supergroup inliers: geology, tectonic development and relationship with the Bushveld Complex, South Africa. *Journal of African Earth Sciences* 21, p. 521–547.

Hatton C.J., Schweitzer, J.K., 1995, Evidence for synchronous extrusive and intrusive Bushveld magmatism. *J. Afr. E. Sci.*, 21, p 579-94.

Hayes, J.M., Kaplan, I.R., Wedekind, K.W., 1983. Precambrian organic geochemistry: preservation of the record. In: Schopf, J.W. (Ed.), *Earth's Earliest Biosphere: Its Origin and Evolution*. Princeton University Press, p. 93–148.

Herring, G., 1928 The Pilgrim Diggers of the'70s a short history of Pilgrim's Rest.

Henderson, P., Henderson, G.M., 2009, The Cambridge Handbook of Earth Science Data. Cambridge University Press, 179 pp.

Henry, G., Clendenin, C.W & Charlesworth, E.G., 1990, Depositional facies of the Black Reef Quartzite Formation in the eastern Transvaal. *Geo Congress '90 (Cape Town, South Africa): Extended Abstracts*, p. 230-33.

Hoefs, J., 2009. Stable Isotope Geochemistry (6th Edition). Springer-Verlag, Berlin, Heidelberg.

Hoering, T.C., 1962, The stable isotopes of carbon in the carbonate and reduced carbon of Precambrian sediments *Carnegie Inst. Washington, Yearb.*, p. 190–191.

Jackson, S.E., 2001. The application of Nd:YAG lasers in LA-ICP-MS. Principles and Applications of Laser Ablation-Mass Spectrometry in the Earth. Mineralogical Association of Canada Short Course Series 29, 29-46

Jensen, M . L., 1967, Sulphur isotopes and mineral genesis. In *Geochemistry of Hydrothermal Ore Deposits* (ed. Barnes, H. L.). New York, Holt, Rinehart and Winston, Inc., p. 143-165.

Kamo, S. L., Davis, D. W., 1994, Reassessment of Archean crustal development in the Barberton Mountain Land, South Africa, based on U-Pb dating. *Tectonics*, 13, p. 167–192.

Kasemann S., Meixner A., Rocholl A., Vennemann T., Schmitt A., and Wiedenbeck M., 2001, Boron and oxygen isotope composition of certified reference materials NIST SRM 610/612, and reference materials JB-2G and JR-2G. *Geostandards Newsletter*, 25, p. 405-416.

Kirschner D.L., Sharp Z.D., Masson, H., 1995, Oxygen isotope thermometry of quartz–calcite veins: unravelling the thermal-tectonic history of the subgreenschist facies Morcles nappe (Swiss Alps). *Geological Society of America Bulletin*, 107, p. 1145–56.

Klausen, M.B., Söderlund, U., Olssen, J.R., Ernst, R.E., Armoogam, M., Mkhize, S.W., Petzer, G., 2010, Petrological discrimination among Precambrian dyke swarms: Eastern Kaapvaal craton (South Africa). *Precambrian Research*, 183, p. 501-522

Klünder, M.H., Karup-Møller, S., Makovicky, E., 2003, Exploratory studies on substitutions in the tetrahedrite-tennantite solid solution series Part 3. The solubility of bismuth in tetrahedrite-tennantite containing iron and zinc. *Neues Jahrbuch für Mineralogie Monatshefte*, p. 153-175.

Knudsen, T.-L. et al., 2000. In situ hafnium and lead isotope analyses of detrital zircons from the Devonian sedimentary basin of NW Greenland: a record of repeated crustal reworking. *Contributions to Mineralogy and Petrology*, 141, 83-94

Martin, D. McB., Clendenin, C. W., Krapez, B., McNaughton, N. J., 1998, Tectonic and geochronological constraints on late Archean and Palaeoproterozoic stratigraphic correlation within and between the Kaapvaal and Pilbara Cratons. *J. Geol. Soc. London.*, 155, p. 311-145.

Maslennikov, V.V., Maslenikova, S.P., Large, R.R., Danyushevsky, L.V., 2009 Study of Trace Element Zonation in Vent Chimneys from the Silurian Yaman-Kasy Volcanic-Hosted Massive Sulphide Deposit (Southern Urals, Russia) Using Laser Ablation-Inductively Coupled Plasma Mass Spectrometry (LA-ICPMS). *Econ. Geol.*, 104, p. 1111-1141.

Mathez, E.aWaight, T.E., 2003, Lead isotopic disequilibrium between sulphide and plagioclase in the Bushveld Complex and the chemical evolution of large layered intrusions. *Geochimica et Cosmochimica Acta*, 67, p. 1875-1888.

_____, **Kent, A.J.R.,** 2007, Variable initial Pb isotopic compositions of rocks associated with the UG2 chromitite, eastern Bushveld Complex. *Geochimica et Cosmochimica Acta*, 71, p. 5514-5527.

Merle, O., Vendeville, B., 1992 Mod61isation analogique de chavauchements induits par des intrusions magmatiques (Experiments on thin-skinned thrusting as related to magmatic intrusion). *C.R. Acad. Sci. Paris*, 315, Set. II, pp. 1541-1547.

Meyer, F. M., Welke, H. J., Robb, L. J., 1986, Mineralogical and chemical characteristics of flat reefs in the Sabie-Pilgrim's Rest Goldfield. *Geoecongress '86 Geol. Soc S. Afr. Johannesburg, South Africa*, p. 535-540.

_____, 1988, Environment of ore formation in the Sabie-Pilgrim's Rest Goldfield, South Africa. *Abstr. Congr. '88, Geol. Soc. S. Afr.*, p. 427-430.

_____, **Robb, L. J.,** 1996, The Geochemistry of Black Shales from the Chuniespoort Group, Transvaal Sequence, eastern Transvaal. *Econ Geol*, 91, p. 111-121.

- Minnitt, R. C. A., Button, A., Kable, E. J. D.**, 1973. The gold content of pre-Malmani argillaceous sediments in the Transvaal Supergroup, northeastern Transvaal. *Economic Geology Research Unit, Univ. Witwatersrand, Johannesburg, Information Circular* 82, 11 pp.
- Norman M., Robinson P., Clark D.**, 2003 Major and trace element analysis of sulphide ores by laser ablation ICPMS, solution ICPMS, and XRF. *Canadian Mineralogist* 41, p. 293-305.
- O'Neil J.R., Clayton R.N., and Mayeda T.K.**, 1969, Oxygen isotope fractionation in divalent metal carbonates. *J. Chem. Phys.* 51, 5547 pp.
- Penniston-Dorland, S.C., Mathez, E.A., Wing, B.A., Farquhar J., Kinnaird, J.A.**, 2012 Multiple sulphur isotope evidence for surface-derived sulphur in the Bushveld Complex. *Earth and Planetary Science Letters*, 337-338, p. 236-242.
- Perrit, S., Roberts, M.**, 2007, Flexural-slip structures in the Bushveld Complex, South Africa. *Journal of structural Geology*, 29, p 1422-1429.
- Pronost, J., Harris, C., Pin, C.**, 2008, Relationship between footwall composition, crustal contamination, and fluid–rock interaction in the Platreef, Bushveld Complex, South Africa. *Mineralium Deposita*, 43, p. 825-848.
- Recko, B.F.F., Eriksson, P.G. & Snyman, C.P.**, 1992, Geochemistry of the shales interbedded in the Magaliberg Formation, Pretoria Group, near Pretoria: paleoenvironmental and diagenetic implications. *Geocongress '92 (Bloemfontein, South Africa): Abstracts*, p. 305-07
- Reich, M., Kesler, S.E., Utsunomiya, S., Palenik, C.S., Chryssoulis, S.L., Ewing, R.C.** 2005, Solubility of gold in arsenian pyrite. *Geochimica et Cosmochimica Acta*, 69, p. 2781-2796.
- Reinecke, L., Stein, W. G. A.**, 1929. Ore bodies of the Pilgrim's Rest Goldfield. *Trans., Geol. Soc. S. Afr.*, 32, p. 65-88.
- Robb, L.**, 2005, Introduction to ore forming processes, *Victoria, Blackwell Publishing*, 373 pp.
- _____, Brandl, G., Anhaeusser, C. R. & Poujol, M., in Johnson, M.r., Anhaeusser, C.R., Thomas, R.J.**, 2006, Archaean granitoid intrusions. *Johannesburg: Geological Society of South Africa and Council for Geoscience*, p. 57-94.
- Ronde, C.E.J., Spooner, E.T.C., de Wit, Maarten, J., Bray, C.J.**, 2008, Shear zone-related, Au quartz vein deposits in the Barberton greenstone belt, South Africa; field and petrographic characteristics, fluid properties, and light stable isotope geochemistry. *Econ. Geol.* 87 p. 366- 402

Rumble D. III., Hoering T.C., 1994, Analysis of oxygen and sulphur isotope ratios in oxide and sulphide minerals by spot heating with a carbon dioxide laser in a fluorine atmosphere. *Accounts of Chemical Research*, 27, p. 237-241.

Rye, R.O., Ohmoto, H., 1974, Sulphur and Carbon Isotopes and Ore Genesis ' A Review. *Econ. Geol.*, 69, p. 826-842.

Saager, R., Köppel, V., 1976, Lead Isotopes and Trace Elements from Sulfides of Archean Greenstone Belts in South Africa – A Contribution to the Knowledge of the Oldest Known Mineralisation. *Econ. Geol.* 71. 44 pp.

S.A.C.S (South African Committee for Stratigraphy), 1980, *Stratigraphy of South Africa: Part 1: Lithostratigraphy of the Republic of South Africa, South West Africa/Namibia and the Republics of Bophuthatswana, Transkei and Venda. Compiled by Kent, L.E. S. Afr. geol. Surv.* 8, 690 pp.

Schidlowski, M., R. Eichmann, and C. E. Junge., 1975, Precambrian sedimentary carbonates: Carbon and oxygen geochemistry and implications for the terrestrial oxygen budget, *Precambrian Res.*, 2, p. 1–69.

Schiffries, C.M., 1989, Liquid-absent aqueous fluid inclusions and phase equilibria in the system CaCl₂ NaCl H₂O. *Geochimica et Cosmochimica Acta*, Vol. 54, p. 611-619.

Schreiber, U.M., 1991, A paleoenvironmental study of the Pretoria Group in the eastern Transvaal. Ph.D. thesis (*unpubl.*) *University of Pretoria*, South Africa.

Schweitzer, J.K. & Hatton, C.J., 1995, chemical alteration within the volcanic roof rocks of the Bushveld Complex. *Econ. Geol.*, 90, p. 2218- 2231.

Sharman-Harris, E.R., Kinnaird, J.A., Harris, C., Horstmann, U.E., 2005, A new look at sulphide mineralisation of the northern limb, Bushveld Complex: a stable isotope study. *Institute of Materials, Minerals and Mining and Australasian Institute of Mining and Metallurgy, Published by Maney*.

_____, 2006, Geochemical and Isotopic Studies of the Platreef with Special Emphasis on Sulphide Mineralisation. M.Sc Thesis, *University of the Witwatersrand, Johannesburg, South Africa*.

Sharp, Z. D., 1990, A laser-based microanalytical method for the in-situ determination of oxygen isotope ratios of silicates and oxides. *Geochimica et Cosmochimica Acta*, 54, p. 1353-1357.

_____, **Z.D., Kirschner, D.L.**, 1994. Quartz calcite oxygen isotope thermometry- a calibration based on natural isotopic variations. *Geochimica et Cosmochimica Acta*, 58, p. 4491-4501.

- Sharpe, M. R.**, 1981. The chronology of magma influxes to the eastern compartment of the Bushveld Complex, as exemplified by its marginal border group. *J. Geol. Soc. London* 138, p. 307–326.
- _____, 1984, Petrography, classification and chronology of mafic intrusions beneath the eastern Bushveld Complex. *Bull. geol. Surv. S. Afr.*, 77, 40 pp.
- Sharpe, M.R.**, 1981. The chronology of magma influxes to the eastern compartment of the Bushveld Complex, as exemplified by its marginal border group. *J. Geol. Soc. London* 138, p. 307–326.
- Sheppard, S.M.F., Schwarcz, H.P.** (1970) Fractionation of carbon and oxygen isotopes and magnesium between coexisting metamorphic calcite and dolomite. *Contrib. Mineral. Petrol.* 26, p. 161–198.
- Shieh, Y. N., and Taylor.**, 1969, Oxygen and carbon isotope studies of contact metamorphism of carbonate rocks. *Journal of Petrology.*, 10, p. 307-331.
- _____, **Zhang, X.**, 1988, Oxygen isotope geochemistry of Precambrian shales in the Kaapvaal craton, South Africa. (abstr.) *W.M. Goldschmidt Conference.*, 74 pp.
- South African Committee for Stratigraphy (SACS)**, 1980, Stratigraphy of South Africa. Part 1. (ed: Kent, L.E.). Lithostratigraphy of the Republic of South Africa, South West Africa/Namibia, and the Republics of Bophuthatswana, Transkei and Venda. *Handb. Geol Surv. Of S. Afr.*, No. 8.
- Spötl, C., Vennemann, T.W.**, 2003, Continuous-flow isotope ratio mass spectrometric analysis of carbonate minerals. *Rapid communications in mass spectrometry*, 17, p. 1004–1006.
- Stacey, J.S., Kramers, J.D.**, 1975. Approximation of terrestrial lead isotope evolution by a two- stage model. *Earth and Planetary Scienc Letters*, 26, p. 207-221.
- Steyn, J. H., Coetsee, F., Walraven, F.**, 1986, 1:250 000 geological series. 2430, Pilgrim's Rest South Africa. *Geol Surv. S. Afr.*
- Stosch, H.G.**, 2004, Einführung in die Isotopen Geochemie. *Institut für Mineralogie und Geochemie Universität Karlsruhe.*
- Strauss, H., Beukes, N.J.**, 1996, Carbon and sulphur isotopic compositions of organic carbon and pyrite in sediments from the Transvaal Supergroup, South Africa. *Precambrian Research*, 79, p. 57-71
- Swiegers, J. U.**, 1949. The gold deposits of the Pilgrim's Rest Gold Mining District, Transvaal. *Trans. Geol. Soc. S. Afr.*, 51, p. 81-148.

- Taussig, D., Maiden, K.** 1986, U-Pb Stratabound copper mineralisation in the Duitschland Formation, Transvaal Basin.
- Tatsumi, T.**, 1965, Sulphur isotopic fractionation between co-existing sulphide minerals from some Japanese ore deposits. *Econ. Geol.*, 60, p. 1645-1659
- Taylor, H.P.**, 1974, The application of oxygen and hydrogen isotope studies to problems of hydrothermal alteration and ore deposition. *Econ. Geol.*, 69, p. 843-883.
- Thompson, J.F.H., Sillitoe, R.H., Baker, T., Lang, J.R., Mortensen, J.K.**, 1999, Intrusion related gold deposits associated with tungsten-tin provinces. *Minerlaium Deposita*, 34, p. 377-400.
- Twist, D., French, B.M.**, 1983, Voluminous acid volcanism in the Bushveld Complex: A review of the Rooiberg felsite. *Bull. Volcanol.*, 46, p. 225-242.
- Tyler, R.**, 1989. Cyclic sedimentation and gold mineralization in the Malmani Dolomite Sub-Group, Pilgrim's Rest-Sabie area, eastern Transvaal. M.Sc. thesis (Unpubl.), *University of the Witwatersrand*.
- Tyler R., Tyler N.**, 1996, Stratigraphic and structural controls on gold mineralization in the Pilgrim's Rest goldfield, eastern Transvaal, South Africa. *Precambrian Res.*, 79, p. 141-169.
- Uken, R.**, 1998, The geology and structure of the Bushveld Complex metamorphic aureole in the Olifants River area. Ph.D. Thesis (Upubl.) *University of Durban Westville*, p. 68-144
- Valley, J.W.**, 2001 Stable Isotope Thermometry at High Temperatures. *Reviews in Mineralogy and Geochemistry*, 43, p. 365-413.
- Valley J.W., Kitchen, N., Kohn, M.J., Niendorf, C.R., and Spicuzza, M.J.**, 1995, UWG-2, a garnet standard for oxygen isotope ratios: strategies for high precision and accuracy with laser heating. *Geochimica et Cosmochimica Acta*, 59, p. 5223-5231.
- Van Achterbergh, E., Ryan, C.G., Jackson, S.E., Griffin, W.L.**, 2001, Appendix 3, data reduction software for LA-ICP-MS, in Sylvester, P. J., ed., LA-ICP-MS in the Earth Sciences, *Mineralogical Association of Canada*, 29, p. 239-243.
- Vaughan, J., Rosso, K.M.**, 2006, Chemical Bonding in Sulphide Minerals. *Reviews in Mineralogy and Geochemistry*, 61 p. 231–264.
- Veizer, J., Plumb, K.A., Clayton, R.N., Hinton, R.W., Grotzinger, J.P.**, 1992, Geochemistry of Precambrian carbonates: V. Late Paleoproterozoic seawater. *Geochimica et Cosmochimica Acta*, 56, p. 2487-2501.

Visser, N.H., Verwoerd, W.J., 1960, The geology of the country north of Nelspruit. Explanation of Sheet 22, (Nelspruit) *Geol Surv.*, 128pp.

Walraven F, Hattingh, J., 1993, Geochronology of the Nebo Granite, Bushveld Complex. *Afr. J. Geol.*, 96, p. 31-41.

_____, **Martini, J.**, 1995, Zircon Pb-evaporation age determinations of the Oaktree Formation, Chuniespoort Group, Transvaal Supergroup: implications for the Transvaal-Gruqualand West basin correlations. *S. Afr. Journal of Geology*. 98, p. 58-67

_____, 1997, Geochronology of the Rooiberg Group, Transvaal Supergroup, South Africa. *Economic Geology Research Unit, Univ. Witwatersrand, Johannesburg, Information Circular*, 316.

Watkeys, M. K., 2002, Development of the Lebombo rifted volcanic margin of southeast Africa. *Geol. Soc. America, Special Paper*, 362.

Wilson, S.A., Ridley, W.R., Koenig, A.E., 2002. Development of sulphide calibration standards for the laser ablation inductively-coupled plasma mass spectrometry technique. *Journal of Analytical Atomic Spectrometry* 17, p. 406-409.

Willemse, J., 1969, The geology of the Bushveld Igneous Complex, the largest repository of magmatic ore deposits in the world. *Econ. Geol. Monogr*, 4, 966 pp.

Wybergh, W. J., 1925, The economic geology of the Sabie-Pilgrim's Rest. Mem. *S. Afr. Geo. Surv.*, 23, 118 pp.

Zakrzewski, M.A., 1989, Members of the freibergite-argentotennantite series and associated minerals from Silvermines, County Tipperary, Ireland. *Mineralogical Magazine*, 53, p 293–298.

Zeh, A., Ovtcharova, M., Wilson, A., Schaltegger, U., 2014, The Rustenburg Layered Suite (Bushveld Complex) crystallised in less than 1.5 million years. *Geophys. Res. Abs.*, 16

Zhang, J., Deng, J., Chen, H., Yang, L., Cooke, D., Danyushevsky, L., Gong, Q., 2014, LA-ICP-MS trace element analysis of pyrite from the Chang'an gold deposit, Sanjiang region, China: Implication for ore-forming process. *Gondwana Research*, 26, p. 557-575

Zhu, Y., An, F., Tan, J., 2011, Geochemistry of hydrothermal gold deposits: A review. *Geoscience Frontiers*, 2, p. 367-374

Zietsman, A.L., 1964, The geology of the Sabie-Pilgrim's Rest Goldfield. M.Sc thesis (*unpubl.*) *University of the Orange Free State, Bloemfontein, South Africa*.

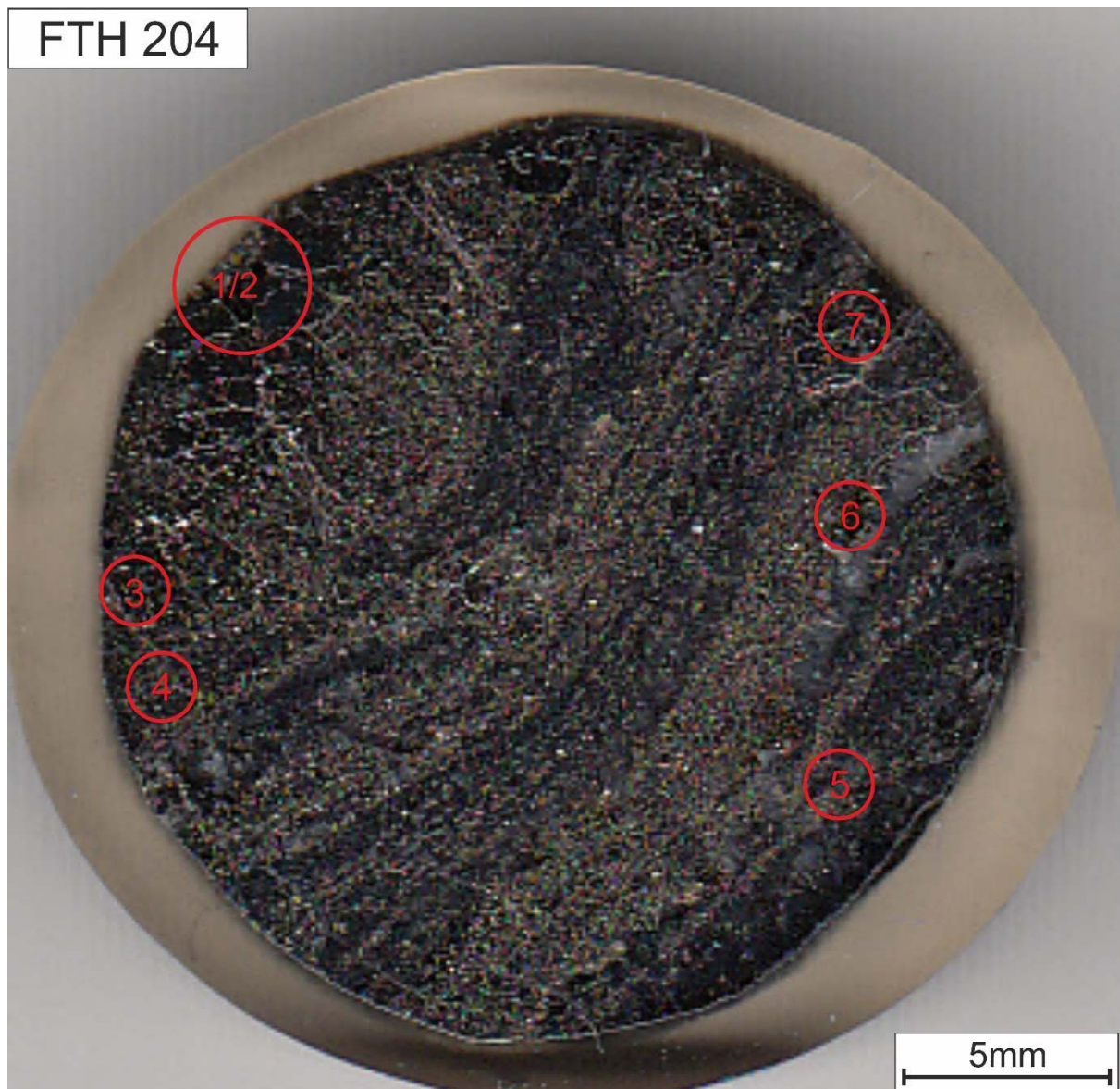
_____, 1967, The relationship between mineralization and structure in the Pilgrim's Rest-Sabie Gold-Field. PhD thesis (*unpubl.*) University of the Orange Free State, Bloemfontein, South Africa.

Zintwana, M.P., Cawthorn, R.G., Ashwal, L.D., Roelofse, F., Cronwright, H., 2011, Mercury in the Bushveld Complex, South Africa, and the Skaergaard Intrusion, Greenland. Chemical Geology, 320-321, p. 147-155.

Appendix

Analysed Polished Stubs

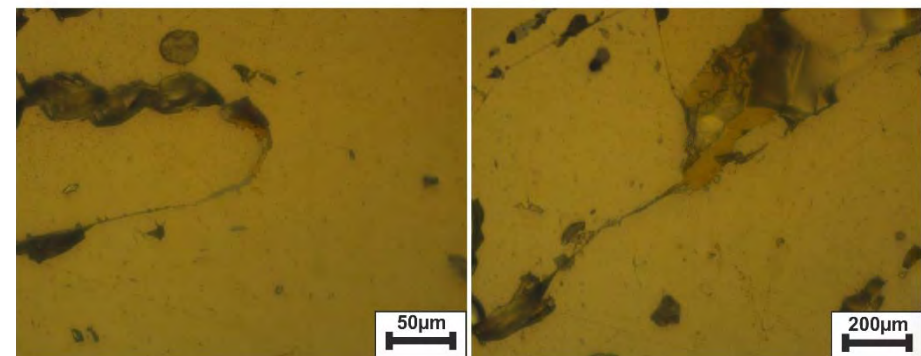
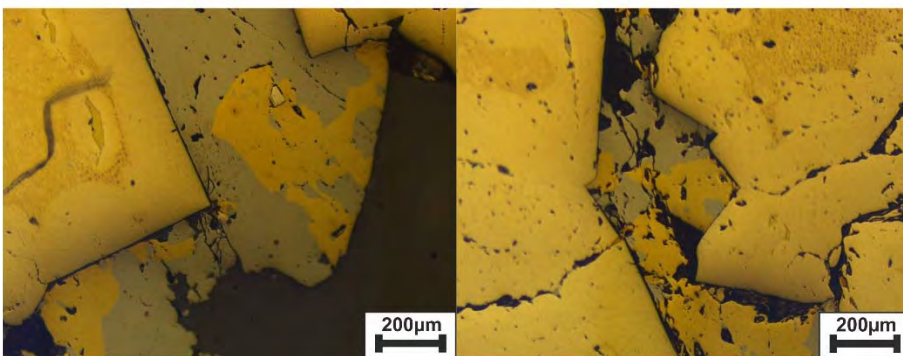
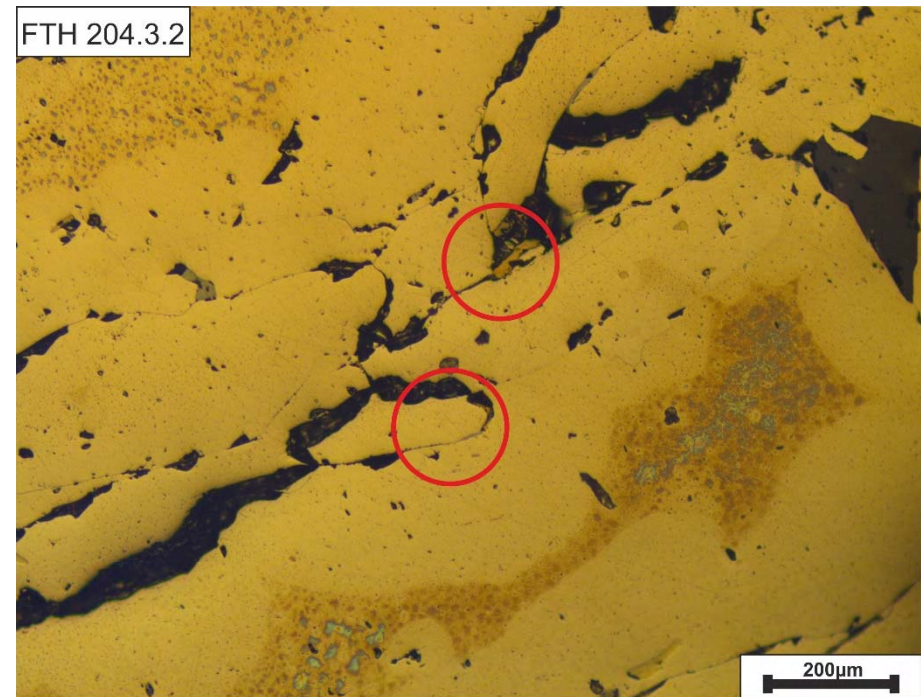
Mineralised stromatolitic structure



FTH 204.3.1



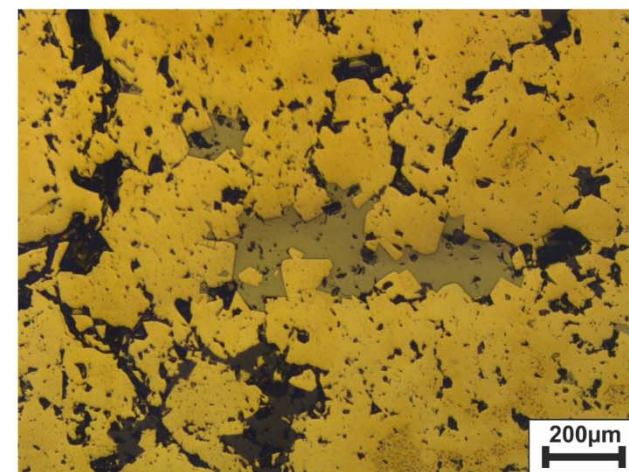
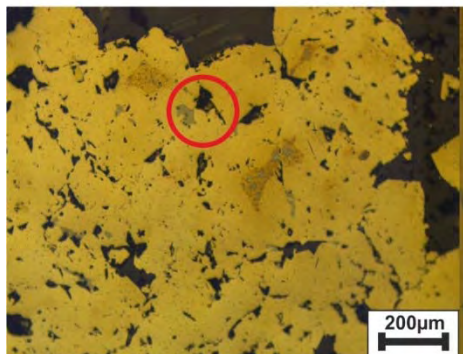
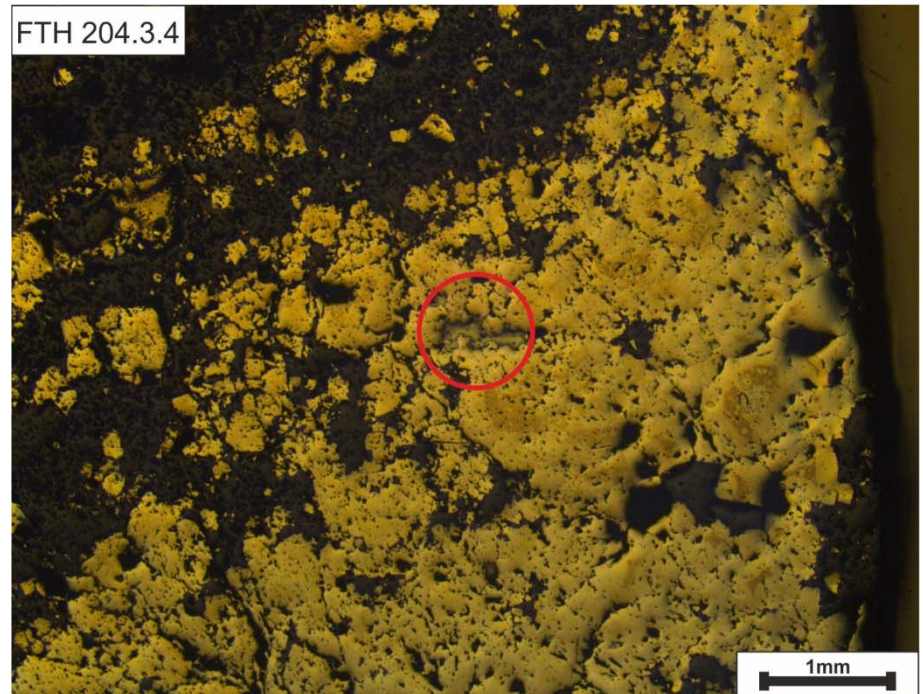
FTH 204.3.2



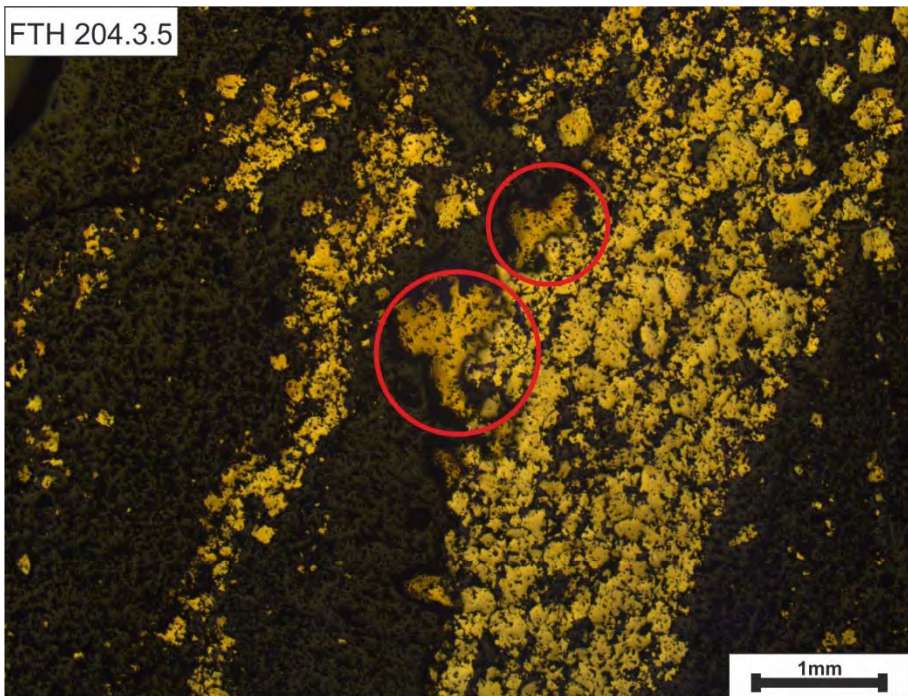
FTH 204.3.3



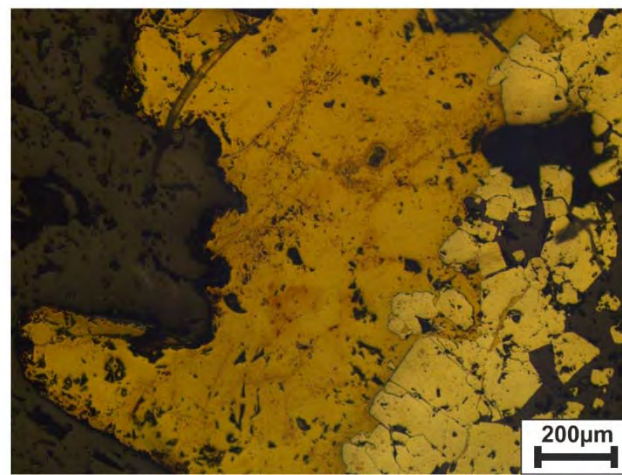
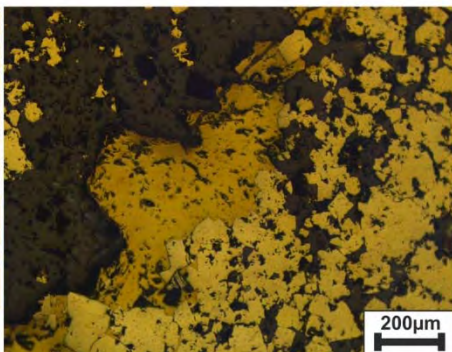
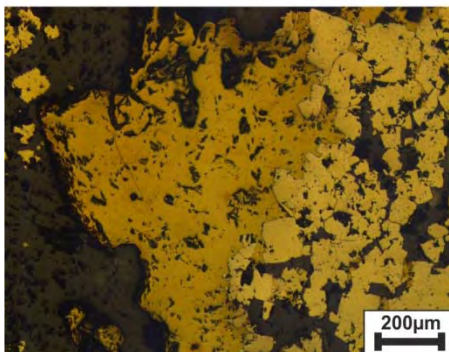
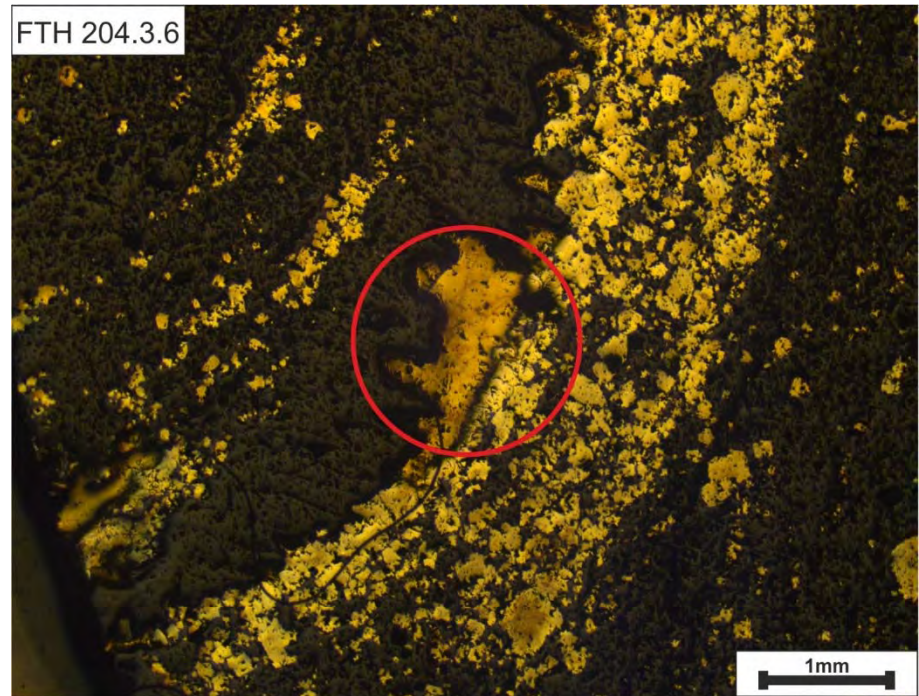
FTH 204.3.4



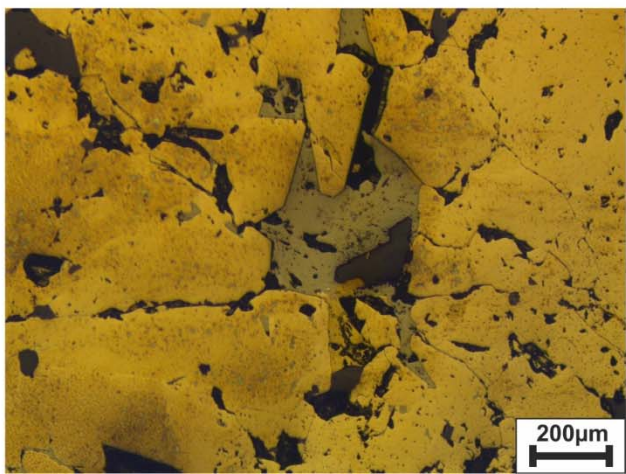
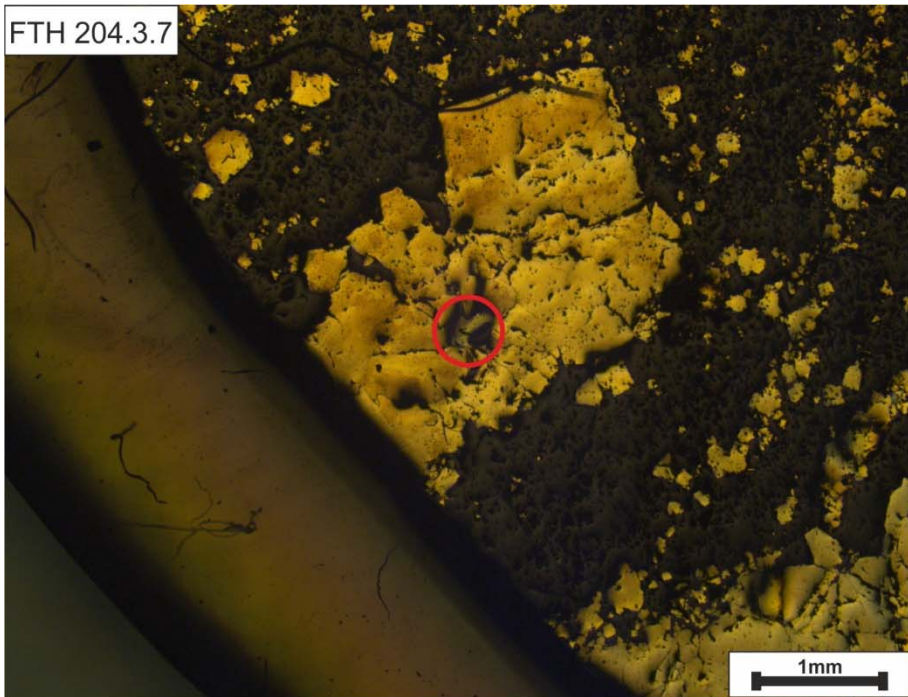
FTH 204.3.5



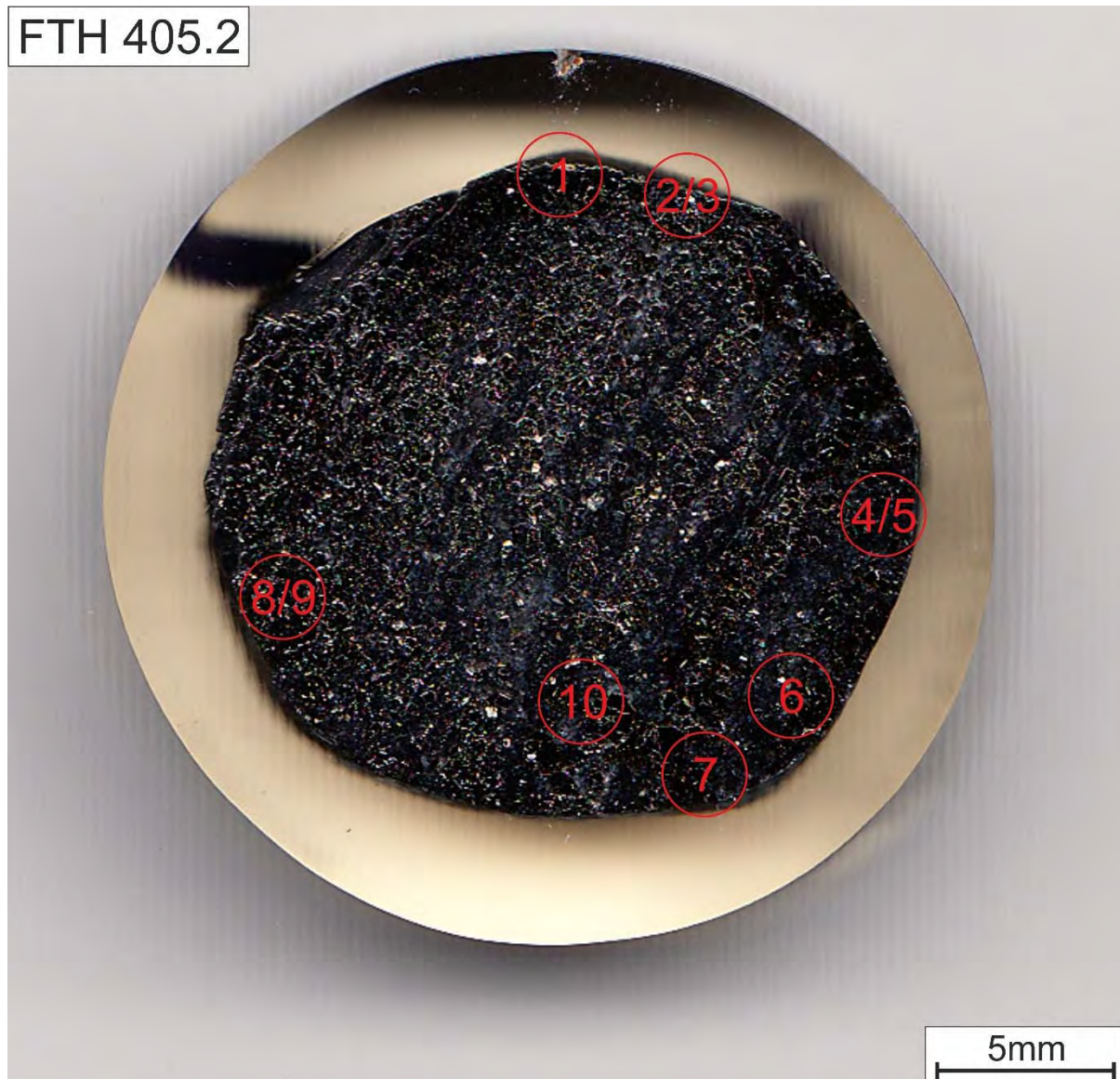
FTH 204.3.6



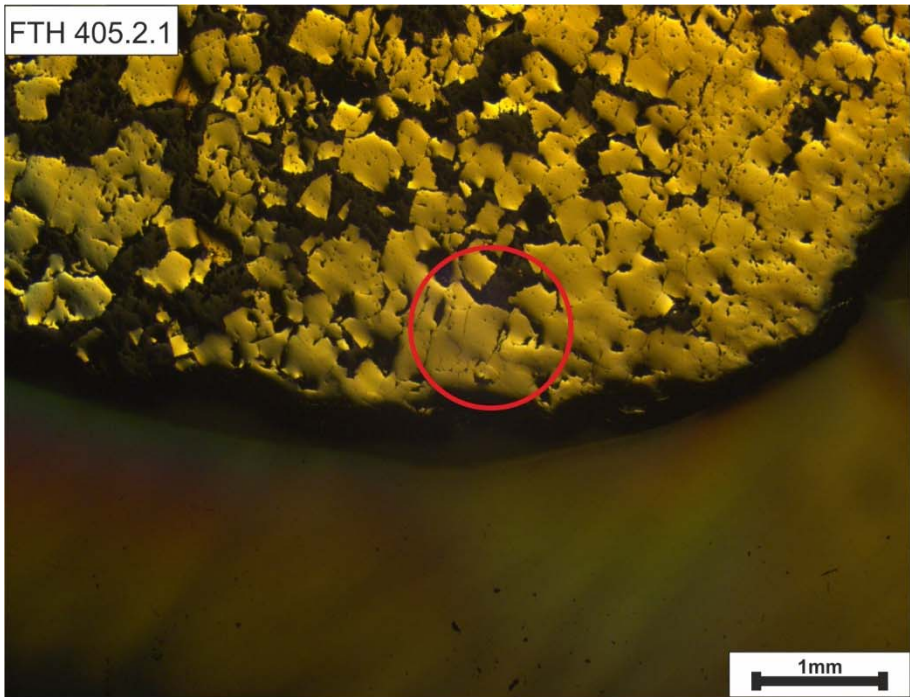
FTH 204.3.7



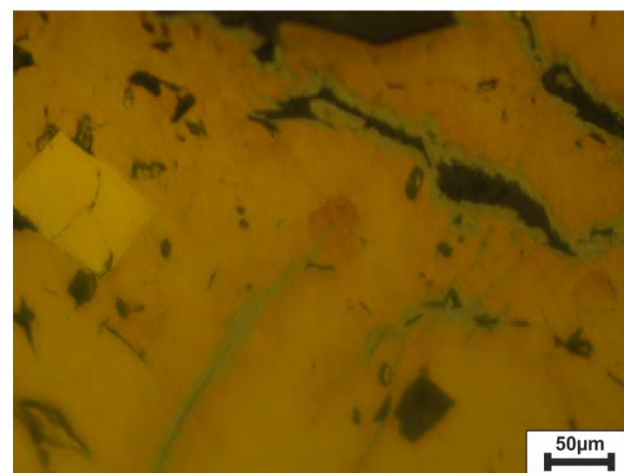
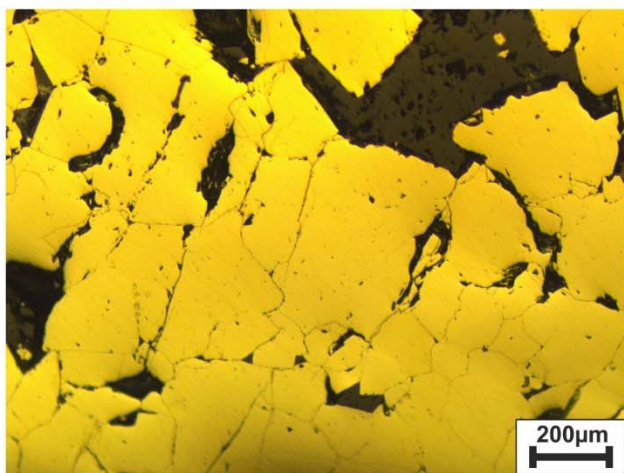
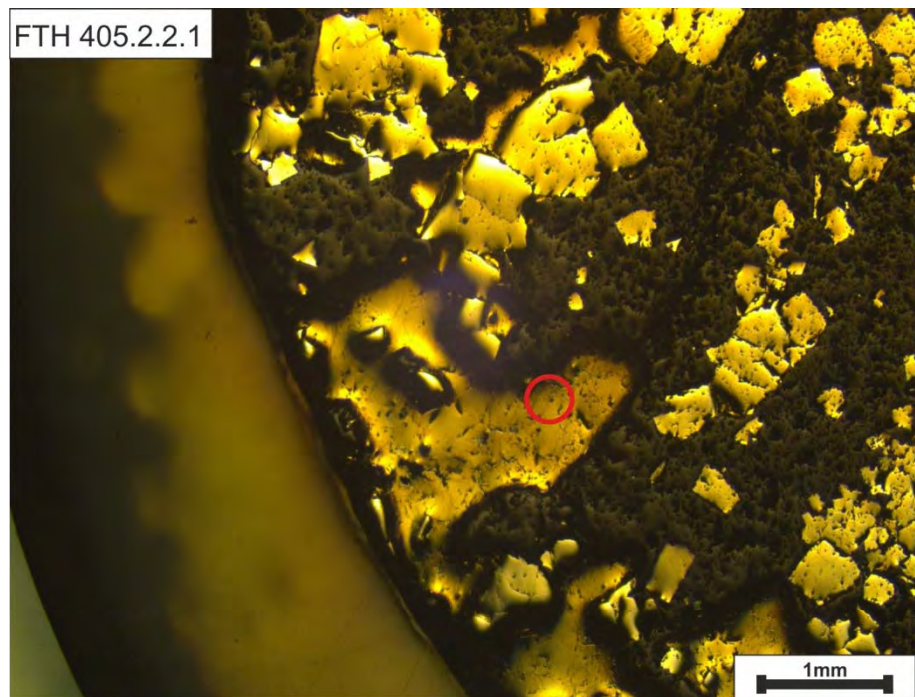
Quartz-chert-carbonate vein

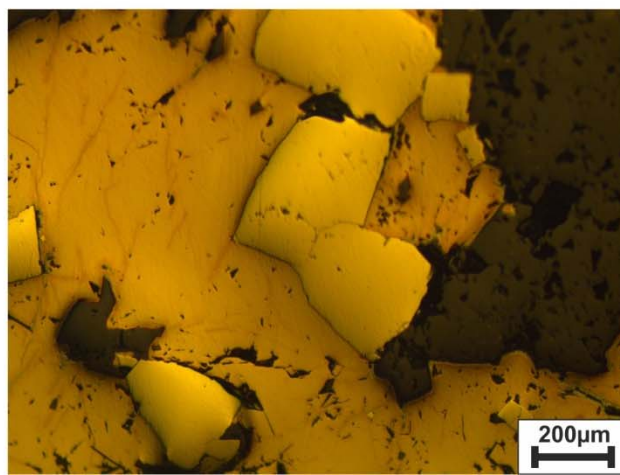
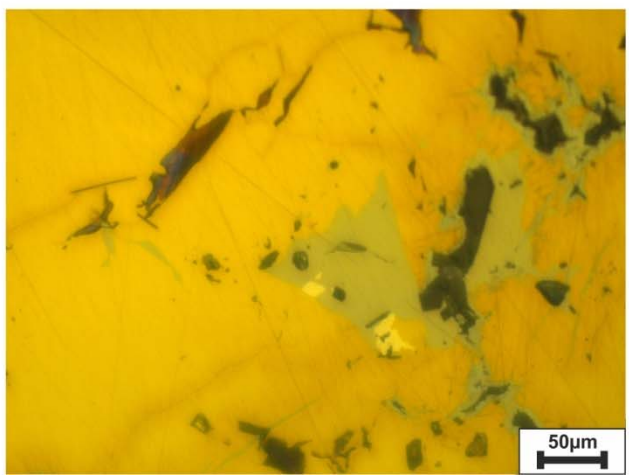
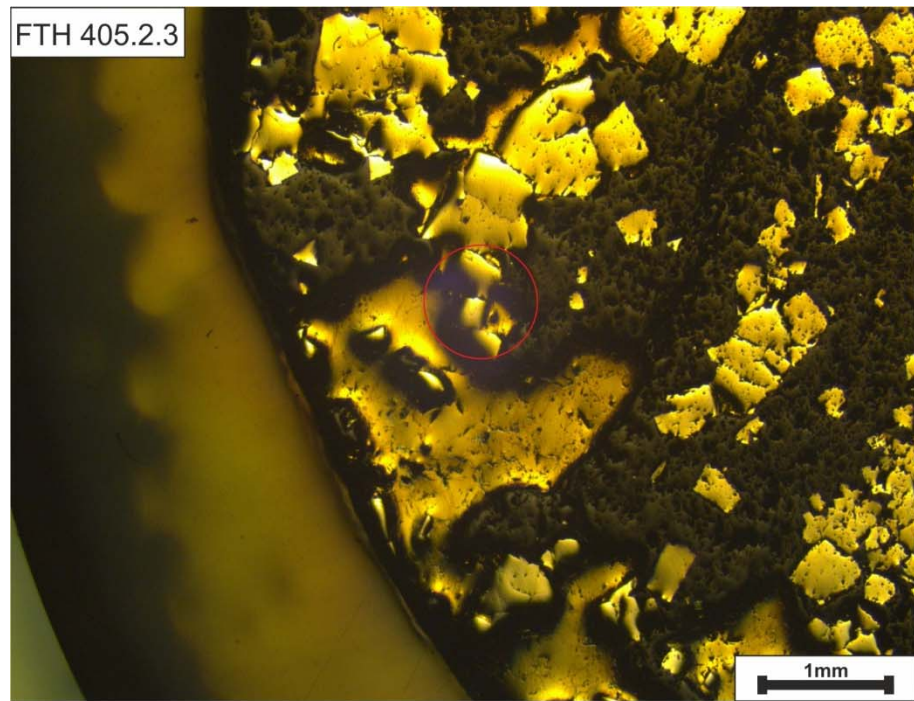
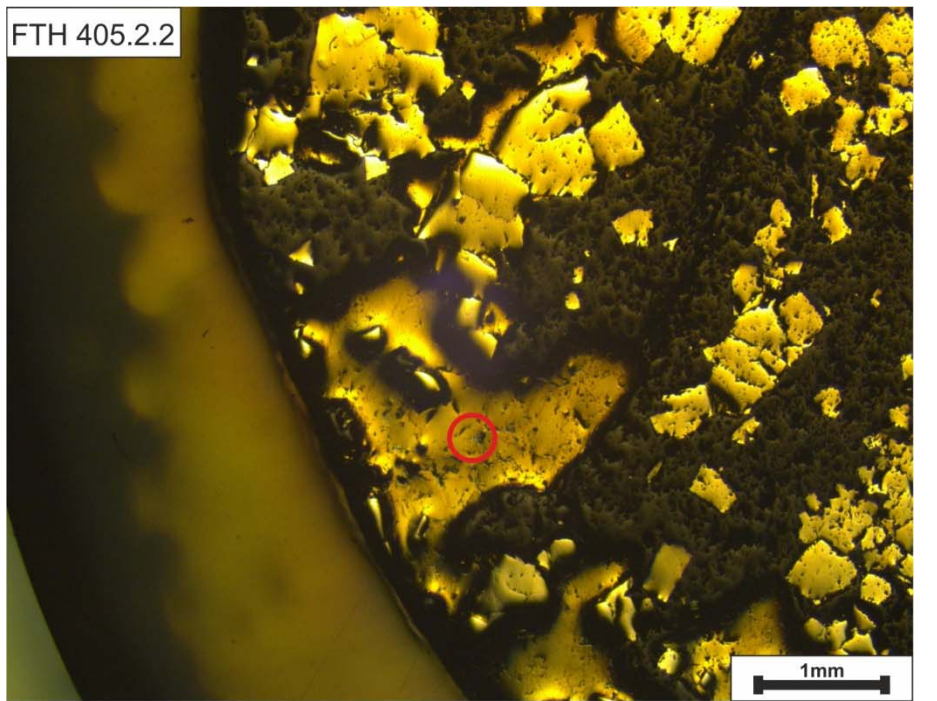


FTH 405.2.1



FTH 405.2.2.1

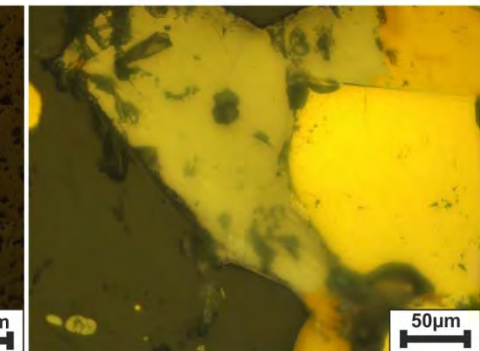
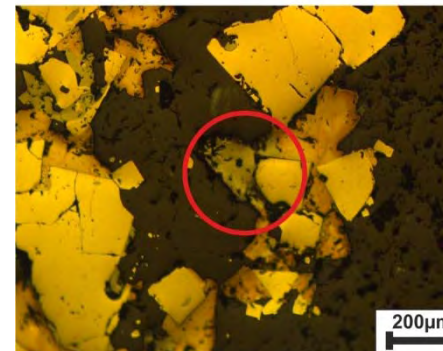
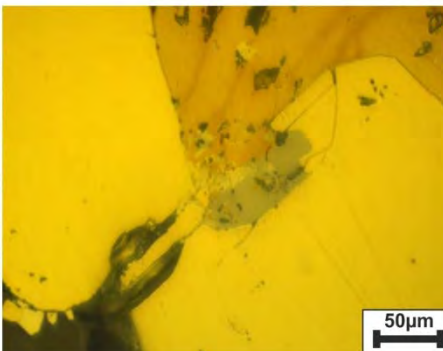
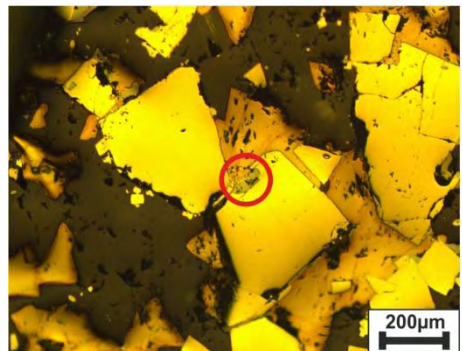




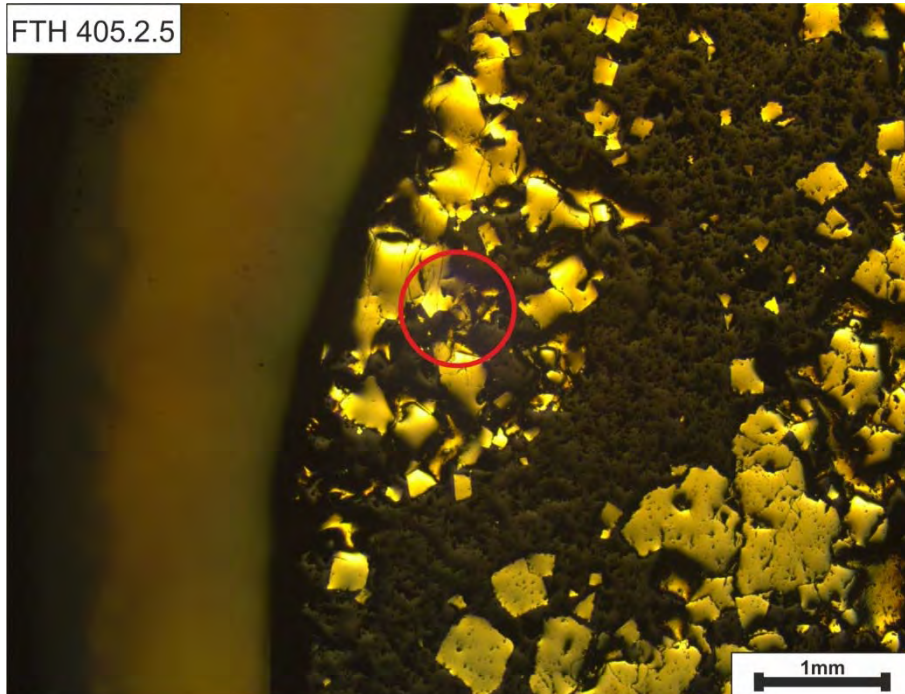
FTH 405.2.4



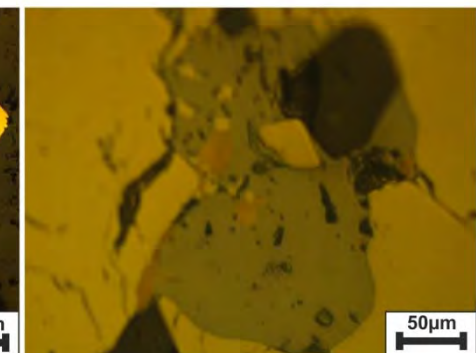
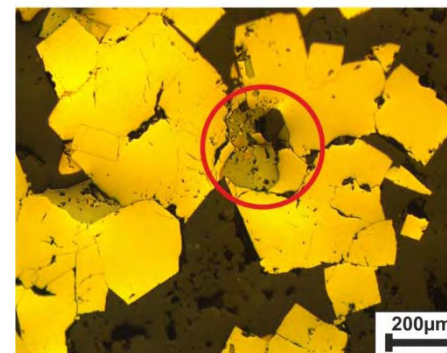
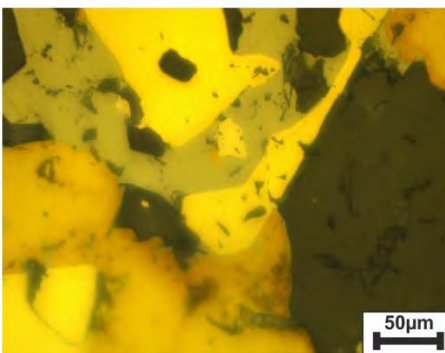
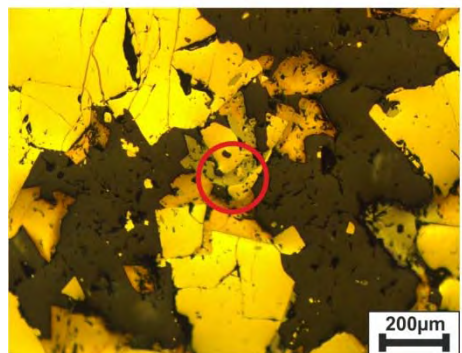
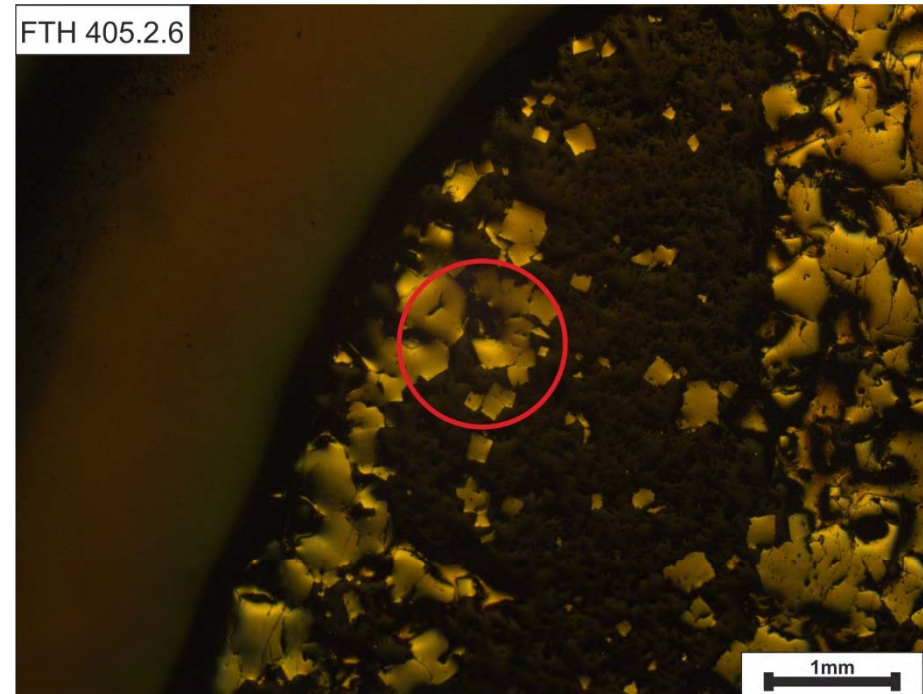
FTH 405.2.5.1



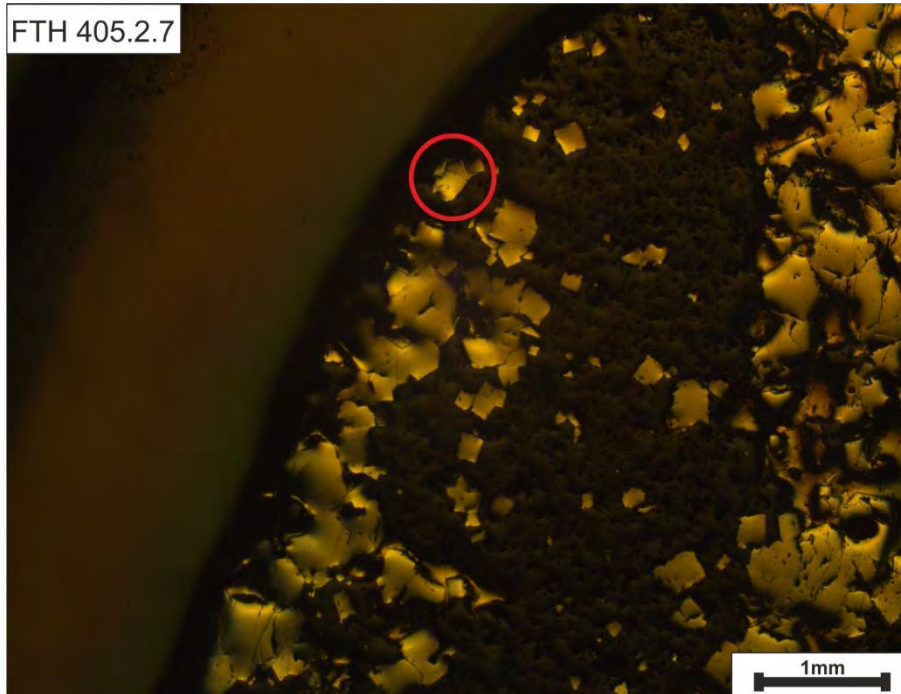
FTH 405.2.5



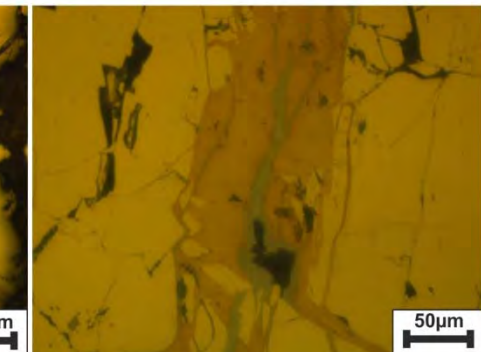
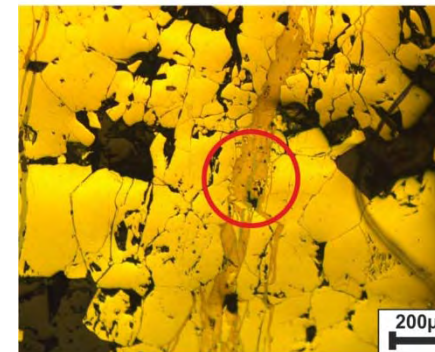
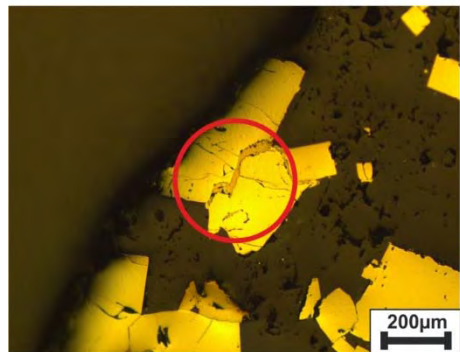
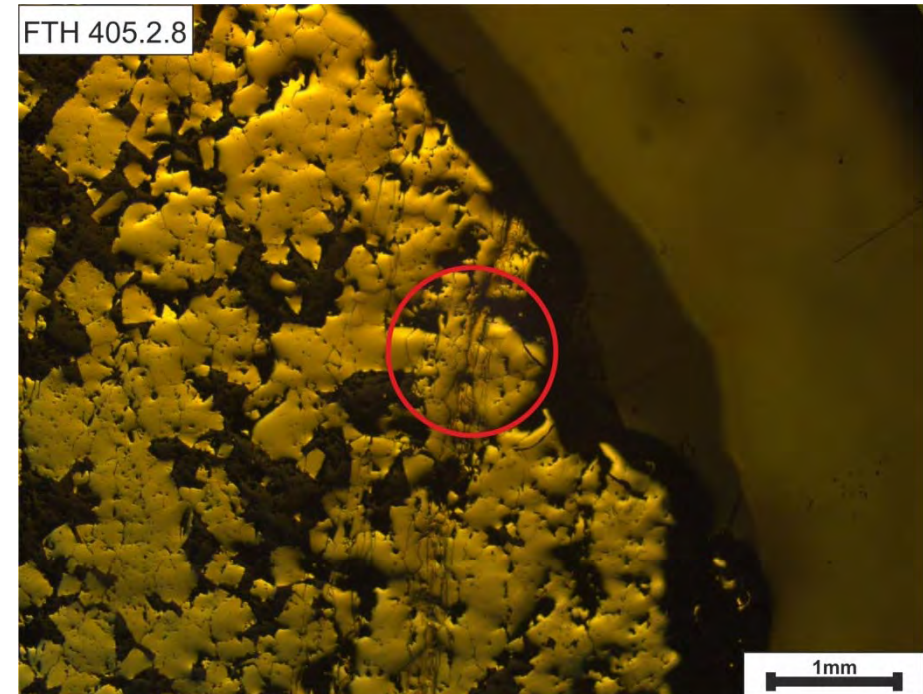
FTH 405.2.6



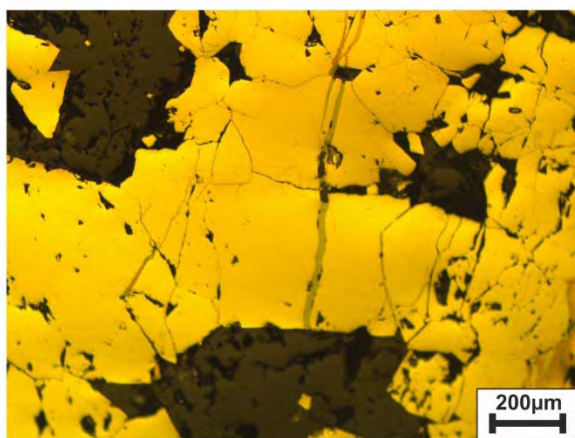
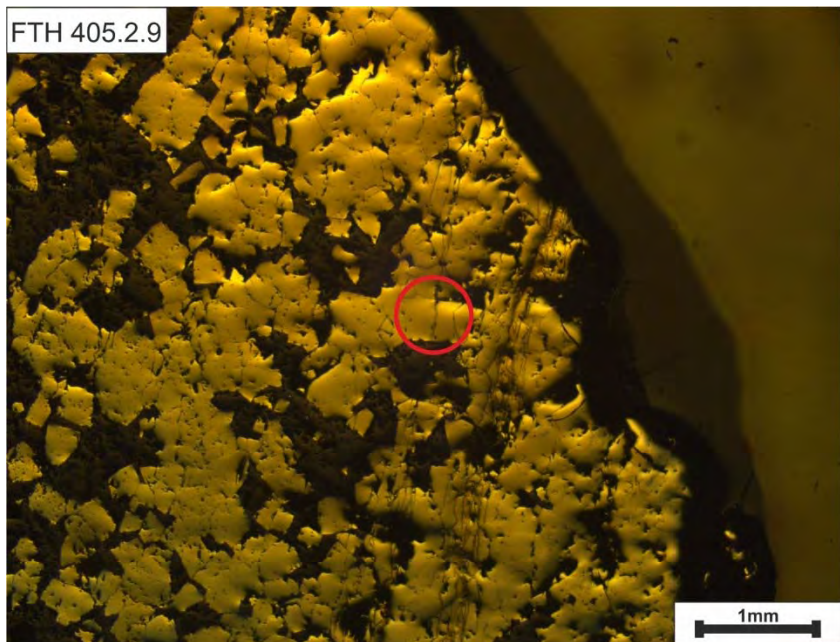
FTH 405.2.7



FTH 405.2.8



FTH 405.2.9

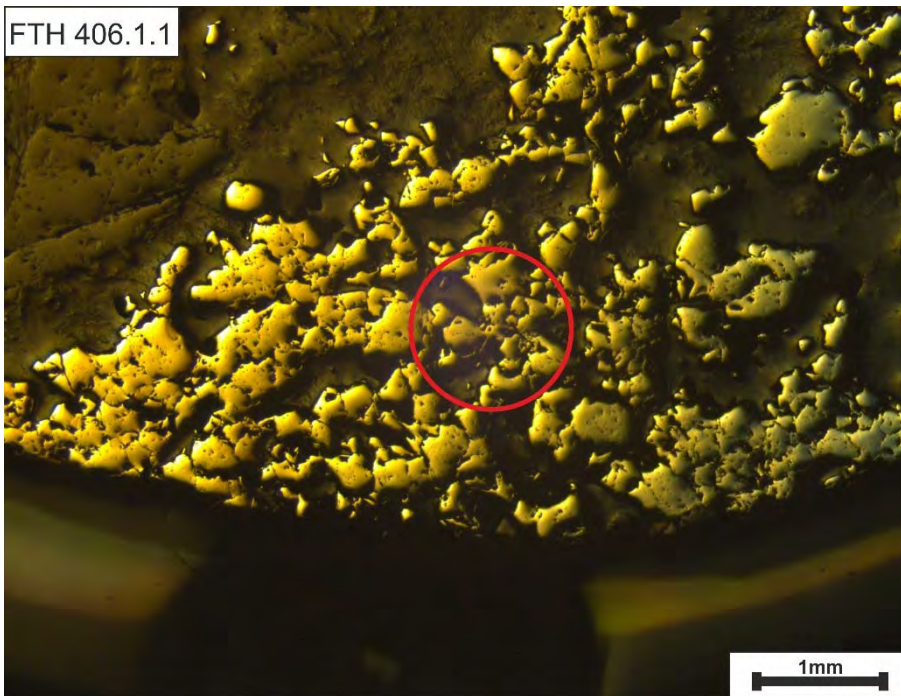


Quartz-carbonate vein

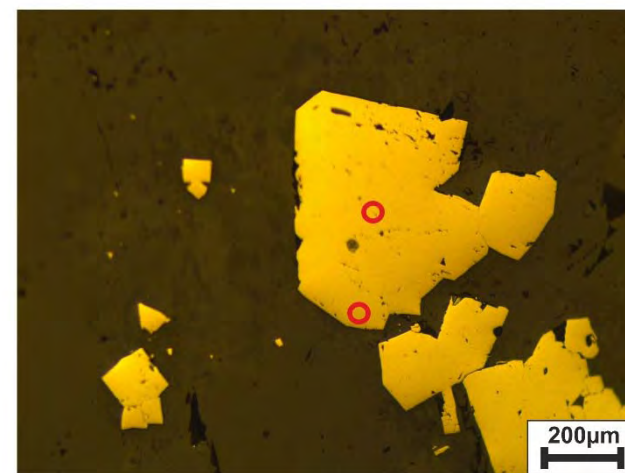
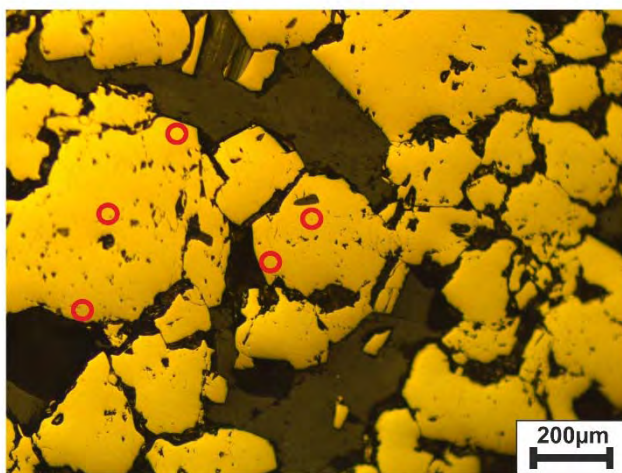
FTH 406.1



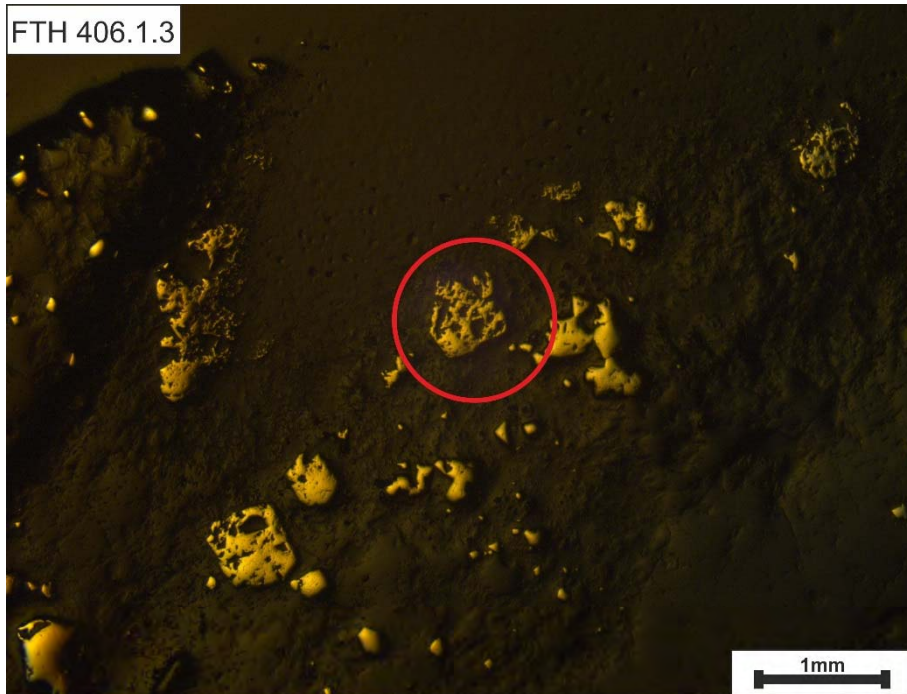
FTH 406.1.1



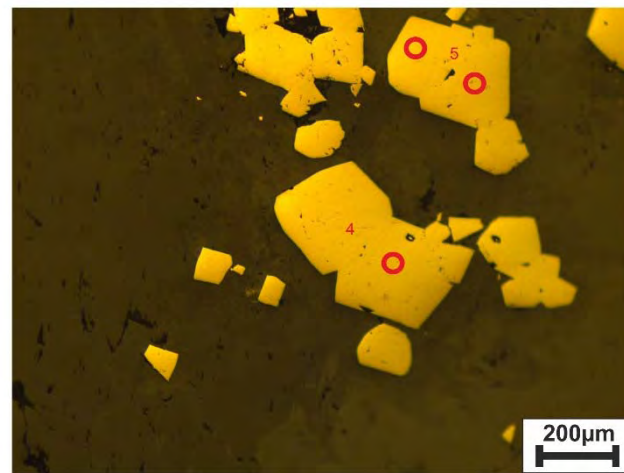
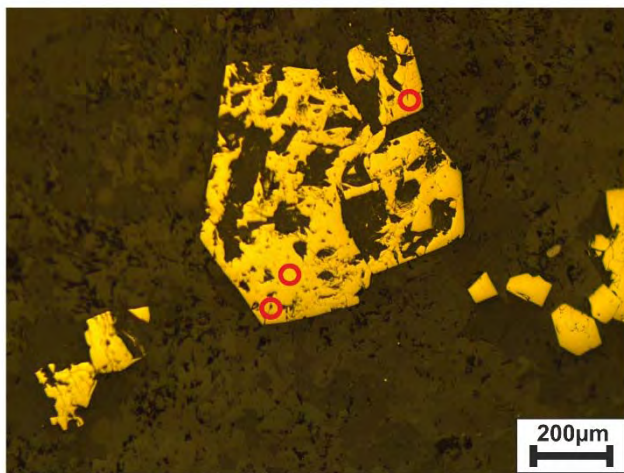
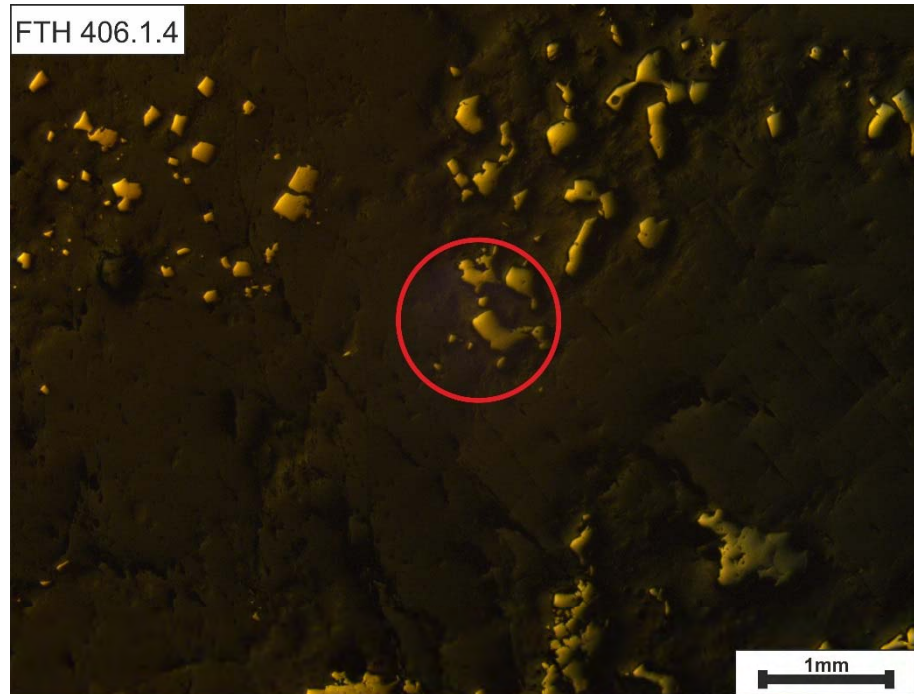
FTH 406.1.2



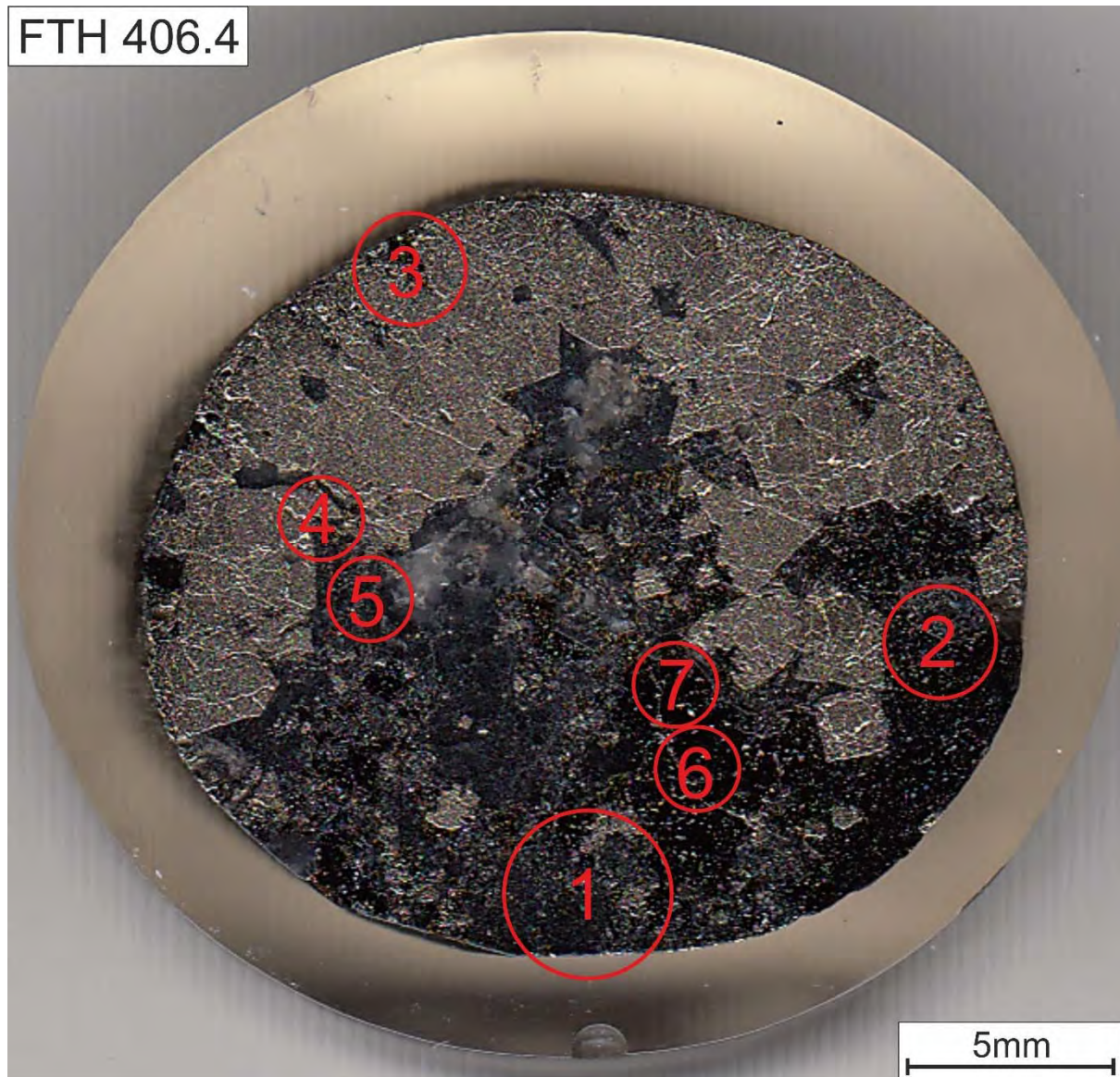
FTH 406.1.3



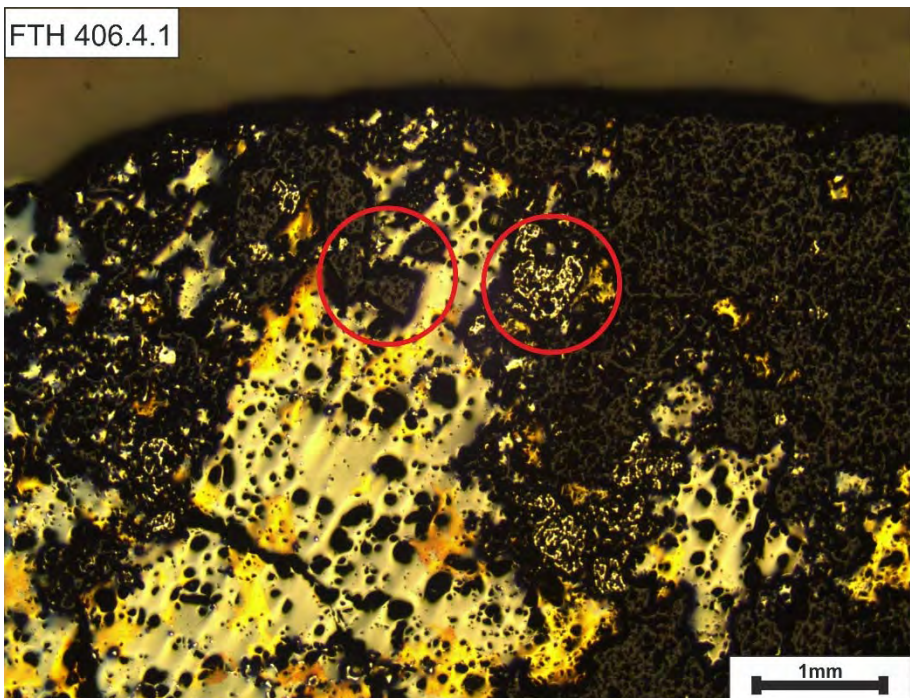
FTH 406.1.4



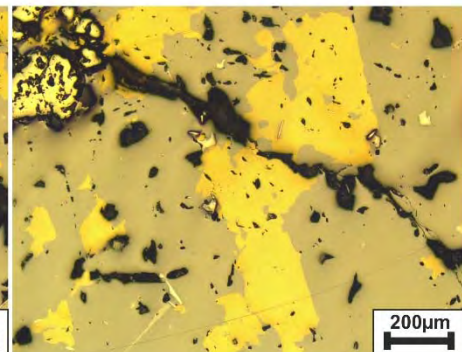
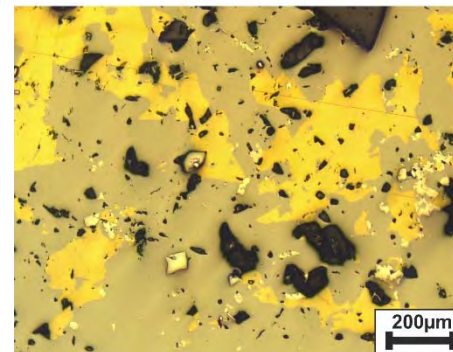
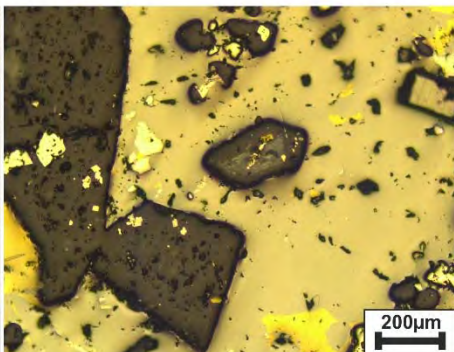
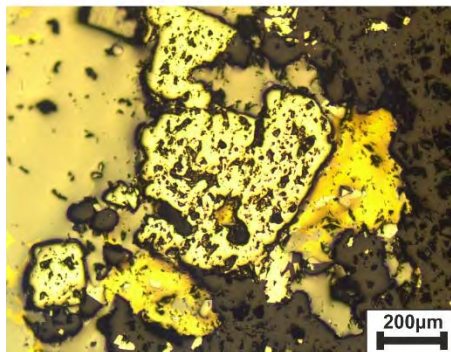
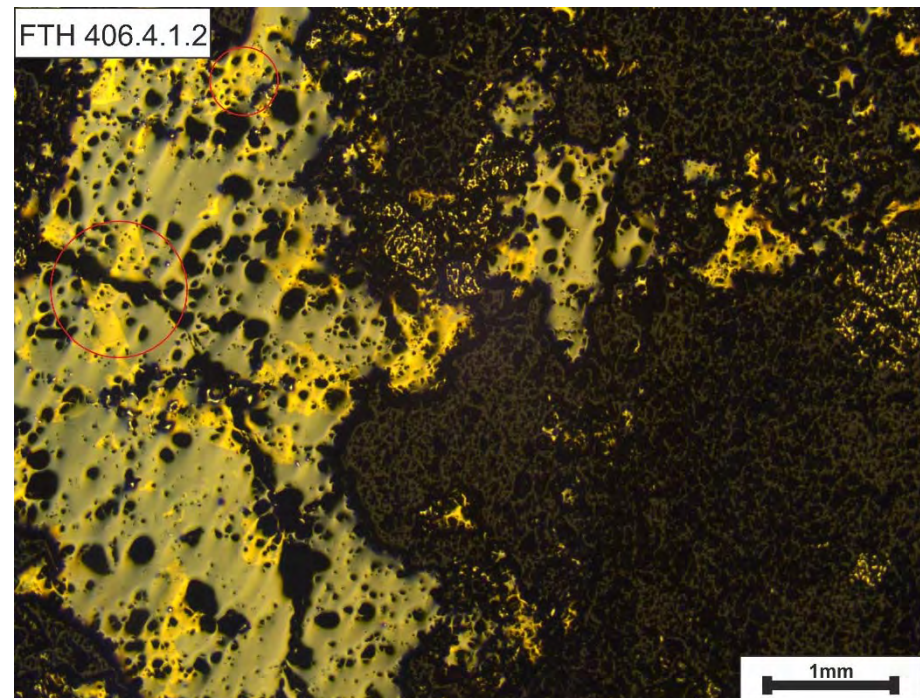
Quartz-carbonate-chert vein



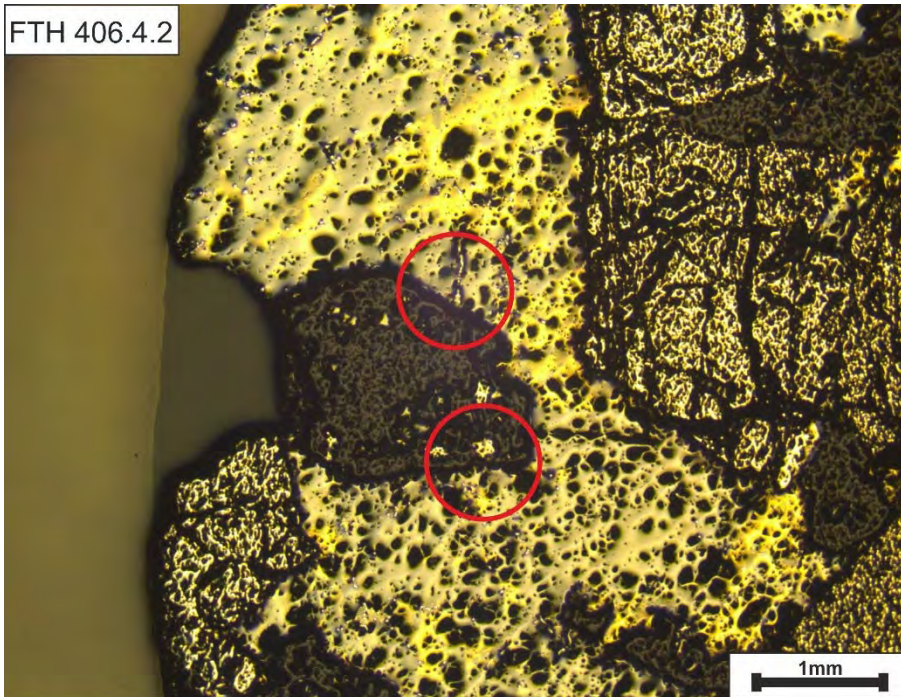
FTH 406.4.1



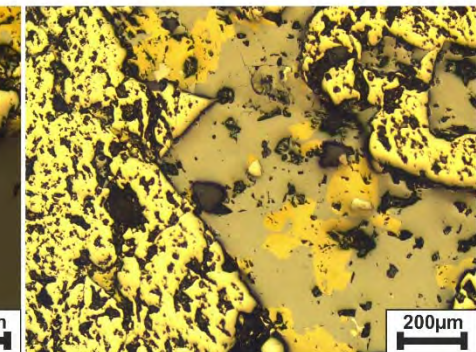
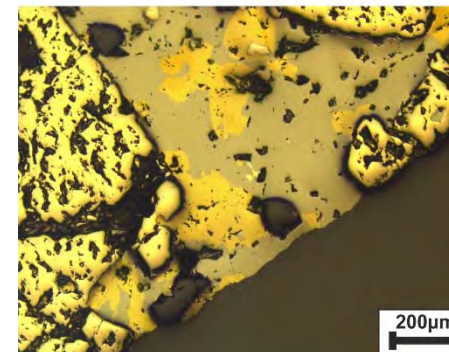
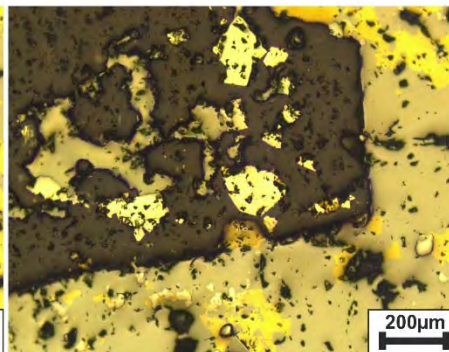
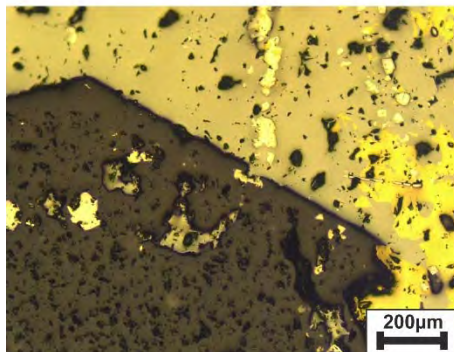
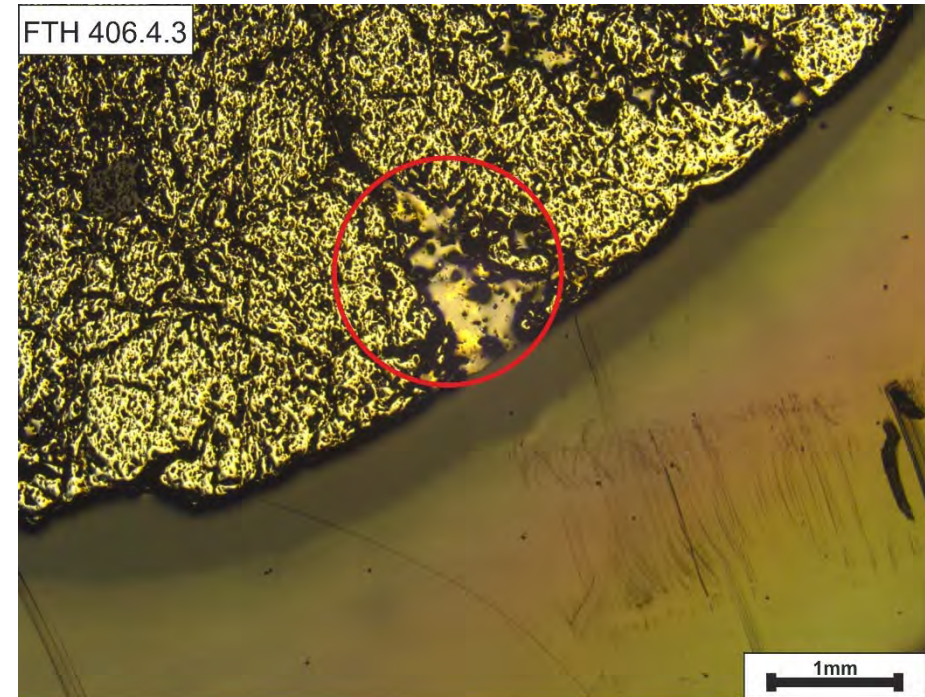
FTH 406.4.1.2



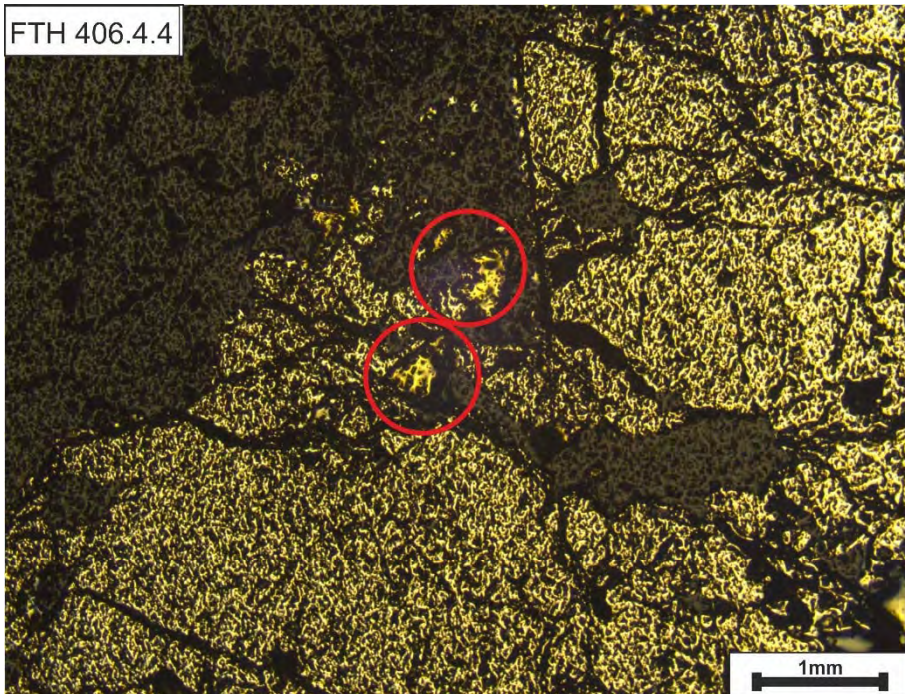
FTH 406.4.2



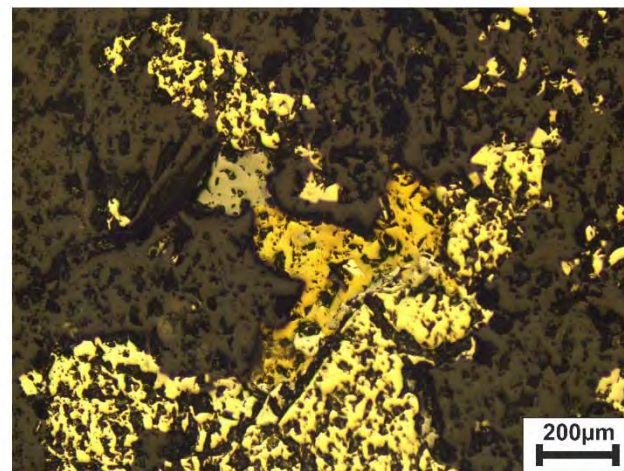
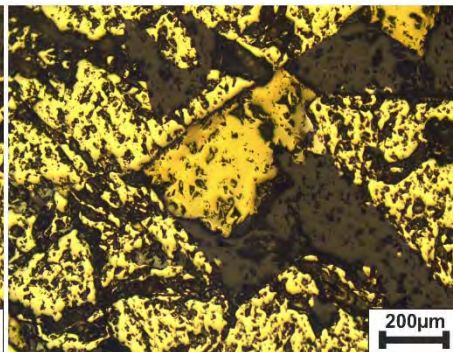
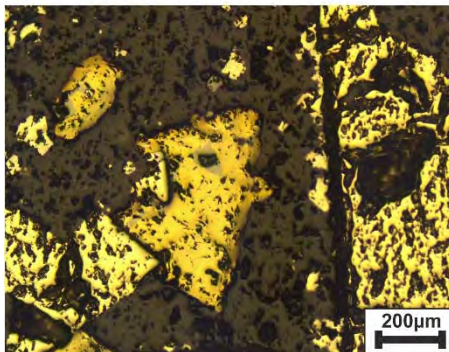
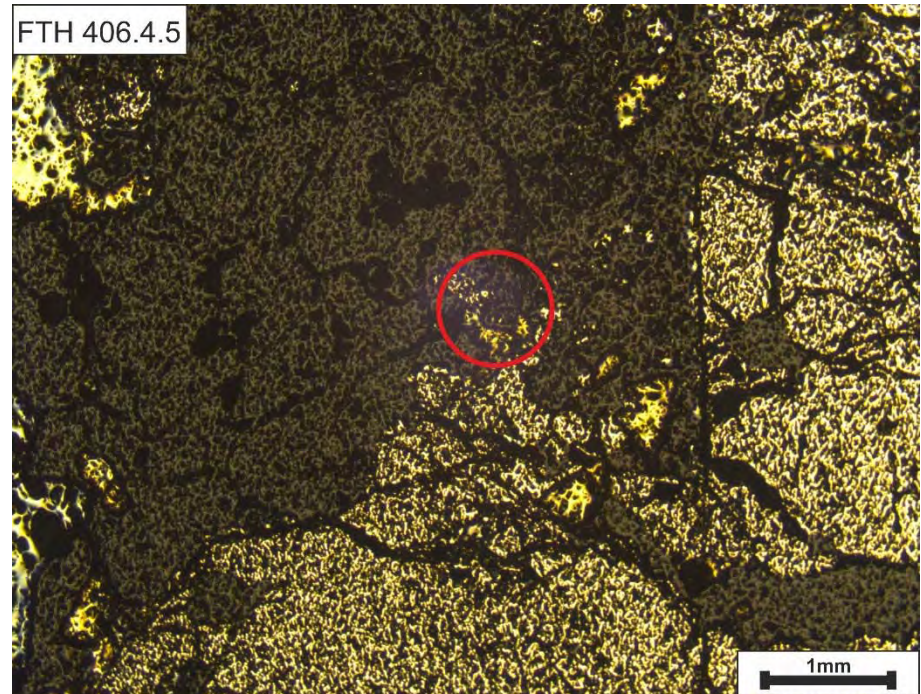
FTH 406.4.3



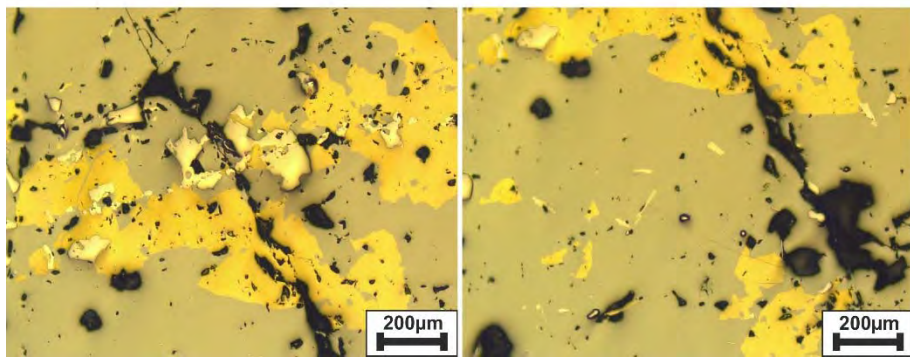
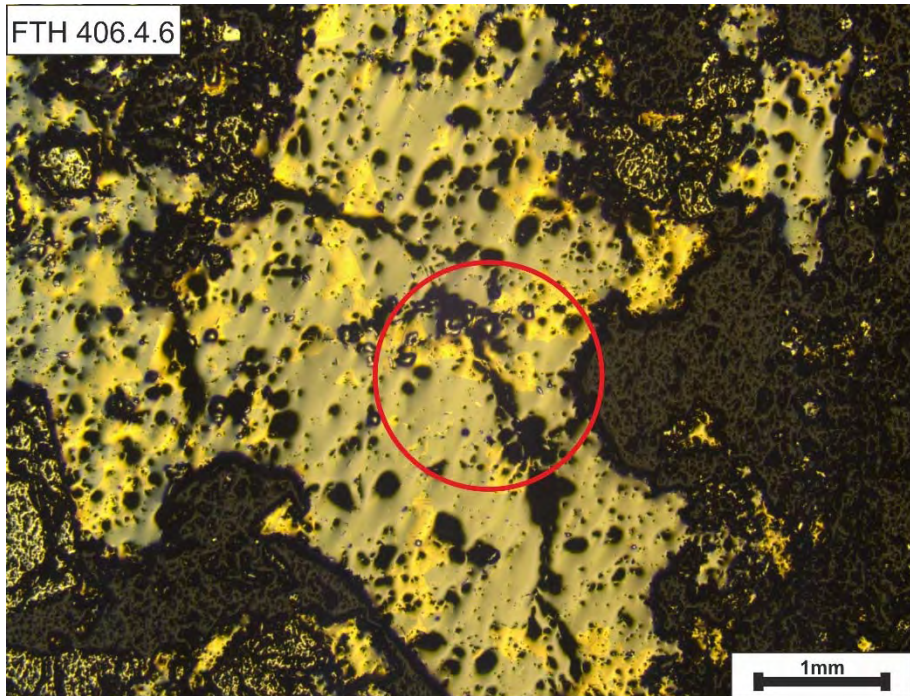
FTH 406.4.4



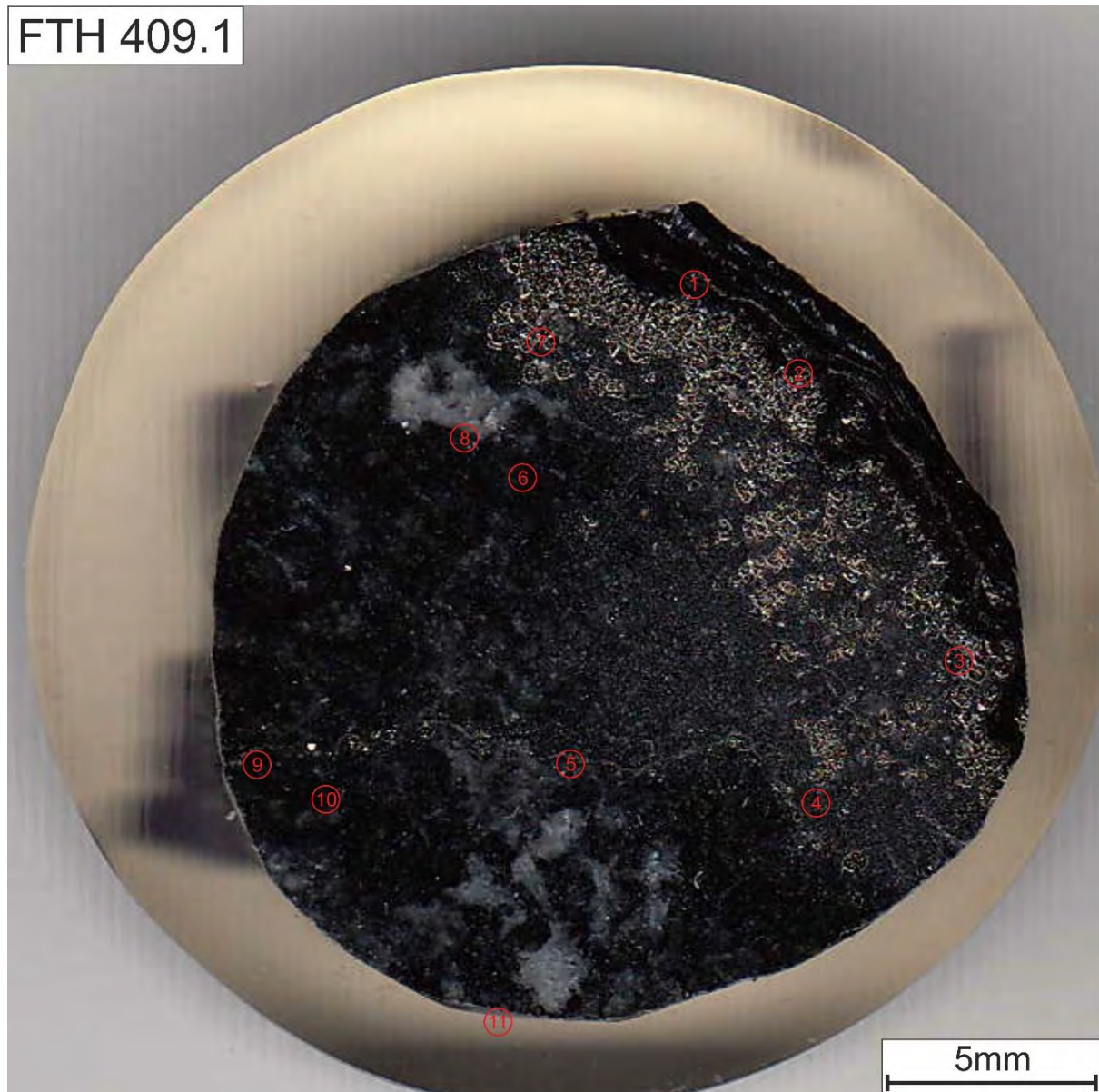
FTH 406.4.5



FTH 406.4.6



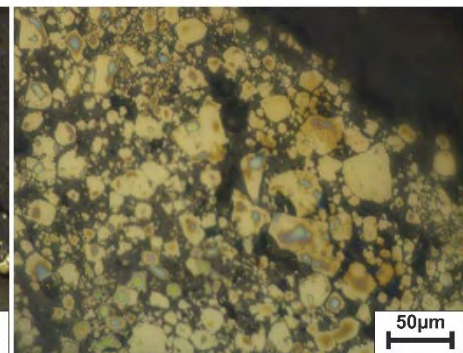
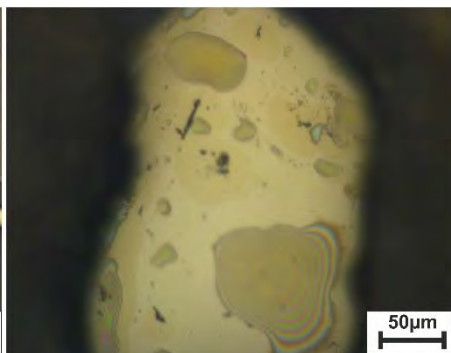
Quartz-carbonate-chert vein and graphitic mudrock

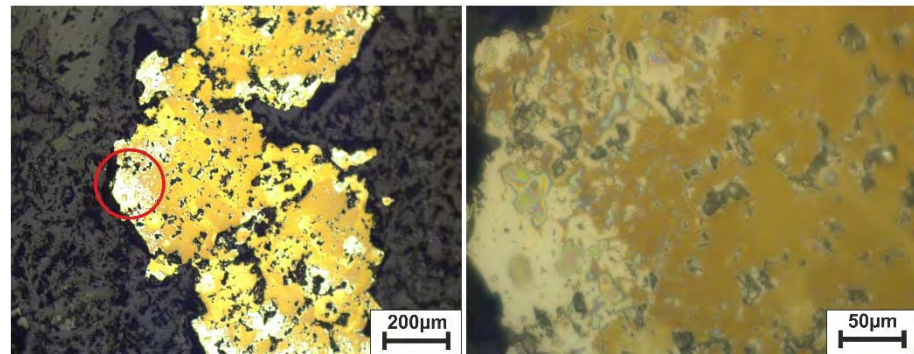
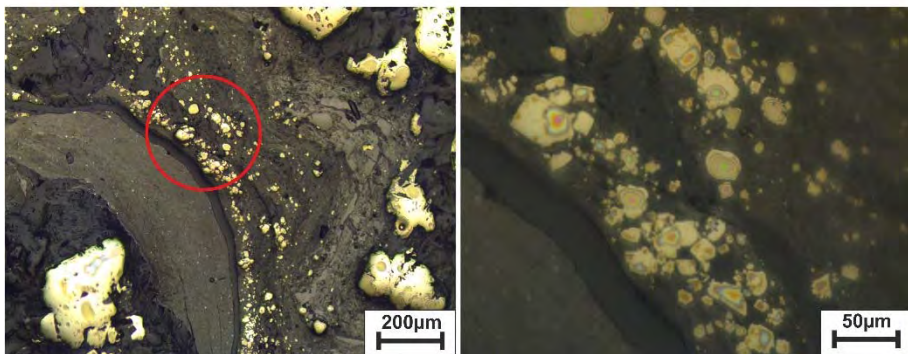
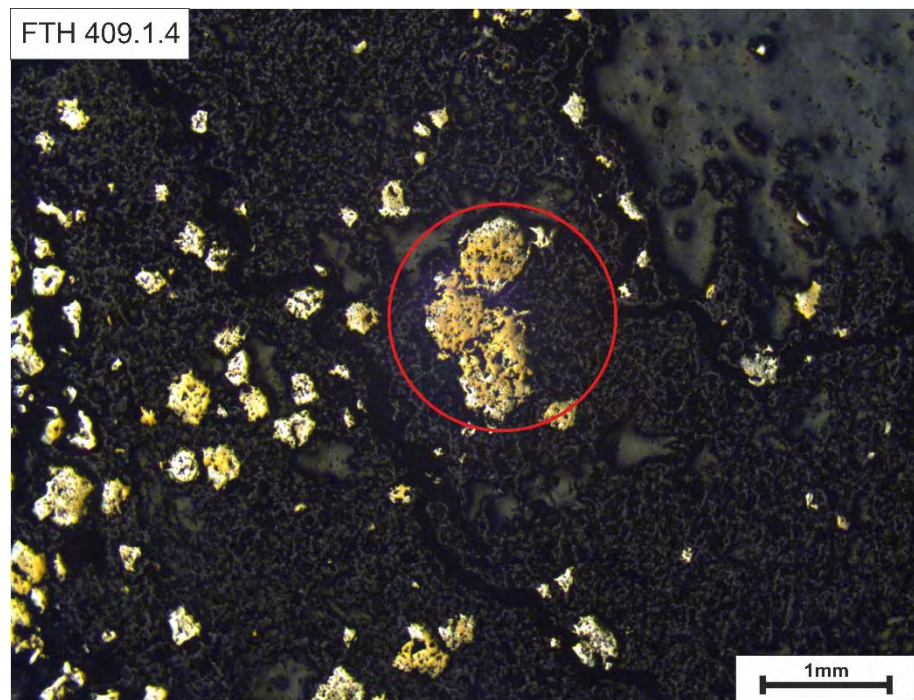
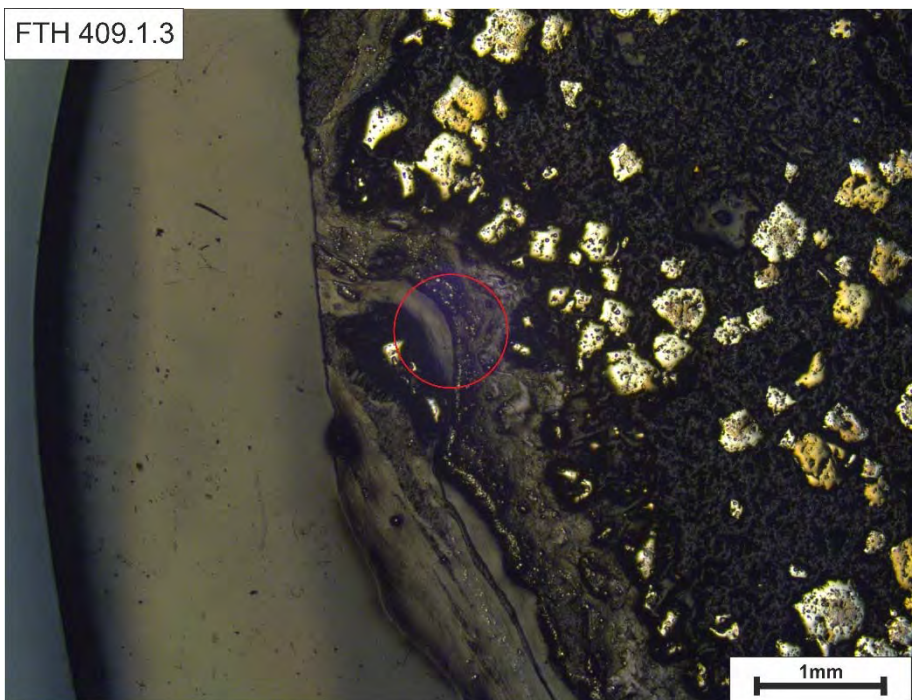


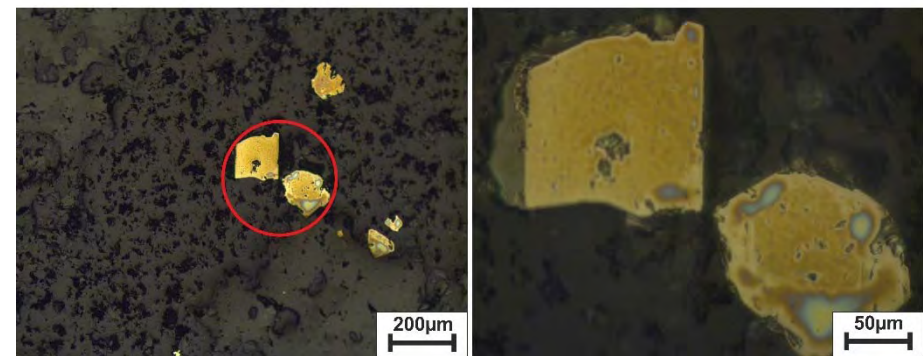
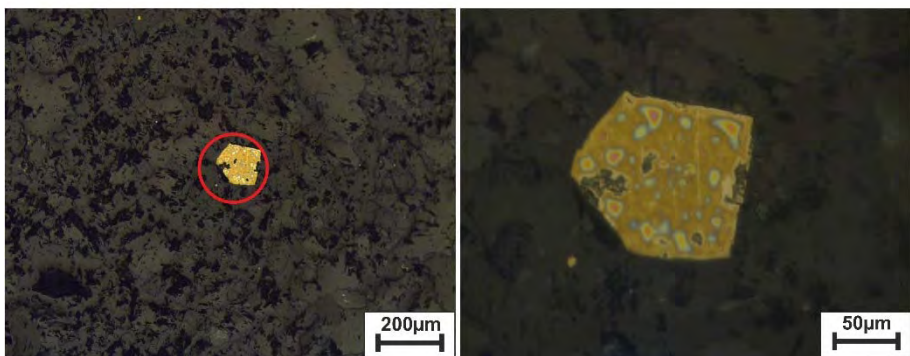
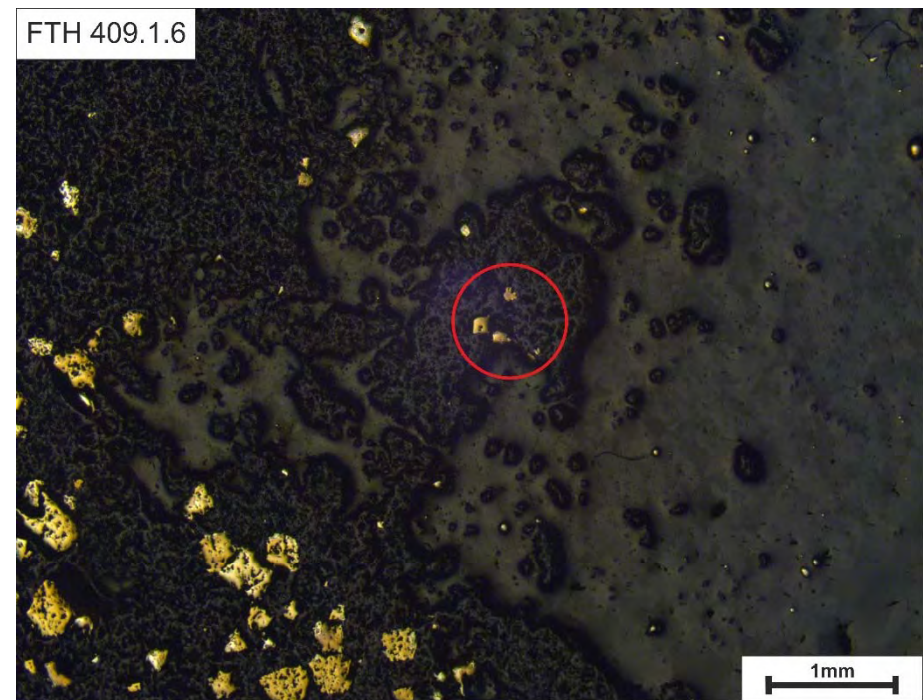
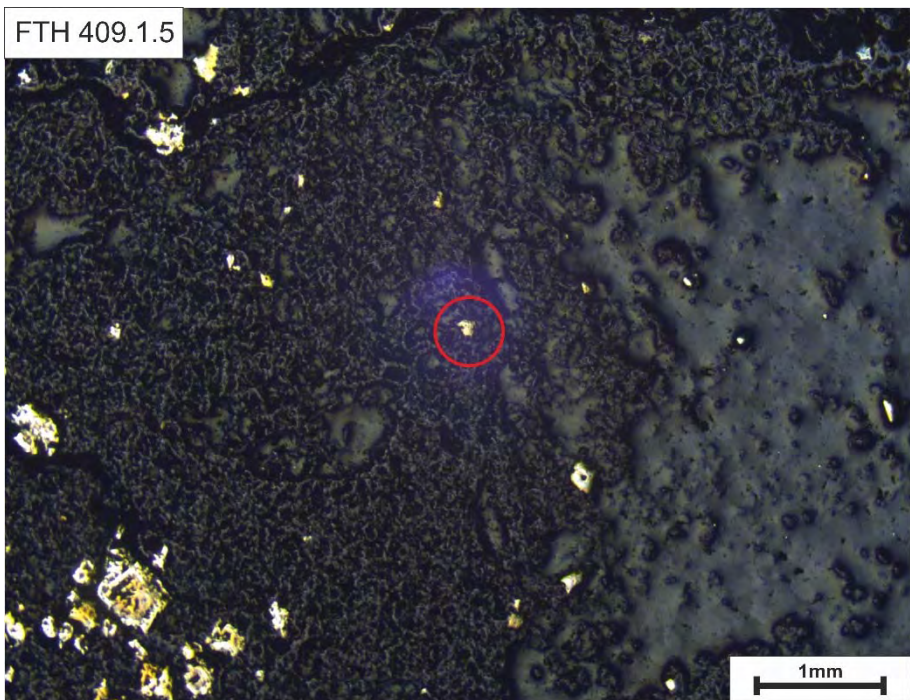
FTH 409.1.1

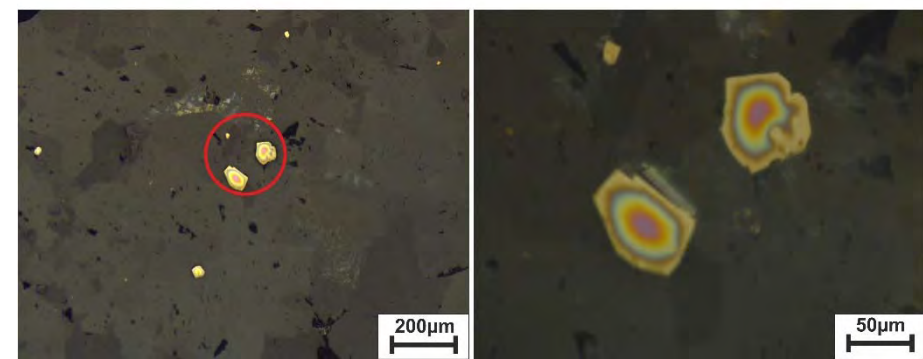
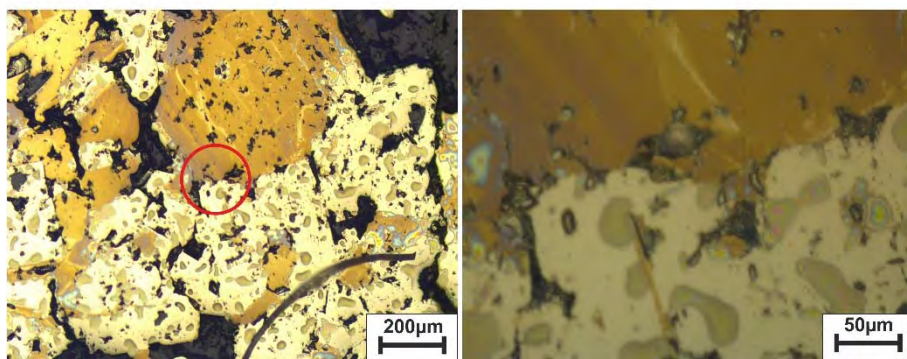


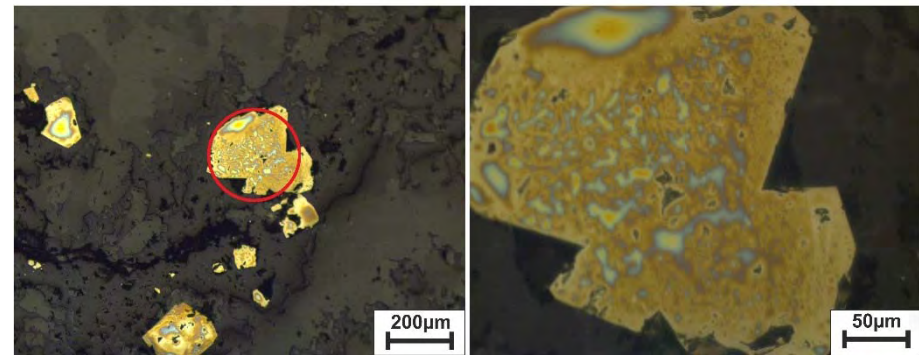
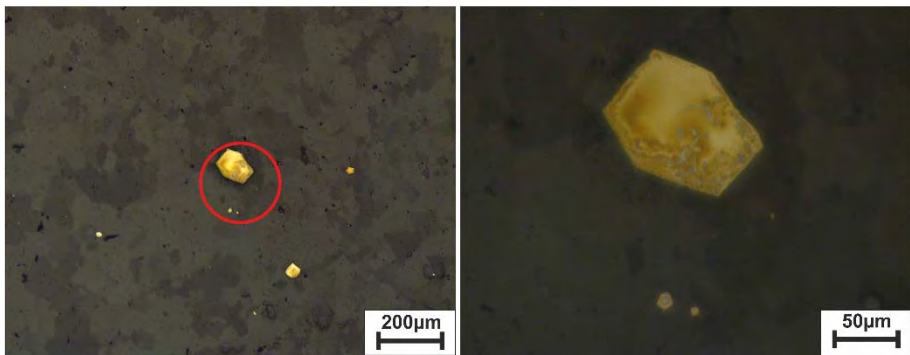
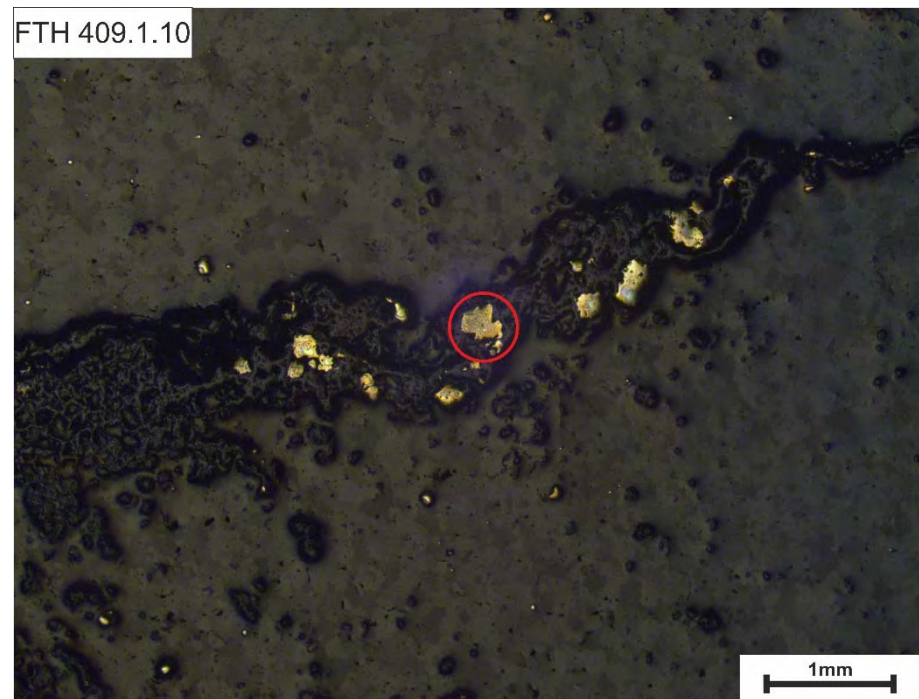
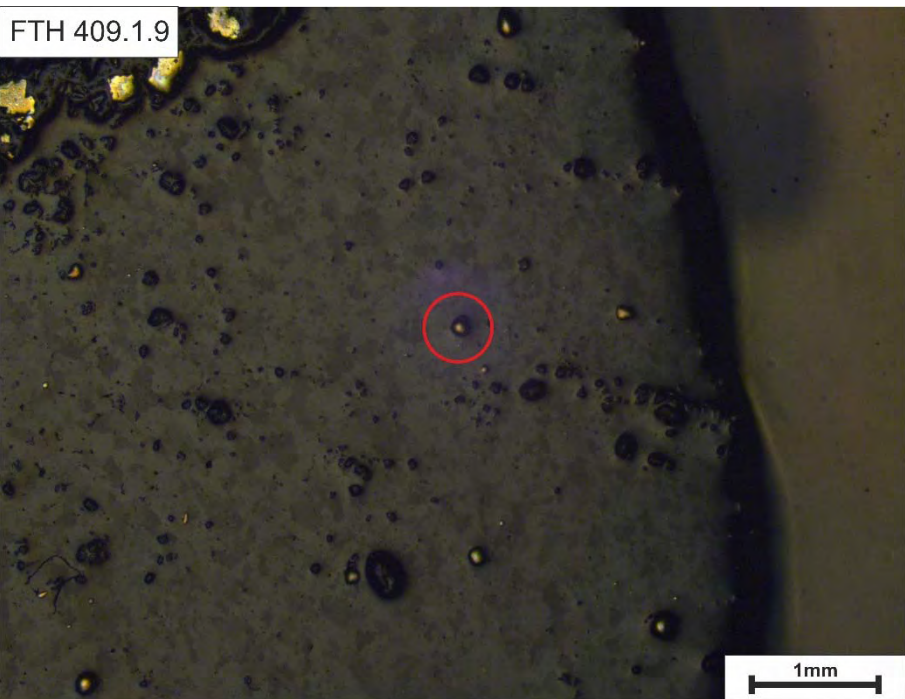
FTH 409.1.2



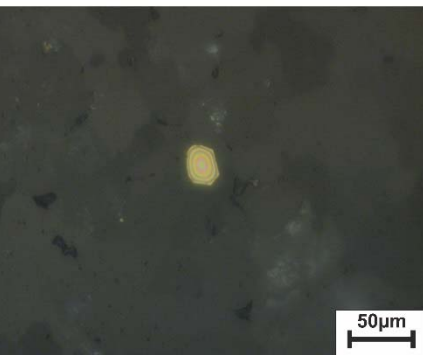
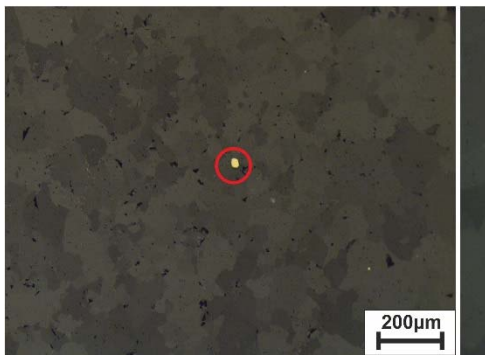
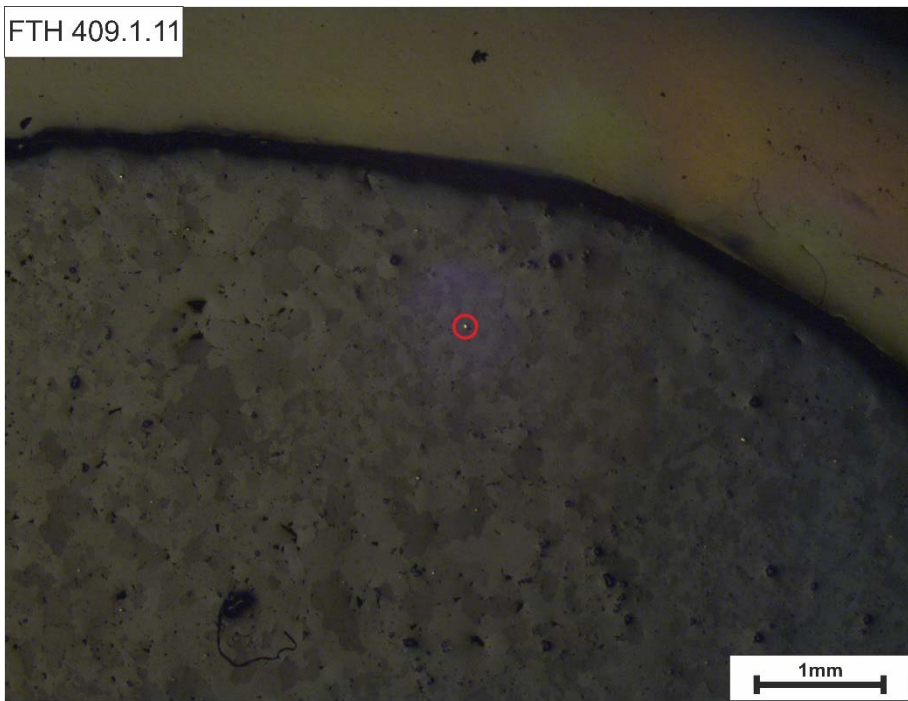








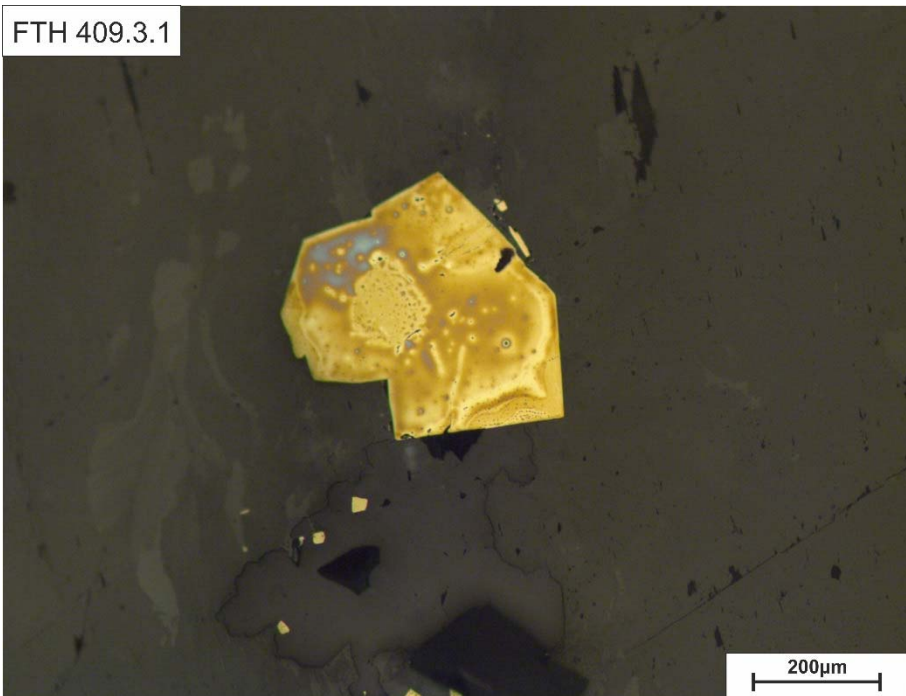
FTH 409.1.11



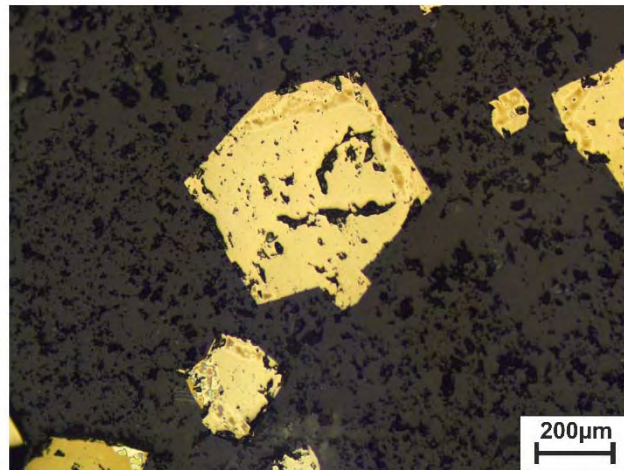
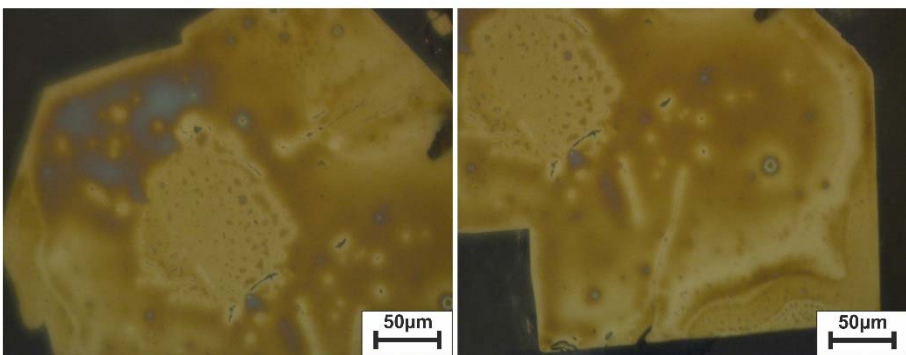
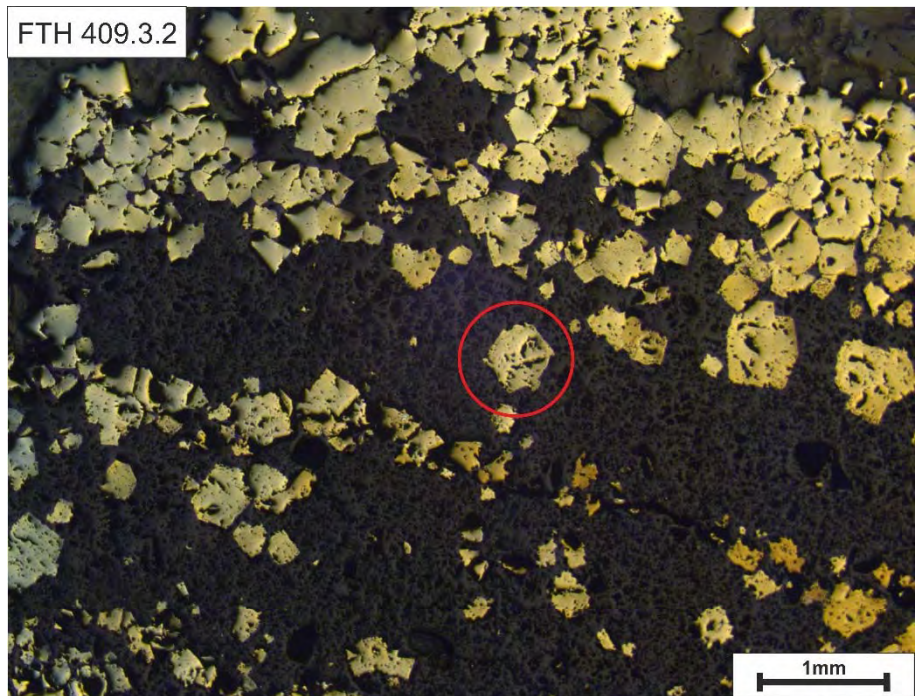
Quartz-carbonate vein and mineralized stromatolite



FTH 409.3.1



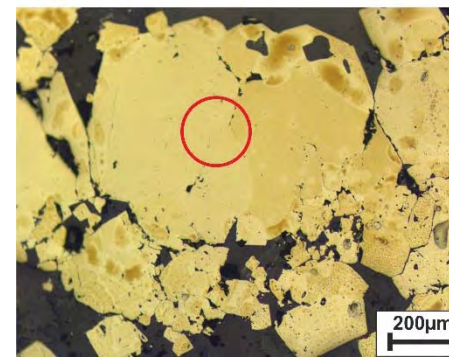
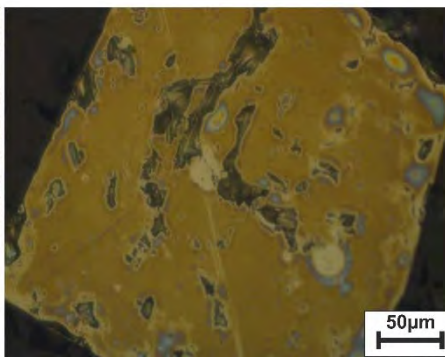
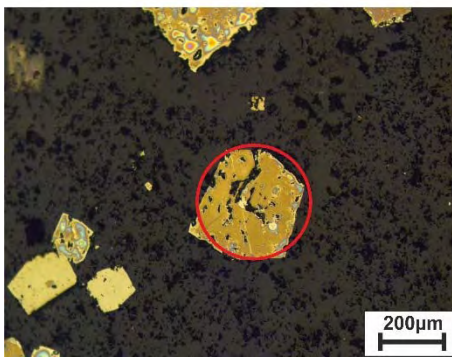
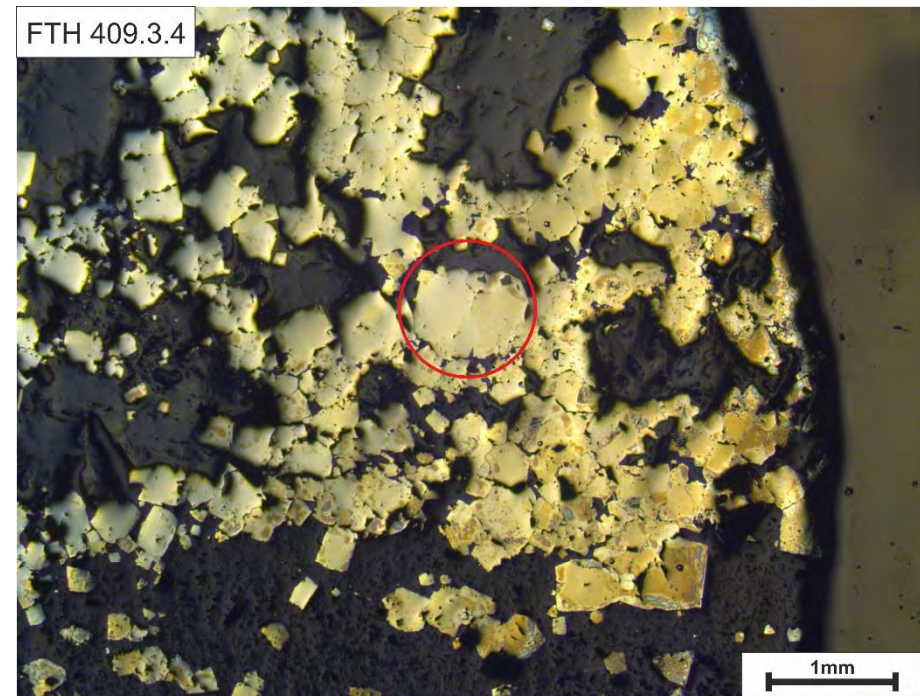
FTH 409.3.2



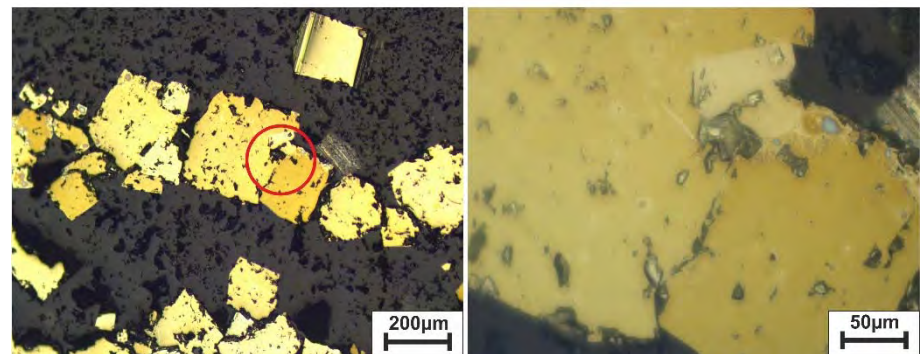
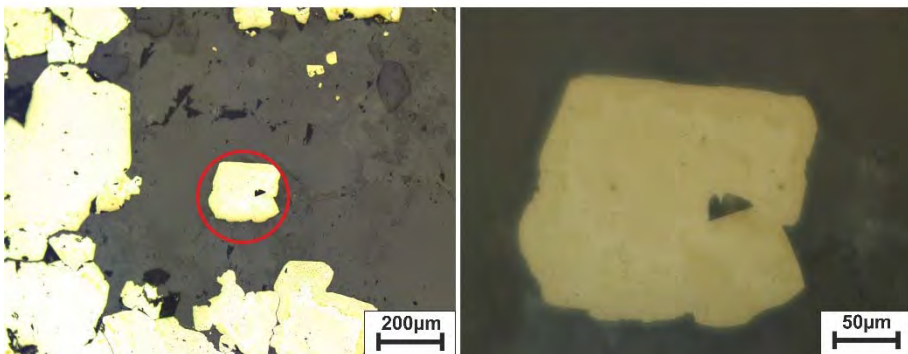
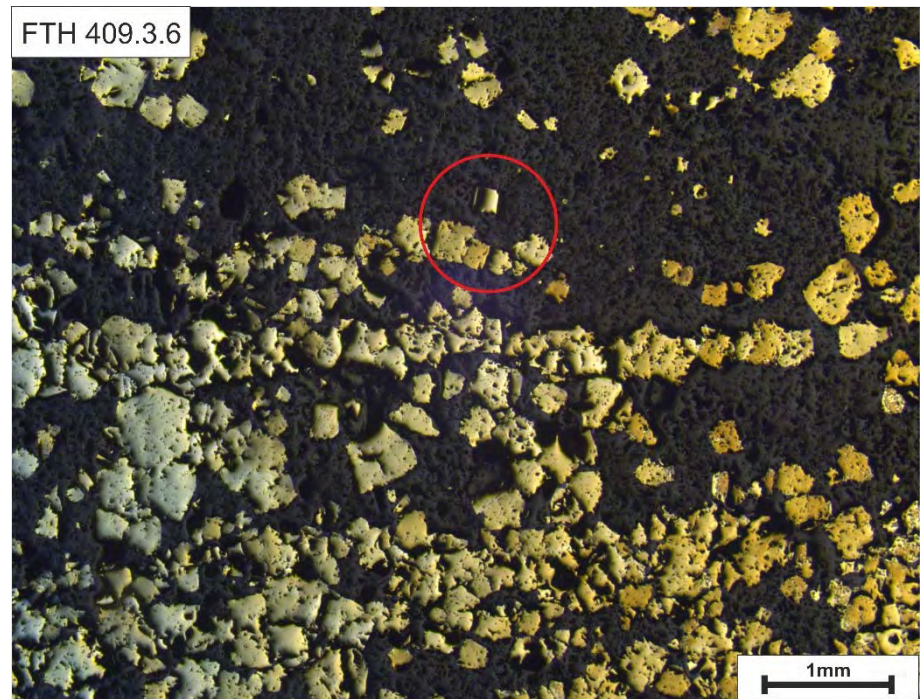
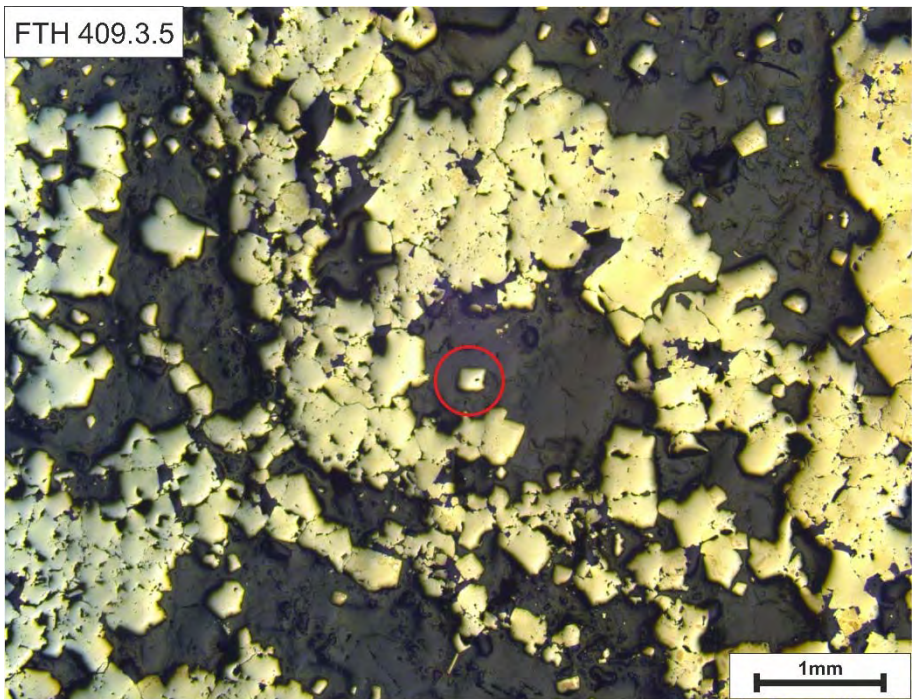
FTH 409.3.3

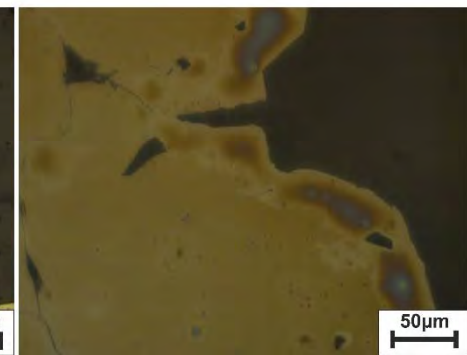
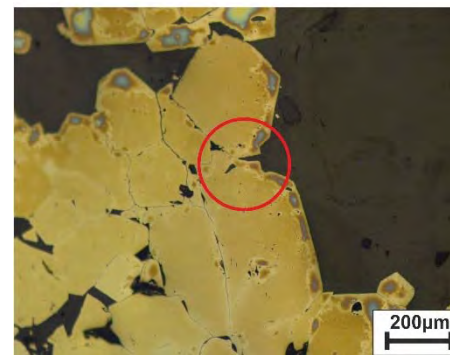
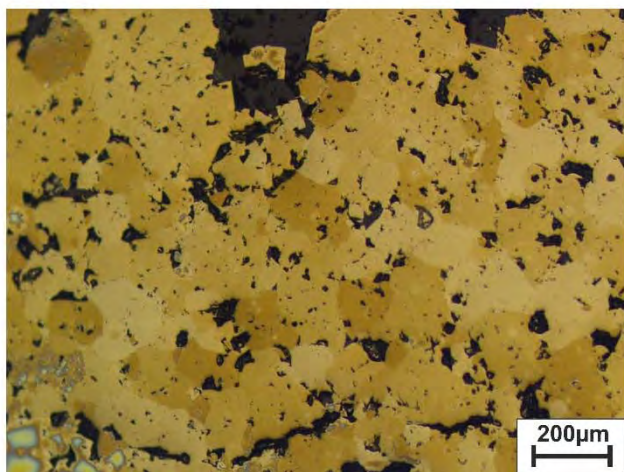
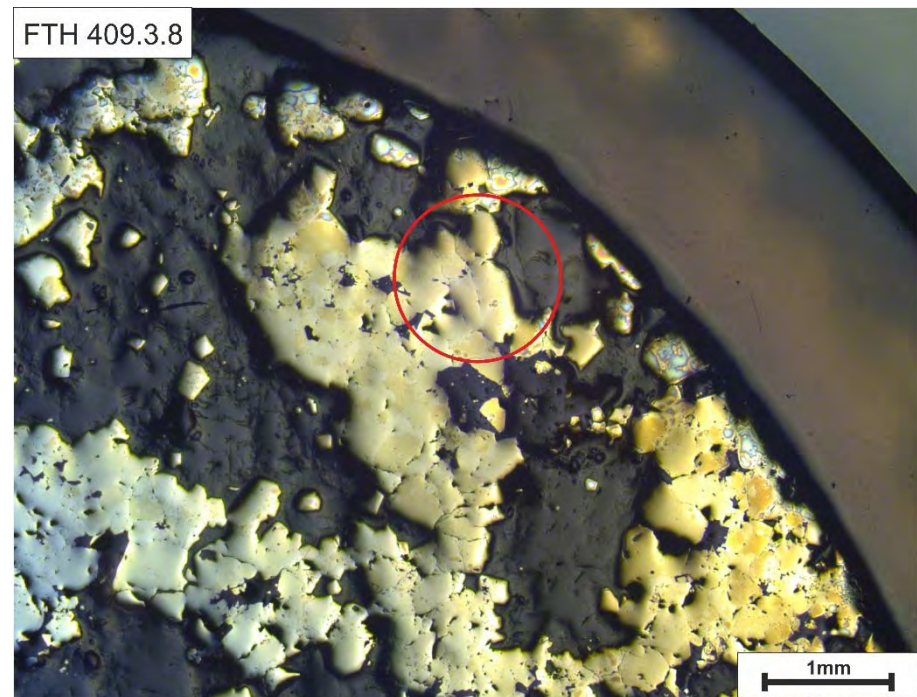
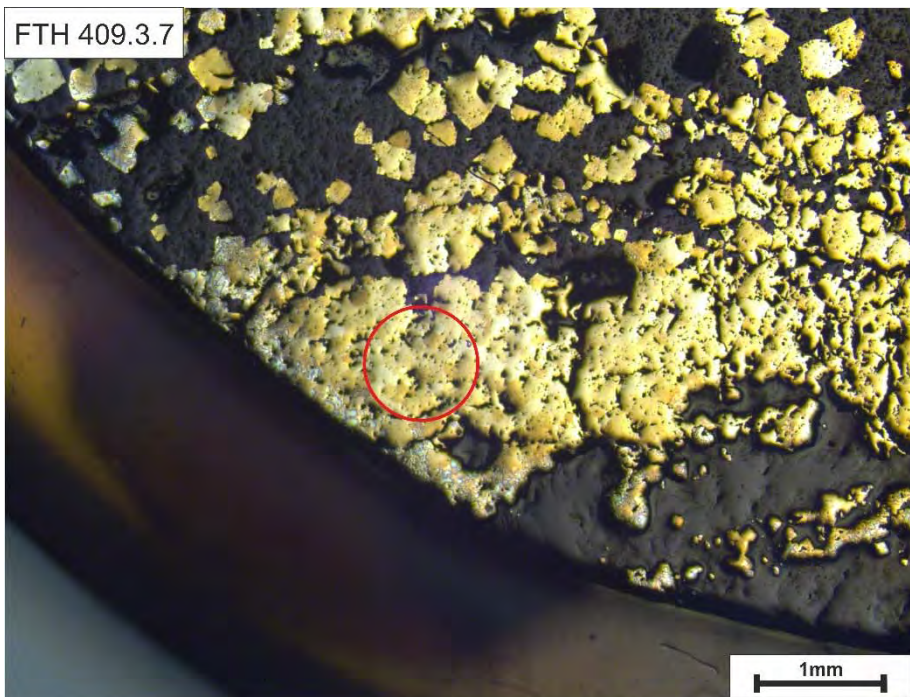


FTH 409.3.4

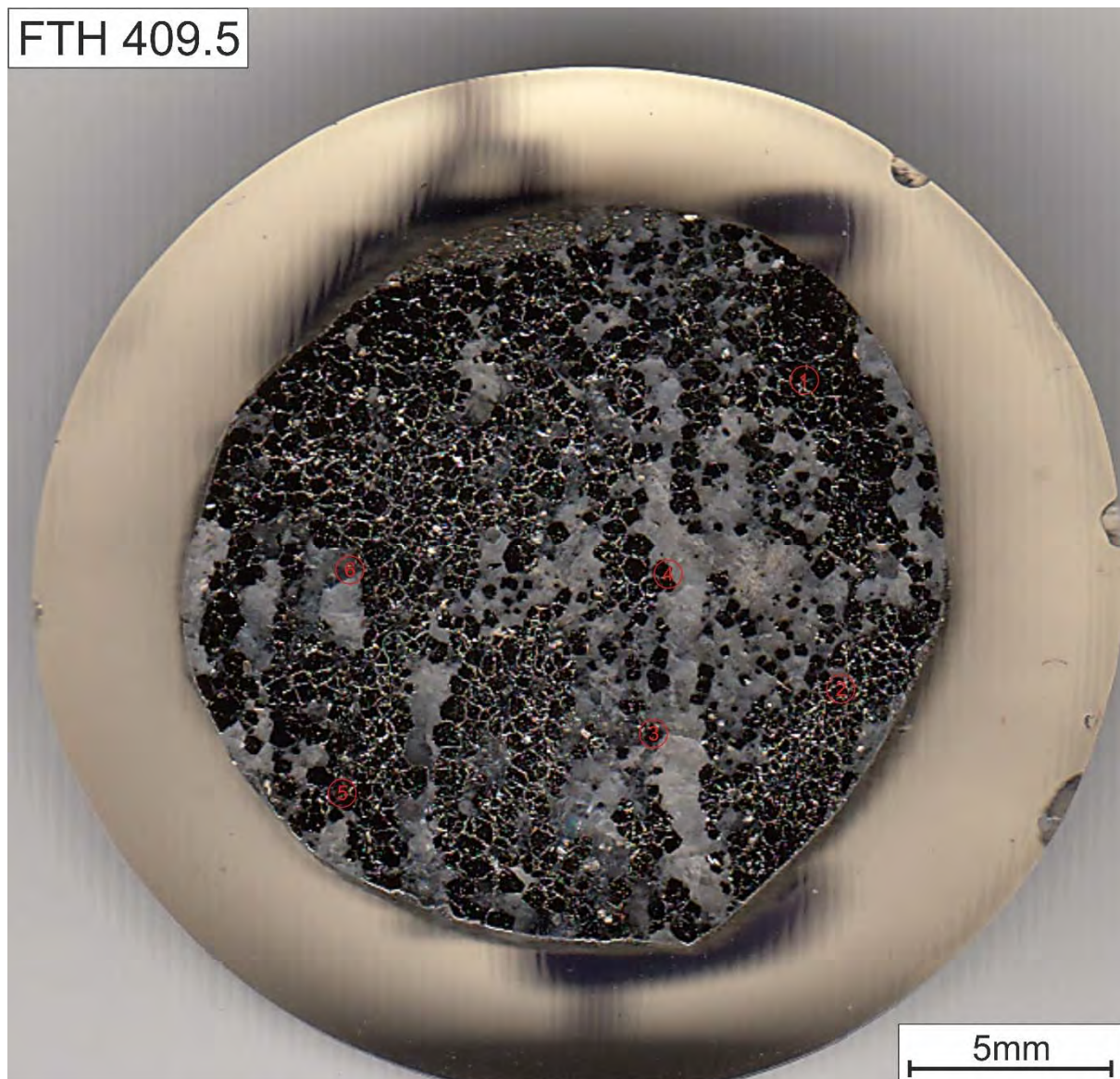


50µm





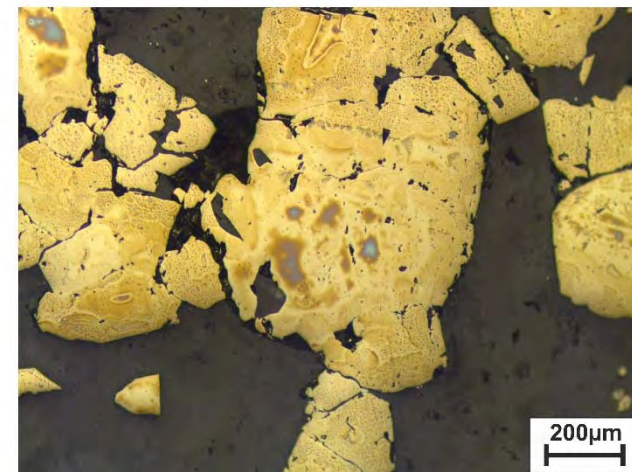
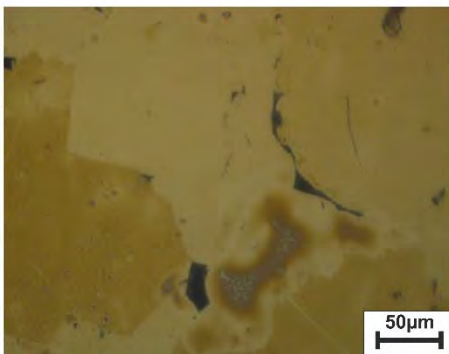
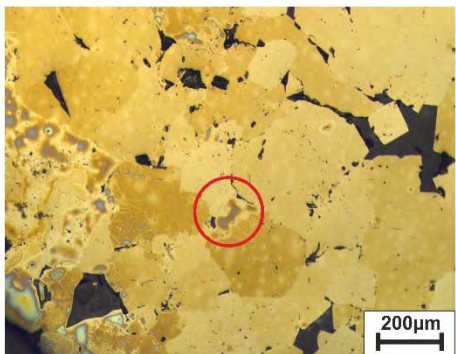
Quartz-carbonate vein



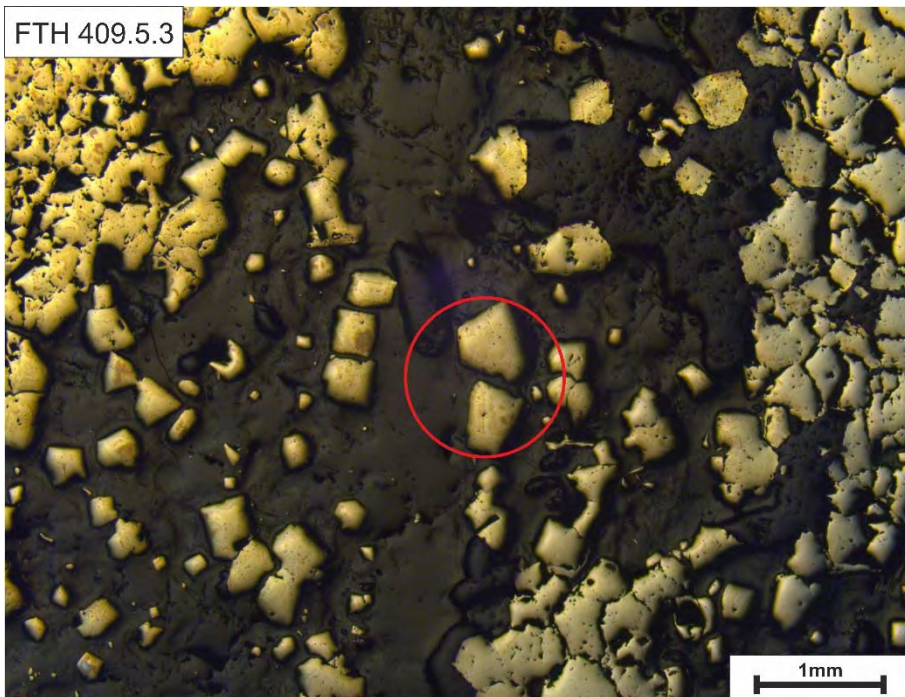
FTH 409.5.1



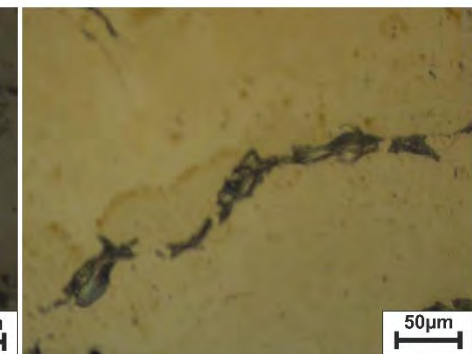
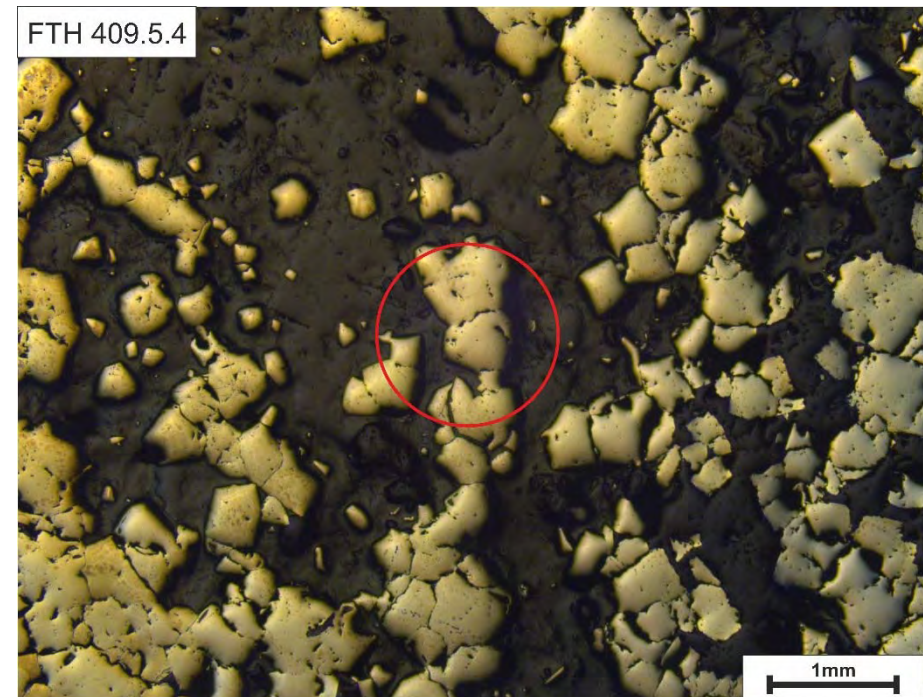
FTH 409.5.2

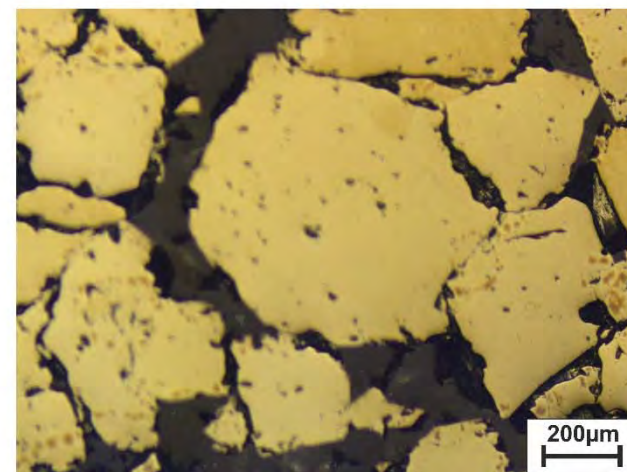
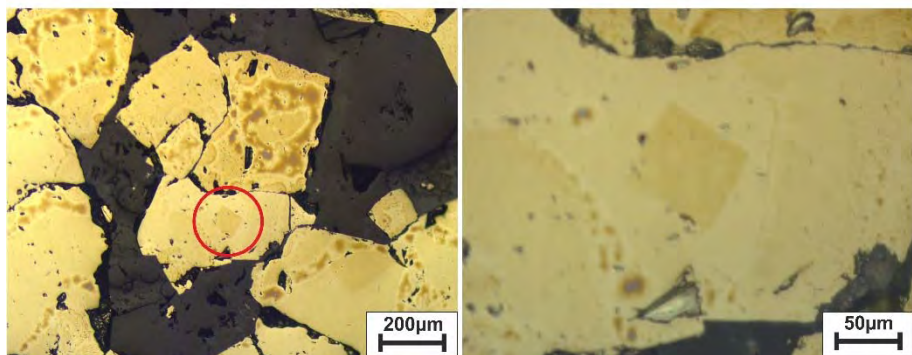
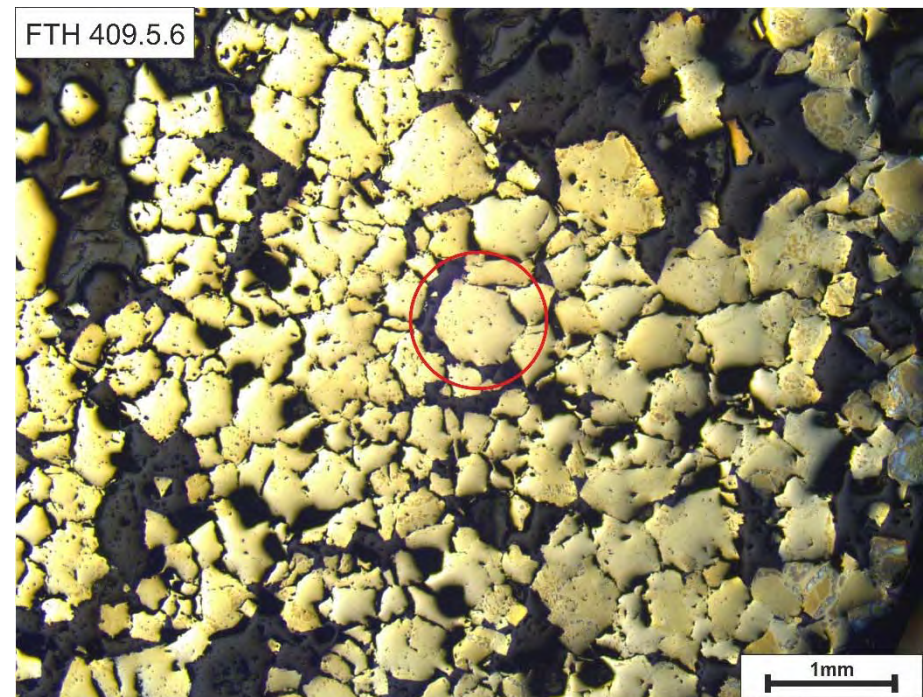


FTH 409.5.3

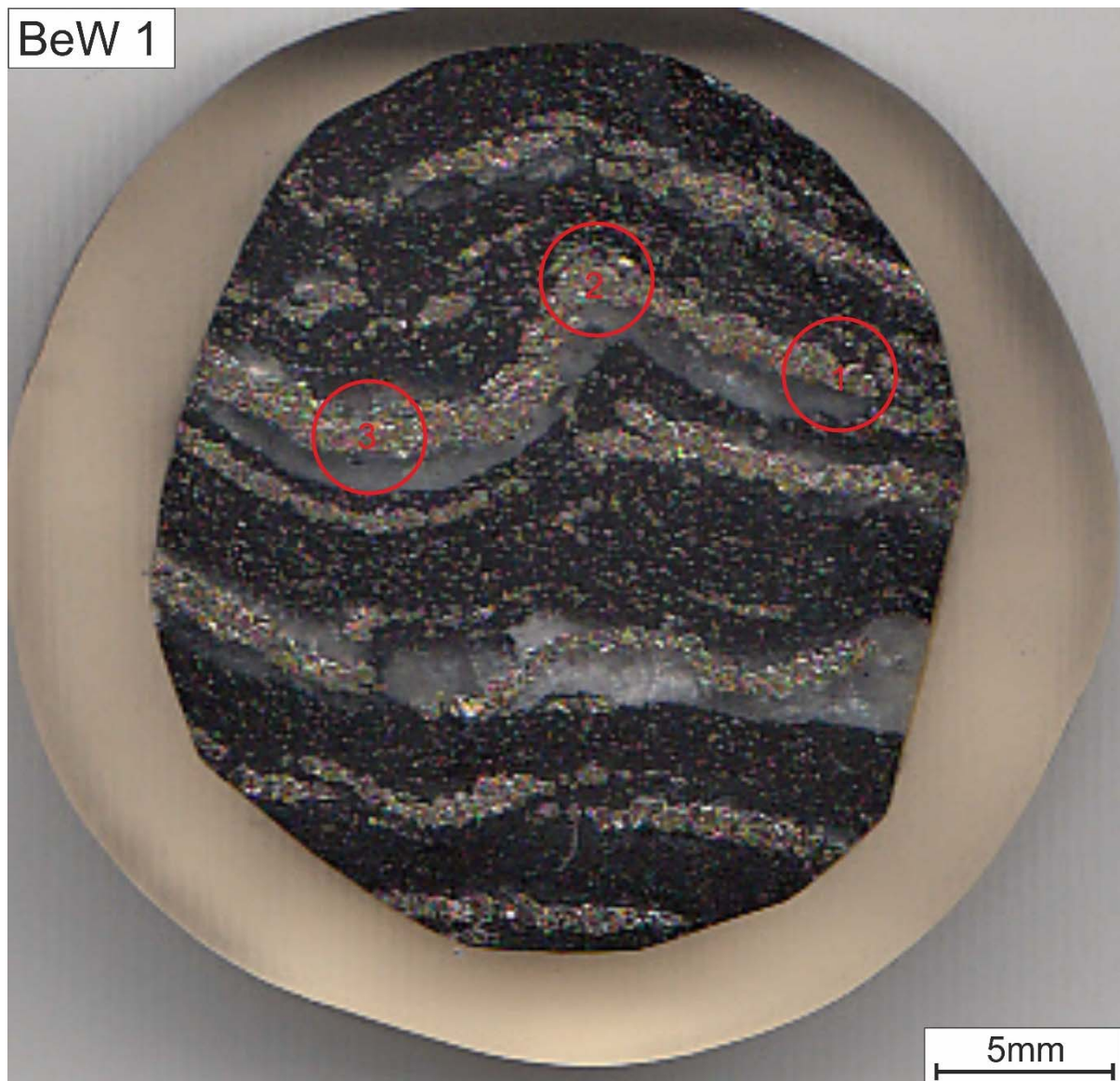


FTH 409.5.4



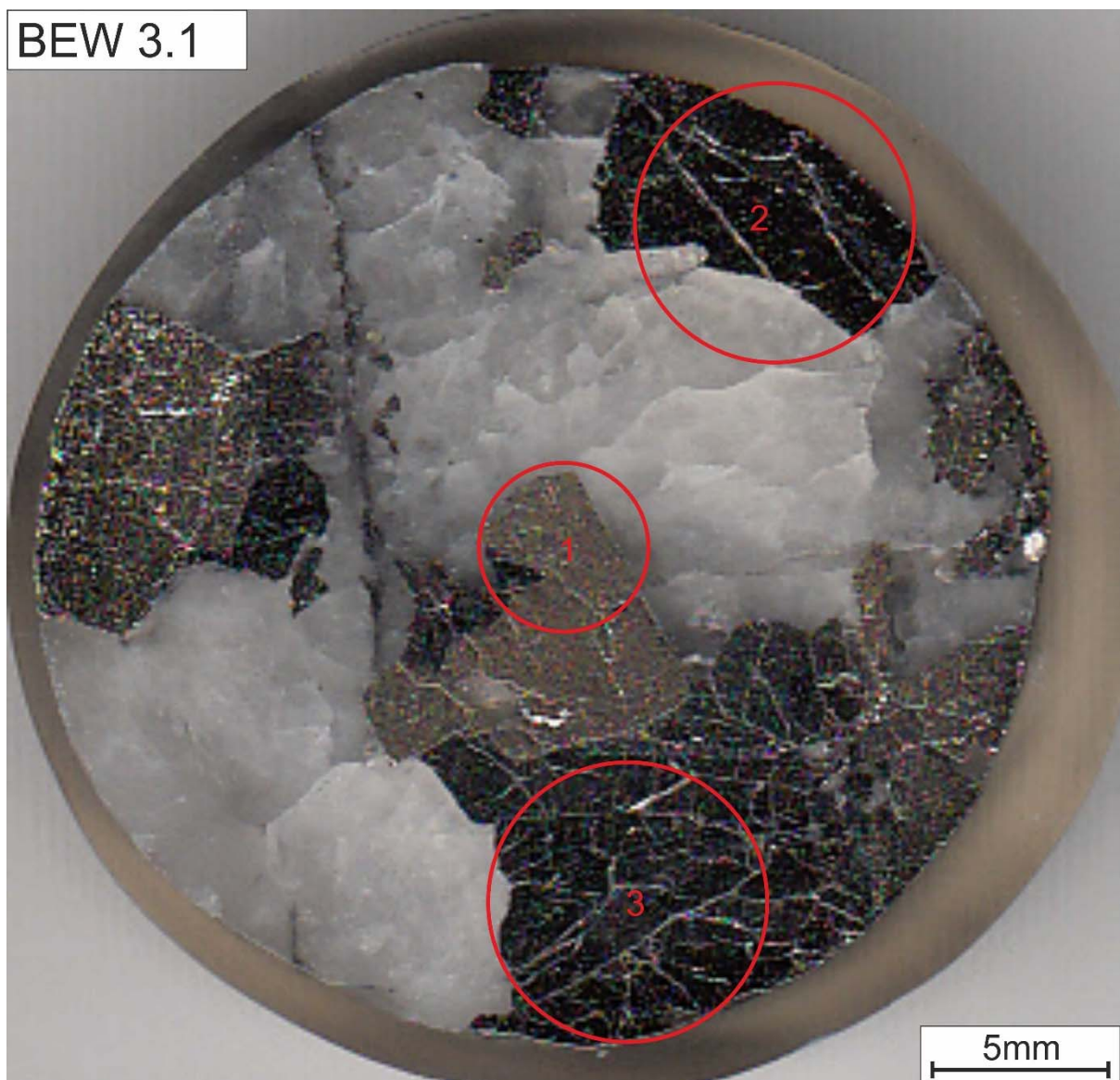


Mineralised black carbonaceous shale

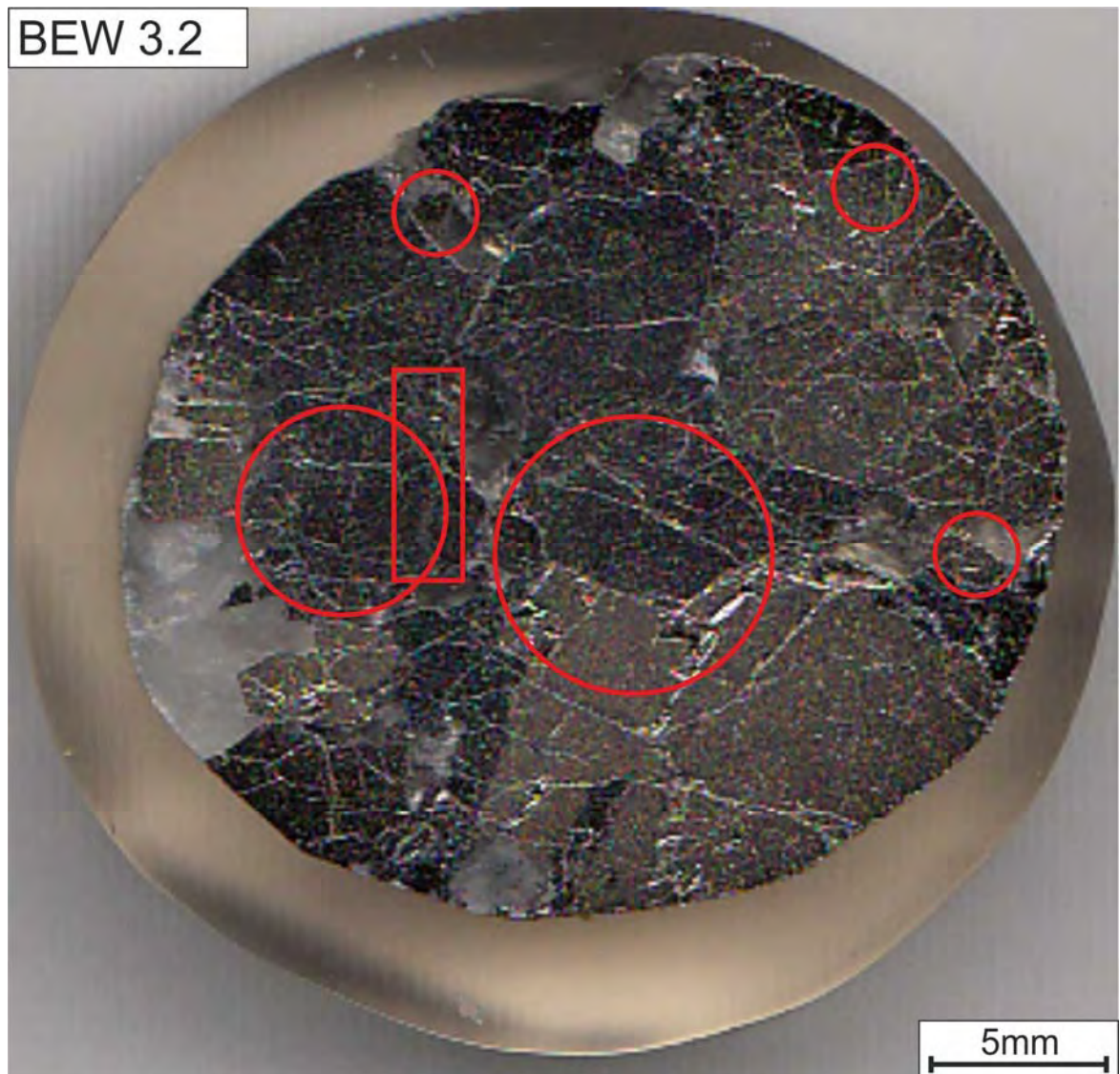


Quartz-carbonate vein

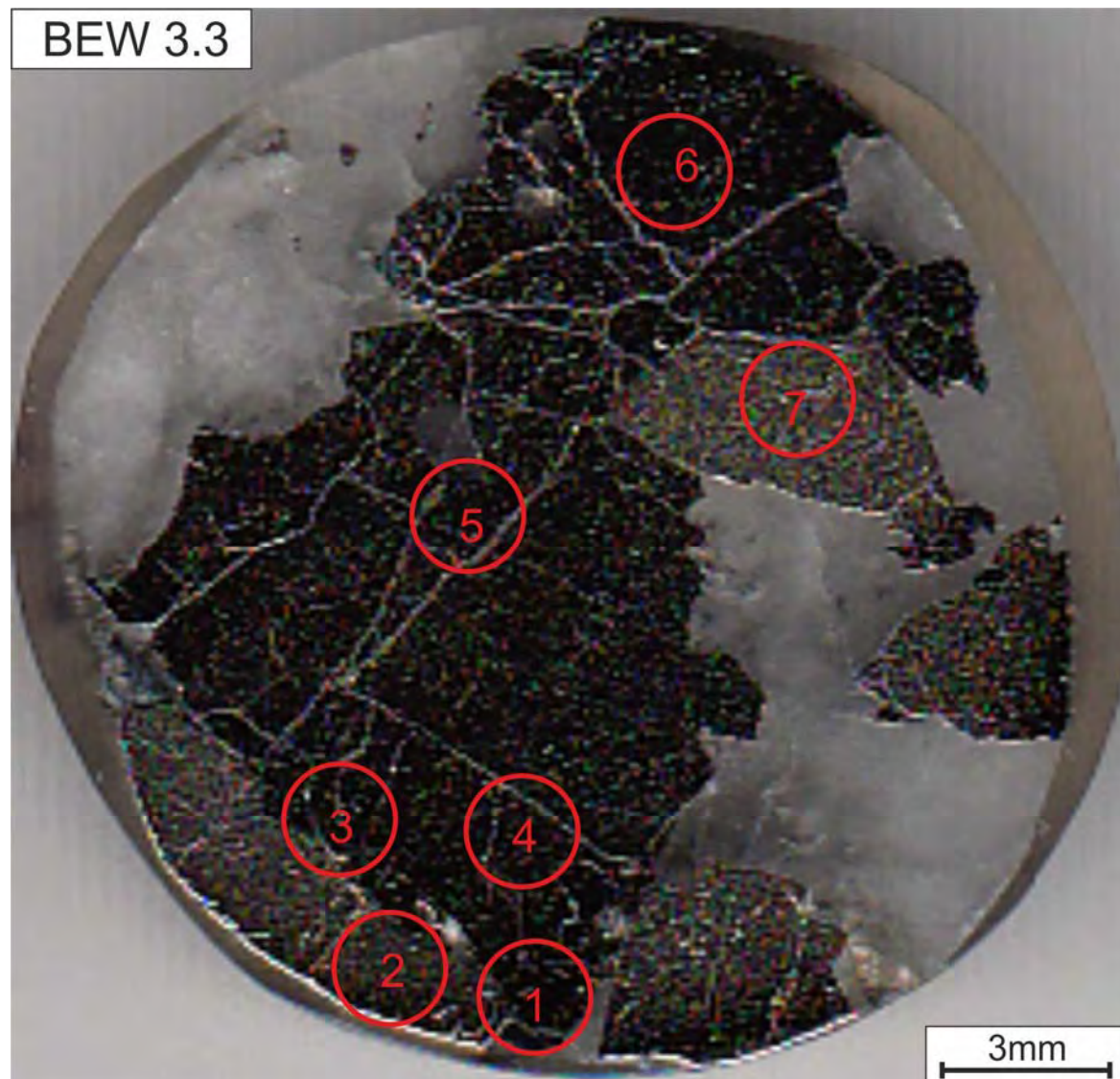
BEW 3.1



Quartz-carbonate vein



Quartz-carbonate vein



GLITTER Software

The GLITTER data reduction was developed to provide a simple, consistent and fast analysis of LA-ICPMS data. The software provides the first real time data reduction and allows the examination of the results before the next spot analysis commenced.

For a precise analysis of the data GLITTER enables the selection of the best interval for background and signal measurement and shows time resolved data for each analysed spot. This allows the immediate recognition of inclusions and data spikes. If the intervals have been changed, the software automatically adapts the tables and plots for the different integration intervals.

In order to provide accurate measurements, the data gets instantaneously adjusted with each additional standard analysis to account for changes in the analytical conditions. To ensure accurate standard values the standard has been measured twice or until the variation of the values is acceptable to provide accurate measurements.

Calibration was done after the widely accepted method using the MASS-1 pressed synthetic polymetal sulphide standard (including all trace elements analysed in this study) from the USGS (Wilson et al., 2002) and Fe was chosen as the internal standard for the data reduction. Every spot analysis is then normalised against the idealised stoichiometry for the different sulphides analysed (pyrite: 47 wt.% Fe; arsenopyrite 36.5 %; chalcopyrite 30.4 %; tetrahedrite/tennantite 7.5 %).

The Table on page 153 shows the Isotopes, analysed, detection limits, concentrations for the calibration standard and the average and standard deviation of the calibration.

Jackson, S.E., 2001; Knudsen, T.-L. et al., 2000; Belousova, E.A. et al., 2001;

Table 1: Ablation and analysis parameters

LA	
Model	NWR UV-213
Wavelength	213 nm
Repetition rate	10 Hz
Spot size	40 μm
Analysis type	Point (depth scan)
Energy density of sample	7 J cm^{-2}
<hr/>	
ICP-MS	
Model	Perkin-Elmer Nexion
Forward power	1500 W
Plasma gas	Ar, 16 l/min
Auxiliary gas	Ar, 1.375 l/min
Carrier gas	Ar, 1.11 l/min
<hr/>	
Data acquisition	
Data acquisition protocol	Time-resolved analysis
Scanning mode	Peak hopping, 1 point per peak
Detector mode	Dual detector
Time/scan	0.29 s
On-peak counting time	10 ms
Data acquisition	ca. 57 s (10 s gas blank, 47 s sample)
Data reduction	GLITTER

Table 2: Isotopes, analysed, detection limits, concentrations for the calibration standard and the average and standard deviation of the calibration.

element	isotope	average detection limit (ppm)	concentrations MASS-1 (ppm)	Standtard Deviation
S	34	328	276000	376
V	51	0.1	63	0.0
Cr	53	1.3	65	0.1
Mn	55	0.3	280	0.9
Fe	57	28	156000	Internal Standard
Co	59	0.1	60	0.2
Ni	60	0.5	97	0.4
Cu	65	0.9	134000	27.8
Zn	66	1.6	210000	613
Ga	71	0.1	64	0.1
As	75	8.1	65	2.3
Se	77	3.5	51	0.3
Mo	95	0.3	59	0.1
Ag	107	0.06	50	0.1
Cd	111	0.4	60	01.
In	115	0.02	50	0.2
Sn	117	0.4	59	0.1
Sb	121	0.12	60	0.1
Te	125	0.7	15	0.1
W	182	0.1	20	0.1
Ir	193	0.03	42	0.1
Au	197	0.08	50	0.2
Hg	202	0.5	57	0.0
Pb	206	0.13	68	0.1
Pb	207	0.16	68	0.2
Pb	208	0.1	68	0.1
Bi	209	0.03	60	0.1

Trace Element Data All values are in ppm

Element	FTh 204.3.1 C1 Chalcopyrite	FTh 204.3.1 R1 Chalcopyrite	FTh 204.3.2 C1 Pyrite	FTh 204.3.2 C2 Pyrite	FTh 204.3.3 Arsenopyrite	FTh 204.3.4 C1 Arsenopyrite	FTh 204.3.4 C2 Arsenopyrite	FTh 204.3.4 C3 Arsenopyrite	FTh 204.3.4 C4 Arsenopyrite	FTh 204.3.5 C1 Arsenopyrite	FTh 204.3.5 C2 Arsenopyrite
S34	410790	401744	258275	253971	122830	125241	123413	134106	127957	114931	124175
V51	1.0	0.7	0.1	0.1	0.1	0.1	0.1	0.1	0.1	0.1	0.1
Cr53	16.5	14.5	4.8	3.8	5.3	3.3	4.2	3.5	4.4	4.0	3.3
Mn55	16.3	4.1	6.8	6.7	5.7	5.5	7.4	5.6	5.8	5.5	5.5
Fe57	303929	303929	469962	469962	365336	365336	365336	365336	365336	365336	365336
Co59	0.7	0.5	0.0	0.0	0.1	0.2	0.1	0.1	0.1	0.1	0.1
Ni60	3.6	2.5	0.1	0.1	0.3	1.3	0.8	0.4	0.3	0.4	0.6
Cu65	407626	408696	5.0	13.6	14.8	5.6	96.5	2.2	1.9	8.6	1.0
Zn66	98.8	62.5	15.3	2.8	1.2	24.3	23.2	0.8	9.8	11.9	1.0
Ga71	2.4	5.8	0.0	0.0	0.1	0.3	0.1	0.1	0.0	0.1	0.1
As75	25.0	19.7	4004	5784	192768	162583	154402	241266	237624	134874	196427
Se77	47.5	49.3	2.8	3.3	23.0	32.4	18.3	15.1	28.7	30.4	33.1
Mo95	1.8	2.1	0.0	0.1	0.1	0.5	0.2	0.1	0.2	0.1	0.1
Ag107	0.5	1.4	0.0	0.0	0.1	0.1	0.4	0.1	0.1	0.1	0.1
Cd111	2.7	1.5	0.2	0.1	0.4	0.2	0.2	0.2	0.2	0.6	0.1
In115	26.9	28.6	0.0	0.0	0.3	0.1	0.2	0.3	0.3	0.2	0.3
Sn117	522	313	0.3	0.3	0.7	0.6	0.5	0.6	0.5	0.8	0.7
Sb121	5.3	9.3	0.1	0.1	55.6	46.7	41.8	60.3	54.4	58.5	88.8
Te125	0.0	0.9	0.0	0.1	1.3	0.1	0.4	0.5	0.5	0.4	0.9
W182	2.4	0.2	0.0	0.0	0.0	0.3	0.0	0.0	0.0	0.1	0.0
Ir193	0.2	0.0	0.0	0.0	0.0	0.0	0.0	0.0	0.0	0.1	0.0
Au197	0.6	1.3	0.1	0.1	1.9	7.5	53.8	19.9	2.6	0.1	0.8
Hg202	6.6	4.9	0.2	0.3	1.2	1.4	1.0	1.5	1.2	0.9	1.5
Pb206	2.0	5.4	0.0	0.1	1.0	0.2	4.6	0.7	0.3	0.1	0.4
Pb207	4.4	7.8	0.5	0.1	1.1	0.4	5.6	0.8	0.3	0.3	0.5
Pb208	2.0	7.1	0.8	0.1	0.9	0.2	5.2	0.6	0.3	0.1	0.4
Bi209	3.5	11.8	0.2	0.3	8.2	3.2	16.8	6.1	2.9	1.5	10.5

Continued

Element	FTh 204.3.5 R2 Arsenopyrite	FTh 204.3.5 R3 Arsenopyrite	FTh 204.3.5 R4 Arsenopyrite	FTh 204.3.6 C1 Arsenopyrite	FTh 204.3.6 C2 Arsenopyrite	FTh 204.3.6 C3 Arsenopyrite	FTh 204.3.6 C4 Arsenopyrite	FTh 204.3.6 R1 Arsenopyrite	FTh 204.3.7 C1 Pyrite	FTh 204.3.7 C2 Pyrite	FTh 405.2.1.1 Pyrite
S34	126596	124292	126095	125164	121747	121285	115716	122927	213864	207068	327985
V51	0.1	0.1	0.1	0.1	0.1	0.1	0.1	0.1	0.1	0.1	0.2
Cr53	4.5	3.4	5.2	3.9	3.3	4.5	4.6	4.0	5.8	5.3	6.4
Mn55	5.8	5.5	5.5	5.5	5.6	5.1	5.5	5.4	7.2	7.1	12.8
Fe57	365336	365336	365336	365336	365336	365336	365336	365336	469962	469962	469962
Co59	0.1	0.1	0.1	0.1	0.1	0.1	0.1	0.1	0.3	2.0	0.9
Ni60	0.6	0.5	0.3	0.5	0.5	0.8	0.4	0.4	0.4	1.7	4.7
Cu65	27.1	3.1	11.9	4.7	3.5	1.1	112	2.2	12.4	9.7	29.5
Zn66	9.1	5.1	0.9	6.8	1.6	1.4	52.8	2.5	30.6	2.0	61.5
Ga71	0.1	0.1	0.1	0.1	0.1	0.1	0.0	0.1	0.0	0.1	0.1
As75	216504	212549	195259	195356	188143	196910	191396	193171	7796	5783	5561
Se77	32.3	29.7	17.9	16.6	27.1	24.8	18.8	24.8	2.8	2.9	2.3
Mo95	0.1	0.3	0.1	0.3	0.0	0.2	0.2	0.2	0.0	0.2	0.4
Ag107	0.1	0.1	0.1	0.1	0.1	0.1	0.1	0.1	0.1	0.1	0.4
Cd111	0.5	0.1	0.1	0.5	0.2	0.3	0.3	0.1	0.3	0.1	0.3
In115	0.3	0.3	0.3	0.3	0.3	0.3	0.3	0.3	0.0	0.0	0.0
Sn117	1.3	0.7	0.7	0.7	0.3	0.9	0.5	0.8	0.3	0.6	0.5
Sb121	55.8	45.5	58.6	128	88.3	63.3	56.9	60.0	0.2	0.5	1.7
Te125	0.2	0.8	1.0	0.2	0.4	0.9	0.9	0.1	0.0	0.5	0.1
W182	0.0	0.0	0.0	0.3	0.0	0.0	0.0	0.0	0.0	0.0	0.0
Ir193	0.0	0.0	0.0	0.0	0.0	0.0	0.0	0.0	0.0	0.0	0.0
Au197	9.4	12.9	63.0	2.8	0.4	7.0	24.8	12.7	3.5	3.0	0.4
Hg202	1.3	1.1	1.4	1.3	1.1	1.4	1.7	1.5	0.5	0.5	1.0
Pb206	0.1	0.7	0.3	0.2	0.2	0.1	0.1	0.4	0.6	1.0	0.7
Pb207	0.2	2.0	0.2	0.4	0.2	0.2	0.2	0.5	0.6	1.4	0.9
Pb208	0.1	0.9	0.4	0.4	0.1	0.1	0.1	0.5	0.6	1.3	1.0
Bi209	2.5	4.9	1.7	18.2	3.4	1.2	0.6	4.3	1.8	7.5	12.6

Continued

Element	FTh 405.2.1.2 Pyrite	FTh 405.2.1.3 Pyrite	FTh 405.2.3.1 C1 Pyrite	FTh 405.2.3.1 R1 Pyrite	FTh 405.2.3.2 C1 Pyrite	FTh 405.2.3.2 R1 Pyrite	FTh 405.2.3.3 Chalcopyrite	FTh 405.2.3.4 Chalcopyrite	FTh 405.2.4.1 C1 Pyrite	FTh 405.2.4.1 R1 Pyrite
S34	337017	320283	310519	335066	325616	303115	315944	318892	266308	269736
V51	1.1	0.1	0.1	0.1	0.1	0.0	0.2	0.2	0.2	0.1
Cr53	8.7	6.0	6.6	6.9	6.7	6.2	5.0	3.9	6.0	6.7
Mn55	12.6	12.0	12.5	11.6	11.8	11.7	8.5	8.2	12.3	11.9
Fe57	469962	469962	469962	469962	469962	469962	303929	303929	469962	469962
Co59	0.5	0.4	2.2	0.3	0.4	0.4	0.2	0.2	0.3	0.6
Ni60	3.5	3.4	5.3	3.0	3.6	2.5	1.0	1.1	3.4	3.9
Cu65	1853	60.4	16.2	47063	16212	1947	295110	339707	48.0	323
Zn66	45.4	3.8	3.2	83.8	13.1	16.2	9.6	12.5	7.3	2.3
Ga71	0.6	0.0	0.1	0.2	0.2	0.1	1.2	0.6	0.1	0.1
As75	4367	5351	4579	4398	4847	5059	2513	1009	5685	4201
Se77	2.1	2.1	2.3	3.3	1.9	1.7	5.1	6.8	2.4	2.2
Mo95	0.1	0.2	0.1	0.2	0.1	0.2	0.4	0.2	0.0	0.1
Ag107	8.3	0.9	0.2	4.6	3.8	5.1	30.0	40.9	0.1	7.9
Cd111	0.1	0.3	0.1	0.4	0.2	0.2	0.6	0.4	0.1	0.2
In115	0.0	0.0	0.0	1.3	0.4	0.1	7.5	9.4	0.0	0.0
Sn117	0.8	0.3	0.5	17.3	5.0	0.8	113	150	0.3	0.2
Sb121	8.3	0.5	0.5	3.6	43.9	4.6	7.3	11.8	0.1	0.1
Te125	0.6	0.1	0.2	0.4	0.4	0.2	1.3	0.2	0.1	0.0
W182	0.1	0.0	0.0	0.0	0.0	0.1	0.0	0.1	0.0	0.0
Ir193	0.0	0.0	0.0	0.0	0.0	0.0	0.0	0.0	0.0	0.0
Au197	0.6	0.1	0.1	0.1	0.4	0.1	0.6	0.2	0.1	0.1
Hg202	1.0	0.7	0.8	0.9	0.9	0.4	3.4	3.1	0.8	0.5
Pb206	2.4	0.7	0.3	2.2	2.2	0.4	0.9	2.6	0.1	0.1
Pb207	2.7	0.2	0.3	2.4	2.2	0.4	1.1	2.7	0.1	0.1
Pb208	2.3	0.2	0.3	2.1	2.1	0.5	1.2	2.4	0.1	0.1
Bi209	27.4	2.5	2.0	14.2	28.4	4.9	9.0	17.2	1.4	1.1

Continued

Element	FTh 405.2.4.1 R2 Pyrite	FTh 405.2.4.1 R3 Pyrite	FTh 405.2.4.1 Tetrahedrite	FTh 405.2.4.2 Chalcopyrite	FTh 405.2.4.2 Tetrahedrite	FTh 405.2.4.3 Chalcopyrite	FTh 405.2.4.4 Pyrite	FTh 405.2.5.1 C1 Pyrite	FTh 405.2.5.1 R1 Pyrite	FTh 405.2.5.2 Tetrahedrite	FTh 405.2.5.3 C1 Pyrite
S34	272519	267238	147612	282629	59306	302106	250995	246842	256848	95241	271837
V51	0.1	0.1	1.5	0.8	2.2	0.4	0.1	0.1	0.1	0.1	2.3
Cr53	6.3	7.3	3.6	6.1	5.1	5.1	8.2	5.9	6.2	1.3	9.7
Mn55	11.4	11.7	8.1	8.0	3.0	9.3	17.6	13.6	12.5	3.0	16.2
Fe57	469962	469962	78975	303929	78975	303929	469962	469962	469962	78975	469962
Co59	0.2	0.5	1.8	0.2	0.3	0.2	0.3	1.4	0.5	0.2	1.2
Ni60	1.5	5.6	11.2	1.6	1.1	1.5	1.2	10.7	2.9	0.5	7.7
Cu65	217	128	267104	300636	53252	293531	82397	897	841	105001	36322
Zn66	3.7	16.0	18263	13.5	2651	8.2	3962	1.6	7.4	3659	1152
Ga71	0.1	0.1	1.0	1.7	1.6	1.1	0.2	0.1	0.1	0.4	1.6
As75	5358	5555	33872	1219	6151	1492	20200	4248	3942	6401	36526
Se77	1.6	1.8	6.0	5.8	1.4	8.2	2.2	1.8	1.6	1.9	11.7
Mo95	0.1	0.0	0.2	0.7	0.2	0.3	0.1	0.2	0.2	0.2	1.5
Ag107	3.9	5.1	609	32.8	141	137	180	14.1	14.2	113	89.7
Cd111	0.2	0.2	77.4	1.0	11.0	1.6	15.4	0.3	0.2	14.1	4.1
In115	0.0	0.0	13.5	7.5	3.4	7.6	2.8	0.0	0.0	3.8	1.6
Sn117	0.3	0.4	4.6	121.1	4.1	114.6	7.6	0.5	0.4	20.5	10.9
Sb121	20.6	5.8	126330	9.2	17551	0.9	28523	0.9	33.6	25443	8127
Te125	0.1	0.2	2.1	0.4	0.1	2.3	0.7	0.4	0.3	0.0	10.3
W182	0.0	0.0	0.1	0.2	0.4	0.0	0.0	0.0	0.0	0.0	0.5
Ir193	0.0	0.0	0.0	0.1	0.0	0.0	0.0	0.0	0.0	0.0	0.0
Au197	0.1	0.1	0.6	0.1	0.8	0.3	0.2	0.2	0.3	0.1	10.8
Hg202	0.7	0.6	122	3.1	17.8	4.9	47.3	0.7	0.4	14.3	13.4
Pb206	0.1	0.3	14.6	1.9	14.4	0.5	9.7	2.3	1.4	1.8	15.5
Pb207	0.2	0.3	17.8	2.1	17.0	0.9	11.1	3.3	1.6	2.2	19.3
Pb208	0.1	0.3	15.7	1.9	14.8	0.6	10.4	2.9	1.5	1.9	17.3
Bi209	3.2	4.5	8661	8.9	1773	2.6	4730	17.6	16.1	1596	1397

Continued

Element	FTh 405.2.5.3 R1 Tetrahedrite	FTh 405.2.5.5 Tetrahedrite	FTh 405.2.5.6 Chalcopyrite	FTh 405.2.5.7 Pyrite	FTh 405.2.5.8 Chalcopyrite	FTh 405.2.5.9 C1 Pyrite	FTh 405.2.5.9 R1 Pyrite	FTh 405.2.5.10 Tetrahedrite	FTh 405.2.5.11 C1 Chalcopyrite	FTh 405.2.5.11 R1 Chalcopyrite
S34	150899	112861	357431	262780	248487	228248	249844	155780	258401	265858
V51	1.1	0.9	1.7	0.7	0.5	0.1	0.1	0.7	1.3	0.4
Cr53	2.6	2.3	9.3	8.6	6.5	9.4	7.7	2.5	7.9	9.3
Mn55	4.7	4.3	11.7	12.6	9.0	14.2	12.4	5.4	10.1	8.3
Fe57	78975	78975	303929	469962	303929	469962	469962	78975	303929	303929
Co59	0.1	0.1	0.5	3.2	0.4	2.6	0.9	0.3	0.6	0.4
Ni60	1.0	0.8	3.3	9.0	1.4	9.4	4.0	1.2	1.8	1.6
Cu65	202246	162410	448834	102517	277194	58	26578	270319	289365	373178
Zn66	15388	6990	2379	658	1291	2.0	1857	17501	179	287
Ga71	0.7	1.0	2.7	0.7	4.4	0.1	0.1	0.6	1.0	0.7
As75	34668	15661	6127	9616	12505	4646	7486	31893	1614	1460
Se77	10.8	4.6	18.2	3.4	27.8	1.8	3.0	12.8	10.4	9.3
Mo95	0.2	0.3	1.5	0.3	0.8	0.3	0.2	0.9	1.1	1.7
Ag107	422	239	453	170	318	0.8	89.0	293	30.8	38.5
Cd111	57.9	24.7	7.9	2.6	4.6	0.6	6.7	70.4	1.5	0.9
In115	11.6	6.4	8.4	2.2	5.9	0.0	1.4	12.8	6.3	6.5
Sn117	3.9	30.8	139	32.3	85.4	0.4	0.5	1.0	111	146
Sb121	98367	46427	13727	3216	6834	5.6	14487	129353	1357	360
Te125	3.7	0.2	0.4	9.4	2.6	0.2	0.6	1.6	0.8	0.4
W182	0.1	0.1	0.1	0.1	0.1	0.0	0.1	0.1	0.0	0.0
Ir193	0.0	0.0	0.0	0.0	0.0	0.0	0.0	0.0	0.0	0.0
Au197	3.0	1.0	0.5	3.4	3.3	0.4	0.5	0.3	0.1	0.2
Hg202	52.8	32.8	30.7	4.9	7.9	0.6	22.0	125	9.8	6.6
Pb206	230	31.3	42.2	22.2	34.3	2.1	3.1	4.6	0.8	6.1
Pb207	256	34.4	44.1	25.0	37.9	2.7	3.3	5.1	1.2	6.6
Pb208	240	31.9	47.6	25.5	34.2	2.3	3.4	4.8	1.1	5.9
Bi209	8792	3423	1371	491	7907	13	900	7668	78.4	40.1

Continued

Element	FTh 405.2.5.12 R1 Pyrite	FTh 405.2.5.13 C1 Pyrite	FTh 405.2.5.13 R1 Pyrite	FTh 405.2.7.1 C1 Pyrite	FTh 405.2.7.1 R1 Pyrite	FTh 405.2.7.2 Chalcopyrite	FTh 405.2.7.3.1 Tetrahedrite	FTh 405.2.7.3.2 Pyrite	FTh 405.2.7.4 Pyrite	FTh 405.2.7.6 Pyrite
S34	230846	228647	235193	221691	227708	295345	219978	272499	248507	274634
V51	0.1	0.1	0.1	0.5	0.1	0.4	0.4	0.9	0.2	1.4
Cr53	7.8	8.7	7.4	9.3	8.4	6.8	4.2	9.6	9.3	10.9
Mn55	11.8	12.3	12.9	13.1	12.5	9.0	4.9	14.7	14.4	14.1
Fe57	469962	469962	469962	469962	469962	303929	78975	469962	469962	469962
Co59	1.4	0.4	0.8	0.4	0.4	0.3	0.5	0.2	0.1	2.8
Ni60	5.0	10.9	7.9	3.3	5.8	2.2	3.1	1.1	1.7	8.5
Cu65	6056	5375	2112	3265	4240	293364	470709	146478	51483	88509
Zn66	24.9	41.5	6.4	46.4	124	1414	24141	7380	2331	5116
Ga71	0.1	0.1	0.1	0.2	0.1	1.6	0.7	0.9	0.4	1.1
As75	1354	5169	3912	5035	5511	6653	74410	30122	26332	17362
Se77	1.9	1.6	1.3	1.4	1.8	7.1	9.5	7.2	3.7	5.9
Mo95	0.2	0.0	0.2	1.0	0.1	0.6	0.0	0.3	0.5	0.5
Ag107	6.5	13.3	22.5	61.0	155	158	1438	477	266	234
Cd111	0.2	0.1	0.1	0.5	0.4	5.7	104	33.5	10.1	18.9
In115	0.2	0.1	0.0	0.0	0.1	5.9	12.3	3.9	1.4	3.6
Sn117	2.1	2.5	0.2	0.6	0.5	76.1	3.0	8.0	5.9	2.4
Sb121	167	69.1	30.2	105	674	11249	193980	58895	19144	36886
Te125	0.4	0.1	0.5	0.1	0.2	2.3	0.0	0.2	3.8	0.3
W182	0.0	0.0	0.0	0.0	0.0	0.0	0.1	0.2	0.1	0.3
Ir193	0.0	0.0	0.0	0.0	0.0	0.0	0.1	0.0	0.0	0.0
Au197	0.2	0.1	0.2	0.5	0.3	1.1	0.6	0.2	3.6	0.8
Hg202	1.1	1.0	0.7	1.6	2.1	11.8	272	119	81.7	58.2
Pb206	0.6	0.3	1.5	4.6	6.4	5.4	4.9	4.8	18.8	111
Pb207	0.6	0.2	1.5	4.7	7.2	6.1	4.6	5.3	22.1	126
Pb208	0.6	0.4	1.3	4.6	7.0	5.0	4.4	4.9	19.7	117
Bi209	17.5	7.7	15.7	184	270	851	12891	3969	1484	3309

Continued

Element	FTh 405.2.8.1 C1 Pyrite	FTh 405.2.8.1 R1 Pyrite	FTh 405.2.8.2 Pyrite	FTh 405.2.8.3 Pyrite	FTh 405.2.9.1 Chalcopyrite	FTh 405.2.9.2 Pyrite	FTh 405.2.9.3 Chalcopyrite	FTh 405.2.9.4 Chalcopyrite	FTh 405.2.9.5 Pyrite	FTh 406.1.1 C1 Pyrite	FTh 406.1.2 C1 Pyrite
S34	212292	222330	240259	247929	265559	214654	265070	208353	218660	405017	351552
V51	0.1	0.1	0.1	0.1	1.6	0.3	3.4	0.4	0.1	0.1	0.1
Cr53	8.0	8.2	7.9	8.0	15.0	8.8	8.5	5.1	8.4	11.5	10.8
Mn55	12.9	12.3	12.3	12.5	15.2	13.0	18.9	23.0	31.7	23.5	22.5
Fe57	469962	469962	469962	469962	303929	469962	303929	303929	469962	469962	469962
Co59	0.3	0.4	0.3	0.2	8.1	39.6	5.0	8.7	32.9	1.3	0.4
Ni60	2.4	4.8	3.4	5.3	11.8	423	7.0	10.4	31.7	5.4	3.1
Cu65	96.2	3301	18741	63338	351069	4534	352177	275585	34074	6.3	35.5
Zn66	20.5	18.2	9.7	137.9	73.2	2.3	11.1	4.6	6.0	51.4	8.4
Ga71	0.1	0.1	0.1	0.2	1.6	0.1	2.0	1.2	0.1	0.1	0.0
As75	4626	6357	9421	27661	218	1249	821	1953	2198	8084	4055
Se77	2.1	2.3	2.8	8.3	21.0	7.0	16.6	9.9	5.2	5.3	3.1
Mo95	0.1	0.0	0.4	0.1	3.8	0.2	1.7	1.5	0.1	0.1	0.2
Ag107	13.3	23.8	92.0	316	88.7	4.1	301	145	37.7	0.2	0.1
Cd111	0.6	0.4	0.3	0.4	0.6	0.5	2.4	1.4	0.1	0.3	0.2
In115	0.0	0.0	0.3	1.5	8.1	0.1	7.0	5.9	0.8	0.0	0.1
Sn117	0.3	1.0	5.7	18.8	183	3.2	115	92.7	12.5	0.4	0.3
Sb121	21.2	155	166	809	19.7	1.8	13.3	7.3	3.1	1.8	1.2
Te125	0.1	0.7	1.7	6.9	0.8	0.3	0.4	1.6	0.3	0.2	0.2
W182	0.0	0.0	0.0	0.0	0.0	0.0	0.1	0.0	0.0	0.0	0.0
Ir193	0.0	0.0	0.0	0.0	0.5	0.0	0.0	0.1	0.0	0.0	0.0
Au197	0.1	0.7	2.2	11.0	1.1	0.2	1.4	1.9	0.5	0.5	0.2
Hg202	0.7	0.9	1.0	1.7	13.0	0.9	9.4	6.9	1.2	0.8	0.3
Pb206	35.0	101	559	398	7.4	0.8	9.9	8.5	2.9	2.9	1.6
Pb207	39.4	114	623	435	7.2	1.1	10.5	8.9	3.3	3.5	2.2
Pb208	37.1	107	573	409	8.1	0.8	9.6	7.7	3.1	3.5	1.8
Bi209	447	3907	28308	62472	59.7	8.6	31.5	72.1	25.6	20.0	5.1

Continued

Element	FTh 406.1.2 R1 Pyrite	FTh 406.1.2 R1 Pyrite	FTh 406.1.2 R2 Pyrite	FTh 406.1.3 C1 Pyrite	FTh 406.1.3 R1 Pyrite	FTh 406.1.4 C1 Pyrite	FTh 406.1.4 R1 Pyrite	FTh 406.1.4 R2 Pyrite	FTh 406.1.5.1 Pyrite	FTh 406.1.5.2 Pyrite	FTh 406.1.5.3 Pyrite
S34	387924	362018	351679	285792	287133	267576	288839	270686	268779	270970	277034
V51	0.0	0.1	1.2	0.1	0.0	0.2	3.3	0.1	0.2	0.1	0.0
Cr53	10.1	10.6	11.0	9.6	9.0	9.0	10.8	8.5	9.4	8.7	8.0
Mn55	22.2	22.2	961.3	23.2	18.7	18.1	1387	35.1	18.2	17.0	31.5
Fe57	469962	469962	469962	469962	469962	469962	469962	469962	469962	469962	469962
Co59	0.1	0.1	0.1	0.2	0.1	0.1	0.5	0.4	0.4	0.1	0.1
Ni60	0.6	1.8	0.3	8.7	5.1	0.5	1.8	1.2	5.2	6.0	1.7
Cu65	16.0	26.7	4.3	6.1	7.9	5.7	11.1	9.0	20.3	6.3	5.0
Zn66	43.0	9.4	28.1	50.6	19.1	2.1	3.9	3.2	2.0	2.3	3.4
Ga71	0.0	0.0	0.1	0.0	0.1	0.0	1.9	0.0	0.1	0.1	0.1
As75	4909	6466	2517	6045	5927	4138	1894	3949	7167	7585	6128
Se77	2.5	4.3	3.4	2.8	2.6	3.1	3.4	2.4	3.8	2.5	2.1
Mo95	0.1	0.1	0.2	0.1	0.1	0.1	0.2	0.0	0.2	0.1	0.1
Ag107	0.4	0.0	0.1	0.1	0.1	0.0	0.3	0.1	0.1	0.1	0.1
Cd111	0.1	0.2	0.2	0.3	0.2	0.2	0.2	0.2	0.3	0.3	0.3
In115	0.0	0.0	0.4	0.0	0.0	0.0	0.1	0.0	0.0	0.0	0.0
Sn117	0.2	0.3	0.3	0.3	0.3	0.3	1.9	0.4	0.3	0.3	0.3
Sb121	0.7	0.1	0.9	1.4	1.2	0.2	2.1	0.6	1.4	0.8	0.8
Te125	0.6	0.1	0.4	0.5	0.2	0.6	0.6	0.4	0.2	0.4	0.3
W182	0.0	0.0	0.9	0.0	0.0	0.0	0.6	0.0	0.1	0.0	0.1
Ir193	0.0	0.0	0.0	0.0	0.0	0.0	0.0	0.0	0.0	0.0	0.0
Au197	0.3	0.1	0.0	0.3	0.3	0.0	0.2	0.1	0.4	0.2	0.2
Hg202	0.6	0.5	0.5	0.5	0.4	0.5	0.5	0.4	0.6	0.6	0.4
Pb206	4.1	0.2	1.3	1.2	0.7	0.2	7.9	1.1	0.8	0.4	0.7
Pb207	4.5	0.2	1.3	1.2	0.9	0.1	9.0	1.1	1.2	0.7	0.8
Pb208	4.1	0.2	1.1	1.1	0.8	0.1	8.0	1.1	1.0	0.3	0.8
Bi209	22.4	1.6	4.5	10.6	9.9	1.7	16.4	5.5	12.0	7.8	6.6

Continued

Element	FTh 406.1.5.4 Pyrite	FTh 406.4.2 C1 Pyrite	FTh 406.4.2 C2 Pyrite	FTh 406.4.3 C1 Chalcopyrite	FTh 406.4.3 R1 Chalcopyrite	FTh 406.4.4 C1 Arsenopyrite	FTh 406.4.4 C2 Arsenopyrite	FTh 406.4.5 C1 Arsenopyrite	FTh 406.4.5 C2 Arsenopyrite	FTh 406.4.5 R1 Arsenopyrite	FTh 406.4.6 C1 Arsenopyrite
S34	266221	247011	243533	376484	320974	123911	143234	129230	124278	134618	118090
V51	0.1	0.0	0.1	1.0	0.5	0.1	0.1	0.1	0.1	0.1	0.1
Cr53	8.3	4.8	4.8	17.8	11.6	4.8	5.8	4.0	4.8	5.3	5.6
Mn55	92.5	7.0	6.8	8.7	10.4	5.6	6.2	5.8	5.8	5.9	5.5
Fe57	469962	469962	469962	303929	303929	365336	365336	365336	365336	365336	365336
Co59	0.1	0.0	0.0	0.9	0.4	0.1	0.3	0.1	0.1	0.0	0.1
Ni60	3.7	0.2	0.1	3.7	10.6	0.4	0.6	0.4	0.9	0.4	0.6
Cu65	6.4	534	3.2	427158	412728	1200	3204.34.43	13.7	3.6	18.1	1.2
Zn66	9.6	43.3	15.1	713	35.8	20.9	20.7	1.1	0.9	2.9	0.8
Ga71	0.1	8.1	0.1	3.0	3.7	0.1	0.1	0.1	0.1	0.1	0.1
As75	5835	1.4	4467	34.2	18.4	147690	160050	229627	231976	238223	203690
Se77	2.2	4.1	2.5	31.8	26.1	34.1	17.4	35.5	52.5	19.9	30.2
Mo95	0.2	0.1	0.1	2.3	0.9	0.1	0.4	0.3	0.2	0.2	0.2
Ag107	0.1	0.5	0.0	9.2	0.4	0.4	0.4	0.1	0.1	0.1	0.1
Cd111	0.2	0.2	0.1	3.8	2.9	0.3	0.5	0.4	0.2	0.2	0.2
In115	0.0	11.6	0.0	20.2	20.6	0.3	1.9	0.4	0.4	0.3	0.3
Sn117	0.3	484	1.3	515	496	2.3	129	0.4	1.4	0.9	0.4
Sb121	0.8	0.7	0.3	6.6	3.6	57.8	48.9	114	74.6	139	92.0
Te125	0.2	0.0	0.2	0.6	3.4	0.2	0.3	0.3	2.2	0.3	0.6
W182	0.0	0.0	0.0	0.8	0.1	0.0	0.0	0.1	0.0	0.4	0.0
Ir193	0.0	0.0	0.0	0.5	0.1	0.0	0.0	0.0	0.0	0.0	0.0
Au197	0.1	0.0	0.1	0.5	0.2	5.9	2.3	2.1	0.2	2.0	2.8
Hg202	0.4	0.3	0.2	6.1	3.5	1.0	1.6	0.8	1.6	1.2	1.2
Pb206	1.4	0.1	0.0	2.8	2.3	4.2	12.7	0.1	4.5	3.0	0.3
Pb207	1.6	0.1	0.1	1.9	2.9	4.6	17.7	0.2	5.0	3.6	0.2
Pb208	1.6	0.2	0.0	1.3	2.3	4.2	14.8	0.2	4.2	3.2	0.4
Bi209	5.7	5.8	0.0	0.9	1.7	15.5	115	6.7	4.4	17.0	12.6

Continued

Element	FTh 406.4.6 R1 Arsenopyrite	FTh 406.4.7.1 Pyrite	FTh 409 1 R.1 Pyrite	FTh 409.1 C.1 Pyrite	FTh 409.1 C.2 Pyrite	FTh 409.1.2 C1 Pyrite	FTh 409.1.2 C2 Pyrite	FTh 409.1.2 C3 Pyrite	FTh 409.1.2 C4 Pyrite	FTh 409.1.2 C5 Pyrite	FTh 409.1.3.1 Pyrite
S34	118484	213611	379968	385899	400020	589257	497517	570614	495927	556273	600194
V51	0.1	0.2	0.4	3.9	1.6	51.8	33.2	35.0	61.5	49.8	133
Cr53	4.0	5.9	6.2	12.3	6.8	133	70.5	78.8	97.9	97.6	139
Mn55	5.5	7.1	7.1	7.6	7.0	40.2	30.9	30.1	32.8	41.5	39.1
Fe57	365336	469962	469962	469962	469962	469962	469962	469962	469962	469962	469962
Co59	0.1	0.1	214	919	722	109	124	163	182	179	55.2
Ni60	0.6	0.4	1413	1899	2195	855	868	914	901	863	649
Cu65	0.6	3.2	17.1	548	59.2	625	611	402	310	493	299
Zn66	79.6	0.9	24.6	29.3	9.4	15.5	27.3	10.8	21.3	5.0	24.5
Ga71	0.1	0.1	0.1	1.7	0.6	12.7	8.7	7.2	14.8	13.7	36.6
As75	201137	3211	2624	1362	3054	4331	5662	5293	5291	5272	3273
Se77	38.4	2.9	6.1	17.6	18.5	13.0	12.4	13.1	19.3	17.5	8.7
Mo95	0.2	0.2	0.1	0.2	0.3	64.1	41.4	314	92.8	194	33.7
Ag107	0.1	0.2	0.1	0.6	0.1	5.9	6.8	5.7	6.6	6.6	2.9
Cd111	0.3	0.3	0.7	0.6	0.6	0.5	0.4	0.1	0.4	0.4	0.6
In115	0.3	0.0	0.0	0.0	0.0	0.0	0.1	0.0	0.1	0.1	0.2
Sn117	1.1	2.8	0.2	1.1	0.3	6.1	4.4	3.6	4.6	4.5	6.5
Sb121	70.9	0.8	0.5	4.9	1.9	27.2	26.7	31.4	37.8	26.6	34.3
Te125	0.8	0.0	0.8	0.7	0.2	9.4	10.9	16.2	13.5	13.5	5.0
W182	0.0	0.0	0.0	0.5	0.1	22.9	12.1	25.5	14.0	39.3	13.7
Ir193	0.0	0.0	0.0	0.0	0.0	0.0	0.0	0.0	0.0	0.0	0.0
Au197	0.1	0.2	0.1	0.2	0.1	0.5	0.5	0.8	0.8	0.7	0.5
Hg202	1.4	0.6	0.7	0.8	0.8	2.2	1.7	2.2	2.3	1.8	4.3
Pb206	0.6	1.3	0.3	2.9	1.6	272	284	240	344	283	233
Pb207	0.7	1.1	0.4	2.9	1.7	343	359	306	438	352	302
Pb208	0.5	1.1	0.4	3.0	1.6	314	329	278	404	324	277
Bi209	2.3	4.5	5.3	19.5	9.5	120	159	215	191	192	84.2

Continued

Element	FTh 409.1.3.2 Pyrite	FTh 409.1.3.3 Pyrite	FTh 409.1.3.4 Pyrite	FTh 409.1.3.5 Pyrite	FTh 409.1.4 C4 Pyrite	FTh 409.1.4 C5 Pyrite	FTh 409.1.4 C6 Pyrite	FTh 409.1.4 C7 Pyrite	FTh 409.1.4 C8 Pyrite	FTh 409.1.4 C1 Pyrite	FTh 409.1.4 C2 Pyrite
S34	480328	569472	514699	521430	285263	285902	310560	273861	275278	289230	292992
V51	128	187	64.8	54.7	0.1	0.1	2.0	0.1	0.1	0.1	0.1
Cr53	166	220	93.4	62.1	6.9	6.1	8.2	6.3	6.7	6.5	6.4
Mn55	44.4	35.6	30.3	68.8	7.6	8.0	46.4	8.7	8.7	7.3	8.2
Fe57	469962	469962	469962	469962	469962	469962	469962	469962	469962	469962	469962
Co59	90.3	96.2	155	162	8.0	6.3	5.5	65.7	17.4	83.3	203
Ni60	886	833	831	967	21.8	129	63.9	159	96.7	562	522
Cu65	604	521	322	125	7.6	5.4	7.9	0.8	6.4	7.7	25.5
Zn66	34.8	88.6	6.6	4.0	27.8	2.6	8.9	1.7	1532	3.4	44.9
Ga71	35.4	64.2	17.8	15.7	0.1	0.1	1.0	0.0	0.1	0.1	0.1
As75	3385	4267	5360	1431	2708	1671	2979	2222	2592	2152	1712
Se77	11.1	14.3	14.2	16.8	1.4	1.6	2.2	1.8	1.9	3.6	2.2
Mo95	46.7	35.6	54.9	8.7	0.1	0.2	0.2	0.2	0.1	0.3	0.1
Ag107	3.6	3.6	6.8	2.8	0.0	0.1	0.2	0.1	0.1	0.1	0.4
Cd111	0.7	0.8	0.4	1.1	0.3	0.5	0.4	0.6	2.3	0.3	0.4
In115	0.1	0.1	0.1	0.2	0.0	0.0	0.0	0.0	0.0	0.0	0.0
Sn117	7.6	12.6	4.6	3.1	0.2	0.3	0.4	0.4	0.3	0.2	0.4
Sb121	35.4	35.6	30.5	16.2	0.1	0.1	2.5	0.2	0.8	0.3	1.7
Te125	8.5	4.6	12.2	3.0	0.0	0.0	1.8	0.4	0.3	0.1	0.6
W182	25.7	21.1	12.6	4.5	0.0	0.0	0.3	0.0	0.0	0.0	0.0
Ir193	0.0	0.1	0.0	0.0	0.0	0.0	0.0	0.0	0.0	0.0	0.0
Au197	0.4	0.5	0.5	0.6	0.0	0.0	0.2	0.0	0.2	0.1	0.2
Hg202	3.2	5.2	2.8	1.2	0.3	0.4	0.4	0.3	0.6	0.6	0.6
Pb206	339	263	306	129	0.4	0.4	6.0	0.2	0.9	0.2	9.0
Pb207	446	341	386	157	0.4	0.1	6.3	0.2	1.2	0.2	11.7
Pb208	409	316	355	156	0.5	0.3	5.8	0.2	1.1	0.1	10.6
Bi209	111	100	172	80.6	1.8	0.7	33.5	1.7	8.4	5.4	14.9

Continued

Element	FTh 409.1.4 R1 Pyrite	FTh 409.1.5 C2 Pyrite	FTh 409.1.6 C1 Pyrite	FTh 409.1.6 C2 Pyrite	FTh 409.1.6 R1 Pyrite	FTh 409.1.7.1 Pyrite	FTh 409.1.7.2 Pyrite	FTh 409.1.8 C1 Pyrite	FTh 409.1.8 C2 Pyrite	FTh 409.3.1 C1 Pyrite	FTh 409.3.1 R1 Pyrite
S34	290867	275810	276648	265822	259528	252368	253627	250990	244891	407717	407881
V51	0.1	0.1	0.1	0.1	0.1	0.1	0.2	0.1	0.2	0.1	0.1
Cr53	6.0	6.9	6.5	7.0	7.3	8.2	6.8	7.4	8.2	7.6	5.0
Mn55	7.7	8.7	8.4	8.4	9.2	11.6	159	75.5	506	9.8	10.1
Fe57	469962	469962	469962	469962	469962	469962	469962	469962	469962	469962	469962
Co59	3.2	77.3	116	9.2	82.9	26.3	4.7	60.8	56.2	0.1	0.1
Ni60	19.2	378	497	42.4	450	208	99.8	574	429	0.4	0.5
Cu65	6.9	4.4	5.8	8.9	27.6	244	136	264	22.9	5.5	2.8
Zn66	7.3	20.6	2.1	3.6	10.6	2.0	2.2	1.8	2.9	3.4	3.9
Ga71	0.1	0.1	0.1	0.1	0.1	0.1	0.2	0.1	0.1	0.1	0.0
As75	2747	3188	3991	2487	2173	9.7	14.2	493	1150	5879	2901
Se77	1.5	1.8	1.9	1.8	2.4	4.6	4.1	6.4	3.0	6.1	7.8
Mo95	0.0	0.1	0.1	0.1	0.1	0.2	0.2	0.3	0.1	0.2	0.1
Ag107	0.1	0.0	0.1	0.1	0.3	0.1	0.1	0.9	0.1	0.2	0.1
Cd111	0.4	0.3	0.5	0.3	0.1	0.6	0.6	0.5	0.4	0.3	0.6
In115	0.0	0.0	0.0	0.0	0.0	0.0	0.0	0.0	0.0	0.0	0.0
Sn117	0.3	0.2	0.5	0.4	0.5	0.6	0.4	0.5	0.4	0.5	0.6
Sb121	0.9	0.6	1.7	0.4	1.1	0.3	0.4	9.5	1.0	1.3	0.2
Te125	0.3	0.0	0.7	0.5	0.5	0.1	0.1	0.3	0.3	1.1	0.0
W182	0.0	0.0	0.0	0.0	0.0	0.0	0.0	0.0	0.0	0.2	0.0
Ir193	0.0	0.0	0.0	0.0	0.0	0.0	0.0	0.0	0.0	0.0	0.0
Au197	0.1	0.1	0.2	0.0	0.1	0.0	0.0	0.2	0.0	0.1	0.0
Hg202	0.3	0.4	0.4	0.4	0.3	0.7	0.6	0.5	0.5	0.8	0.8
Pb206	0.6	0.5	1.4	0.3	0.9	5.4	3.1	22.7	4.8	0.7	0.3
Pb207	0.6	0.6	1.6	0.2	1.2	6.6	4.2	30.9	4.1	0.9	0.3
Pb208	0.6	0.4	1.4	0.3	1.1	6.2	3.7	26.4	4.3	0.8	0.3
Bi209	6.5	4.3	14.0	2.8	6.9	0.1	2.0	21.9	7.9	8.9	2.3

Continued

Element	FTh 409.3.2 C1 Pyrite	FTh 409.3.2 R1 Pyrite	FTh 409.3.3 C2 Pyrite	FTh 409.3.3 C2 Pyrite	FTh 409.3.3 R1 Pyrite	FTh 409.3.4 C1 Pyrite	FTh 409.3.4 C2 Pyrite	FTh 409.3.4 C3 Pyrite	FTh 409.3.4 R1 Pyrite	FTh 409.3.4 R1 Pyrite	FTh 409.3.4 R2 Pyrite
S34	424712	438682	357857	362599	369297	341744	342242	316714	388908	335426	320771
V51	0.1	0.1	0.1	0.1	0.2	0.1	0.1	0.1	2.9	0.1	0.2
Cr53	5.5	5.8	8.5	6.7	6.3	7.9	8.6	8.0	6.7	7.7	6.6
Mn55	9.0	9.2	11.8	11.8	10.8	12.7	13.3	13.0	34.9	13.8	1105
Fe57	469962	469962	469962	469962	469962	469962	469962	469962	469962	469962	469962
Co59	0.1	0.1	0.2	0.1	0.1	0.1	3.7	0.1	0.8	0.2	0.1
Ni60	0.6	0.3	2.8	0.4	0.6	1.6	16.8	0.7	1.6	0.7	3.8
Cu65	7.8	3.4	1.4	0.9	1.2	316	20.8	26.9	8378	2.6	11.7
Zn66	5.2	3.3	4.2	2.6	3.4	5.1	3.1	12.0	13.8	12.2	72.5
Ga71	0.1	0.1	0.1	0.1	0.2	0.1	0.1	0.1	2.7	0.1	0.1
As75	5686	4881	7068	5758	4545	8227	6413	1760	41461	3537	482
Se77	8.6	9.9	7.0	6.9	14.8	7.1	12.0	7.7	16.7	11.6	9.5
Mo95	0.2	0.1	0.3	0.2	0.2	0.2	0.3	0.2	0.5	0.4	0.1
Ag107	0.1	0.1	0.1	0.1	0.1	0.1	0.2	0.3	3.1	0.1	0.3
Cd111	0.3	0.4	0.4	0.5	0.2	0.9	0.8	1.0	0.1	1.0	0.9
In115	0.0	0.0	0.0	0.0	0.0	0.0	0.0	0.0	0.3	0.0	0.1
Sn117	0.4	0.4	0.3	0.4	0.7	0.3	0.4	0.5	2.0	0.6	0.7
Sb121	0.7	0.4	0.1	0.1	0.2	1.3	1.5	0.3	38.1	0.3	1.4
Te125	0.5	0.0	0.4	0.3	0.6	0.3	1.5	0.6	10.8	1.5	1.4
W182	0.1	0.0	0.0	0.0	0.0	0.0	0.0	0.0	0.0	0.0	0.0
Ir193	0.0	0.0	0.0	0.0	0.0	0.0	0.0	0.0	0.0	0.0	0.0
Au197	0.2	0.1	0.1	0.1	0.0	1.3	0.9	0.1	47.3	0.1	0.1
Hg202	0.7	0.6	0.6	0.7	0.8	0.7	0.8	0.8	1.0	0.9	0.8
Pb206	0.5	0.3	0.1	0.1	0.4	0.3	2.4	0.7	9.7	0.6	1.9
Pb207	0.8	0.2	0.2	0.2	0.6	1.1	3.6	0.7	11.2	0.5	2.3
Pb208	0.7	0.3	0.1	0.2	0.5	0.3	3.1	0.7	10.4	0.6	2.3
Bi209	12.9	3.7	0.4	0.8	1.0	3.3	14.2	10.9	56.4	2.2	11.6

Continued

Element	FTh 409.3.4 R3 Pyrite	FTh 409.3.5 C1 Pyrite	FTh 409.3.5 R1 Pyrite	FTh 409.3.6 C1 Pyrite	FTh 409.3.6 C2 Pyrite	FTh 409.3.6. R1 Pyrite	FTh 409.3.6.2 R2 Pyrite	FTh 409.3.7.1 Pyrite	FTh 409.3.7.2 Pyrite	FTh 409.3.7.3 Pyrite	FTh 409.3.8 C1 Pyrite
S34	424712	438682	357857	362599	369297	341744	342242	316714	388908	335426	320771
V51	0.1	0.1	0.1	0.1	0.2	0.1	0.1	0.1	2.9	0.1	0.2
Cr53	5.5	5.8	8.5	6.7	6.3	7.9	8.6	8.0	6.7	7.7	6.6
Mn55	9.0	9.2	11.8	11.8	10.8	12.7	13.3	13.0	34.9	13.8	1105
Fe57	469962	469962	469962	469962	469962	469962	469962	469962	469962	469962	469962
Co59	0.1	0.1	0.2	0.1	0.1	0.1	3.7	0.1	0.8	0.2	0.1
Ni60	0.6	0.3	2.8	0.4	0.6	1.6	16.8	0.7	1.6	0.7	3.8
Cu65	7.8	3.4	1.4	0.9	1.2	316	20.8	26.9	8378	2.6	11.7
Zn66	5.2	3.3	4.2	2.6	3.4	5.1	3.1	12.0	13.8	12.2	72.5
Ga71	0.1	0.1	0.1	0.1	0.2	0.1	0.1	0.1	2.7	0.1	0.1
As75	5686	4881	7068	5758	4545	8227	6413	1760	41461	3537	482
Se77	8.6	9.9	7.0	6.9	14.8	7.1	12.0	7.7	16.7	11.6	9.5
Mo95	0.2	0.1	0.3	0.2	0.2	0.2	0.3	0.2	0.5	0.4	0.1
Ag107	0.1	0.1	0.1	0.1	0.1	0.1	0.2	0.3	3.1	0.1	0.3
Cd111	0.3	0.4	0.4	0.5	0.2	0.9	0.8	1.0	0.1	1.0	0.9
In115	0.0	0.0	0.0	0.0	0.0	0.0	0.0	0.0	0.3	0.0	0.1
Sn117	0.4	0.4	0.3	0.4	0.7	0.3	0.4	0.5	2.0	0.6	0.7
Sb121	0.7	0.4	0.1	0.1	0.2	1.3	1.5	0.3	38.1	0.3	1.4
Te125	0.5	0.0	0.4	0.3	0.6	0.3	1.5	0.6	10.8	1.5	1.4
W182	0.1	0.0	0.0	0.0	0.0	0.0	0.0	0.0	0.0	0.0	0.0
Ir193	0.0	0.0	0.0	0.0	0.0	0.0	0.0	0.0	0.0	0.0	0.0
Au197	0.2	0.1	0.1	0.1	0.0	1.3	0.9	0.1	47.3	0.1	0.1
Hg202	0.7	0.6	0.6	0.7	0.8	0.7	0.8	0.8	1.0	0.9	0.8
Pb206	0.5	0.3	0.1	0.1	0.4	0.3	2.4	0.7	9.7	0.6	1.9
Pb207	0.8	0.2	0.2	0.2	0.6	1.1	3.6	0.7	11.2	0.5	2.3
Pb208	0.7	0.3	0.1	0.2	0.5	0.3	3.1	0.7	10.4	0.6	2.3
Bi209	12.9	3.7	0.4	0.8	1.0	3.3	14.2	10.9	56.4	2.2	11.6

Continued

Element	FTh 409.3.8 C3 Pyrite	FTh 409.3.8 R1 Pyrite	FTh 409.3.8.2 C2 Pyrite	FTh 409.3.8.2 R2 Pyrite	FTh 409.5.1.2 Pyrite	FTh 409.5.2.1 Pyrite	FTh 409.5.2.2 Pyrite	FTh 409.5.2.3 Pyrite	FTh 409.5.2.4 Pyrite	FTh 409.5.2.5 Pyrite	FTh 409.5.2.6 Pyrite
S34	278658	277021	296802	308999	988116	491027	462893	463850	444021	428082	424252
V51	0.1	0.1	0.1	0.3	43.8	0.1	0.0	0.1	0.4	0.1	0.3
Cr53	4.9	5.2	5.0	6.9	801.7	5.2	4.7	5.6	5.5	5.4	5.3
Mn55	7.2	411	157	3986	257	7.6	6.9	81.1	1377	23.8	7.6
Fe57	469962	469962	469962	469962	469962	469962	469962	469962	469962	469962	469962
Co59	0.0	0.1	0.1	0.1	34.9	0.1	0.2	0.2	1.5	0.0	1.3
Ni60	0.7	0.5	0.5	0.5	174	0.3	0.5	1.1	3.9	0.8	5.8
Cu65	2.9	2.7	3.3	24.6	398	4.6	25.7	52.7	110	20.1	26.4
Zn66	1.4	3.1	1.6	3.2	1459	4.6	5.6	37.3	30.8	67.3	44.9
Ga71	0.1	0.1	0.1	0.1	63.8	0.1	0.0	0.1	0.1	0.1	0.0
As75	4865	4505	5419	2171	14891	6450	7309	5990	9091	5641	7515
Se77	5.2	7.1	4.2	6.9	6039	9.4	5.6	7.8	7.6	7.0	5.9
Mo95	0.1	0.0	0.1	0.5	106	0.7	0.1	0.2	1.3	0.1	0.1
Ag107	0.0	0.1	0.1	0.4	16.0	0.0	0.0	0.4	0.8	0.2	0.2
Cd111	0.6	0.7	0.1	0.6	299	0.3	0.2	0.0	0.1	0.3	0.2
In115	0.0	0.0	0.0	0.1	0.6	0.0	0.0	0.0	0.1	0.0	0.0
Sn117	0.3	0.4	0.3	0.3	200	0.3	0.3	0.4	0.3	0.3	0.3
Sb121	0.1	2.2	0.2	1.0	42.0	0.7	0.4	1.5	8.6	1.2	2.4
Te125	0.1	0.3	0.6	0.3	0.0	1.5	0.0	0.6	1.4	0.9	1.1
W182	0.0	0.0	0.0	0.2	0.0	0.0	0.0	0.0	0.2	0.2	0.0
Ir193	0.0	0.0	0.0	0.0	0.0	0.0	0.0	0.0	0.0	0.0	0.0
Au197	0.0	0.2	0.1	0.0	58.9	0.3	0.1	0.4	0.8	0.7	1.2
Hg202	0.6	0.7	0.4	0.9	291	1.1	0.7	0.7	0.8	0.8	0.5
Pb206	0.3	1.1	0.4	4.1	112	0.7	0.2	4.3	7.6	0.8	2.1
Pb207	0.5	1.3	0.6	4.0	149	0.9	0.3	4.7	8.5	0.9	2.7
Pb208	0.4	1.2	0.4	4.1	79.6	0.8	0.3	4.2	8.4	1.0	2.3
Bi209	1.0	5.5	2.0	15.2	105	6.3	3.2	18.3	27.0	10.0	21.8

Continued

Element	FTh 409.5.3.1 C.2 Pyrite	FTh 409.5.3.1 R.1 Pyrite	FTh 409.5.3.2 C.1 Pyrite	FTh 409.5.3.2 C.2 Pyrite	FTh 409.5.3.2 C.3 Pyrite	FTh 409.5.3.2 C.4 Pyrite	FTh 409.5.3.2 C.5 Pyrite	FTh 409.5.3.2 R.1 Pyrite	FTh 409.5.3.2 R.2 Pyrite	FTh 409.5.4 C1 Pyrite
S34	408063	398936	415598	413354	420765	412545	407442	401608	411380	397541
V51	0.1	0.1	0.1	0.1	0.1	0.1	0.0	0.1	1.0	0.1
Cr53	5.2	5.9	4.6	5.0	5.4	4.5	4.7	4.7	6.9	6.3
Mn55	112	17.0	7.4	6.4	6.6	6.6	6.7	73.2	2875	6.9
Fe57	469962	469962	469962	469962	469962	469962	469962	469962	469962	469962
Co59	0.4	0.0	0.1	0.0	0.1	0.0	0.0	0.1	0.1	0.1
Ni60	2.7	0.4	0.3	0.7	1.3	0.2	0.2	1.0	6.9	0.5
Cu65	41.9	1.1	17.0	38.6	29.5	22.9	15.6	1.6	4.3	19.4
Zn66	25.7	14.1	137	11.5	11.2	3.2	18.3	2.6	26.9	45.8
Ga71	0.0	0.1	0.0	0.1	0.1	0.1	0.0	0.1	0.1	0.1
As75	7034	7426	6051	8074	8323	7709	6592	6650	5496	5616
Se77	6.1	7.8	6.1	5.2	5.1	5.6	5.1	8.6	7.6	8.7
Mo95	0.2	0.0	0.2	0.1	0.1	0.1	0.0	0.1	0.2	0.3
Ag107	0.2	0.0	0.0	0.1	0.0	0.0	0.2	0.0	0.3	0.0
Cd111	0.3	0.6	0.6	0.4	0.2	0.3	0.3	0.3	0.3	0.6
In115	0.0	0.0	0.0	0.0	0.0	0.0	0.0	0.0	0.3	0.0
Sn117	0.3	0.4	0.3	0.2	0.3	0.3	0.2	0.4	0.5	0.4
Sb121	0.8	0.2	0.5	0.6	0.5	0.1	0.4	0.3	1.1	0.5
Te125	0.3	0.0	0.2	0.5	0.2	0.1	0.4	0.2	0.2	0.1
W182	0.0	0.1	0.1	0.0	0.0	0.0	0.0	0.0	0.8	0.0
Ir193	0.0	0.0	0.0	0.0	0.0	0.0	0.0	0.0	0.0	0.0
Au197	0.1	0.0	0.1	0.2	0.1	0.3	0.1	0.0	0.1	0.2
Hg202	0.5	0.9	0.6	0.4	0.5	0.5	0.5	0.9	0.7	0.7
Pb206	1.2	0.2	0.3	0.6	0.2	0.1	0.6	0.6	6.5	0.7
Pb207	1.5	0.2	0.3	0.4	0.3	0.1	0.7	0.7	7.4	0.5
Pb208	1.4	0.2	0.3	0.6	0.3	0.1	0.7	1.0	6.6	0.6
Bi209	7.5	1.5	4.6	5.9	3.6	1.0	7.9	2.6	10.7	4.0

Continued

Element	BeW 1.1.1 Pyrite	BeW 1.1.2 Pyrite	BeW 1.1.3 Pyrite	BeW 3.1.1.1 Pyrite	BeW 3.1.1.2 Pyrite	BeW 3.1.1.3 Arsenopyrite	BeW 3.1.1.4 Pyrite	BeW 3.1.1.5 Pyrite	BeW 3.1.1.6 Pyrite	BeW 3.1.1.7 Pyrite
S34	201361	215160	228909	230566	233822	134452	232407	235112	231401	235761
V51	0.1	0.6	1.2	0.1	0.1	0.1	0.1	0.1	0.1	0.1
Cr53	6.3	6.0	7.6	6.9	6.8	5.6	5.8	6.8	5.9	7.5
Mn55	6.4	6.9	6.8	9.0	18.2	7.4	9.0	8.8	9.1	8.9
Fe57	469962	469962	469962	469962	469962	365336	469962	469962	469962	469962
Co59	41.7	6.4	196	0.1	0.4	0.1	0.2	0.7	0.7	0.2
Ni60	393	68.5	1395	2.8	1.2	0.6	0.4	1.2	0.9	0.3
Cu65	6.8	9.6	41.3	590	31.4	2.6	29.3	1.3	7.6	7.8
Zn66	2.7	13.3	19.6	4.4	9.5	2.0	80.2	14.2	0.7	3.0
Ga71	0.1	0.0	0.1	0.1	0.1	0.1	0.1	0.1	0.1	0.0
As75	3755	3086	2673	447	2076	239930	9069	6392	6556	9954
Se77	14.9	9.1	31.9	35.7	2.4	26.4	2.9	2.4	4.2	2.9
Mo95	0.0	0.0	0.2	0.3	0.2	0.5	0.2	0.3	0.1	0.4
Ag107	0.1	0.3	1.9	0.1	0.5	0.1	0.1	0.0	0.0	0.0
Cd111	0.1	0.1	0.1	0.2	0.6	0.1	0.1	0.0	0.4	0.1
In115	0.0	0.0	0.0	0.0	0.0	0.3	0.0	0.0	0.0	0.0
Sn117	0.1	0.3	0.4	0.5	0.4	0.5	0.5	0.4	0.4	0.4
Sb121	0.9	4.1	9.4	34.3	17.2	48.3	0.1	0.0	0.1	0.2
Te125	0.1	0.3	0.5	0.6	0.4	0.1	0.0	0.0	0.0	0.1
W182	0.1	0.9	1.0	0.0	0.0	0.0	0.0	0.0	0.0	0.0
Ir193	0.0	0.0	0.0	0.0	0.0	0.1	0.0	0.0	0.0	0.0
Au197	0.2	0.5	0.6	0.0	0.6	5.7	0.4	0.2	0.3	1.3
Hg202	0.3	0.3	0.4	0.5	0.5	0.9	0.4	0.4	0.5	0.4
Pb206	4.1	5.4	45.3	1829	21.1	0.5	0.2	0.1	0.1	0.1
Pb207	4.2	5.4	45.5	2018	19.5	0.6	0.2	0.1	0.1	0.1
Pb208	3.8	4.8	42.2	1934	19.7	0.3	0.1	0.1	0.1	0.1
Bi209	18.9	36.9	107	20880	6291	12.9	0.3	0.3	0.2	0.1

Continued

Element	BeW 3.1.1.8 Pyrite	BeW 3.1.1.9 Arsenopyrite	BeW 3.1.1.10 Pyrite	BeW 3.1.1.11 Pyrite	BeW 3.1.1.12 Pyrite	BeW 3.1.1.13 Pyrite	BeW 3.1.1.14 Pyrite	BeW 3.1.1.15 Pyrite	BeW 3.1.1.16 Pyrite
S34	240103	132212	237161	227692	227092	223689	221693	232872	224958
V51	0.1	0.4	0.1	0.1	0.1	0.1	0.1	0.1	0.1
Cr53	7.1	5.0	8.0	7.2	6.7	6.5	5.8	6.8	7.5
Mn55	9.2	7.7	9.6	9.4	9.0	9.1	20.0	9.3	9.3
Fe57	469962	365336	469962	469962	469962	469962	469962	469962	469962
Co59	0.7	0.1	0.2	0.3	0.2	0.4	0.2	0.1	0.1
Ni60	0.6	0.6	0.4	0.5	0.3	0.8	0.4	0.3	0.3
Cu65	18.7	14.7	0.5	4.0	7.9	11.9	10.5	4.1	4.7
Zn66	1.2	1.2	14.8	3.7	9.0	9.5	3.3	4.1	12.1
Ga71	0.1	0.1	0.1	0.1	0.1	0.1	0.1	0.1	0.1
As75	2173	234521	9824	7899	3705	8172	9018	9155	7833
Se77	2.5	33.7	4.4	3.0	3.7	3.4	3.6	2.3	3.4
Mo95	0.2	0.2	0.1	0.3	0.0	0.2	0.2	0.0	0.2
Ag107	0.1	0.1	0.1	0.0	0.1	0.0	0.2	0.0	0.0
Cd111	0.4	0.4	0.6	0.4	0.3	0.1	0.0	0.0	0.1
In115	0.0	0.3	0.0	0.0	0.0	0.0	0.0	0.0	0.0
Sn117	0.6	0.9	0.3	0.6	0.6	0.4	0.4	0.2	0.5
Sb121	1.2	86.3	0.1	0.1	0.0	0.1	0.9	0.4	0.2
Te125	0.2	0.5	0.1	0.0	0.1	0.1	0.0	0.6	0.6
W182	0.0	0.0	0.1	0.0	0.0	0.0	0.0	0.0	0.0
Ir193	0.0	0.0	0.0	0.0	0.0	0.0	0.0	0.0	0.0
Au197	0.1	5.1	1.1	2.3	0.1	1.4	3.1	0.3	1.2
Hg202	0.5	0.8	0.4	0.4	0.4	0.3	0.4	0.4	0.4
Pb206	46.6	3.3	0.1	0.1	0.1	0.1	1.2	1.3	0.2
Pb207	49.4	1.8	0.1	0.1	0.1	0.4	1.5	1.9	0.4
Pb208	49.0	1.6	0.0	0.1	0.0	0.0	1.4	1.6	0.3
Bi209	506	12.6	0.4	0.0	0.1	0.1	11.2	0.7	3.1

Continued

Element	BeW 3.1.1.17 Pyrite	BeW 3.1.1.18 Pyrite	BeW 3.1.1.19 Pyrite	BeW 3.1.1.20 Pyrite	BeW 3.1.2.1 Arsenopyrite	BeW 3.1.2.2 Arsenopyrite	BeW 3.1.2.3 Arsenopyrite	BeW 3.2.1.1 Chalcopyrite	BeW 3.2.1.2 Chalcopyrite
S34	216075	219192	219081	219544	161667	325232	137033	401877	318671
V51	0.1	0.1	0.1	0.1	49.4	42.4	0.7	0.8	0.4
Cr53	6.9	5.9	7.6	7.4	734	636	8.4	12.3	7.4
Mn55	9.7	9.2	9.4	8.9	127	102	9.2	5.7	13.0
Fe57	469962	469962	469962	469962	365336	365336	365336	303929	303929
Co59	0.1	0.0	0.1	0.6	38.8	25.9	0.5	0.4	0.2
Ni60	0.5	0.3	0.4	0.4	210	115	2.2	2.9	1.9
Cu65	25	295	478	0.8	1721	1065	8.2	414413	411127
Zn66	16.8	18.8	26.7	1.4	2178	990	10.5	87.7	120
Ga71	0.1	3.4	6.1	0.1	50.8	44.9	0.7	4.1	4.7
As75	1645	3148	1143	5739	725613	1277352	290938	204	179
Se77	2.6	3.6	4.0	2.7	902	982	20.2	21.7	13.1
Mo95	0.2	0.5	0.1	0.2	267	103	0.7	1.2	0.2
Ag107	0.0	0.2	0.4	0.0	37.1	37.9	0.2	0.2	0.2
Cd111	0.1	0.2	0.3	0.0	46.8	30.1	0.5	1.9	1.2
In115	0.0	3.5	17.2	0.0	16.0	6.8	0.3	27.4	31.2
Sn117	0.5	279	476	0.3	223	294	4.0	110	422
Sb121	0.1	1.2	1.3	0.2	267	584	69.0	2.4	1.4
Te125	0.1	0.1	0.0	0.1	259	0.0	0.0	0.3	2.3
W182	0.0	0.0	0.0	0.0	0.0	0.0	0.0	0.0	0.0
Ir193	0.0	0.0	0.0	0.0	23.0	0.0	0.0	0.0	0.0
Au197	0.2	0.9	0.2	0.1	3.9	0.0	7.5	0.4	0.5
Hg202	0.5	0.4	0.4	0.4	286	229	3.4	6.7	2.9
Pb206	0.1	0.2	0.3	0.1	51.5	32.8	0.6	1.2	1.0
Pb207	0.1	0.3	0.5	0.1	66.3	58.5	0.8	1.3	1.1
Pb208	0.1	0.3	0.5	0.0	44.8	18.6	0.5	1.1	1.3
Bi209	0.4	11.3	16.9	0.1	12.4	37.2	2.2	4.8	3.5

Continued

Element	BeW 3.2.1.3 Chalcopyrite	BeW 3.2.1.4 Chalcopyrite	BeW 3.2.1.5 Chalcopyrite	BeW 3.2.1.6 Chalcopyrite	BeW 3.2.1.7 Chalcopyrite	BeW 3.2.1.8 Chalcopyrite	BeW 3.2.1.9 Chalcopyrite	BeW 3.2.1.10 Chalcopyrite	BeW 3.2.1.11 Chalcopyrite
S34	299636	299224	296807	286352	270149	274705	276017	282717	289155
V51	0.3	0.3	0.4	0.2	0.2	0.2	0.3	0.2	0.3
Cr53	6.3	5.9	5.7	4.3	4.4	4.8	4.6	6.0	5.0
Mn55	8.8	4.4	3.8	4.4	5.3	4.6	4.2	4.6	4.4
Fe57	303929	303929	303929	303929	303929	303929	303929	303929	303929
Co59	0.2	0.2	0.2	0.1	0.1	0.2	0.2	0.2	0.2
Ni60	1.7	1.1	1.1	0.7	1.0	1.0	0.8	1.1	0.9
Cu65	415270	422162	406716	408606	412488	418320	418168	410255	411790
Zn66	97.3	103	107	109	140	116	105	212	180
Ga71	4.2	3.2	2.4	3.5	4.1	4.3	4.5	4.3	4.2
As75	167	175	165	131	110	108	105	118	131
Se77	12.7	12.2	12.6	9.1	9.1	8.5	9.2	8.1	10.6
Mo95	0.9	0.8	0.9	0.5	0.3	0.0	0.4	0.2	0.5
Ag107	0.4	0.2	0.2	0.2	0.3	1.0	0.3	0.3	0.3
Cd111	1.0	1.0	0.9	0.7	1.2	1.0	1.0	1.1	1.5
In115	31.2	31.8	30.8	29.4	34.2	31.4	31.7	31.6	31.1
Sn117	247	296	345	331	407	347	367	365	406
Sb121	2.5	2.4	1.0	0.8	4.6	1.0	1.7	3.7	1.2
Te125	0.0	1.8	0.2	0.0	1.0	0.0	0.0	1.4	2.3
W182	0.0	0.0	0.0	0.0	0.3	0.0	0.0	0.0	0.3
Ir193	0.0	0.0	0.0	0.0	0.0	0.0	0.0	0.0	0.1
Au197	0.5	0.6	0.5	0.6	0.7	0.6	0.5	1.2	0.2
Hg202	2.3	1.6	3.1	2.3	1.4	1.3	2.3	1.2	1.7
Pb206	1.4	1.6	1.0	1.0	1.0	0.7	1.4	1.4	0.4
Pb207	1.7	1.5	1.0	1.1	13.9	1.0	1.3	1.8	0.7
Pb208	1.6	1.8	1.1	1.0	0.9	0.8	1.3	1.7	0.7
Bi209	3.8	5.2	2.7	3.6	3.1	3.2	4.3	4.4	1.8

Continued

Element	BeW 3.2.1.12 Chalcopyrite	BeW 3.2.1.13 Chalcopyrite	BeW 3.2.1.14 Chalcopyrite	BeW 3.2.1.15 Chalcopyrite	BeW 3.2.1.16 Chalcopyrite	BeW 3.2.1.17 Chalcopyrite	BeW 3.2.1.18 Chalcopyrite	BeW 3.2.1.19 Chalcopyrite	BeW 3.2.1.20 Chalcopyrite
S34	284455	274294	282893	290388	270755	274242	279036	275687	281836
V51	0.3	0.2	0.3	0.3	0.3	0.3	0.3	0.2	0.2
Cr53	4.4	4.5	5.0	4.9	4.1	4.0	4.5	4.1	5.9
Mn55	4.4	4.7	4.7	4.8	4.7	4.7	4.9	4.8	6.8
Fe57	303929	303929	303929	303929	303929	303929	303929	303929	303929
Co59	0.1	0.1	0.2	0.2	0.1	0.1	0.1	0.1	0.1
Ni60	1.1	0.9	0.9	1.1	1.0	0.9	1.0	0.7	1.2
Cu65	415894	412780	410808	407610	413244	417307	411866	411303	403024
Zn66	248	222	712	154	149	134	255	580	193
Ga71	3.7	3.8	2.7	2.4	3.1	3.5	2.9	2.3	2.1
As75	122	108	135	123	122	100	118	128	138
Se77	10.3	8.6	9.0	8.1	8.8	12.5	15.1	11.6	11.6
Mo95	0.0	0.1	1.0	1.0	0.8	0.2	0.1	0.5	0.2
Ag107	0.2	0.3	0.3	0.2	0.4	0.4	0.4	0.7	1.1
Cd111	1.5	1.2	1.9	1.5	1.3	0.5	1.8	3.1	2.1
In115	32.3	32.7	31.7	30.4	32.6	32.1	31.0	33.4	31.0
Sn117	538	428	713	320	404	355	426	512	604
Sb121	1.4	0.7	6.8	2.8	0.4	0.7	15.7	18.3	42.1
Te125	0.0	1.5	0.0	1.7	0.0	0.0	0.0	0.0	0.1
W182	0.0	1.6	0.0	0.0	0.0	0.0	0.0	0.0	0.0
Ir193	0.0	0.0	0.0	0.0	0.0	0.0	0.1	0.0	0.0
Au197	0.4	0.6	0.7	0.5	0.6	0.6	1.1	1.4	1.6
Hg202	1.4	1.8	1.8	2.5	1.4	1.7	1.7	1.7	2.1
Pb206	0.7	0.6	0.4	1.0	0.7	1.7	3.3	5.3	9.7
Pb207	1.2	0.7	0.8	1.1	0.7	2.2	3.9	5.8	10.9
Pb208	1.0	0.6	0.6	1.2	0.7	1.9	3.4	5.3	9.9
Bi209	3.9	2.1	2.1	3.0	2.2	6.0	7.6	10.8	17.1

Continued

Element	BeW 3.2.2.1 Pyrite	BeW 3.2.2.2 Pyrite	BeW 3.2.2.3 Pyrite	BeW 3.2.2.4 Pyrite	BeW 3.2.2.5 Pyrite	BeW 3.2.2.6 Pyrite	BeW 3.2.2.7 Pyrite	BeW 3.2.2.8 Pyrite	BeW 3.2.2.9 Pyrite	BeW 3.2.2.10 Pyrite
S34	240252	241951	235997	238567	240995	240374	245580	236932	253261	240252
V51	0.1	0.1	0.1	0.1	0.1	0.1	0.1	0.1	0.1	0.1
Cr53	5.9	5.9	6.9	6.6	6.7	5.8	6.7	6.6	5.5	5.9
Mn55	8.1	7.3	7.8	7.0	7.7	7.6	7.5	8.6	8.0	8.1
Fe57	469962	469962	469962	469962	469962	469962	469962	469962	469962	469962
Co59	0.2	0.1	0.1	0.1	0.1	0.0	0.1	0.1	0.1	0.2
Ni60	0.3	0.3	0.4	0.4	0.4	0.3	0.3	0.6	0.2	0.3
Cu65	6941	75.6	731	527	700	552	474	498	226	6941
Zn66	45.2	37.9	72.2	35.0	37.1	22.6	18.2	39.2	21.9	45.2
Ga71	3.4	0.8	3.2	6.5	7.5	6.6	5.2	4.7	2.5	3.4
As75	213	6554	882	38.1	46.0	704	1245	85.5	4023	213
Se77	4.9	6.4	6.6	7.8	6.3	7.6	6.5	6.9	4.7	4.9
Mo95	0.2	0.2	0.2	0.2	0.2	0.0	0.0	0.2	0.0	0.2
Ag107	3.4	0.1	0.8	0.3	0.5	0.4	0.3	0.4	0.3	3.4
Cd111	0.2	0.1	0.1	0.1	0.1	0.3	0.2	0.2	0.2	0.2
In115	4.0	0.5	6.8	7.3	10.3	4.0	2.9	8.0	1.6	4.0
Sn117	239	70.1	224	509	720	455	436	335	188	239
Sb121	2.8	0.2	1.3	1.0	1.1	1.4	1.6	1.7	0.9	2.8
Te125	0.1	0.5	0.5	0.0	0.0	0.0	0.1	0.1	0.0	0.1
W182	0.0	0.0	0.0	0.0	0.0	0.0	0.0	0.0	0.0	0.0
Ir193	0.0	0.0	0.0	0.0	0.0	0.0	0.0	0.0	0.0	0.0
Au197	0.5	2.7	0.2	0.0	0.1	0.4	0.3	0.4	0.4	0.5
Hg202	0.4	0.4	0.4	0.4	0.4	0.4	0.4	0.3	0.3	0.4
Pb206	9.5	0.3	6.0	0.3	0.3	0.9	0.3	2.6	0.6	9.5
Pb207	10.7	0.4	6.8	0.3	0.6	1.2	0.4	2.8	0.6	10.7
Pb208	9.9	0.3	6.5	0.3	0.5	1.1	0.3	2.6	0.8	9.9
Bi209	50.6	2.6	52.3	9.2	11.1	8.5	14.2	19.9	9.0	50.6

Continued

Element	BeW 3.2.3.1 Pyrite	BeW 3.2.3.2 Pyrite	BeW 3.2.3.3 Pyrite	BeW 3.2.3.4 Pyrite	BeW 3.2.3.5 Pyrite	BeW 3.2.3.6 Pyrite	BeW 3.2.3.7 Pyrite	BeW 3.2.3.8 Pyrite	BeW 3.2.3.9 Pyrite	BeW 3.2.3.10 Pyrite
S34	250535	250988	265736	257838	246731	254020	249572	253714	238758	249783
V51	0.1	0.1	0.1	0.1	0.1	0.1	0.1	0.1	0.2	0.1
Cr53	5.9	6.1	6.4	6.4	6.5	6.5	7.4	6.1	7.5	6.3
Mn55	8.3	8.7	8.4	8.1	11.3	8.4	8.1	8.3	14.6	8.3
Fe57	469962	469962	469962	469962	469962	469962	469962	469962	469962	469962
Co59	0.1	0.1	0.1	0.1	0.4	0.1	0.1	0.1	0.1	0.1
Ni60	0.3	0.3	0.7	0.4	1.2	0.3	0.5	0.5	0.6	1.0
Cu65	66.3	2.0	51.4	7.6	29.9	703	481	1125	75.9	514
Zn66	2.8	9.3	1.3	1.3	6.6	37.0	29.0	16.0	3.6	15.5
Ga71	0.1	0.3	0.0	0.1	0.1	11.3	5.8	4.8	0.6	4.3
As75	8017	7424	5274	8283	3111	177	99.0	2931	5259	262
Se77	4.8	3.4	3.2	3.1	3.4	5.4	3.7	3.3	5.1	6.5
Mo95	0.2	0.2	0.0	0.2	0.2	0.4	0.0	0.1	0.1	0.3
Ag107	0.6	0.1	0.3	0.1	1.1	0.7	0.6	0.7	0.1	0.6
Cd111	0.6	0.0	0.3	0.3	0.4	0.5	0.2	0.3	0.1	0.5
In115	0.0	0.0	0.0	0.0	0.0	22.1	4.6	5.5	0.3	1.7
Sn117	0.4	0.4	0.5	0.7	0.4	704	497	295	57.6	362
Sb121	4.5	2.6	0.6	0.6	3.3	1.7	1.9	1.8	0.9	2.0
Te125	0.1	0.0	0.5	0.1	0.4	0.6	0.1	0.1	0.0	0.0
W182	0.0	0.0	0.0	0.1	0.0	0.0	0.0	0.0	0.0	0.0
Ir193	0.0	0.0	0.0	0.0	0.0	0.0	0.0	0.0	0.0	0.0
Au197	2.3	0.7	0.4	1.8	2.4	0.1	0.2	0.9	2.7	0.3
Hg202	0.4	0.4	0.5	0.4	0.3	0.5	0.4	0.4	0.3	0.4
Pb206	26.6	6.2	2.5	2.0	21.7	1.0	2.3	3.3	1.5	8.5
Pb207	32.8	7.0	3.0	2.5	26.6	1.2	3.1	4.5	1.7	10.6
Pb208	30.7	6.4	2.8	2.3	24.3	1.1	2.5	4.3	1.6	9.4
Bi209	40.7	6.4	14.7	3.7	62.1	14.4	23.3	15.3	10.9	32.2

Continued

Element	BeW 3.2.4.1 Chalcopyrite	BeW 3.2.4.2 Chalcopyrite	BeW 3.2.4.3 Chalcopyrite	BeW 3.2.4.4 Chalcopyrite	BeW 3.2.4.5 Chalcopyrite	BeW 3.2.4.6 Chalcopyrite	BeW 3.2.4.7 Chalcopyrite	BeW 3.2.4.8 Chalcopyrite	BeW 3.2.4.9 Chalcopyrite
S34	419013	305404	319070	201320	226487	197244	290694	285866	262537
V51	0.8	0.4	0.5	0.2	0.4	0.2	0.4	0.5	0.4
Cr53	12.2	7.2	6.3	5.7	5.0	5.1	6.5	6.7	7.0
Mn55	4.5	6.6	6.2	7.7	10.3	7.7	7.3	6.5	12.0
Fe57	303929	303929	303929	365336	365336	365336	303929	303929	303929
Co59	0.5	0.2	0.4	0.2	0.2	0.2	0.3	0.2	0.2
Ni60	2.4	1.3	1.5	1.2	1.1	0.8	1.9	1.8	1.3
Cu65	408119	402822	405857	119222	170954	137380	367371	360917	333718
Zn66	43.6	108	246	47.6	129	63.7	224	252	466
Ga71	1.4	1.5	0.6	0.3	0.6	0.4	1.3	1.2	1.0
As75	1008	241	125	200465	183149	201327	26848	31043	50225
Se77	25.4	12.9	17.5	27.3	22.7	21.2	10.6	17.1	12.4
Mo95	3.5	0.9	1.3	1.4	0.9	0.5	1.0	1.4	0.8
Ag107	2.9	1.6	1.6	2.0	0.9	1.9	1.2	0.5	1.5
Cd111	3.9	2.1	1.7	0.7	1.3	0.8	2.2	1.3	2.7
In115	27.0	30.4	29.3	10.7	13.2	9.3	25.4	22.5	24.4
Sn117	108	271	558	565	768	87.5	910	397	615
Sb121	16.7	28.2	34.0	100	67.4	61.3	30.2	25.5	29.3
Te125	0.0	2.5	2.5	0.7	0.4	0.2	0.6	3.8	0.4
W182	0.9	0.4	0.0	0.1	0.0	0.2	0.0	0.0	0.0
Ir193	0.0	0.1	0.0	0.0	0.0	0.0	0.0	0.0	0.0
Au197	1.6	3.2	2.8	3.6	2.4	25.3	3.1	2.0	0.9
Hg202	5.5	3.3	3.1	1.2	1.5	1.0	2.0	2.6	2.0
Pb206	16.3	16.9	11.7	33.2	13.1	7.6	10.8	13.6	14.5
Pb207	19.2	17.6	13.7	38.9	12.0	8.3	13.0	13.5	16.7
Pb208	19.4	17.0	12.1	34.6	11.2	8.3	13.0	11.2	15.5
Bi209	17.6	35.6	27.8	84.7	42.6	43.5	26.6	20.4	58.7

Continued

Element	BeW 3.2.4.10 Arsenopyrite	BeW 3.2.5.1 Arsenopyrite	BeW 3.2.5.2 Arsenopyrite	BeW 3.2.5.3 Arsenopyrite	BeW 3.2.5.4 Arsenopyrite	BeW 3.2.5.5 Arsenopyrite	BeW 3.2.5.6 Arsenopyrite	BeW 3.2.5.7 Arsenopyrite	BeW 3.2.5.8 Arsenopyrite
S34	162765	131261	124813	122897	123642	125489	126894	128165	125630
V51	0.2	0.2	0.1	0.1	0.1	0.1	0.1	0.2	0.2
Cr53	6.8	6.9	4.7	5.5	6.6	6.9	7.6	7.7	5.9
Mn55	8.1	8.0	7.7	7.6	7.8	9.0	8.2	7.9	7.6
Fe57	365336	365336	365336	365336	365336	365336	365336	365336	365336
Co59	0.1	0.1	0.1	0.1	0.1	0.1	0.1	0.1	0.1
Ni60	0.7	0.7	0.6	0.5	0.5	0.6	0.7	0.8	0.6
Cu65	48021	12.4	2.1	3.7	1.2	90.3	2.7	1.0	4.0
Zn66	26.5	1.4	2.3	1.3	0.8	0.9	1.2	0.8	3.3
Ga71	0.1	0.2	0.1	0.1	0.1	0.1	0.2	0.1	0.2
As75	204821	236023	240035	233571	234679	240602	248906	225691	232060
Se77	9.1	18.3	22.4	19.2	19.3	29.8	43.9	24.5	15.0
Mo95	0.4	0.1	0.6	0.4	0.7	0.5	0.5	0.6	0.5
Ag107	0.2	0.2	0.2	0.1	0.1	0.2	0.2	0.1	0.2
Cd111	0.3	0.2	0.4	0.4	0.0	0.2	0.5	0.6	0.0
In115	4.0	0.3	0.3	0.2	0.3	0.3	0.3	0.2	0.2
Sn117	42.1	0.7	0.4	0.4	0.4	0.9	0.5	0.7	0.5
Sb121	131	71.0	50.3	51.0	50.0	64.9	61.5	71.3	50.2
Te125	0.2	0.3	0.1	0.7	0.2	0.4	0.2	0.2	0.4
W182	0.9	0.1	0.0	0.0	0.0	0.0	0.0	0.1	0.0
Ir193	0.0	0.0	0.0	0.0	0.0	0.0	0.0	0.0	0.0
Au197	1.7	11.2	28.0	36.9	16.7	3.9	13.0	4.7	83.3
Hg202	0.8	0.9	0.6	0.6	0.6	0.7	1.1	0.7	0.7
Pb206	3.4	3.5	4.1	0.3	0.3	2.4	1.2	0.6	0.4
Pb207	4.0	4.0	5.0	0.2	0.2	3.3	1.3	1.2	0.7
Pb208	3.7	4.0	4.6	0.3	0.2	3.1	1.4	0.8	0.5
Bi209	28.2	17.4	11.1	1.2	2.6	14.8	10.9	8.8	5.9

Continued

Element	BeW 3.2.5.9 Arsenopyrite	BeW 3.2.5.10 Arsenopyrite	BeW 3.2.5.11 Arsenopyrite	BeW 3.2.5.12 Arsenopyrite	BeW 3.2.5.13 Arsenopyrite	BeW 3.2.5.14 Arsenopyrite	BeW 3.2.5.15 Arsenopyrite	BeW 3.2.5.16 Arsenopyrite	BeW 3.2.5.17 Arsenopyrite
S34	127625	130268	125724	117019	117296	116172	113921	111123	111129
V51	0.1	0.2	0.2	0.2	0.1	0.2	0.1	0.1	0.1
Cr53	5.0	7.9	4.6	5.5	5.4	9.1	5.3	5.7	5.0
Mn55	8.3	8.0	7.8	8.9	8.6	9.1	8.3	8.3	8.1
Fe57	365336	365336	365336	365336	365336	365336	365336	365336	365336
Co59	0.1	0.1	0.1	0.2	0.2	0.2	0.2	0.3	0.1
Ni60	0.9	0.8	0.6	0.8	1.1	1.4	0.9	1.5	1.2
Cu65	1.9	1.2	4.7	125	2.2	5.5	1.2	4.6	1.4
Zn66	1.1	0.9	6.4	4.0	2.4	1.7	1.6	2.6	1.2
Ga71	0.1	0.2	0.2	0.2	0.1	0.2	0.2	0.1	0.2
As75	243124	242101	240722	126925	129819	135014	118976	124837	121271
Se77	31.5	17.6	46.8	15.8	18.4	33.0	24.9	48.1	18.8
Mo95	0.6	1.1	0.7	0.7	0.4	0.5	0.5	0.3	0.2
Ag107	0.1	0.1	0.1	0.2	0.1	0.2	0.1	0.1	0.1
Cd111	0.1	0.6	0.8	0.1	0.5	0.4	0.1	0.0	0.4
In115	0.3	0.2	0.3	0.2	0.3	0.3	0.3	0.3	0.3
Sn117	0.6	0.5	0.7	1.0	0.5	0.8	0.4	1.0	1.0
Sb121	43.0	134	87.0	147	46.6	54.0	38.1	68.0	50.1
Te125	0.1	1.0	1.0	0.1	0.1	0.9	0.1	0.4	0.2
W182	0.0	1.0	0.2	0.8	0.0	0.0	0.0	0.0	0.0
Ir193	0.0	0.0	0.1	0.0	0.0	0.1	0.0	0.0	0.0
Au197	12.9	1.7	1.4	3.0	49.8	33.8	36.9	14.4	67.1
Hg202	0.8	0.7	0.9	0.8	0.8	0.7	1.0	0.9	0.7
Pb206	0.2	0.1	0.2	3.0	0.6	2.3	0.4	0.6	0.6
Pb207	0.2	0.3	0.3	3.5	0.6	2.8	0.5	0.8	0.7
Pb208	0.2	0.3	0.3	3.4	0.5	2.7	0.5	0.7	0.5
Bi209	2.9	13.2	7.3	25.1	4.8	19.2	2.4	5.1	7.9

Continued

Element	BeW 3.2.5.18 Arsenopyrite	BeW 3.2.5.19 Arsenopyrite	BeW 3.2.5.20 Arsenopyrite	BeW 3.2.6.1 Arsenopyrite	BeW 3.2.6.2 Arsenopyrite	BeW 3.2.6.3 Arsenopyrite	BeW 3.2.6.4 Arsenopyrite	BeW 3.2.6.5 Arsenopyrite	BeW 3.2.6.6 Arsenopyrite
S34	114377	114432	111858	110216	110247	112323	110160	111094	112859
V51	0.2	0.1	0.1	0.1	0.2	0.2	0.2	0.2	0.2
Cr53	5.3	5.0	5.4	5.3	6.1	3.1	6.4	6.0	6.1
Mn55	9.0	8.6	8.6	8.6	8.3	8.4	8.8	8.2	8.5
Fe57	365336	365336	365336	365336	365336	365336	365336	365336	365336
Co59	0.1	0.1	0.1	0.1	0.2	0.1	0.2	0.1	0.1
Ni60	0.7	0.7	0.8	0.7	0.6	0.7	1.0	0.9	0.6
Cu65	1.4	1.3	3.9	30.8	1.0	0.8	1.8	9.6	1.2
Zn66	1.0	1.1	0.7	3.2	1.5	1.2	1.0	0.9	1.2
Ga71	0.1	0.1	0.1	0.2	0.2	0.2	0.2	0.1	0.2
As75	120102	115765	110189	111250	108078	107959	105554	103364	97370
Se77	29.3	24.5	27.2	14.2	31.3	11.1	15.4	36.1	12.6
Mo95	0.3	0.5	0.1	0.4	0.4	0.4	0.4	0.5	0.4
Ag107	0.0	0.1	0.1	0.1	0.1	0.0	0.1	0.1	0.1
Cd111	0.1	0.1	0.0	0.7	0.0	0.5	0.8	0.7	0.5
In115	0.3	0.3	0.2	0.2	0.2	0.3	0.3	0.3	0.2
Sn117	0.3	0.6	0.6	0.7	0.7	0.7	0.5	0.5	0.8
Sb121	72.3	48.6	65.7	46.8	100	183	41.7	82.7	176
Te125	0.1	0.4	0.5	0.0	0.6	0.1	0.6	0.3	1.0
W182	0.0	0.0	0.0	0.0	0.0	1.2	0.2	0.0	0.8
Ir193	0.0	0.0	0.0	0.0	0.0	0.0	0.0	0.0	0.0
Au197	4.8	21.5	5.3	71.9	0.4	2.0	63.0	0.3	1.5
Hg202	0.6	0.7	0.8	0.7	0.9	0.7	1.0	0.8	0.8
Pb206	0.3	1.0	0.4	0.7	0.1	0.1	0.6	0.2	0.1
Pb207	0.5	1.2	0.8	0.5	0.1	0.3	1.2	0.2	0.2
Pb208	0.5	0.9	0.6	0.5	0.1	0.1	1.0	0.3	0.1
Bi209	4.7	8.8	6.0	4.9	4.7	23.6	10.7	4.5	20.5

Continued

Element	BeW 3.2.6.7 Arsenopyrite	BeW 3.2.6.8 Arsenopyrite	BeW 3.2.6.9 Arsenopyrite	BeW 3.2.6.10 Arsenopyrite	BeW 3.2.7.1 Chalcopyrite	BeW 3.4.1.1 Arsenopyrite	BeW 3.4.1.2 Arsenopyrite	BeW 3.4.1.3 Arsenopyrite	BeW 3.4.1.4 Arsenopyrite
S34	113263	111831	109770	110193	277976	143272	142755	140976	204268
V51	0.2	0.2	0.1	0.1	1.0	0.1	0.1	0.1	0.0
Cr53	6.2	5.6	6.0	6.2	14.9	5.3	2.7	4.4	4.9
Mn55	8.3	8.3	8.4	8.4	6.4	4.9	5.3	5.1	5.1
Fe57	365336	365336	365336	365336	303929	365336	365336	365336	365336
Co59	0.1	0.2	0.1	0.1	0.8	0.1	0.0	0.1	0.6
Ni60	0.5	0.8	0.9	0.9	5.3	0.5	0.4	0.3	1.2
Cu65	0.6	21.6	1.8	1.5	376328	3.5	46.6	18.2	2.7
Zn66	0.9	5.1	1.1	1.1	148.1	1.2	4.0	31.1	8.4
Ga71	0.1	0.4	0.2	0.2	1.6	0.1	0.1	0.1	0.0
As75	96866	96176	96929	94251	3542	204742	196490	194934	18403
Se77	12.8	11.8	25.4	27.2	19.3	41.3	26.8	27.1	3.9
Mo95	0.4	0.4	0.4	0.1	0.9	0.1	0.0	0.2	0.1
Ag107	0.0	0.2	0.1	0.1	0.6	0.4	0.1	0.1	0.0
Cd111	0.2	0.5	0.2	0.2	1.7	0.3	0.3	0.3	0.0
In115	0.3	0.3	0.3	0.3	24.5	0.3	0.4	0.3	0.0
Sn117	0.6	0.8	0.9	0.8	199	0.6	0.6	0.3	0.3
Sb121	171	40.6	60.1	67.8	3.7	90.8	54.7	55.9	2.1
Te125	0.3	0.1	1.0	0.9	0.6	0.2	0.7	0.1	0.1
W182	1.3	0.0	0.0	0.0	0.1	0.0	0.0	0.0	0.0
Ir193	0.0	0.0	0.0	0.0	0.0	0.0	0.0	0.0	0.0
Au197	2.0	51.2	22.5	22.1	0.7	1.9	8.3	5.3	0.5
Hg202	0.7	0.9	0.8	1.1	4.6	0.8	1.1	0.8	0.3
Pb206	0.2	0.4	0.6	0.6	0.9	4.8	2.1	2.1	0.1
Pb207	0.1	0.5	0.4	1.1	2.5	5.7	2.3	2.5	0.2
Pb208	0.2	0.6	0.6	0.8	0.9	5.1	2.3	2.4	0.1
Bi209	12.1	17.3	8.2	7.8	10.6	17.0	8.5	11.8	1.0

Continued

Element	BeW 3.4.1.5 Arsenopyrite	BeW 3.4.1.6 Arsenopyrite	BeW 3.4.2.1 Arsenopyrite	BeW 3.4.2.2 Arsenopyrite	BeW 3.4.2.3 Pyrite	BeW 3.4.2.4 Arsenopyrite	BeW 3.4.2.5 Arsenopyrite	BeW 3.4.2.6 Arsenopyrite	BeW 3.4.2.7 Arsenopyrite
S34	138455	139844	141545	138050	252139	136361	135310	143241	135437
V51	0.1	0.1	0.1	0.1	0.0	0.1	0.1	0.1	0.1
Cr53	4.8	5.1	5.3	5.4	6.6	5.6	4.4	2.9	5.2
Mn55	5.1	8.9	5.3	5.2	7.6	4.8	5.2	5.4	5.5
Fe57	365336	365336	365336	365336	469962	365336	365336	365336	365336
Co59	0.1	1.3	0.1	0.1	0.1	0.1	0.1	0.1	0.1
Ni60	0.5	0.4	0.7	1.1	0.3	0.8	0.4	0.5	0.5
Cu65	4.1	141	11.7	73.7	19.2	10.3	3.2	3.2	1.5
Zn66	1.1	7.4	1.0	28.4	8.0	12.8	3.9	6.8	2.0
Ga71	0.1	0.1	0.1	0.1	0.0	0.2	0.1	0.1	0.2
As75	210008	198759	178252	176415	25001	189557	189901	151706	147055
Se77	19.1	17.2	28.6	32.9	4.3	30.0	25.9	14.2	29.3
Mo95	0.3	0.0	0.1	0.3	0.0	0.2	0.2	0.4	0.1
Ag107	1.0	0.2	0.2	0.5	0.4	0.2	0.1	0.1	0.1
Cd111	0.3	0.2	0.2	0.5	0.2	1.0	0.3	0.1	0.0
In115	0.3	0.5	0.3	0.3	0.0	0.3	0.3	0.3	0.3
Sn117	0.3	0.5	0.4	0.5	0.2	0.3	0.5	0.8	0.5
Sb121	48.0	61.8	67.3	89.8	5.9	77.9	79.2	138	86.6
Te125	0.3	0.1	0.4	0.9	0.1	0.2	0.6	0.1	0.2
W182	0.0	0.0	0.2	0.1	0.0	0.0	0.1	0.7	0.1
Ir193	0.0	0.0	0.0	0.0	0.0	0.1	0.0	0.0	0.0
Au197	50.8	3.8	16.9	9.2	2.1	2.7	2.1	2.3	0.4
Hg202	0.9	0.9	0.9	0.6	0.4	1.0	0.8	0.8	1.3
Pb206	28.2	12.2	1.8	74.2	6.4	0.2	0.2	0.5	0.1
Pb207	36.9	14.1	2.6	91.3	7.0	0.3	0.2	0.5	0.1
Pb208	34.1	13.1	2.1	83.2	6.9	0.3	0.1	0.5	0.1
Bi209	29.9	15.1	41.4	1400	94.2	4.1	4.5	18.2	3.8

Continued

Element	BeW 3.4.3.1 C Pyrite	BeW 3.4.3.2 Pyrite	BeW 3.4.4.1 Pyrite	BeW 3.4.4.2 Pyrite	BeW 3.4.4.3 Pyrite	BeW 3.4.5.1 Arsenopyrite	BeW 3.4.5.2 Arsenopyrite	BeW 3.4.5.3 Arsenopyrite	BeW 3.4.5.4 Arsenopyrite
S34	249223	241252	246041	256064	254238	136461	136235	134956	134140
V51	0.2	0.1	0.1	0.0	0.0	0.1	0.1	0.1	0.1
Cr53	5.7	6.1	6.0	6.3	5.2	3.6	5.4	4.1	3.8
Mn55	6.7	7.9	7.3	6.6	6.8	5.6	5.7	5.7	5.6
Fe57	469962	469962	469962	469962	469962	365336	365336	365336	365336
Co59	0.1	0.2	0.5	0.4	0.8	0.1	0.0	0.1	0.1
Ni60	0.2	0.2	0.5	0.3	0.5	0.4	0.3	0.5	0.6
Cu65	7.3	40.1	2.0	2.1	2.0	160	209	1.6	1.6
Zn66	2.6	2.3	1.7	2.1	1.8	3.0	1.6	7.3	3.5
Ga71	0.1	0.1	0.0	0.1	0.1	0.1	0.1	0.1	0.1
As75	7096	6505	4568	6068	5681	160203	174893	152833	144612
Se77	3.0	3.3	3.0	2.8	4.1	25.8	10.7	25.0	22.0
Mo95	0.2	0.0	0.1	0.2	0.0	0.2	0.2	0.1	0.3
Ag107	0.0	0.3	0.1	0.0	0.0	0.4	1.8	0.1	0.1
Cd111	0.2	0.1	0.2	0.2	0.5	0.3	0.3	0.1	0.2
In115	0.0	0.0	0.0	0.0	0.0	0.4	0.6	0.3	0.2
Sn117	0.4	2.9	0.3	0.3	0.4	0.4	18.4	0.3	0.7
Sb121	0.3	0.7	0.6	0.1	0.1	50.9	42.9	51.8	41.4
Te125	0.0	0.0	0.1	0.0	0.2	0.8	0.4	0.2	0.1
W182	0.0	0.0	0.0	0.0	0.0	0.0	0.0	0.0	0.0
Ir193	0.0	0.0	0.0	0.0	0.0	0.0	0.0	0.0	0.0
Au197	1.7	1.2	0.3	1.2	2.1	6.6	23.0	3.6	31.3
Hg202	0.5	0.4	0.4	0.4	0.5	0.7	0.5	1.2	0.8
Pb206	0.2	1.9	0.3	0.1	0.1	11.9	22.2	1.2	0.7
Pb207	0.1	2.4	0.2	0.2	0.1	13.2	26.2	1.6	0.6
Pb208	0.1	2.3	0.2	0.1	0.1	12.5	23.9	1.2	0.6
Bi209	2.6	21.3	5.2	0.2	0.2	35.2	90.8	5.8	6.2

Continued

Element	BeW 3.4.5.5 Arsenopyrite	BeW 3.4.5.6 Pyrite	BeW 3.4.5.7 Pyrite
S34	132966	229764	228906
V51	0.1	0.1	0.0
Cr53	6.3	7.0	7.0
Mn55	5.6	8.4	8.7
Fe57	365336	469962	469962
Co59	0.1	0.2	0.4
Ni60	0.3	0.9	1.1
Cu65	30.6	250	10.4
Zn66	4.0	75.3	5.4
Ga71	0.1	3.1	0.1
As75	155571	2523	5389
Se77	32.2	7.0	3.5
Mo95	0.2	0.0	0.3
Ag107	0.5	5.8	0.4
Cd111	0.3	1.6	0.1
In115	0.3	2.7	0.0
Sn117	0.4	151	0.2
Sb121	52.7	8.3	1.2
Te125	2.0	0.4	0.0
W182	0.0	0.0	0.0
Ir193	0.0	0.0	0.0
Au197	7.9	2.4	0.9
Hg202	0.7	0.5	0.4
Pb206	41.9	277	3.1
Pb207	47.1	316	2.2
Pb208	44.4	292	1.7
Bi209	609	963	19.5

Electron Microprobe Data

Electron microprobe analysis has been used to confirm a number of the set standards. The results show that there are variations within the Fe content of minerals of the tetrahedrite-tennantite series. For this study a set standard has been used, thereby introducing an error on the analysis. Pyrite, arsenopyrite and chalcopyrite show a composition close to the stoichiometric composition.

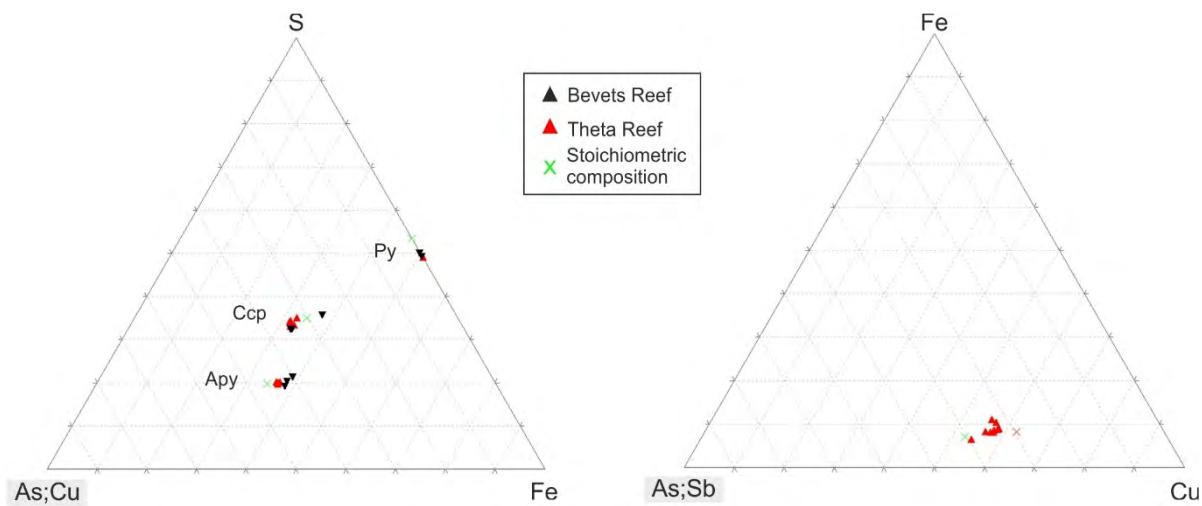


Figure 5.3.2: Ternary diagrams showing the stoichiometric composition of pyrite, arsenopyrite, chalcopyrite (left) and of minerals of the tetrahedrite-tennantite series (right) in relation to the idealized stoichiometry (in the right diagram ✕ indicates the idealised composition of tetrahedrite and ✖ of tennantite).

All values are in wt%

No.	As	Cu	Fe	S	Ni	Sb	Co	Pb	Total
FTh 406.4.1 Dark 1	0.0	33.8	31.2	33.4	0.0	0.0	0.0	0.0	98.5
FTh 406.4.1 Dark 2	43.5	0.4	36.8	19.9	0.0	0.0	0.0	0.0	101
FTh 406.4.1 Dark 3	43.8	0.3	36.5	19.8	0.0	0.0	0.0	0.2	101
FTh 406.4.1 Light	9.4	40.3	5.8	25.5	0.0	14.2	0.0	0.0	95.2
FTh 406.4.1 Pyrite	0.5	0.0	47.7	49.5	0.0	0.0	0.1	0.1	98.0
FTh 406.4.1 Dark	0.0	33.6	31.5	31.9	0.0	0.1	0.0	0.1	97.2
FTh 406.4.6 Dark	0.0	33.7	31.4	31.7	0.0	0.0	0.0	0.1	97.0
FTh 406.4.6 Light	43.9	0.2	36.6	19.5	0.0	0.0	0.0	0.1	100
FTh 406.4.6 Light	45.1	0.2	37.1	20.4	0.0	0.0	0.0	0.2	103
FTh 406.4.6 Light	9.1	40.3	5.5	23.9	0.0	14.7	0.0	0.0	93.5
FTh 406.4.6 Light	1.6	38.2	4.3	23.1	0.0	26.2	0.0	0.0	93.5
FTh 406.4.3 Pyrite	9.0	40.2	5.5	24.2	0.0	15.6	0.0	0.0	94.4
FTh 406.4.3 Intermediate	10.2	40.5	5.9	24.3	0.0	12.7	0.0	0.0	93.6
FTh 406.4.3 Darkest	12.2	41.1	6.0	24.8	0.0	10.8	0.0	0.0	95.0
FTh 406.4.3 Lightest	8.1	39.8	5.4	23.5	0.0	16.2	0.0	0.0	93.0
bew3.3 1 As-Pyrite	40.9	0.0	37.4	20.4	0.0	0.0	0.0	0.0	98.7
bew3.3 1 As-Pyrite dark	39.5	0.0	38.2	21.4	0.0	0.0	0.0	0.2	99.3
bew3.3 1 Pyrite	0.7	0.0	48.2	47.3	0.0	0.0	0.0	0.1	96.4
bew3.3 2 As-pyrite	41.7	0.0	37.4	19.2	0.0	0.0	0.0	0.0	98.2
bew3.3 1 Chalcopyrite	0.1	21.5	30.0	28.9	0.0	0.0	0.0	0.0	80.4
bew3.3 2 Chalcopyrite	0.0	33.4	31.8	31.7	0.0	0.0	0.0	0.0	96.9
bew3.3 2 Arsenopyrite	0.0	33.6	31.5	31.5	0.0	0.0	0.0	0.0	96.7
bew3.3 2 Pyrite	0.8	0.0	48.1	47.5	0.0	0.0	0.0	0.2	96.7
Minimum	0.0	0.0	4.3	19.2	0.0	0.0	0.0	0.0	80.4
Maximum	45.1	41.1	48.2	49.5	0.0	26.2	0.1	0.2	103
Average	15.7	20.5	27.4	28.0	0.0	4.8	0.0	0.1	96.4
Sigma	18.7	18.7	15.7	9.2	0.0	7.9	0.0	0.1	4.4

No.	As	Cu	Fe	S	Ni	Sb	Co	Pb	Total
FTh 204.3.1 Dark	0.0	33.8	31.4	33.8	0.0	0.0	0.0	0.0	99.2
FTh 204.3.1 Light	8.2	39.3	5.6	25.5	0.0	16.8	0.0	0.0	95.3
FTh 204.3.1 Light	7.9	39.8	5.7	25.4	0.0	17.3	0.0	0.0	96.1
FTh 204.3.2 Lark	0.0	32.7	32.0	32.2	0.0	0.0	0.0	0.2	97.2
FTh 204.3.3 Light	12.0	40.3	7.8	25.8	0.0	11.8	0.0	0.2	97.9
FTh 204.3.3 Pyrite	0.0	0.0	48.1	50.2	0.0	0.0	0.0	0.2	98.5
FTh 204.3.4 Light	12.0	40.8	7.2	26.1	0.0	11.3	0.0	0.0	97.4
FTh 204.3.6 Dark	0.0	33.7	31.5	33.4	0.0	0.0	0.0	0.0	98.7
Minimum	0.0	0.0	5.6	25.4	0.0	0.0	0.0	0.0	95.3
Maximum	12.0	40.8	48.1	50.2	0.0	17.3	0.0	0.2	99.2
Average	5.0	32.6	21.2	31.5	0.0	7.2	0.0	0.1	97.5
Sigma	5.6	13.6	16.5	8.4	0.0	7.9	0.0	0.1	1.3

Pb-Isotope Analysis

Lead isotope ratios have been calculated using LA-ICP-MS results in counts per second (cps). $^{207}/^{206}\text{Pb}$ and $^{208}/^{206}\text{Pb}$ ratios have been calculated for all samples with a ^{206}Pb content over 600 cps.

The calculated $^{207}/^{206}\text{Pb}$ and $^{208}/^{206}\text{Pb}$ have been standardised against the real $^{207}/^{206}\text{Pb}$ and $^{208}/^{206}\text{Pb}$ of the USGS MASS 1 standard and then normalised against the measured average of the Massst 1 $^{207}/^{206}\text{Pb}$ and $^{208}/^{206}\text{Pb}$ ratios.

Pb-Isotope Data

Sample	FTh405.2.4.1 Tetrahedrite	FTh405.2.4.2 Tetrahedrite	FTh405.2.4.4 Pyrite	FTh405.2.5.3 R1 Tetrahedrite	FTh405.2.5.5 Tetrahedrite	FTh405.2.5.7 Pyrite	FTh405.2.5.8 Chalcopyrite	FTh405.2.7.1 R1 Pyrite
Pb206	1044	3687	1116	14599	2315	2031	1539	1031
Pb207	991	3369	990	12635	1984	1775	1321	904
Pb208	2261	7627	2398	30850	4786	4734	3108	2281
Pb 207/206	0.95	0.91	0.89	0.87	0.86	0.87	0.86	0.88
Pb 208/206	2.17	2.07	2.15	2.11	2.07	2.33	2.02	2.21
Pb 207/206 Real	0.78							
Pb 208/206 Real	1.94							
Pb 207/206 Real/Mean	0.82	0.85	0.88	0.90	0.91	0.89	0.91	0.89
Pb 208/206 Real/Mean	0.90	0.94	0.90	0.92	0.94	0.83	0.96	0.88
Average MASS1 Pb 207/201	1.00							
Average MASS1 Pb 208/206	0.96							
Normalised vs Standard								
Pb 207/206	0.95	0.91	0.89	0.87	0.86	0.87	0.86	0.88
Pb 208/206	2.07	1.98	2.06	2.02	1.98	2.23	1.93	2.12

Continued

Sample	FTh405.2.7.6 Pyrite	FTh405.2.8.1 C1 Pyrite	FTh405.2.8.1 R1 Pyrite	FTh405.2.8.2 Pyrite	FTh405.2.8.3 Pyrite	FTh 406.1.2 C1 Pyrite	FTh 406.1.2 R1 Pyrite
Pb206	6388	4495	15575	77597	43043	614	1642
Pb207	5643	3929	13702	67225	36502	524	1461
Pb208	13627	9624	33319	160561	89219	1250	3436
Pb 207/206	0.88	0.87	0.88	0.87	0.85	0.85	0.89
Pb 208/206	2.13	2.14	2.14	2.07	2.07	2.04	2.09
Pb 207/206 Real	0.78						
Pb 208/206 Real	1.94						
Pb 207/206 Real/Mean	0.88	0.89	0.88	0.90	0.92	0.91	0.87
Pb 208/206 Real/Mean	0.91	0.91	0.91	0.94	0.94	0.95	0.93
Average MASS1 Pb 207/201	1.00					1.01	
Average MASS1 Pb 208/206	0.96					0.96	
Normalised vs Standard							
Pb 207/206	0.88	0.87	0.88	0.87	0.85	0.86	0.89
Pb 208/206	2.04	2.05	2.05	1.98	1.98	1.96	2.02

Continued

Sample	FTh 406.4.4 C1 Arsenopyrite	FTh 406.4.4 C2 Arsenopyrite	FTh 406.4.5 R2 Arsenopyrite	FTh 406.4.5 C3 Arsenopyrite	FTh409.1.2 C1 Pyrite	FTh409.1.2 C2 Pyrite	FTh409.1.2 C4 Pyrite
Content [cps]							
Pb206	999	651	1095	716	34872	55085	53107
Pb207	864	620	1180	613	33823	53483	52108
Pb208	2057	1509	2572	1350	80131	126943	124317
Pb 207/206	0.86	0.95	1.08	0.86	0.97	0.97	0.98
Pb 208/206	2.06	2.32	2.35	1.89	2.30	2.30	2.34
Pb 207/206 Real	0.78				0.78		
Pb 208/206 Real	1.94				1.94		
Pb 207/206 Real/Mean	0.90	0.82	0.72	0.91	0.80	0.80	0.79
Pb 208/206 Real/Mean	0.94	0.84	0.83	1.03	0.84	0.84	0.83
Average MASS1 Pb 207/201	1.01				1.01		
Average MASS1 Pb 208/206	0.96				0.97		
Normalised vs Standard							
Pb 207/206	0.87	0.96	1.08	0.86	0.98	0.98	0.99
Pb 208/206	1.98	2.23	2.26	1.82	2.24	2.24	2.28

Continued

Sample	FTh409.1.2 C5 Pyrite	FTh409.1.3.1 Pyrite	FTh409.1.3.2 Pyrite	FTh409.1.3.3 Pyrite	FTh409.1.3.4 Pyrite	FTh409.1.3.5 Pyrite	FTh409.1.4 C2 Pyrite	FTh409.1.4 C6 Pyrite
Content [cps]								
Pb206	34879	14205	30857	11172	31778	13028	1482	1109
Pb207	33379	14198	31261	11145	30910	12258	1488	911
Pb208	79624	33661	74155	26745	73656	31502	3496	2170
Pb 207/206	0.96	1.00	1.01	1.00	0.97	0.94	1.00	0.82
Pb 208/206	2.28	2.37	2.40	2.39	2.32	2.42	2.36	1.96
Pb 207/206 Real	0.78							
Pb 208/206 Real	1.94							
Pb 207/206 Real/Mean	0.81	0.78	0.77	0.78	0.80	0.83	0.77	0.95
Pb 208/206 Real/Mean	0.85	0.82	0.81	0.81	0.84	0.80	0.82	0.99
Average MASS1 Pb 207/201	1.01							
Average MASS1 Pb 208/206	0.97							
Normalised vs Standard								
Pb 207/206	0.97	1.01	1.02	1.01	0.98	0.95	1.01	0.83
Pb 208/206	2.22	2.31	2.34	2.33	2.26	2.35	2.30	1.90

Continued

Sample	FTh409.1.7.1 Pyrite	FTh409.5.2.3 Pyrite	FTh409.5.2.4 Pyrite	FTh409.5.3.2 R.2	BEW3.1.1.8 Pyrite	BEW3.1.1.1 Pyrite
Content [cps]						
Pb206	2848	848	1538	1029	6729	264039
Pb207	2994	729	1340	927	5537	226560
Pb208	6620	1720	3433	2126	14088	556650
Pb 207/206	1.05	0.86	0.87	0.90	0.82	0.86
Pb 208/206	2.32	2.03	2.23	2.07	2.09	2.11
Pb 207/206 Real	0.78					
Pb 208/206 Real	1.94					
Pb 207/206 Real/Mean	0.74	0.90	0.89	0.86	0.95	0.91
Pb 208/206 Real/Mean	0.83	0.96	0.87	0.94	0.93	0.92
Average MASS1 Pb 207/201	1.01	0.99			1.00	
Average MASS1 Pb 208/206	0.97	0.95			0.97	
Normalised vs Standard						
Pb 207/206	1.06	0.85	0.87	0.89	0.82	0.86
Pb 208/206	2.26	1.93	2.13	1.97	2.04	2.05

Continued

Sample	BEW3.1.1.2 Pyrite	BEW3.2.4.4 Chalcopyrite	BEW3.2.3.10 Pyrite	BEW3.2.3.5 Pyrite	BEW3.2.3.2 Pyrite	BEW3.2.3.1 Pyrite	BEW3.2.2.3 Pyrite
Content [cps]							
Pb206	3019	1781	1357	3898	1158	4792	1048
Pb207	2172	1624	1314	3735	1022	4609	929
Pb208	5622	3699	3002	8741	2372	11045	2296
Pb 207/206	0.72	0.91	0.97	0.96	0.88	0.96	0.89
Pb 208/206	1.86	2.08	2.21	2.24	2.05	2.30	2.19
Pb 207/206 Real	0.78						
Pb 208/206 Real	1.94						
Pb 207/206 Real/Mean	1.08	0.85	0.80	0.81	0.88	0.81	0.88
Pb 208/206 Real/Mean	1.04	0.93	0.88	0.86	0.95	0.84	0.89
Average MASS1 Pb 207/201	1.00						
Average MASS1 Pb 208/206	0.97						
Normalised vs Standard							
Pb 207/206	0.72	0.91	0.97	0.96	0.88	0.96	0.89
Pb 208/206	1.81	2.02	2.15	2.18	1.99	2.24	2.13

Structural Data

Strike	Dip	Strike	Dip	Strike	Dip
Stop 5		Stop 9		Stop 20	
180	12	160	12	156	6
190	20	160	10	160	8
194	12	160	10	166	10
200	15	172	12	170	8
208	20	188	7	170	10
210	4	190	6		
220	14	192	10	Stop 21	
		192	8	130	8
Stop 6		216	6	160	8
120	10			170	7
122	10	Stop 10		180	6
130	16	176	10	200	8
130	10	185	8		
134	14	188	5		
		196	8		
Stop 7		224	6		
142	6				
144	9	Stop 11			
160	12	136	8		
170	8	184	10		
170	7	194	20		
194	7	217	12		
200	12	224	8		
200	10	226	6		
204	18	254	6		
224	10				
		Stop 14			
Stop 8		160	8		
145	30	178	16		
148	22	200	4		
150	6	202	24		
154	28	202	14		
158	26	220	14		
160	36				
160	22	Stop 15			
164	5	170	5		
168	20	180	4		
168	5	182	6		
170	22	184	5		
170	10	198	4		
175	32				
178	16	Stop 17			
180	30	160	6		
194	10	166	10		
196	10	200	8		
202	10				
214	14				

Fractures

Strike	Dip	Strike	Dip	Strike	Dip
Set 9		Set 13		Set 16	
038	90	034	84	060	88
040	89	040	76	062	88
040	84	056	85	064	88
042	88	065	84	064	86
042	90	286	86	064	88
048	89	300	80	064	90
050	90	308	82	068	88
270	88	310	82	068	90
272	86			070	88
280	90	Set 14		312	78
288	88	40	90	312	84
288	84	254	88	314	86
288	82	260	87	315	80
292	88	268	86	318	82
300	84	270	86		
302	88	282	88	Set 17	
		290	84	005	90
Set 10				012	88
010	84	Set 15		018	88
038	90	002	88	062	84
040	78	004	90	062	80
292	86	004	84	066	88
300	88	008	90	070	86
320	90	010	90	298	88
		010	90	308	80
Set 11		056	90	310	88
054	88	060	88	312	90
056	84	062	80	314	88
058	90	064	88	320	80
060	88	065	78		
060	86	066	86		
068	90	066	90		
306	90	066	90		
306	88	066	82		
308	82	338	84		
314	82	348	84		
		348	90		
Set 12		350	88		
038	90	354	84		
046	90	358	88		
054	86	360	80		
056	88	360	84		
056	86				
058	88				
272	90				
285	88				
286	90				
288	90				

Strike	Dip	Strike	Dip	Strike	Dip
Set 18		Set 19		Set 21	
19	82	4	82	2	86
20	86	6	90	2	88
20	80	10	90	4	88
22	82	10	80	4	88
24	90	12	86	4	90
24	88	286	82	7	90
24	74	290	88	10	90
30	88	292	86	55	74
30	88	294	86	58	82
30	82	296	86	60	72
34	76	350	88	60	90
36	86	356	80	62	86
38	86			64	74
38	90	Set 20		68	82
40	74	4	88	70	84
46	86	6	90	284	82
46	84	8	90	294	86
50	86	10	90	294	90
52	88	10	84	296	82
294	90	10	88	300	83
297	88	12	88	302	88
298	86	246	90	352	84
298	90	254	88	354	82
298	90	256	86	356	80
298	88	258	88	356	86
300	90	260	86	356	85
300	84	260	84	358	78
302	90	260	88	358	88
308	82	262	86	358	88
312	84	268	84	358	90
316	86	270	88	360	90
317	82	300	90	360	84
318	80	304	88	360	88
318	88	306	88		
318	82	308	86		
318	90	310	88		
320	84				
322	82				
326	86				